MICROSTRUCTURAL CHARACTERIZATION, VISUALIZATION, AND SIMULATION OF Ti-B MATERIALS

A Dissertation
Presented to
The Academic Faculty

by

Scott I. Lieberman

In Partial Fulfillment
of the Requirements for the Degree
Doctor of Philosophy in the
School of Materials Science and Engineering

Georgia Institute of Technology
May 2007

MICROSTRUCTURAL CHARACTERIZATION, VISUALIZATION, AND SIMULATION OF Ti-B MATERIALS

Approved by:

Dr. Arun M. Gokhale, Advisor
School of Materials Science & Engineering
Georgia Institute of Technology

Dr. Samuel Graham
School of Mechanical Engineering
Georgia Institute of Technology

Dr. Hamid Garmestani
School of Materials Science & Engineering
Georgia Institute of Technology

Dr. Kimberly E. Kurtis
School of Civil & Environmental Engineering
Georgia Institute of Technology

Dr. David L. McDowell
School of Mechanical Engineering
Georgia Institute of Technology

Date Approved: March 16, 2007

ACKNOWLEDGEMENTS

Completion of this work would not have been possible without the expert guidance of my advisor, Professor Arun Gokhale. His calm and relaxed attitude has made this research a thoroughly enjoyable experience, even when circumstances required 16 hour days in the lab.

This research is part of a wider focus on materials characterization and materials design, and the collaborative efforts with colleagues Gautam Patel, Dr. Asim Tewari, Dr. Soon Gi Lee, Harpreet Singh, Arun Sreeranganathan, and Yuxiong Mao over the last few years are greatly appreciated. Additionally, my friends and colleagues in the School of Materials Science and Engineering have provided assistance, advice, and useful distractions without which my time at Georgia Tech would not have been so much fun. I must also thank my committee members, Professor Hamid Garmestani, Professor David McDowell, Professor Samuel Graham, and Professor Kimberly Kurtis, for their guidance and support of this work.

A crucial role in this research was contributed by the engineers at the Air Force Research Laboratory at Wright-Patterson Air Force Base that I have had the pleasure of working with, most notably Dr. Seshacharyulu Tamirisakandala, Dr. Jonathan Spowart, Dr. Daniel Miracle, Dr. Dale McEldowney, and Johnathan Johnson. Spending time at the AFRL facilities in Ohio was a highlight of this work.

This research has been supported through research grants from the Air Force Office of Scientific Research (AFOSR grant numbers F49620-01-1-0045 and FA95550-05-1-0062). Dr. Craig Hartley, Dr. Jaimie S. Tiley, and Dr. Brett Conner have been the

AFOSR Program Managers for these grants. This research has also been supported through a research grant from the Division of Materials Research of the United States National Science Foundation (NSF grant number DMR-0404668). Dr. Harsh Deep Chopra and Dr. Bruce A. MacDonald have been the NSF Program Managers for this grant. The financial support of both organizations is gratefully acknowledged.

Lastly, I would like to thank my family, both my parents and sister back home and all of my family members in Atlanta, for their consistent support and encouragement during my time at Georgia Tech.

TABLE OF CONTENTS

LIST OF TABLES

LIST OF FIGURES

SUMMARY

Additions of boron in modified titanium alloys and Ti-B composites result in the in situ formation during high temperature processing of TiB reinforcement phases that improve the mechanical properties and wear resistance of unreinforced titanium alloys, while still utilizing the high strength-to-weight ratio and excellent corrosion resistance of titanium. Several boron-modified titanium alloys and Ti-B composites in a Ti-6Al-4V matrix have been investigated to determine the effect of processing parameters on the TiB reinforcement phases and resultant microstructures and mechanical properties. Using optical microscopy, scanning electron microscopy, conventional characterization techniques, and newly developed methodologies for three-dimensional visualization, the microstructures of these Ti-B materials have been studied. Observations included a similar anisotropic whisker morphology with roughly hexagonal cross-sections among all TiB phases; alignment of all TiB phases with extrusion, with the extent of alignment affected by thermomechanical processing parameters; brittle fracture behavior of TiB whiskers, with fracture down the length of whiskers not aligned in the tensile direction and across the width of whiskers aligned in the tensile direction; and discoveries of the anisotropic morphologies of the coarse primary TiB phase and the sub-micron precipitated TiB phase. It has been observed that extruded boron-modified alloys with compositions in the hypoeutectic regime of the quaternary system of titanium, alloying elements aluminum and vanadium, and boron, containing a unimodal size distribution of eutectic TiB whiskers, significantly improve the strength and stiffness compared to unreinforced Ti-6Al-4V alloy while also demonstrating tensile elongation to failure

within the fracture-critical limits required for aerospace structural applications. Materials design methodologies have been developed using Ti-B materials, and they show promise for predicting the effects of processing parameters and the resultant microstructures and mechanical properties for boron-modified titanium alloys and Ti-B composites optimized for a variety of commercial and industrial applications.

CHAPTER 1

PROBLEM FORMULATION AND RESEARCH OBJECTIVES

In the development of titanium alloys and composite materials, the addition of boron has emerged as an effective way to provide significant improvements to important properties including strength, stiffness, and wear resistance. Innovations made with Ti-B materials to this point have resulted from conventional metallurgical techniques that have been similarly used to create other metal alloys and composites. The TiB reinforcement phase in boron-modified titanium, however, is unique in that it forms in situ during processing. In addition, Ti-B materials have been formed using a wide variety of processing methods and conditions, and with a range of initial constituent materials.

The complexity of the microstructures of Ti-B materials, along with the variety of processing schemes and the in situ formation of TiB, mean that traditional research and development methods are insufficient for complete and accurate application of these alloys and composites. The viability of different processing methods have been verified, and the mechanical properties of many of these Ti-B materials have been studied, but an in-depth understanding of the relationships between the microstructure, processing, and resultant properties has required further investigation. To design a Ti-B material with a desired set of properties, it is essential to know how the processing methods affect the microstructure, and how the microstructure affects the properties of interest. This is especially of relevance for Ti-B materials because sufficient processing flexibility exists for the generation of a wide range of different microstructures.

The focus of this research has been to investigate the microstructures of Ti-B materials, and determine the relationships between the microstructure, processing methods, and resultant properties. It is hoped that this work will result in more efficient materials design of Ti-B modified alloys and composites. More specifically, research objectives included:

1. Unbiased quantitative characterization and representation of the microstructures of Ti-B materials utilizing conventional and newly developed stereological methods on two-dimensional (2D) examples.
2. Creation of digital three-dimensional (3D) microstructures of Ti-B materials using serial sectioning techniques.
3. Determining the relationships between the processing methods of these materials and the critical aspects of the microstructures with respect to the resultant mechanical properties of interest.
4. Developing the foundation for the methods to be developed for the simulation of real microstructures and the creation of virtual microstructures to be used in materials design of Ti-B modified alloys and composites.

The results of this work have provided the groundwork for a modern and efficient materials design methodology combining traditional metallurgical techniques with computer simulations, a vast improvement over what has historically been a haphazard, trial-and-error materials development approach. In addition, knowledge gained and

discoveries made during this research will help with the implementation of Ti-B materials in a variety of commercial and industrial applications.

CHAPTER 2

BACKGROUND AND LITERATURE REVIEW

2.1 Introduction

The high strength-to-weight ratio and excellent corrosion resistance of titanium began to garner interest in the metal soon after World War II, following the invention and development of the commercial Kroll production process. However, the poor wear resistance and relatively low modulus of pure titanium and early alloys spawned research into titanium-based modified alloys and metal matrix composite materials (MMCs) to improve the overall mechanical properties. With the development of discontinuously reinforced titanium matrix MMCs (also known as DRTi composites), and modified alloys containing titanium boride whiskers, it has been shown that adding even relatively small additions of boron to conventional titanium alloys can provide significant improvements to important properties, including strength, stiffness, wear resistance, and microstructural stability.

The in situ formation of TiB reinforcement has been achieved using a variety of processing methods and numerous initial constituent compositions [1]. Titanium MMCs with TiB whisker reinforcement and boron-modified titanium alloys are already in some commercial use in the aerospace and automotive industries and for some sporting goods applications, and show promise for a further variety of applications in these fields as well as for the biomedical industry. Ti-B materials are beginning to compete with steel alloys, particularly in applications where the superior corrosion resistance and lighter weight are important. Cost factors, however, are preventing most commercial interests from looking

into further development of Ti-B alloys and composites, with the traditional research and development methods too complex for the economic viability of a change in material. Further understanding of Ti-B materials, providing for a more efficient materials development scheme, will make the upgrade from steel a legitimate design option.

2.2 Titanium Alloys and Composites

Titanium was a lab curiosity until the mid-1940s, when Kroll developed a commercial production process, reducing titanium tetrachloride ($TiCl_4$) with magnesium. The metal's high strength-to-weight ratio and excellent corrosion resistance led to research into titanium use as an alternative to steel and aluminum. By the late 1950s, titanium was dubbed the "wonder metal". The excellent mechanical properties of titanium alloys showed promise, but the high costs led to development mostly in aerospace applications, particularly the SR-71 reconnaissance jet and the F-22 fighter jet, with approximately 45 percent of the latter constructed from titanium alloys and MMCs [2, 3].

The poor wear resistance and relatively low modulus of early unreinforced titanium alloys led to the development of titanium matrix MMCs. Early work on titanium MMCs used the lessons learned from research and development of aluminum matrix MMCs, utilizing similar reinforcement choices and production processes. Significant early work by NASA and the aerospace industry, the military, and Formula 1 auto racing teams unfortunately was not published or studied in detail beyond the projects' specific scope.

Research into Ti-B alloys and composites began in the late 1950s, but commercial applications were not established until the 1980s [4]. Prior composite reinforcements,

including Al_2O_3, SiC, Si_3N_4, and B_4C, that had proven compatible in other metal matrices such as steel and aluminum alloys, were found to be unsuitable in titanium alloys due to the reactivity of molten titanium. Adding boron, forming Ti-B modified alloys and composites, proved to be compatible with conventional processing techniques developed for unreinforced titanium alloys.

Metal matrix composites have become a class of established engineering materials relatively recently, and there is no simple definition for MMCs that is generally accepted within the materials community [5]. Recent efforts to establish a consensus have proposed that MMCs are materials where the reinforcement remains distinct throughout the process history. Therefore, Ti-B materials that have hypereutectic compositions are best classified as discontinuously reinforced titanium MMCs; Ti-B materials with hypoeutectic compositions are considered boron-modified titanium alloys, because unlike MMCs they have microstructures, processing, and property combinations similar to alloys without boron [6]. In a similar attempt to standardize the terminology in the field, the organizers of the 2005 conference "A Workshop on Titanium Alloys Modified with Boron" have proposed that the term "Ti-B materials" be used for both titanium MMCs with TiB reinforcement and for boron-modified titanium alloys, materials that have previously been referred to in published literature as "Ti-TiB", "Ti/TiB", "TMC", "TiB dispersed titanium composite", "TiB/Ti", and "TiB reinforced titanium MMC".

2.2.1 Ti-6Al-4V Alloy

The most widely used titanium alloy is Ti-6Al-4V, which accounts for more than half of the overall worldwide titanium tonnage [1]. It is considered the "workhorse of the titanium industry" [7]. The aluminum addition stabilizes the hcp α phase, which

increases the overall strength of the resultant alloy. The vanadium addition introduces bcc β phase into the α matrix, increasing ductility and fracture toughness. Ti-6Al-4V is considered an α-rich α+β alloy.

Ti-6Al-4V allows for a wide spectrum of mechanical property combinations depending on the thermomechanical processing (TMP) history [8]. The β-transus temperature, where the phase transformation $\alpha+\beta \rightarrow \beta$ takes place, is the critical parameter for TMP of this alloy, and has been reported to be approximately 1000°C [9]. Entirely different microstructures evolve depending on whether the alloy is processed above or below this temperature. For what is known as β or primary processing, above the β-transus, the microstructure consists of lamellar colonies of α and β in large β grains of approximately 200 μm, and the resultant alloy has high strength and fracture toughness. For α+β or secondary processing, below the β-transus, the resultant alloy has an equiaxed microstructure, with excellent ductility and resistance to crack initiation under low-cycle fatigue loading. Recent research has begun efforts to develop rigorous methods for quantifying the important features of these complex microstructures [10].

Oxygen content also affects the mechanical properties of the alloy, with the element acting as an α stabilizer. The standard grade, used for strength-critical applications, contains 0.16-0.20 wt % O. The extra-low interstitial (ELI) grade, used for toughness-critical applications, contains 0.10-0.13 wt % O.

Although Ti-6Al-4V has a high strength-to-weight ratio, there are some poor mechanical properties associated with the alloy. Along with other titanium alloys, it has notoriously poor tribological properties, including wear and abrasion resistance [11]. Ti-6Al-4V also has poor high temperature properties, softening at 300°C, although this does

allow for superplastic forming (SPF), which is now a well-established commercial process for this alloy [1]. Extreme reactivity restricts casting of the alloy, and it forms reaction products with SiC, Al_2O_3, Si_3N_4, and B_4C. Molten titanium also poorly wets nearly all commercial reinforcements.

2.2.2 TiB Reinforcement

Lack of compatibility with traditional metal matrix composite reinforcements led researchers to examine other material options. The Ti-B binary phase system was a viable choice, as shown in the Ti-B phase diagram in Figure 2.1 [12]. Boron is essentially insoluble in titanium, leading to a stable TiB intermetallic phase which forms from a eutectic reaction. The phase diagram also predicts that small amounts of boron in titanium will form a relatively high volume fraction of TiB.

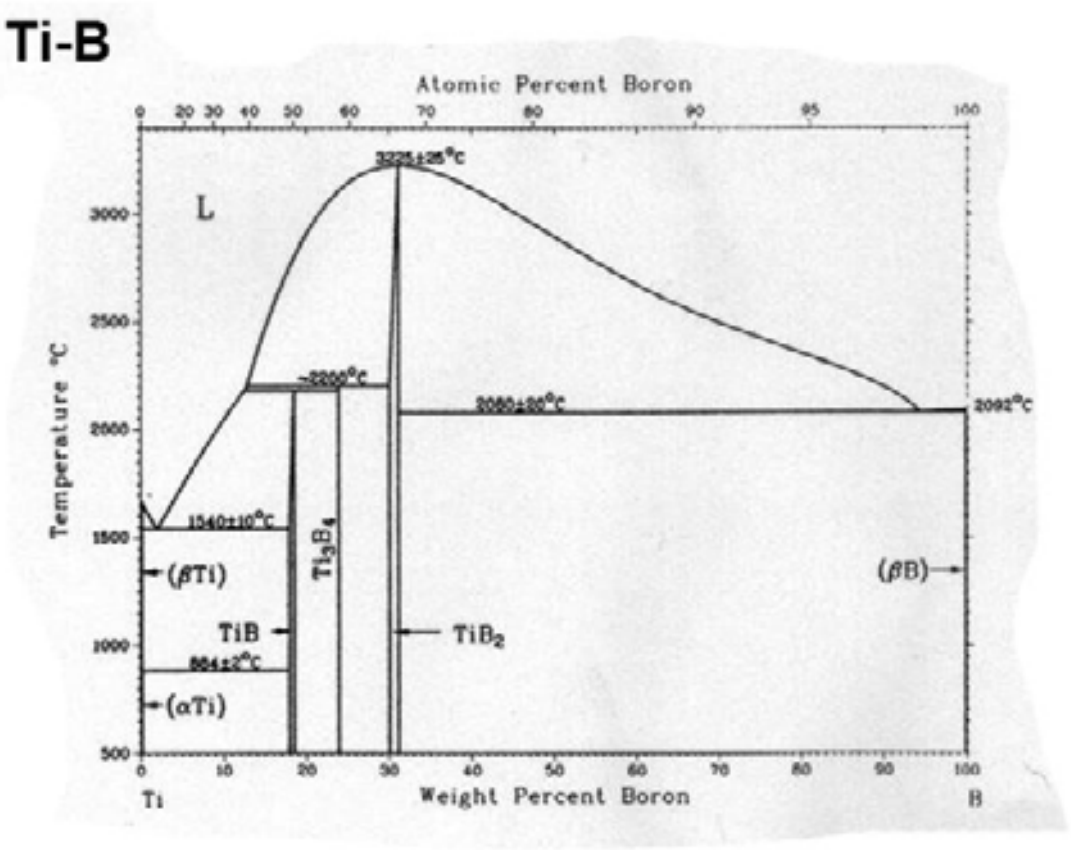

Figure 2.1 Ti-B binary alloy phase diagram [12].

Significant studies have been conducted investigating the thermodynamics and kinetics of the Ti-B system [13, 14]. It has been shown that TiB is stable only in a titanium matrix, due to the thermodynamics of the reactions forming TiB from titanium and TiB_2, with TiB more stable than TiB_2 only when excess moles of titanium are present. TiB forms in situ from the addition of either titanium and boron or titanium and TiB_2, and can form both primary and eutectic phases from the eutectic reaction as well as precipitate a sub-micron phase from the supersaturation of boron in titanium. Previous studies suggested that the morphology of the primary phase was faceted, equiaxed

clusters, while the morphology of the eutectic phase was a more desirable needle-like whisker [15, 16]. TiB has a linear coefficient of thermal expansion approximately the same as that of titanium, which is ideal for processing and applications at elevated temperatures. Once formed in the titanium matrix, the TiB phases show in situ growth at a parabolic rate.

The crystal structure of titanium monoboride, TiB, is an orthorhombic unit cell, shown in Figure 2.2. Its stable form is the orthorhombic B27 structure (FeB type), characterized by zigzag chains of boron atoms parallel to the [010] direction, with each boron atom lying at the center of a trigonal prism of six titanium atoms [17]. It has an anisotropic axis of growth along the [010] direction, which corresponds to the closest spacing of planes [18]. The crystal structure of TiB_2 is hcp, and is shown in Figure 2.3.

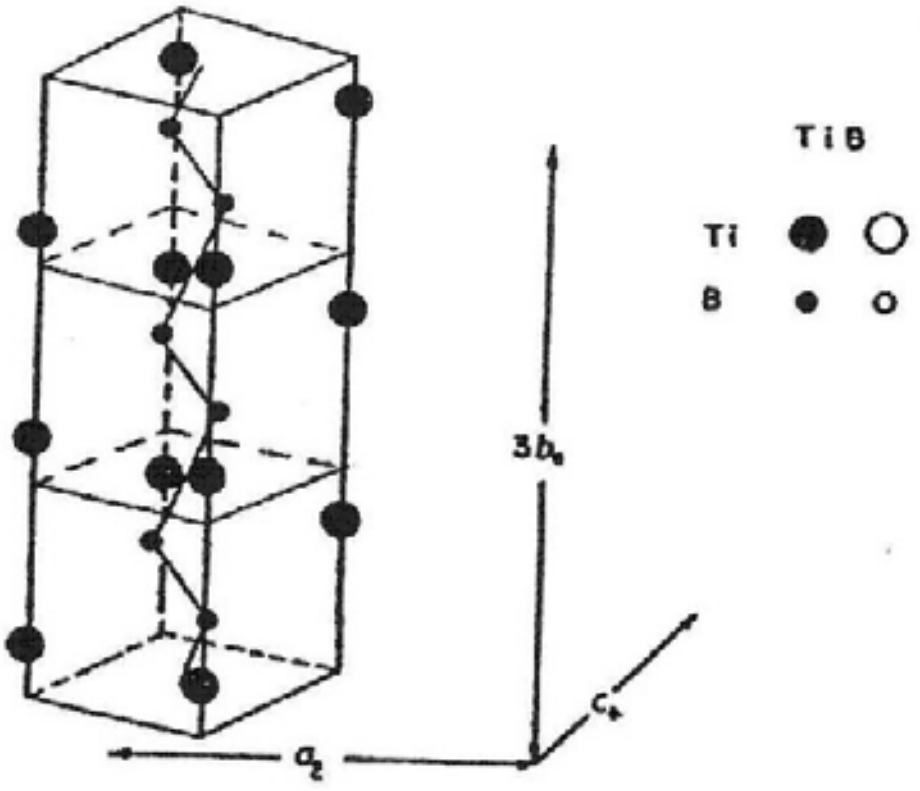

Figure 2.2 The crystal structure of TiB [19].

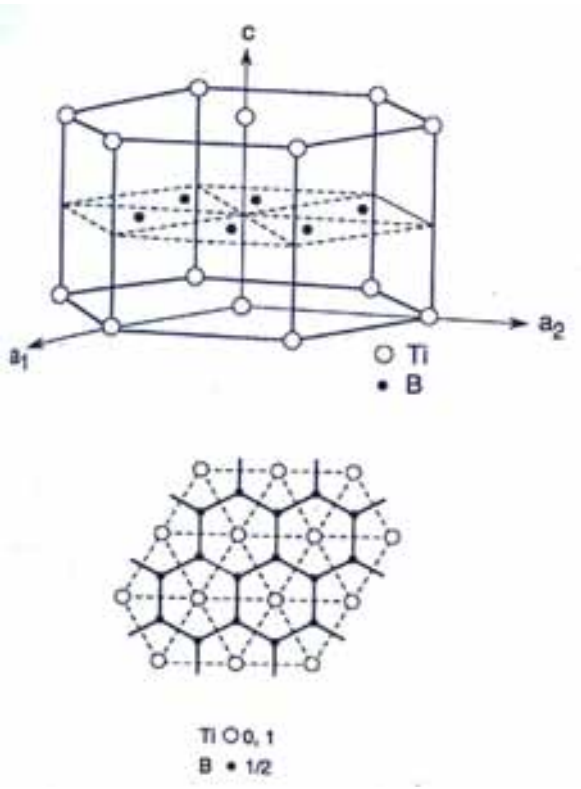

Figure 2.3 The crystal structure of TiB_2 [20].

The stable form of TiB is shown as single-crystal needles, with the aspect ratio typically between 4 and 10. There is also a metastable form, having a B_f structure and in the form of relatively fine needles with a high defect density of stacking faults, with the relationship between the B27 and B_f structures exactly analogous to the relationship between hcp and fcc atomic structures [21, 22]. Typical TiB whiskers have a roughly hexagonal cross-section. Studies have observed whisker alignment with deformation, showing promise for controlled anisotropy of Ti-B modified alloys and composites [23].

The microstructure of Ti-B modified alloys and composites is typically a fine-grained equiaxed matrix microstructure with TiB particles uniformly distributed throughout the matrix. The interface between the titanium matrix and the TiB phase is nearly perfect – it is in thermodynamic equilibrium, it is a coherent phase boundary, it is

atomically flat, and studies have shown there is no evidence of a chemical reaction zone [24-27]. It has also been shown that the TiB whiskers effectively pin the grain boundaries of the titanium alloy matrix so that a fine grain structure is retained even well above the β-transus and after cooling back into the α+β phase field [28, 29].

2.2.3 Ti-B Modified Alloy and Composite Mechanical Properties

Because TiB is stable only within a titanium matrix, accurate determination of the mechanical properties is a goal of current research. Several studies have attempted to determine the properties of both the TiB phase alone and the overall modified alloys and composites. Consensus in the field of the properties of TiB remains a goal of these investigations.

Gorsse and Miracle observed a significant strengthening effect of TiB reinforcement in Ti-6Al-4V-TiB composites [30, 31]. They determined the elastic modulus of compacted 20 volume percent TiB MMC, E = 161 GPa; extruded 20% TiB MMC, E = 168 GPa; and extruded 40% TiB MMC, E = 199 GPa, which approaches the elastic modulus of standard steel alloys. The elastic modulus of unreinforced Ti-6Al-4V alloy is approximately 110 GPa. They also used the Halpin-Tsai model in an attempt to extract the elastic modulus for TiB, and to determine the influence of the orientation of the TiB whisker reinforcement. They calculated the elastic modulus of TiB in the longitudinal direction, E_L = 450 GPa; in the transverse direction, E_T = 514 GPa; and an overall elastic modulus E = 482 GPa.

Atri, Ravi Chandran, and Jha observed that dynamic elastic and shear modulus values increased with increasing TiB volume fraction in Ti-B composites with high TiB whisker content (30-83 vol.%) [32]. Using the technique of impulse excitation of

vibration, combined with the Halpin-Tsai prediction method, they calculated the elastic modulus of TiB whiskers to be 371 GPa, and the shear modulus to be 140 GPa.

Constantinides, Ravi Chandran, Ulm, and Van Vliet developed a grid indentation analysis technique in an attempt to determine the elastic modulus of TiB in Ti-B composites [33]. They used massive array nanoindentation on reaction hot sintered Ti-B composite materials to generate statistical average mechanical properties. Their methods estimated the elastic modulus of TiB whiskers to be 406 GPa.

Soboyejo, Shen, and Srivatsan studied fatigue crack nucleation and growth in cast and extruded Ti-6Al-4V-TiB composite [34]. They observed crack initiation at approximately 20% of total fatigue life, meaning that crack growth components dominate the fatigue life of the composite. They also observed crack blunting by the β phase of the titanium alloy matrix. During cyclic loading, a single dominant crack did not evolve. They found that fatigue crack growth rates in the unreinforced alloy are comparable to the rates of the composite in middle and high ΔK regimes, but in the lower ΔK regime, the Ti-B composite exhibited faster crack growth rates than the alloy. The composite also showed evidence of strain softening to failure, with the fracture surfaces essentially ductile. They observed that dislocations pile up at the Ti-TiB interface until debonding occurs around the TiB inclusions. Overall, they determined that there is no fatigue motivation for the use of Ti-B composites.

Research at DERA by Godfrey, Wisbey, Goodwin, Bagnall, and Ward-Close investigated the tensile properties of Ti-6Al-4V-TiB composites [35]. They showed that above 0.5 wt.% boron added to Ti-6Al-4V alloy, both tensile strength and ductility decrease as the boron content increases. Samples with larger amounts of boron showed

brittle intergranular fracture, with boride particles observed on the fracture surface. Heat treatment at 1050°C improved the ductility of the composite, due to increased β phase in the matrix. They also observed that extrusion of the composite, aligning the TiB whiskers in the working direction, improved the tensile properties.

Gorsse and Miracle produced extruded 20 vol.% TiB composite, and found the ultimate tensile strength (UTS) improved more than 30% from the unreinforced Ti-6Al-4V alloy [30]. They observed significant whisker damage in the composite samples, but no debonding, with cracks propagating through the TiB whiskers preferentially along the whisker axis. Strength and tensile ductility were limited by the presence of TiB aggregates which could play the role of crack initiator at low strain, and should be eliminated with improved powder processing.

Research at the Air Force Research Laboratory (AFRL) headed by Boehlert has investigated tensile deformation of boron-modified Ti-6Al-4V alloy by performing in situ scanning electron microscopy (SEM) tensile tests at both room temperature and elevated temperature [36]. They observed tensile deformation evolution to fracture, with the TiB phase taking a load-sharing role in the mechanical behavior of the material. They concluded that the boron addition, and resultant in situ formation of TiB, significantly strengthens the Ti-6Al-4V alloy without changing the fracture mode.

Alman and Hawk studied the wear resistance of titanium matrix composites, and found that adding TiB_2 to the titanium matrix, forming in situ TiB and TiB_2 phases, was effective in improving wear resistance over the unreinforced alloy [11]. They found that the composite possessed significantly lower wear coefficients than the unreinforced titanium alloy, with TiB-reinforced titanium composite more wear resistant than TiC-

reinforced titanium composite which was also examined. They observed that strong interfacial bonding between the titanium matrix and the TiB whisker reinforcement prevents preferential pullout of either of the phases during abrasion.

Several studies have examined the creep behavior of Ti-B composites [37-39]. High-temperature deformation characteristics are important for various hot processing techniques, and for load-bearing structural applications at elevated temperatures. Important factors in the creep behavior of Ti-B modified alloys and composites are the titanium matrix microstructure (α-β transition), and TiB whisker alignment/orientation. The studies found that at low temperature and high stress, TiB whiskers act as a strong barrier to dislocation movement, and are sites of dislocation pileup. At high temperature and low stress, the matrix phase transformation from bcc β to hcp α results in a reduced retardation effect of the TiB reinforcement, essentially rendering the TiB whiskers irrelevant in the creep behavior of the composite. In general, it was found that matrix grain refinement, whisker-dislocation interactions, and the load/stress transfer to the whiskers leads to the Ti-B composite having much better creep resistance than the unreinforced titanium alloy.

A summary of published data for the mechanical properties of titanium, TiB, and TiB_2 is shown in Table 2.1. Multiple values are listed for properties that vary in the literature.

Table 2.1 Published data for the mechanical properties of titanium, TiB, and TiB_2.

	E	CTE	T_m	ρ	HV	hardness
Ti	110 GPa	$9x10^{-6}$/K	1813 K 1900 K	4.5 g/cm^3	130	2.8 GPa
TiB	482 GPa 370 GPa	$8.6x10^{-6}$/K $6.2x10^{-6}$/K	2500 K	4.51 g/cm^3 4.56 g/cm^3	>1100 1800	27-28 GPa
TiB_2	550 GPa	$8.1x10^{-6}$/K	3193 K 3600 K	4.5 - 4.62 g/cm^3	3400	22.5-35.7 GPa

2.2.4 Ti-B Modified Alloy and Composite Processing

A wide variety of processing methods have proven successful in producing Ti-B modified alloys and composites [14, 15, 21, 26, 28, 35, 38-51]. There has been extensive published work demonstrating that Ti-B materials can be produced using standard powder metallurgy (P/M) techniques, including pre-alloying, mechanical alloying, blended elemental P/M, hot isostatic pressing (HIP), direct powder extrusion, functionally graded material (FGM), laser cladding, reaction sintering, and self-propagating high-temperature synthesis (SHS). Conventional ingot metallurgy techniques, including vacuum arc remelting, induction skull melting, and vacuum induction melting have been published as well. Rapid solidification techniques, such as gas atomization and ribbon melt spinning have also produced Ti-B alloys and composites. In addition, secondary hot forming techniques, including extrusion, swaging, rolling, and forging, have been used in the Ti-B material production process.

The Center for the Accelerated Maturation of Materials (CAMM) at the Ohio State University, under the direction of Fraser, has conducted research investigating the production of Ti-B alloys and composites using the laser-engineered net-shaping (LENS™) process [16, 27, 52]. In this technique, a high-powered laser is used to melt

successive layers of powder metal feedstock according to a CAD design. The group has produced Ti-B materials with refined and homogeneous microstructures.

A promising characteristic of Ti-B alloy and composite processing is realignment of the TiB whisker reinforcement, allowing for the possibility of the processing methods to take advantage of anisotropy of the microstructure for particular applications. Schuh and Dunand observed gradual alignment of TiB whiskers during tensile deformation by transformation and superplasticity between 840 and 1030°C [23]. The TiB whiskers aligned along the external loading axis, showing no evidence of whisker fracture or interfacial debonding during reorientation. Tamirisakandala, Vedam, and Bhat published processing maps (strain rate versus temperature), for hot working of Ti-B composites [1]. Other published work has observed TiB whisker alignment from hot extrusion, forging, and swaging.

2.2.5 Ti-B Modified Alloy and Composite Applications

The high strength-to-weight ratio, excellent corrosion resistance, and improved high temperature properties compared to the unreinforced alloy have made Ti-B modified alloys and composites an increasingly viable choice for applications within the automotive industry. Froes, Friedrich, Kiese, and Bergoint analyzed the potential for titanium alloy and composite use in automobiles, and concluded that the main obstacle to increased titanium use is cost versus steel [53]. Currently, a titanium-based part will cost more than 10 times that of a comparable steel part, and this needs to be reduced to approximately twice that of steel in order to see cost-performance benefits to justify a material switch. Their study noted the use of Ti-B composite connecting rods in the Volkswagen CCO diesel concept vehicle, where the reduced weight of the titanium

composite part leads to significantly reduced noise, vibration, and harshness (NVH), and quieter engine performance in the vehicle that has a fuel economy of 250 miles per gallon (mpg).

Significant research into Ti-B composites has been conducted at Toyota Central Research and Development Laboratories by Saito [41, 54-58]. Toyota started development of a cost-effective powder metallurgy forging process in the late 1980s, and since 1998 the company has produced Ti-20 vol.% TiB composite intake and exhaust engine valves for the Altezza, which is sold in the United States as the Lexus IS. These Ti-B composite valves replaced a 21-4N heat-resistant steel alloy part, resulting in a 40% lighter valve weight. With the composite valves installed, maximum engine revolutions increased by 700 rpm, high-rev engine noise decreased by 30%, reduction of friction decreased camshaft driving torque by 20%, and overall fuel economy improved by 1-2 mpg.

Although relatively little of the research has been published, titanium matrix alloys and composites have been developed for the aerospace industry over the last half-century. Ti-B composite was used in the nozzle actuator piston rod for the Pratt & Whitney F-119 engine developed in 1995 for the F-22 fighter jet, and in the nozzle link for the General Electric F-110 engine developed in 1999 for the F-16 fighter jet [59]. In the industry, Ti-B modified alloys and composites are currently being considered as potential candidates for aerospace structural components requiring high strength, high stiffness, and low density; to replace high-strength steels due to Ti-B materials' superior wear and corrosion resistance; and for elevated temperature applications where standard unreinforced titanium alloys are unsuitable [40]. For fracture-critical aerospace

applications, a minimum of 7% tensile elongation to failure is required by structural designers [6].

Dynamet Technology has developed a powder metallurgy cold and hot isostatic pressing (CHIP) process to produce a range of products for sporting goods and biomedical applications [60-62]. Marketed as CermeTi®, they produce Ti-6Al-4V-based composites with either TiB or TiC reinforcement. They have produced golf driver inserts, as well as knife blades and hockey skate blades, where the lighter weight and improved corrosion resistance over a traditional steel part are particularly useful.

Titanium alloys and composites with boron are now being considered for use in certain biomedical applications. Research has investigated using titanium modified alloys and composites for load-bearing biomedical implants, such as femoral ball and lumbar disc replacements [1]. The matrix would be a Ti-Al-Fe alloy, since vanadium is toxic in vivo, but Ti-5.5Al-1Fe has been deemed a suitable substitute for Ti-6Al-4V. In addition to its corrosion resistance, high strength-to-weight ratio, biocompatibility, and osseo-integration, titanium alloys and composites do not obscure soft-tissue magnetic resonance imaging (MRI), unlike stainless steel and cobalt-chrome alloys. Ti-B materials have also been studied to determine their suitability for near-net shape dental castings used in dental applications such as implants and restorative castings [63].

2.3 Stereology, Image Analysis, and Microstructural Simulation

Completed research has involved conventional stereology and image analysis techniques to gain information about the three-dimensional microstructure of Ti-B modified alloys and composites from two-dimensional metallographic sections [64-66]. These techniques were developed to help quantify a microstructure. Geometrically, a

microstructure is an ensemble of volumes, internal surfaces, lines, and points in three-dimensional space. Each microstructural feature, such as a particle, grain, or pore, has associated with it size, shape, volume, surface area, curvature, etc., and location. All of these facets of microstructural geometry affect the mechanical and physical properties of materials. Quantitative metallographic and stereological methods have been developed (and continue to be developed) for the estimation of microstructural properties.

Stereology involves the estimation of the properties of three-dimensional microstructural features through unbiased sampling of the three-dimensional microstructural space using geometric test probes such as planes, lines, or points. Computer processing, digital imaging, and image analysis software have automated processes that were originally developed to be measured and calculated by hand, and have allowed much larger amounts of information to be gathered to determine the characteristics of a given microstructure. There is still, however, a gap in the understanding of how the microstructural characteristics relate to the overall properties of a material.

The two-point correlation function is a method to quantitatively describe a microstructure [67]. This function, denoted as $<P_{11}(r)>$, is defined as the average probability that both of the end points of a randomly located and oriented straight line of length r are contained in particles of phase 1. Both ends of the straight line need not be in the same particle, only of the same particulate phase. Similarly, the two-point correlation function $<P_{22}(r)>$ is the average probability that both of the end points of a randomly located and oriented straight line of length r are contained in the matrix of phase 2; and $<P_{12}(r)>$ is the average probability that the first end point lies in the particles (phase 1),

and the second end point lies in the matrix (phase 2), or vice versa. These correlation functions are governed by the metric microstructural parameters such as volume fraction, as well as by the spatial arrangement of microstructural features and their spatial correlations. In general, two-point correlation functions are direction dependent, and their orientation-averaged mean values are also of interest.

Two-point correlation function data have been used to quantify microstructural heterogeneities and particle clustering. This data can also be used for modeling the mechanical response of a microstructure using statistical mechanics-based approaches [68-71]. Two-point correlation functions and the microstructural parameters extracted from such data can be used in the development of computer simulated microstructures, also known as digital microstructures, that are statistically similar to the actual microstructures [72, 73]. These digital microstructures can then be implemented in finite element (FE) or other computational software to model the mechanical response of the material [74, 75].

Visualization, characterization, and representation of three-dimensional microstructures are of particular interest for understanding and modeling processing-microstructure-properties relationships [76]. A two-dimensional metallographic section does not contain all of the information concerning the true three-dimensional geometry of the microstructure. As a result, an efficient and unbiased montage serial sectioning technique has been developed for the reconstruction of large volume (~several mm^3), high resolution (~1 μm), three-dimensional microstructures. To generate a large volume of three-dimensional microstructure at high resolution, a small microstructural volume is reconstructed, and then many contiguous small volumes surrounding it are also

reconstructed, their boundaries are perfectly matched, and they are digitally stitched together to generate a large microstructural volume [77-79].

It is effectively a stack of aligned serial sections, which constitutes a volume image data set similar to those in x-ray computed tomography and magnetic resonance imaging (MRI). Therefore, the same three-dimensional microstructure visualization techniques are applicable. The three-dimensional microstructural visualization can be achieved either by volume rendering or by surface rendering. Volume rendered images can be used as representative volume elements (RVEs) for finite element-based computations [80]. Surface rendering involves the rendering of the iso-surface of the region of interest (ROI) from the volume data, whereas volume rendering is the rendering of all volume data by specifying opacity and color of each voxel (3D pixel). Surface rendering leads to a reduction in the size of the data set because only the surface data are retained. Surface rendering requires the fitting of a surface in the volume data. Numerous algorithms are available for surface rendering, including the contour connecting algorithm and the marching cube algorithm [81, 82]. Surface rendering is useful for examination of the structure of the reinforcement phase in a composite material.

For approximately the same metallographic effort, montage-based serial sectioning yields a microstructural volume containing a large number of features (such as pores, grains, or particles), which can provide a sufficiently large statistical sample for the study of topological aspects of microstructure. Recently, montage serial sectioning has been implemented in a completely automated serial sectioning system that utilizes a robotic arm to move a specimen back and forth between the metallographic equipment

(polishing, etching, etc.), and an optical microscope to generate the montage serial sections [83].

CHAPTER 3

PRE-ALLOYED BORON-MODIFIED Ti-6Al-4V ALLOYS

3.1 Introduction

An emerging and potential method used to produce Ti-B materials is powder metallurgy (P/M) using pre-alloyed (PA) Ti-B powder. Pre-alloying is a rapid solidification process where an alloy melt is rapidly solidified into an alloy powder by inert gas atomization. The PA powder can then be processed using conventional powder metallurgy processes, including outgassing to remove any volatile impurities and compaction by techniques such as hot isostatic pressing (HIP) to produce near-net shape products or billet preforms. These billet preforms can then be subjected to thermomechanical processing (TMP) methods such as forging, rolling, or extrusion to manufacture wrought products.

The PA processing approach offers the advantage of producing relatively finer length-scale microstructural features due to shorter times for growth during rapid solidification of the alloy melt into the PA powder [6]. In addition, in boron-modified titanium alloys, the PA approach can produce supersaturated boron due to non-equilibrium cooling conditions. This supersaturated boron can then be forced out of the titanium alloy matrix through subsequent thermal exposure to form a sub-micron precipitated TiB phase via a solid state process.

In this research, samples of boron-modified titanium alloys produced from PA powder were examined to study the effects of composition and processing on the resultant microstructures and mechanical properties. One alloy was produced with a

composition near the eutectic limit, slightly into the hypereutectic regime, while a second alloy was produced in the hypoeutectic regime. Samples from each alloy also underwent extrusion to investigate the effect of that TMP wrought process.

3.2 Hypereutectic Pre-Alloyed Boron-Modified Ti-6Al-4V Alloy

Samples of pre-alloyed Ti-6Al-4V-1.6B alloys were examined, both in the as-compacted condition and following extrusion. This composition is close to the eutectic point in the quaternary system of titanium, alloying elements aluminum and vanadium, and boron, which preliminary research by the Institute for Metal Physics, Ukraine, has shown to be approximately 1.56 wt.% boron [84]. The studies of these samples focused on both the primary and eutectic phases of TiB.

3.2.1 Materials and Processing Details

Pre-alloyed powder of boron-modified Ti-6Al-4V was produced at Crucible Research Corporation, Pittsburgh, Pennsylvania. In this process, the melting procedure involved induction skull (made of titanium) melting of appropriate amounts of the raw materials (titanium, Al-V master alloy, and TiB_2), in a water-cooled copper crucible. Boron additions to the melt were contributed in the form of TiB_2, which dissolves in the liquid melt and forms TiB during solidification by the in situ eutectic phase transformation reaction $Ti + TiB_2 \rightarrow 2TiB$. The liquid melt was then rapidly solidified using inert gas atomization to produce Ti-6Al-4V-1.6B powder. The resultant chemical composition of the powder was 6.13Al, 4.16V, 1.53B, 0.19O, 0.15C, 0.053Fe, and the balance 87.79Ti (all amounts in weight percent). The atomized powder was then sieved to obtain -100 mesh size (average particle size of 150 μm).

Colleagues at the Air Force Research Laboratory, Wright-Patterson Air Force Base, Ohio, then received the pre-alloyed powder for further P/M processing. The Ti-6Al-4V-1.6B powder was packed inside a thick-walled (6.35 mm) can of Ti-6Al-4V, vacuum outgassed at 300°C for 24 hours, and sealed. The can was coated with glass for lubrication and environmental protection, heated to 1200°C, soaked for 1 hour, and then blind-die compacted in an extrusion chamber heated to 260°C. The billet height was reduced by about 30% at a ram speed of 6.35 mm/s. The compact was then held at a pressure of 1400 MPa for 180 seconds and subsequently air-cooled to room temperature. A second billet blind die compacted by the same method was subsequently hot extruded, heated to 1100°C and soaked for 1 hour prior to extrusion through a circular die with an extrusion reduction ratio of 16.5:1, at a ram speed of 6.35 mm/s, and air-cooled to room temperature. Specimens were then sectioned from the compacted billet and extruded rod.

3.2.2 Optical Microscopy and Quantitative Characterization

Specimens of the compacted billet and extruded rod were mounted in thermoplastic using standard techniques for metallography. Conventional sample preparation techniques developed for unreinforced metal alloys were not suitable for Ti-B materials, and led to sample damage when TiB whiskers detached from the material and created deep grooves and scratches across the matrix during polishing. Suitable grinding and polishing schemes were developed for Ti-B modified alloys and composites, taking into account the hardness differences between the relatively soft Ti-6Al-4V alloy matrix and the relatively hard TiB whisker reinforcement. Using these metallographic techniques, a final surface finish of 0.05 μm, suitable for optical microscopy, was obtained.

Samples were examined using a Carl Zeiss, Inc. Axiovert 200 MAT optical microscopy system with AxioVision image analysis software. For each sample, "montages" of a large number of contiguous microstructural fields were constructed by digitally stitching together adjacent fields of view (FOV) imaged at a high magnification. The basic principles for large-area high-resolution montage construction are described in detail by Louis, Tewari, and Gokhale [72, 85, 86].

In the present work, the montages were created using the automated AxioVision digital image analysis system that utilizes the image cross correlation function-based technique for matching the borders between contiguous microstructural fields. For these samples, each montage is a microstructural image of a large area (~1.75 mm^2), having a high resolution (~0.5 μm). Figure 3.1a shows one such montage of 195 fields of view of compacted Ti-6Al-4V-1.6B alloy. The image has been compressed for display. Each region of this montage has the high resolution of the images shown in Figures 3.1b and c.

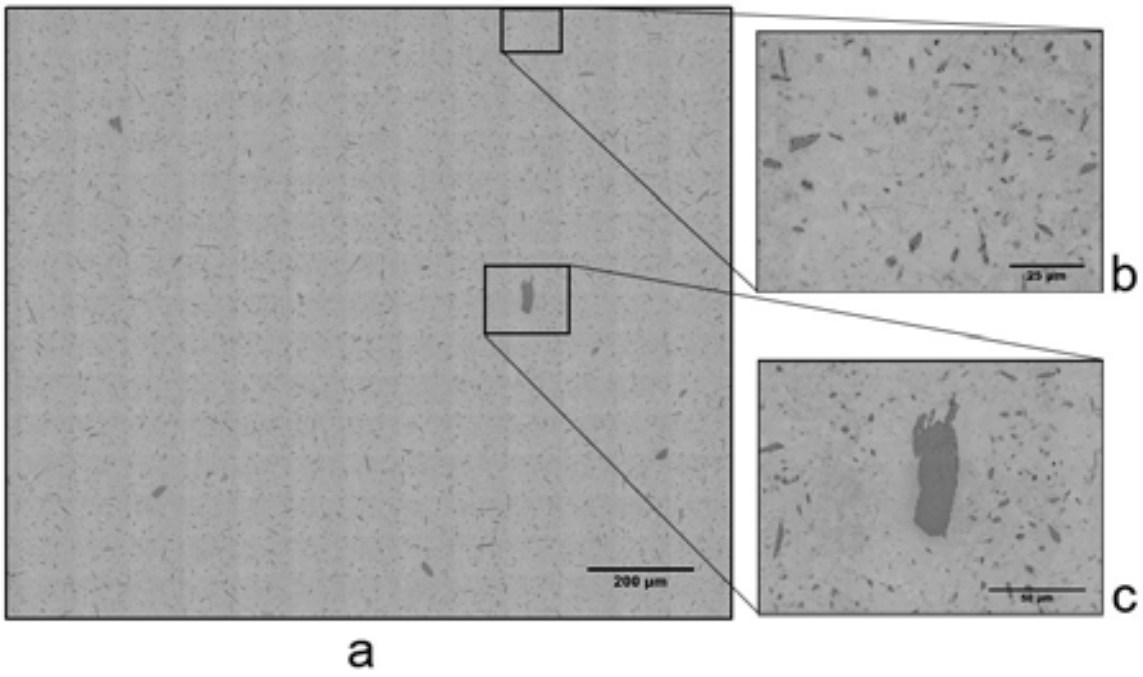

Figure 3.1 (a) Montage of 195 fields of view of compacted Ti-6Al-4V-1.6B modified alloy covering an area of approximately 1.75 mm^2, created by matching contiguous microstructural fields captured at a resolution of approximately 0.5 µm. The montage is digitally compressed for presentation. Each field of view in the montage has been captured at the resolution of the images shown in (b) and (c). (b) Field of view showing eutectic TiB whiskers. (c) Field of view showing both eutectic TiB whiskers and a coarse primary TiB particle.

The micrographs show TiB whiskers randomly dispersed and oriented in a Ti-6Al-4V matrix. In these figures, the TiB phases are a darker gray than the titanium matrix. Montages were taken from different regions and different samples of each alloy specimen to ensure that observations were performed on representative examples of the microstructures. The particles of primary phase TiB are noticeably coarser than the eutectic TiB whiskers, but are similarly randomly dispersed and oriented.

A montage from the extruded sample of Ti-6Al-4V-1.6B alloy is shown in Figure 3.2. The extrusion direction is normal to the plane of the micrograph. As in the micrographs of the compacted boron-modified alloy, the TiB particles are seen as dark gray in a gray matrix of Ti-6Al-4V alloy. Coarser primary TiB particles are seen in the material, along with eutectic TiB whiskers.

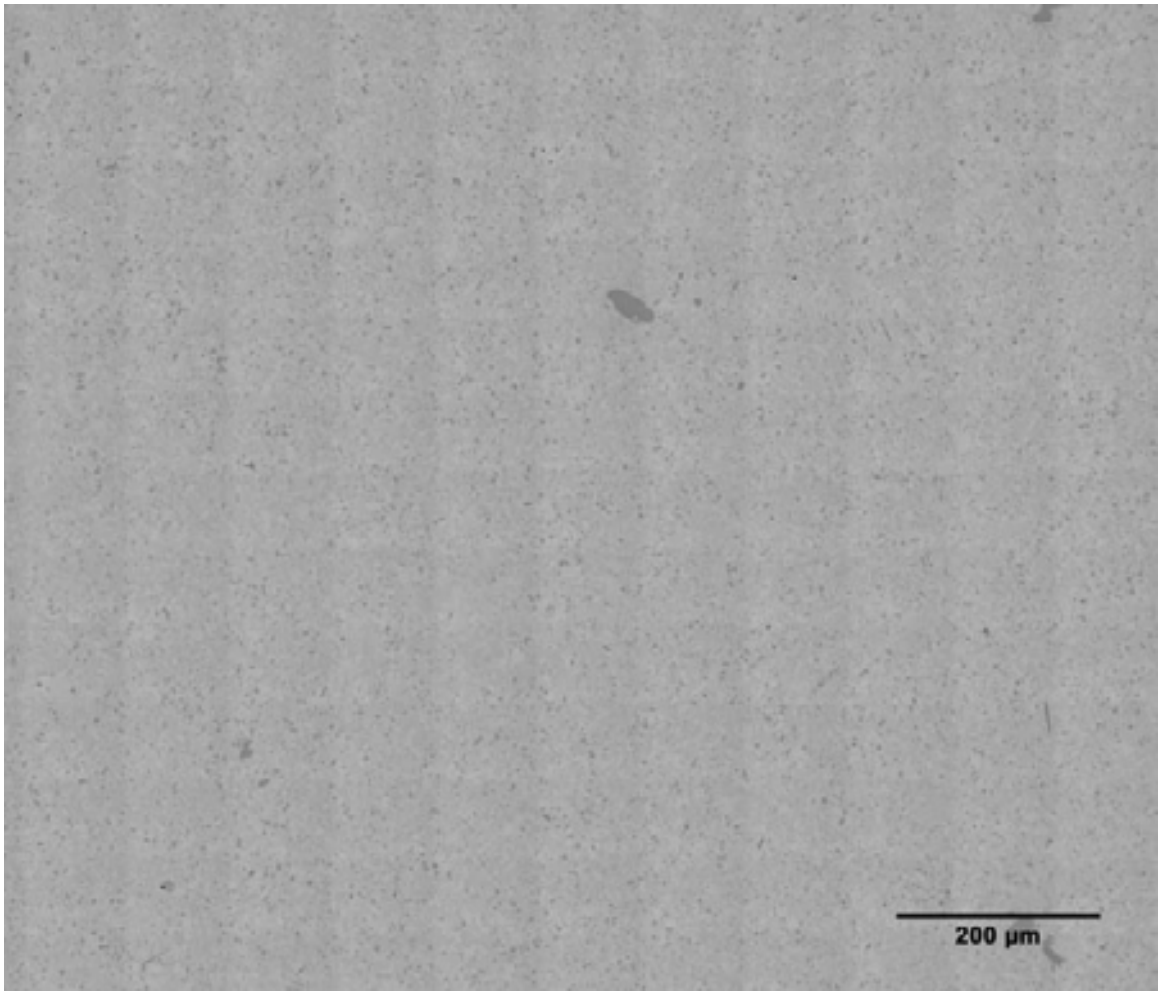

Figure 3.2 Montage of the microstructure of extruded Ti-6Al-4V-1.6B alloy. The extrusion direction is normal to the plane of the micrograph.

Images of the microstructure of the extruded Ti-6Al-4V-1.6B alloy at higher magnification are shown in Figures 3.3 and 3.4. Figure 3.3 shows only the eutectic TiB

phase, and confirms alignment of this phase following extrusion that was previously observed [23]. The roughly hexagonal cross-section of the eutectic TiB whiskers is also seen [87]. Figure 3.4 shows a particle of the coarser primary TiB phase along with other eutectic TiB whiskers. This primary particle suggests a roughly hexagonal cross-section and morphology similar to the finer eutectic TiB whiskers, although this observation is difficult to confirm solely from analysis of two-dimensional metallographic sections.

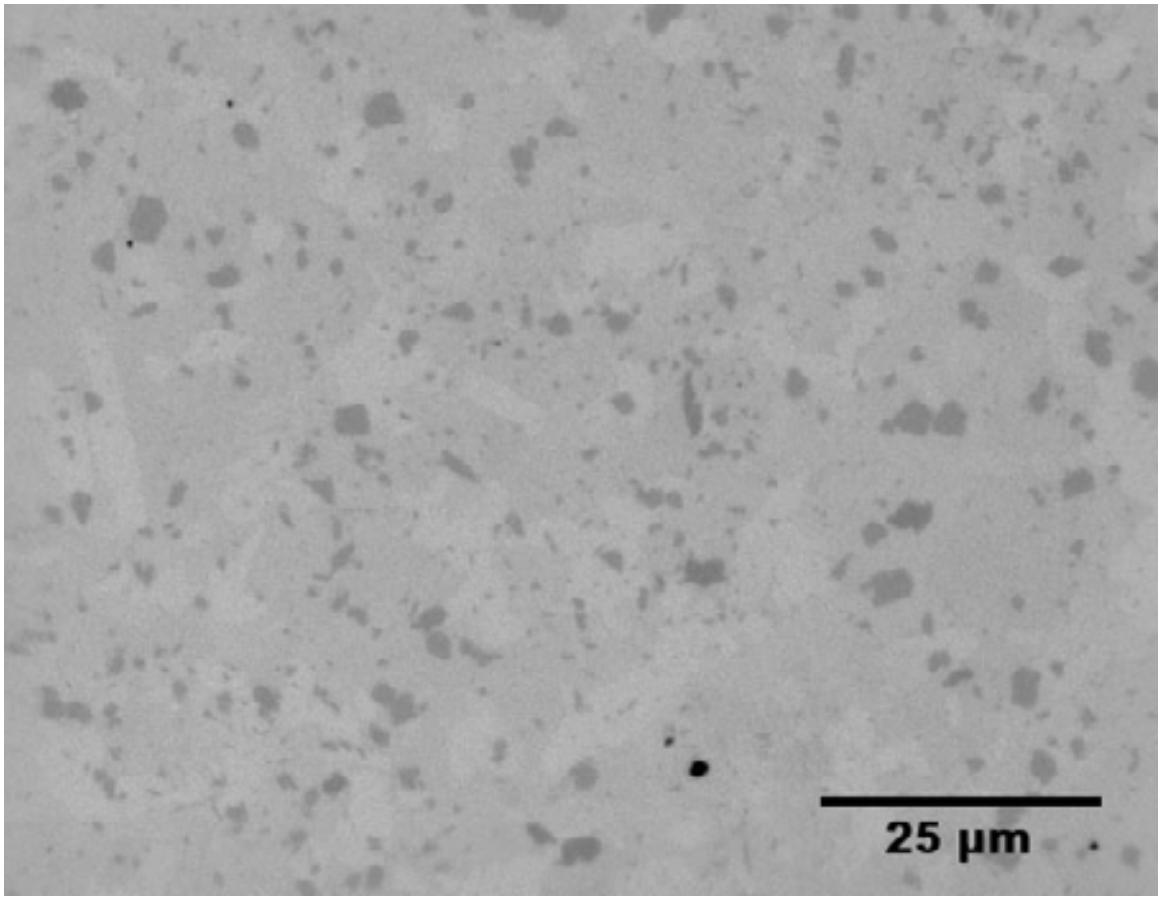

Figure 3.3 Microstructure of extruded Ti-6Al-4V-1.6B alloy showing eutectic TiB whiskers mostly aligned with the extrusion direction normal to the micrograph.

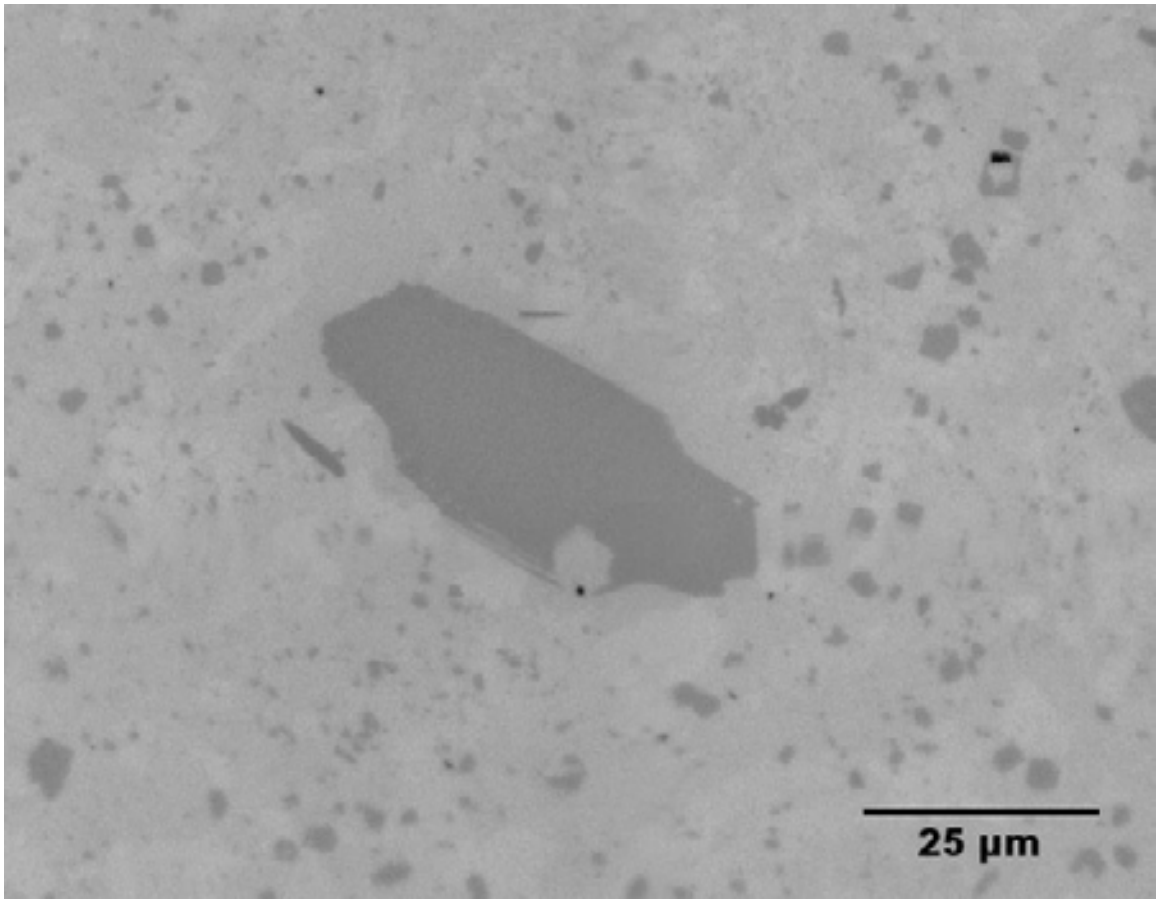

Figure 3.4 Microstructure of extruded Ti-6Al-4V-1.6B alloy showing a coarse primary TiB particle along with finer eutectic TiB whiskers mostly aligned with the extrusion direction normal to the micrograph.

Microstructural data for these compacted and extruded Ti-6Al-4V-1.6B alloy samples were calculated using conventional two-dimensional stereology techniques. For the extruded alloy, measurements were made on montages in the plane parallel as well as on montages in the plane normal to the extrusion direction. Average values are shown in Table 3.1, but these results do not take into account the size difference between the eutectic and primary TiB phases or the stochastic nature of microstructures. Overall, it was found that the eutectic TiB whiskers typically had a length of approximately 25-40 µm and a width of approximately 4-6 µm, for an aspect ratio range of between 4.5 and

10. The primary TiB particles, found with much less frequency in these samples (5-10 primary particles in an area containing more than 20,000 eutectic TiB whiskers), were observed to typically have a length of approximately 200-300 μm and a width of approximately 30-50 μm, for an aspect ratio range of between 4 and 10. The overall volume fraction of TiB whiskers in these samples is approximately 7%. In addition, although the angular orientation of the TiB whiskers was affected by extrusion, the morphology of the TiB phases was not observed to have been affected by extrusion.

Table 3.1 Microstructural data of Ti-6Al-4V-1.6B modified alloy samples calculated using standard two-dimensional stereology techniques.

sample	avg length (μm)	avg width (μm)	aspect ratio	volume fraction
compacted	33.27	4.88	6.82	7.24
extruded	34.76	5.05	6.88	6.98

3.2.3 SEM Fractography

The potential use of Ti-B materials for aerospace structural components demands that the modified alloy or composite be suitable for fracture-critical applications. A value of tensile elongation to failure of a minimum of 7% is often required by structural designers in the field [6]. As a result, the fracture behavior of Ti-B materials must be fully understood to promote their use in the aerospace industry.

Samples of Ti-6Al-4V-1.6B alloy were sectioned from both the compacted billet and from the extruded rod, and machined into ¼”-20 round tensile specimens by colleagues at the Air Force Research Laboratory. These specimens then underwent room temperature tensile tests according to ASTM standard E8-04 [88]. Tensile test results are

shown in Table 3.2. Both the compacted and extruded specimens showed significant improvement over the elastic modulus of unreinforced Ti-6Al-4V alloy of approximately 110 GPa. It is also notable that the strength of the extruded specimen is increased compared to the compacted alloy, and the elongation to failure is nearly doubled compared to the compacted alloy. Prior to examination of the tensile fracture surfaces using scanning electron microscopy (SEM), the specimens underwent ultrasonic cleaning in ethanol for 5 minutes.

Table 3.2 Tensile test results of Ti-6Al-4V-1.6B alloy, using ASTM E8-04.

sample	E (GPa)	σ_y (MPa)	σ_{uts} (MPa)	e (%)
compacted	138	1232	1347	2.4
extruded	152	1350	1420	4.0

The fracture surfaces of the tensile test specimens were examined with a Sirion FEI scanning electron microscope, using secondary electron emission. The fracture surface of the compacted Ti-6Al-4V-1.6B alloy specimen is shown in Figures 3.5-3.9. In Figure 3.5, at a magnification of 250X, a jagged fracture surface can be seen, suggesting relatively brittle fracture behavior of the modified alloy. In Figure 3.6, at a magnification of 350X, a primary TiB particle significantly thicker and larger than the eutectic TiB whiskers can be seen just to the left of the center of the SEM micrograph (circled). At higher magnifications (Figures 3.7-3.9), the fracture surfaces of the eutectic TiB whiskers are clearly visible. Very little, if any, whisker pullout was observed, and fracture has taken place predominantly along the length of each whisker. In addition, the fracture surface has a higher TiB content than the bulk material. The Ti-6Al-4V matrix shows ductile failure.

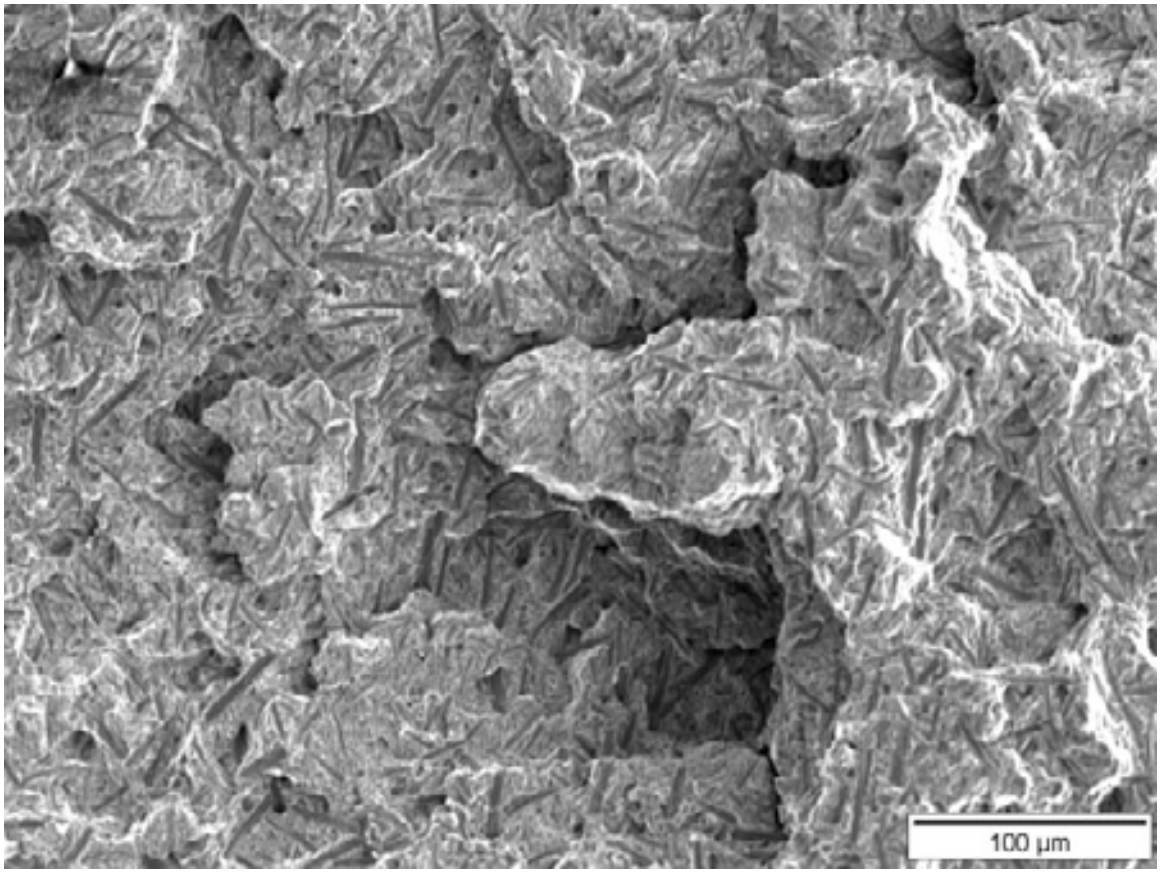

Figure 3.5 Fracture surface of compacted Ti-6Al-4V-1.6B modified alloy showing a jagged fracture surface, suggesting brittle fracture.

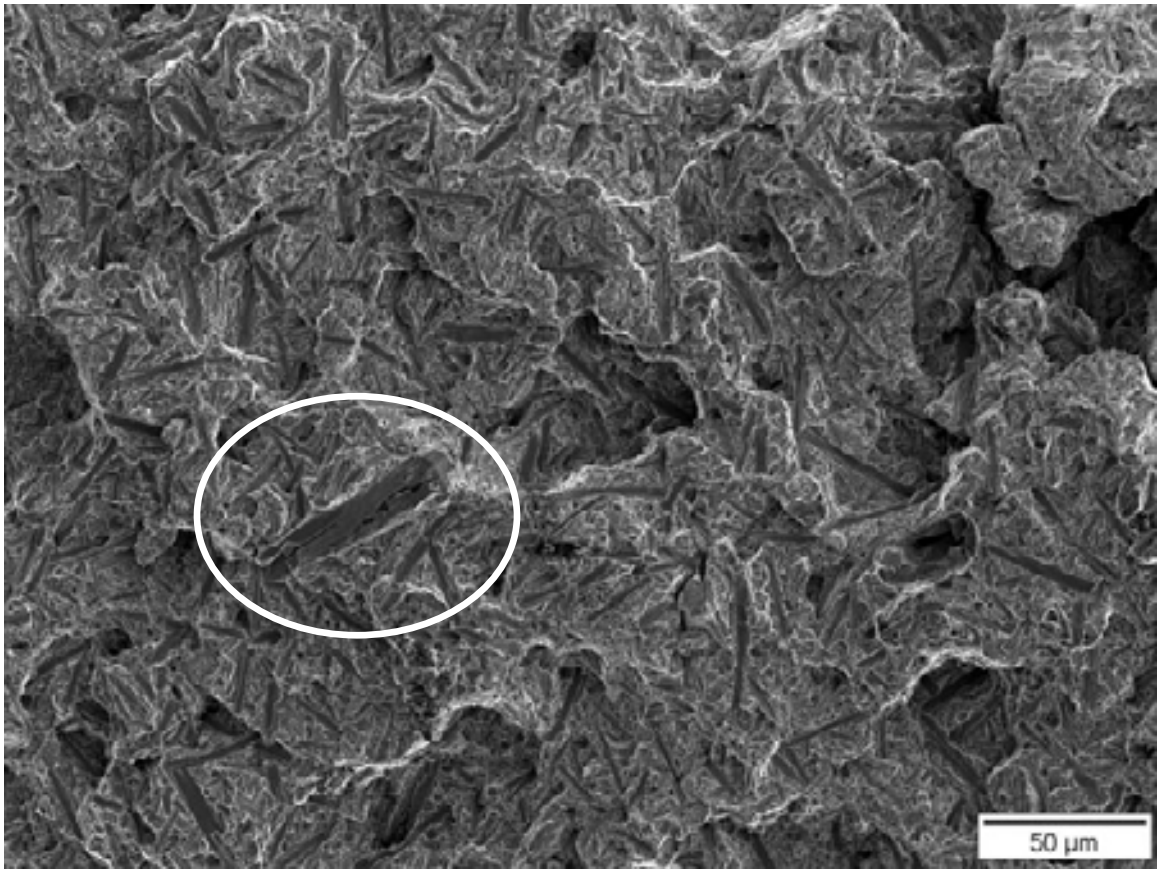

Figure 3.6 Fracture surface of compacted Ti-6Al-4V-1.6B modified alloy, with a primary TiB particle seen just to the left of the center of the SEM micrograph (circled).

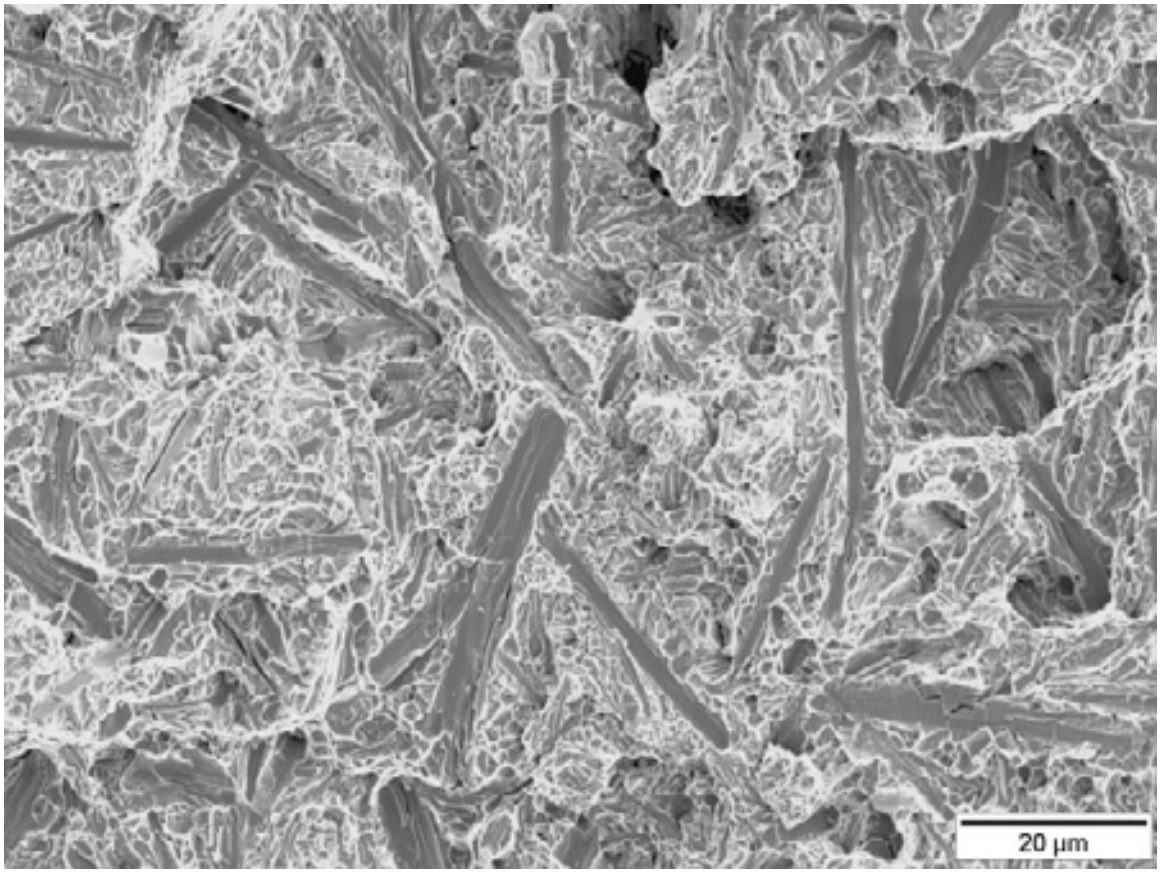

Figure 3.7 Fracture surface of compacted Ti-6Al-4V-1.6B modified alloy, showing brittle fracture down the length of the eutectic TiB whiskers and ductile fracture of the Ti-6Al-4V matrix.

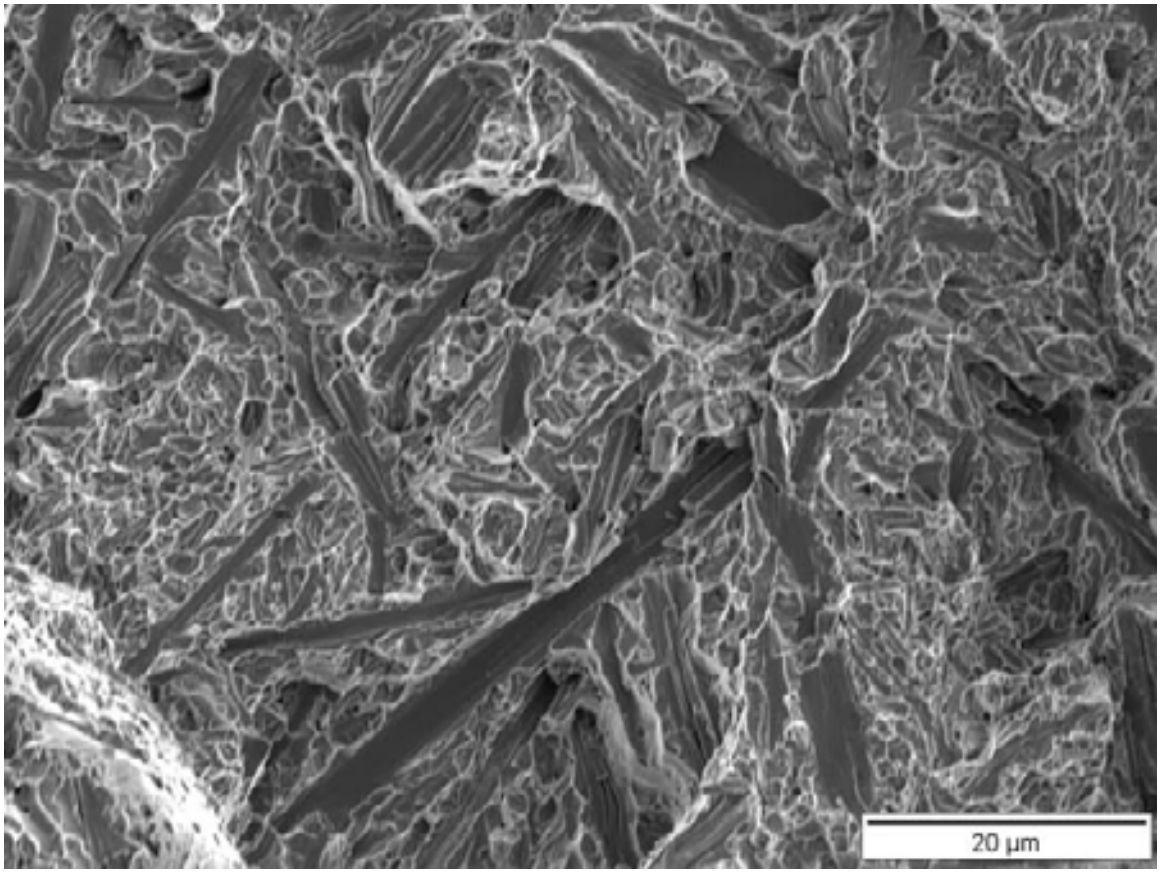

Figure 3.8 Fracture surface of compacted Ti-6Al-4V-1.6B modified alloy, showing brittle fracture down the length of the eutectic TiB whiskers and ductile fracture of the Ti-6Al-4V matrix.

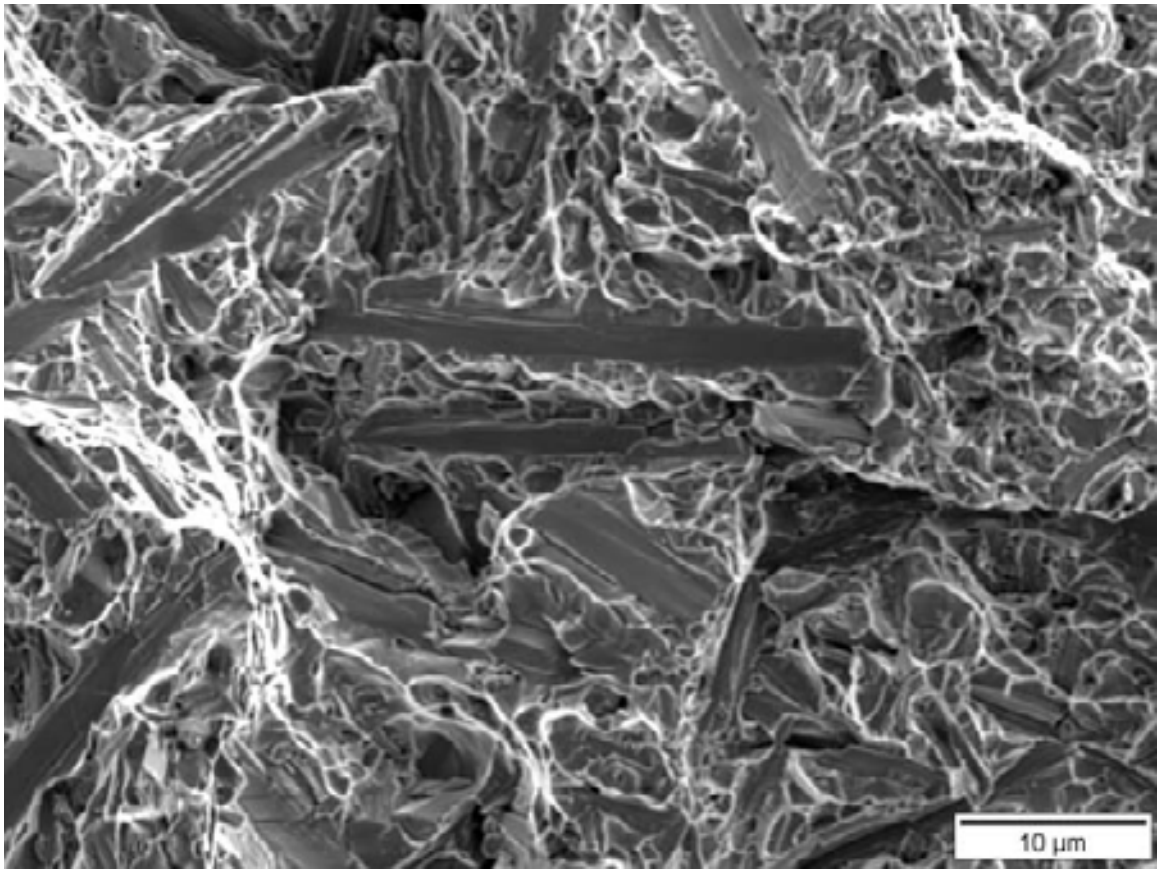

Figure 3.9 Fracture surface of compacted Ti-6Al-4V-1.6B modified alloy, showing brittle fracture down the length of the eutectic TiB whiskers and ductile fracture of the Ti-6Al-4V matrix.

For the extruded Ti-6Al-4V-1.6B alloy specimen, the extrusion direction is parallel to the tensile test direction. The fracture surface of this specimen is shown in Figures 3.10-3.13. In Figure 3.10, the specimen is seen at a magnification of 250X, showing a relatively jagged, brittle fracture surface (although not as brittle as the fracture surface of the compacted sample shown in Figure 3.5). In Figure 3.11, at a magnification of 1200X, a primary TiB particle significantly thicker and larger than the eutectic TiB whiskers can be seen just to the right of the center of the SEM micrograph (circled). In Figures 3.12 and 3.13, the fracture surface is shown at higher magnifications, and the

fracture surfaces of the eutectic TiB whiskers can be clearly seen. Unlike the compacted alloy specimen, fracture of the TiB whiskers is predominantly across the width of the whiskers, not down the length of the whiskers. Very little whisker pullout is observed, and the Ti-6Al-4V matrix shows ductile fracture behavior. As with the compacted specimen, the fracture surface has a higher TiB content than the bulk material.

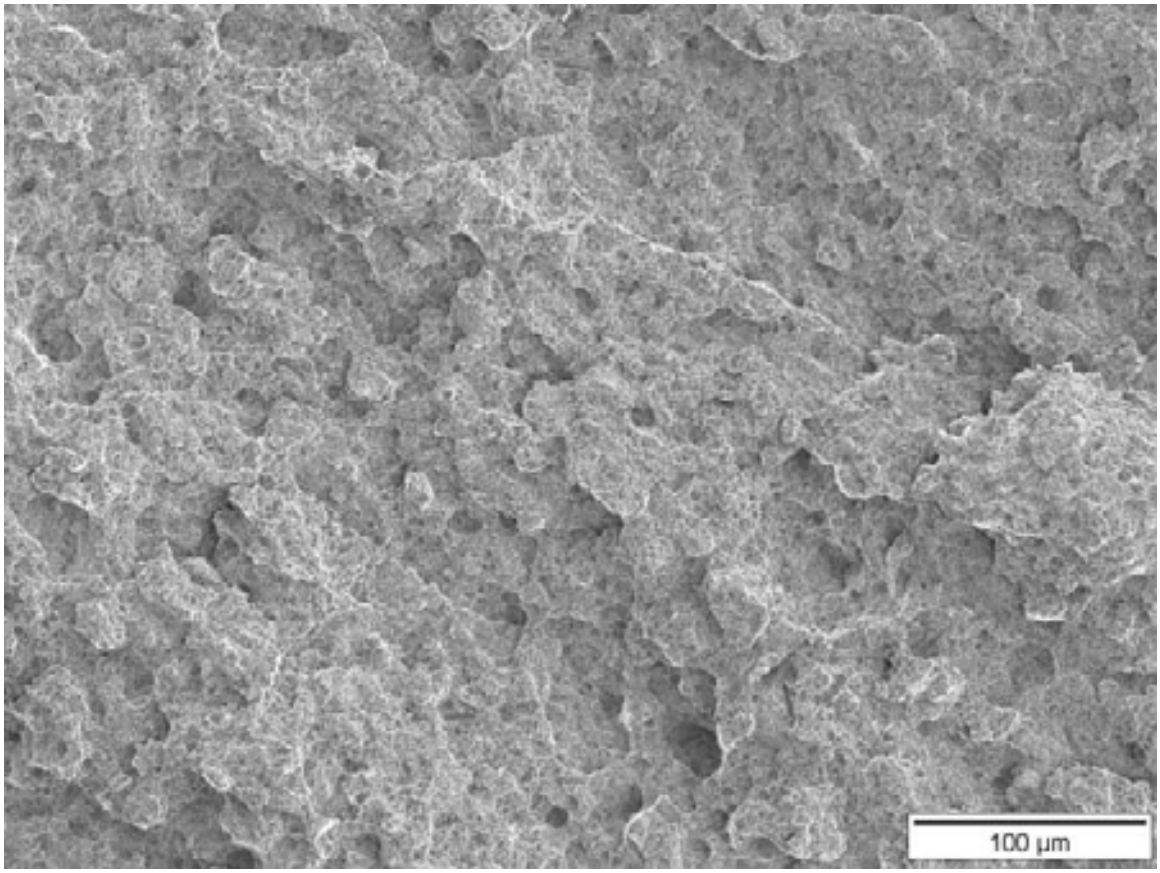

Figure 3.10 Fracture surface of extruded Ti-6Al-4V-1.6B modified alloy showing a jagged fracture surface, suggesting brittle fracture.

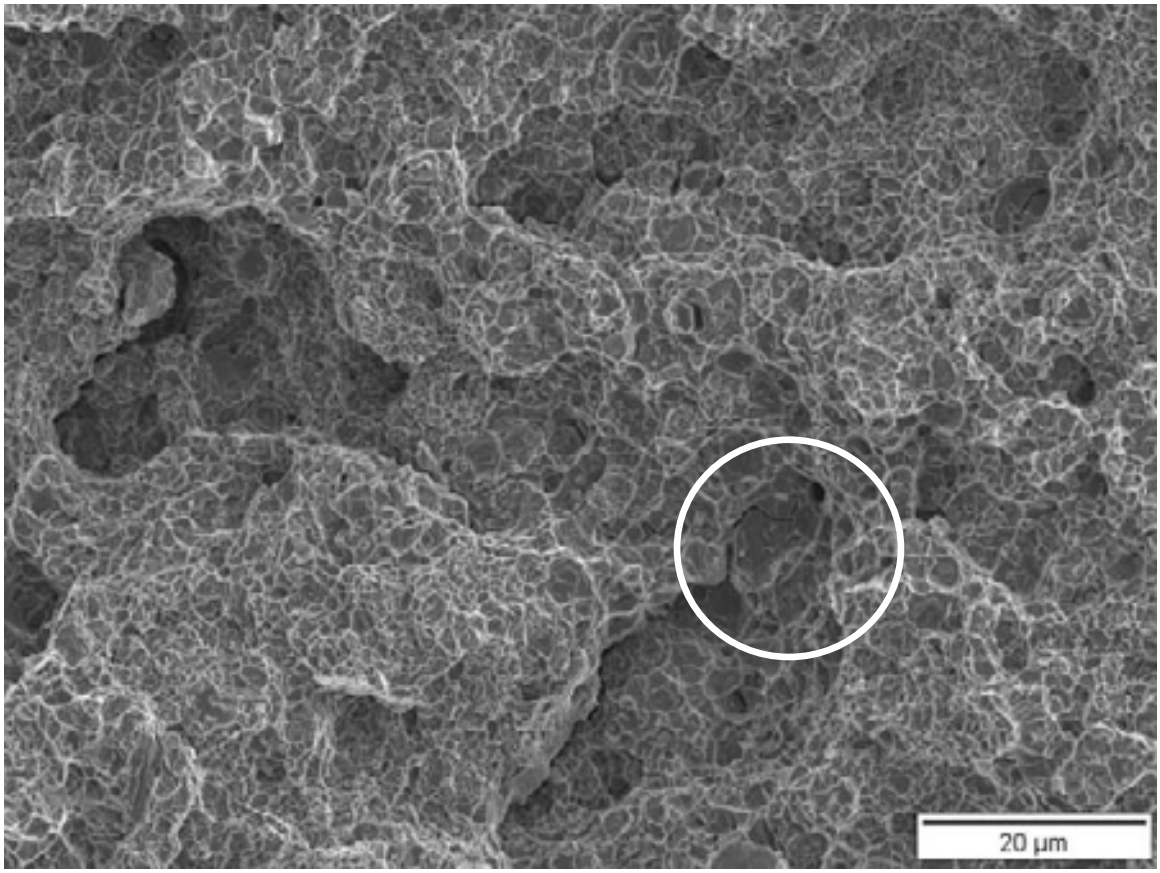

Figure 3.11 Fracture surface of extruded Ti-6Al-4V-1.6B modified alloy, with a primary TiB particle seen just to the right of the center of the SEM micrograph (circled).

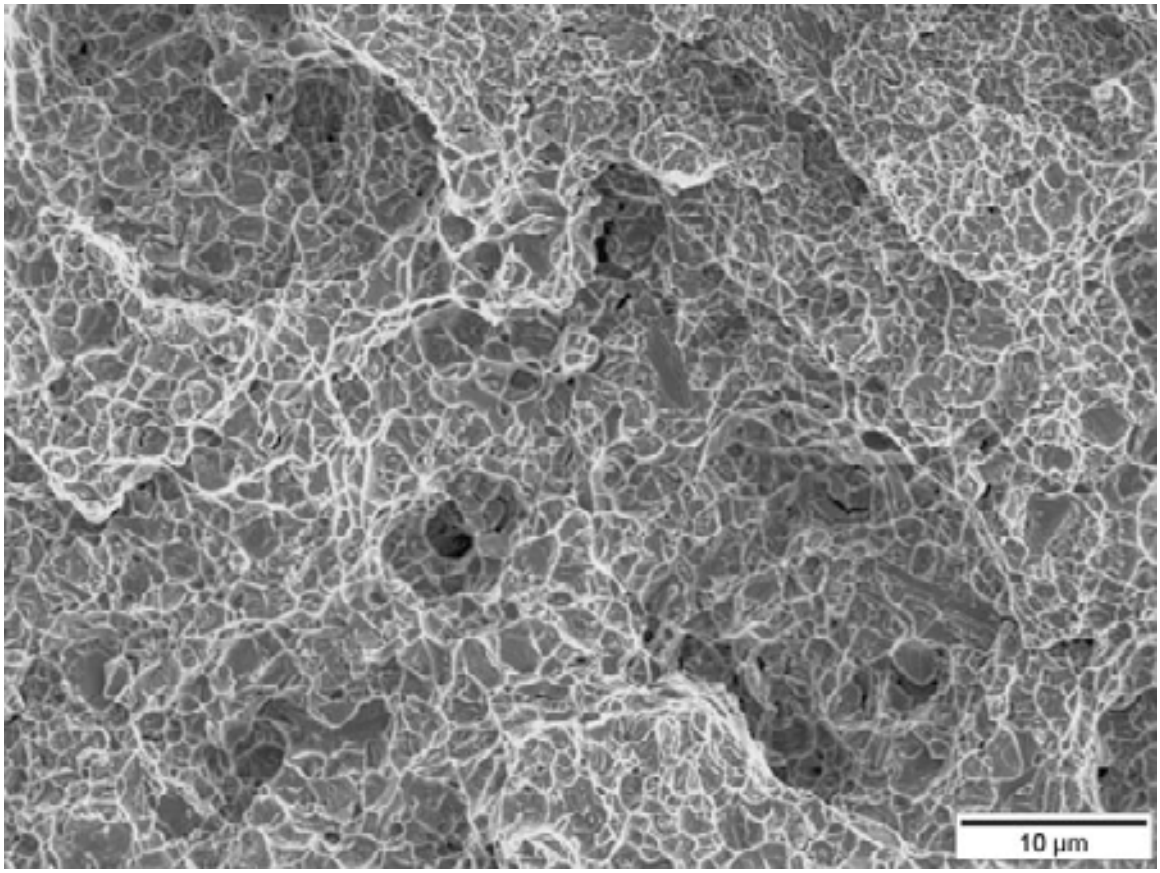

Figure 3.12 Fracture surface of extruded Ti-6Al-4V-1.6B modified alloy, showing brittle fracture across the width of the eutectic TiB whiskers and ductile fracture of the Ti-6Al-4V matrix.

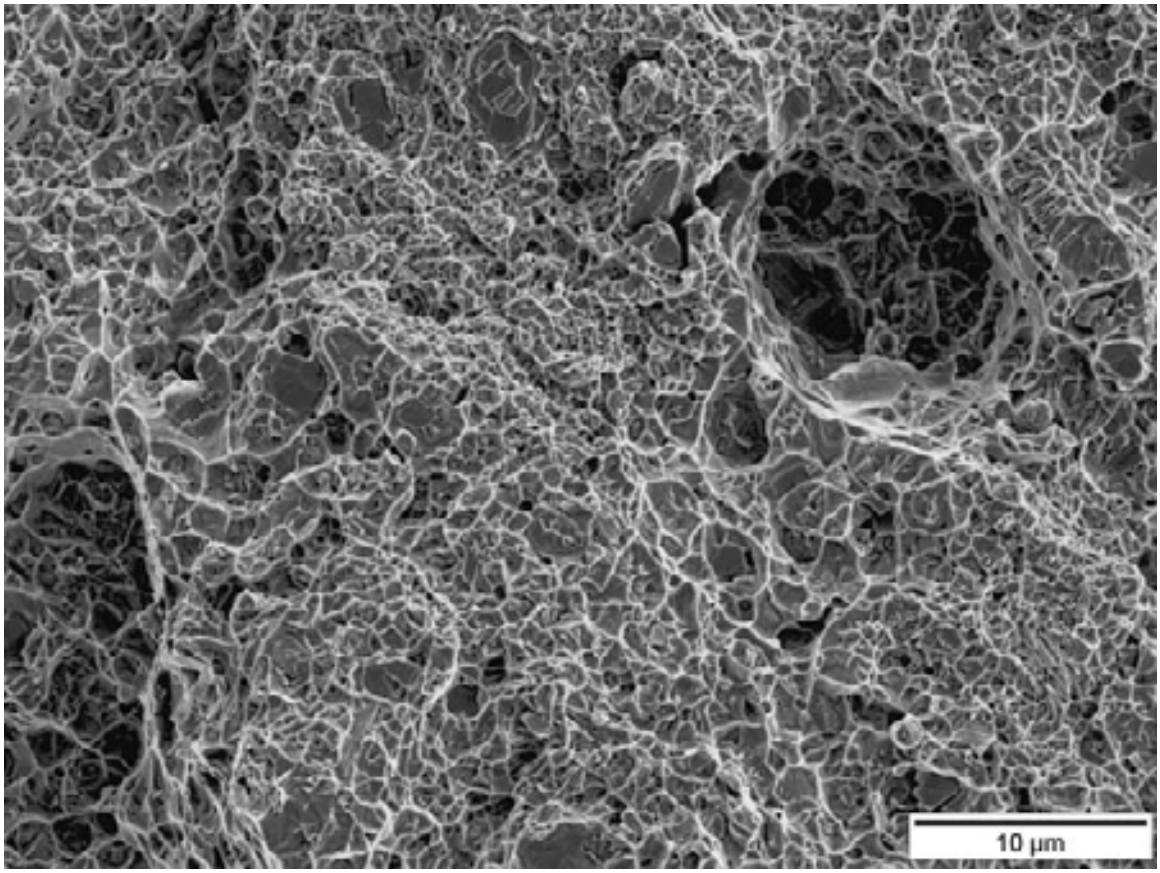

Figure 3.13 Fracture surface of extruded Ti-6Al-4V-1.6B modified alloy, showing brittle fracture across the width of the eutectic TiB whiskers and ductile fracture of the Ti-6Al-4V matrix.

3.2.4 3D Microstructural Visualization

Due to the complexity of the microstructures in Ti-B materials, the information gained from two-dimensional microstructural characterization has proved inadequate for a thorough understanding of the relationships between the processing, microstructure, and properties. The three-dimensional representation and quantification of the microstructure of Ti-B modified alloys and composites would be useful for the characterization, modeling, and simulation of these relationships. The montage serial sectioning technique is particularly suitable for microstructures that contain particles or features with

significantly different length scales and with small interparticle spaces, which require the reconstruction of a large volume of three-dimensional microstructure at a high resolution. These large microstructural volume segments are also suitable to be representative volume elements (RVEs) in finite element-based simulations to predict the mechanical response of the material.

A montage serial sectioning technique was applied for the reconstruction and visualization of TiB particles in both compacted and extruded boron-modified Ti-6Al-4V-1.6B alloy samples. Visualization of the three-dimensional microstructures was used to observe the effects of the processing parameters on the morphology, anisotropy, and spatial distribution of the TiB particles.

In the present work, the montages were created using the automated AxioVision digital image analysis system from Carl Zeiss, Inc., that utilizes the image cross correlation function-based technique for matching the borders between contiguous microstructural fields. In this study, each montage is a microstructural image of an area of approximately 1.75 mm^2, having a high resolution of approximately 0.5 μm. Once the montage of the first serial section was created and stored in the computer memory, a small thickness of the specimen (approximately 1 μm) was removed by polishing, and then a second montage was created at the region exactly below that in the first metallographic plane. This polish-montage-polish procedure was repeated to obtain a stack of 75 montage serial sections.

Microhardness indents were used to locate the exact region of interest in successive serial sections and also to precisely measure the distance between consecutive serial sections [77, 89]. An important practical problem in the reconstruction of a three-

dimensional microstructure from serial sections is that the successive serial sections may not be precisely aligned; they may have some translational and rotational displacement with respect to each other. In the present study, due to slight sample adjustment on the microscope stage, the montages of consecutive serial sections were often displaced by approximately ±10 pixels and ±5 degrees and, therefore, it was essential to precisely align successive serial sections. Alignment can be achieved by locating two common points (the microhardness indents were used for this purpose), in two consecutive serial sections and translating one image until the first common point is aligned in the two images. Then the image is rotated about this point until the second common point is also aligned. In the present work, this was accomplished using the image analysis software KS400 from Carl Zeiss, Inc., in which the images of the montage were digitally translated and rotated until they were aligned within ±1 pixel to the respective previous sections.

The stack of aligned serial sections constituted a volume image data set for three-dimensional microstructure visualization. The marching cube algorithm was employed for surface rendering of the three-dimensional microstructures, using the image analysis software VayTek VoxBlast 3.10 [82]. The effective resolution of the three-dimensional microstructures is approximately 1 μm, which is the depth of material removed between serial sections. Measurements on the three-dimensional rendered images were performed using the image analysis software Image-Pro Plus 3D Suite 5.1 from Media Cybernetics, Inc.

The three-dimensional microstructure visualizations were completed using 75 montage serial sections, with each montage serial section containing 225 contiguous

microstructural fields imaged at a magnification of 800X. Therefore, the resulting three-dimensional data sets are useful for the characterization and visualization of the microstructure at fine as well as at coarse length scales.

Figure 3.14a shows a stack of 20 aligned montage serial sections of the microstructure of the compacted Ti-6Al-4V-1.6B alloy. This figure shows 16 contiguous fields of view cropped from serial sections of 225 contiguous microstructural fields (this figure has been digitally compressed for presentation). Figure 3.14b shows the magnified view of the outlined region in Figure 3.14a, where each section is exactly the stack of serial sections generated by the single field of view-type classical serial sectioning technique [90-95]. This is the magnification at which all microstructural fields of the montages have been imaged. In Figure 3.14b, changes in the sizes of the whiskers at the edges of these serial sections, as well as the appearance and disappearance of features in successive serial sections, can be observed.

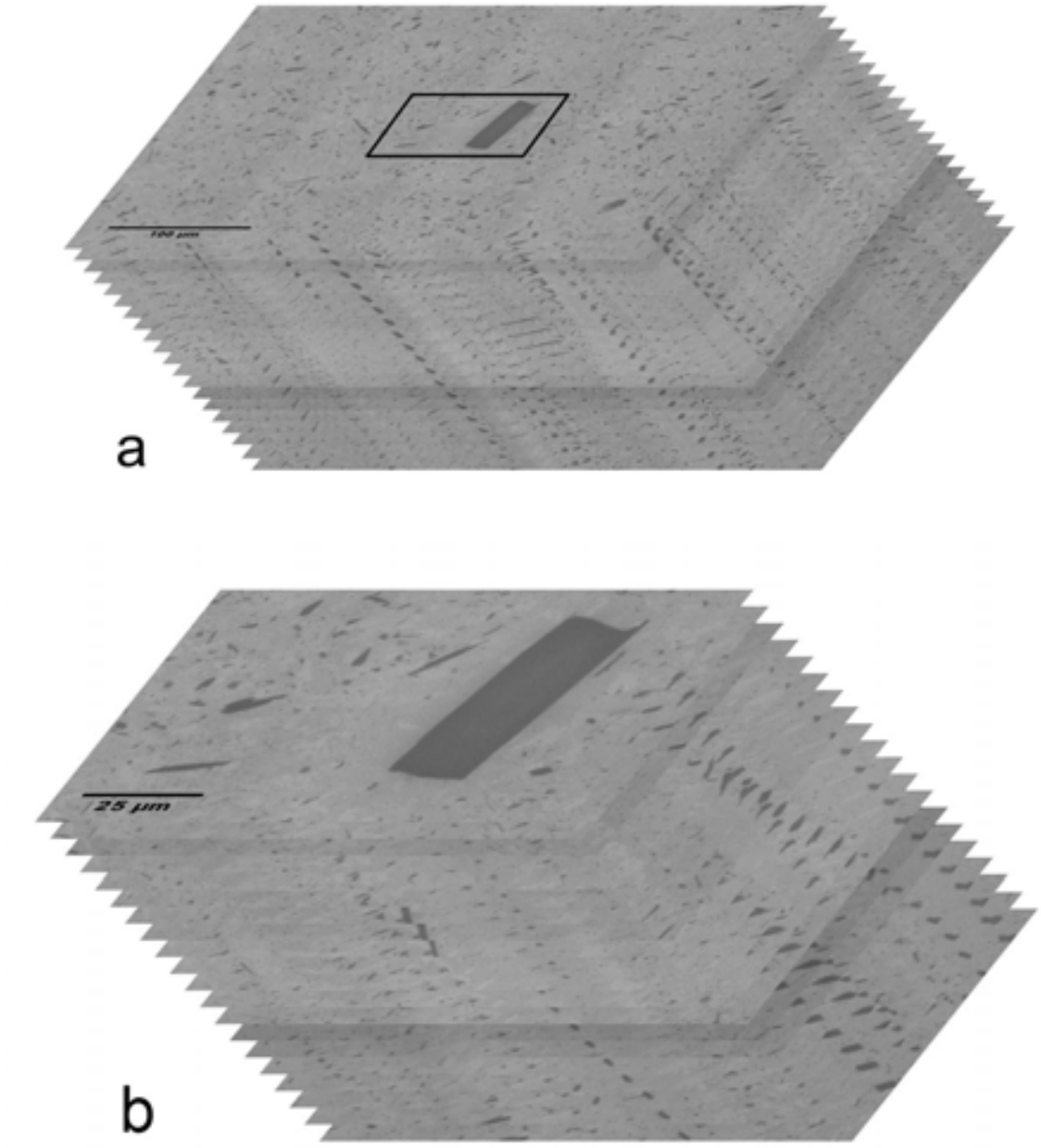

Figure 3.14 (a) Stack of 20 montage serial sections for the compacted Ti-6Al-4V-1.6B alloy microstructure. Each serial section in this figure contains 16 contiguous microstructural fields. (b) The magnified view of the outlined region of the stack of 20 montage serial sections in (a). This is the resolution of the individual microstructural fields.

Figure 3.15a shows a stack of 20 aligned montage serial sections of the microstructure of the extruded Ti-6Al-4V-1.6B alloy with aligned TiB whiskers. The extrusion direction is perpendicular to the plane of the serial sections in this micrograph. This figure shows 16 contiguous fields of view cropped from serial sections of 225 contiguous microstructural fields (this figure has been digitally compressed for presentation). Figure 3.15b shows the magnified view of the outlined region in Figure 3.15a. In Figure 3.15b, as with the compacted alloy, changes in the sizes of the whiskers at the edges of these serial sections, as well as the appearance and disappearance of features in successive serial sections, can be observed.

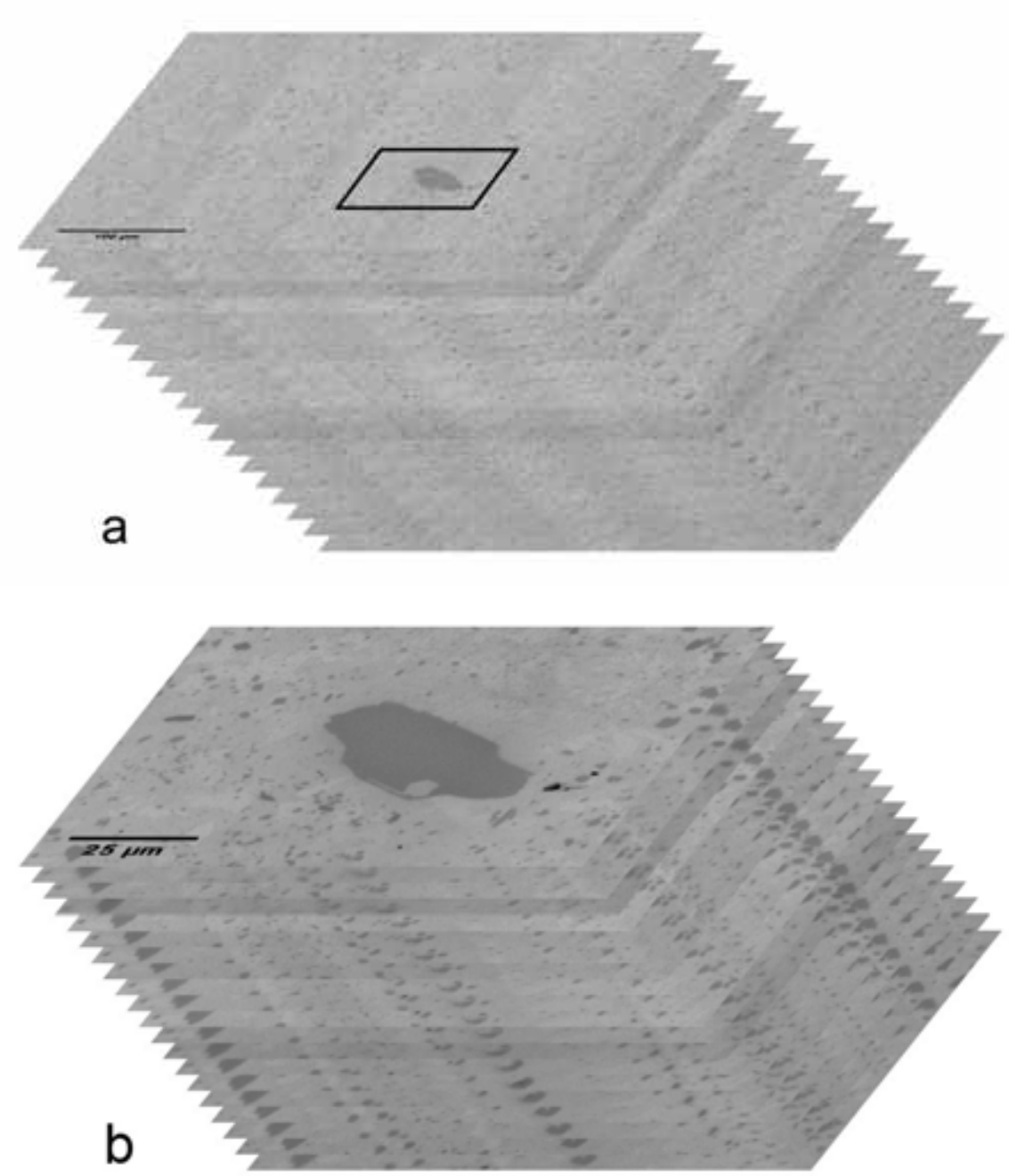

Figure 3.15 (a) Stack of 20 montage serial sections for the extruded Ti-6Al-4V-1.6B alloy microstructure. Each serial section in this figure contains 16 contiguous microstructural fields. (b) The magnified view of the outlined region of the stack of 20 montage serial sections in (a). This is the resolution of the individual microstructural fields.

Figure 3.16 shows a volume segment of the surface rendered three-dimensional microstructure of the compacted Ti-6Al-4V-1.6B alloy containing only eutectic TiB whiskers. In this rendering, images were digitally segmented to completely remove the Ti-6Al-4V matrix and reveal only the TiB phases. Note that this volume segment is only approximately 0.5% of the total microstructure volume collected from the stack of 75 montage serial sections (to produce the three-dimensional rendering at the resolution of the eutectic TiB whiskers). The TiB whiskers in this microstructure are observed to have uniform random angular orientations.

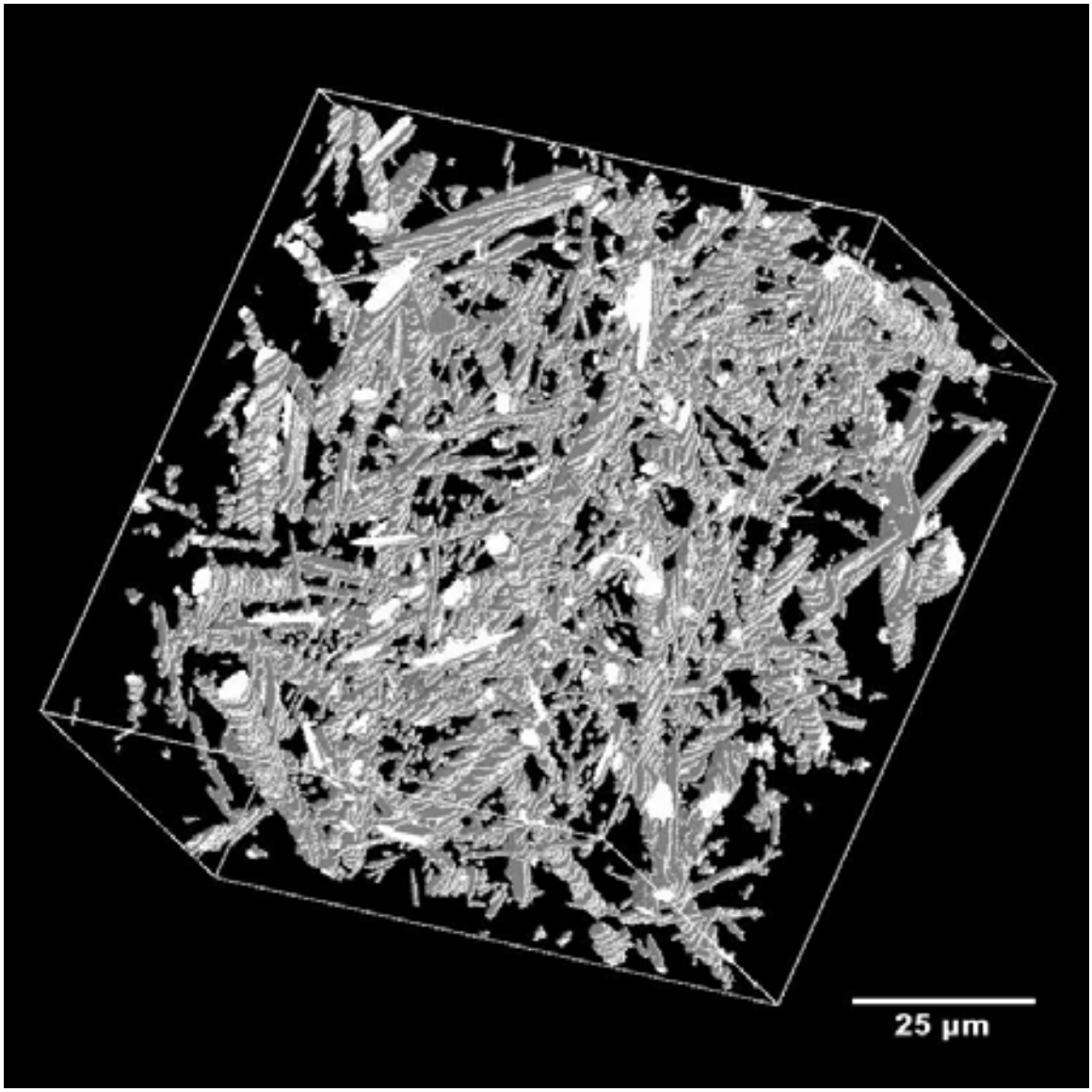

Figure 3.16 Small segment of surface rendered three-dimensional microstructure of compacted Ti-6Al-4V-1.6B alloy revealing uniform random angular orientation of the eutectic TiB whiskers.

Figure 3.17 shows another volume segment of the surface rendered three-dimensional microstructure of the compacted alloy specimen that contains both eutectic TiB whiskers and a coarse primary TiB particle that is approximately an order of magnitude larger than the eutectic TiB whiskers.

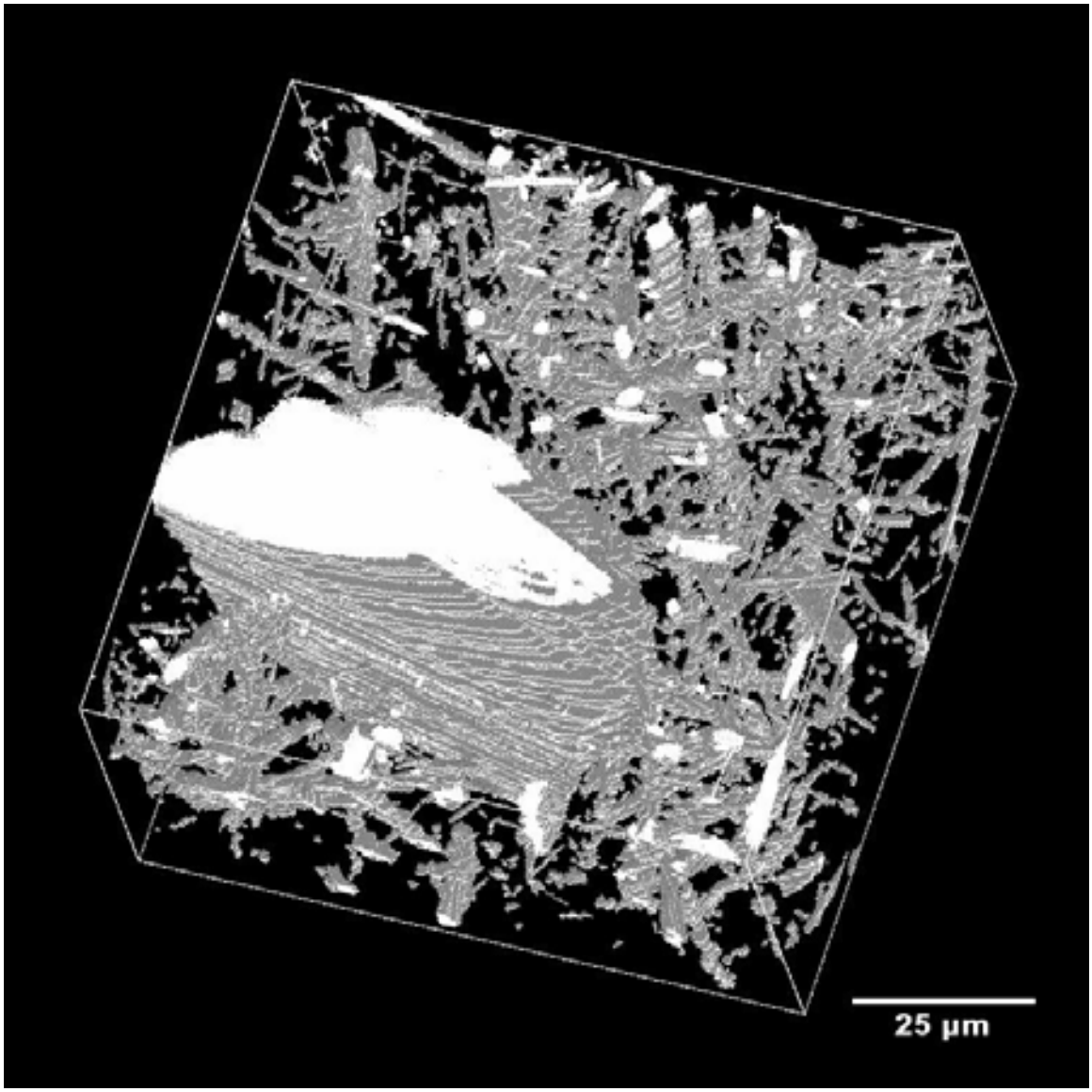

Figure 3.17 Small segment of surface rendered three-dimensional microstructure of compacted Ti-6Al-4V-1.6B alloy, showing both eutectic TiB whiskers and a coarse primary TiB particle.

Figure 3.18 shows a segment of the surface rendered three-dimensional microstructure of the extruded Ti-6Al-4V-1.6B alloy depicting the spatial distribution of anisotropic eutectic TiB whiskers. This figure clearly shows that the eutectic TiB whiskers have anisotropic orientations after extrusion and that the majority of these

whiskers are aligned along the extrusion direction, which is the z-axis of the volume segment.

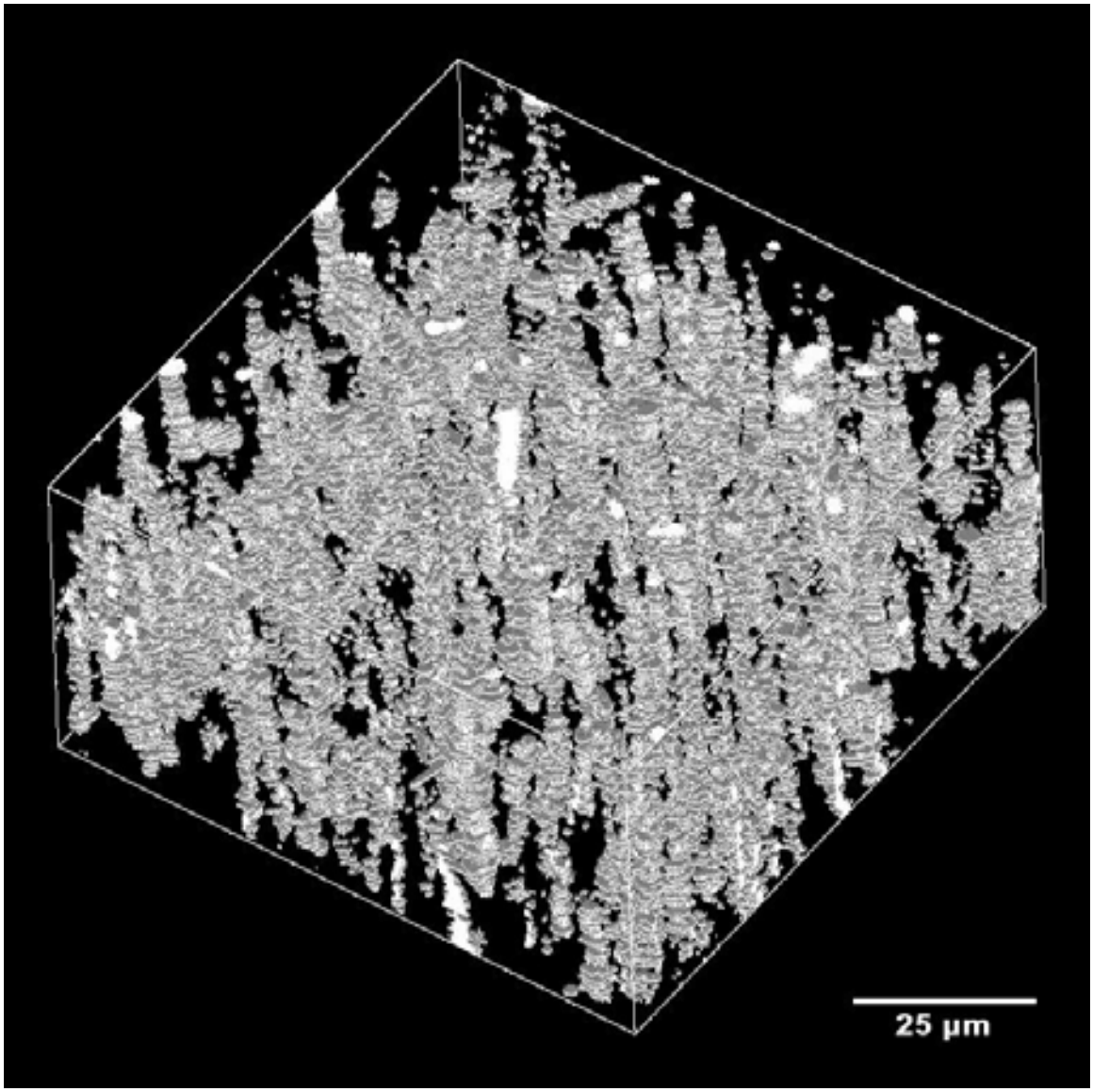

Figure 3.18 Small segment of surface rendered three-dimensional microstructure of extruded Ti-6Al-4V-1.6B alloy, showing the alignment of the majority of the eutectic TiB whiskers along the extrusion direction (which is the z-axis in this figure).

Figure 3.19 shows another volume segment of the surface rendered three-dimensional microstructure of the extruded Ti-6Al-4V-1.6B alloy that contains

anisotropic eutectic TiB whiskers as well as a coarse primary TiB particle in the center of the image that is approximately an order of magnitude larger than the eutectic TiB whiskers.

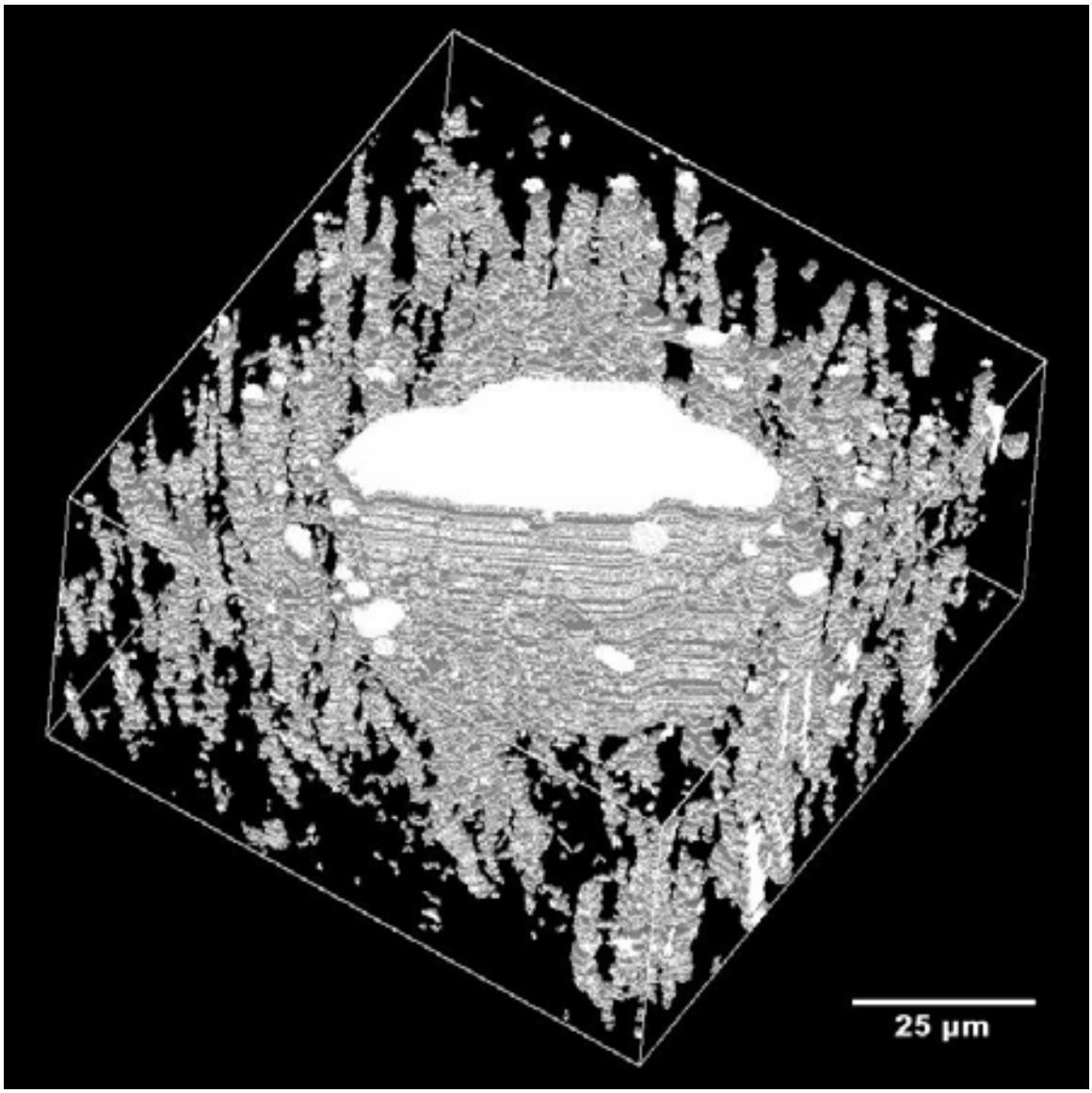

Figure 3.19 Small segment of surface rendered three-dimensional microstructure of extruded Ti-6Al-4V-1.6B alloy, showing eutectic TiB whiskers around a coarse primary TiB particle. This three-dimensional microstructure shows the alignment of the majority of the eutectic TiB whiskers along the extrusion direction (which is the z-axis in this figure).

From these visualizations, it can be concluded that plastic deformation during the extrusion process gives rise to rigid body rotations of the TiB whiskers, which confirms the conclusion reached by Schuh and Dunand on the basis of two-dimensional microstructural observations [23]. Although the morphological orientation distribution of the eutectic TiB whiskers is different in the compacted microstructure as compared to the extruded microstructure, the spatial arrangement of the eutectic TiB whiskers appears to be uniform random in the three-dimensional microstructures of both alloys. Therefore, although the extrusion process leads to TiB whisker rotations, it does not give rise to spatial clustering of the whiskers.

Figure 3.20a shows various three-dimensional views of just the primary TiB particle extracted from Figure 3.19. This primary TiB particle is present in each of the 75 serial sections of the extruded alloy specimen, and it is truncated by the first and the last serial sections. The part of the volume of this particle contained between the first and the last serial sections is approximately 67,000 μm^3, the surface area is approximately 12,300 μm^2, and the axial ratio is 3.76, which provide a lower bound on the true volume, surface area, and axial ratio of the particle. Therefore, the primary TiB particle has an elongated shape rather than an equiaxed shape as reported in the literature [15, 16]. Figure 3.20b shows various three-dimensional views of a single eutectic TiB whisker extracted from the volume segment of the surface rendered three-dimensional microstructure of the compacted alloy specimen in Figure 3.16. This eutectic TiB whisker is approximately an order of magnitude smaller in size than a primary TiB particle. While the surface rendered primary TiB particles have been truncated by the boundaries of the 75 serial sections, the eutectic TiB whisker in Figure 3.20b is whole. Figure 3.20c shows various

three-dimensional views of the coarse primary TiB particle extracted from the three-dimensional microstructure of the compacted alloy specimen in Figure 3.17. The morphology (elongated shape), and the length scale of the primary TiB particle in the compacted alloy (Figure 3.20c) are very similar to the primary TiB particle in the extruded alloy (Figure 3.20a). The primary TiB particle shown in Figures 3.17 and 3.20c is present in 65 of the serial sections, and it is truncated by the last serial section. The part of the volume of this particle contained between the first and the last serial sections is 53,400 μm^3, the surface area is 11,600 μm^2, and the axial ratio is 3.29, which is a lower bound on the true volume, surface area, and axial ratio of the particle.

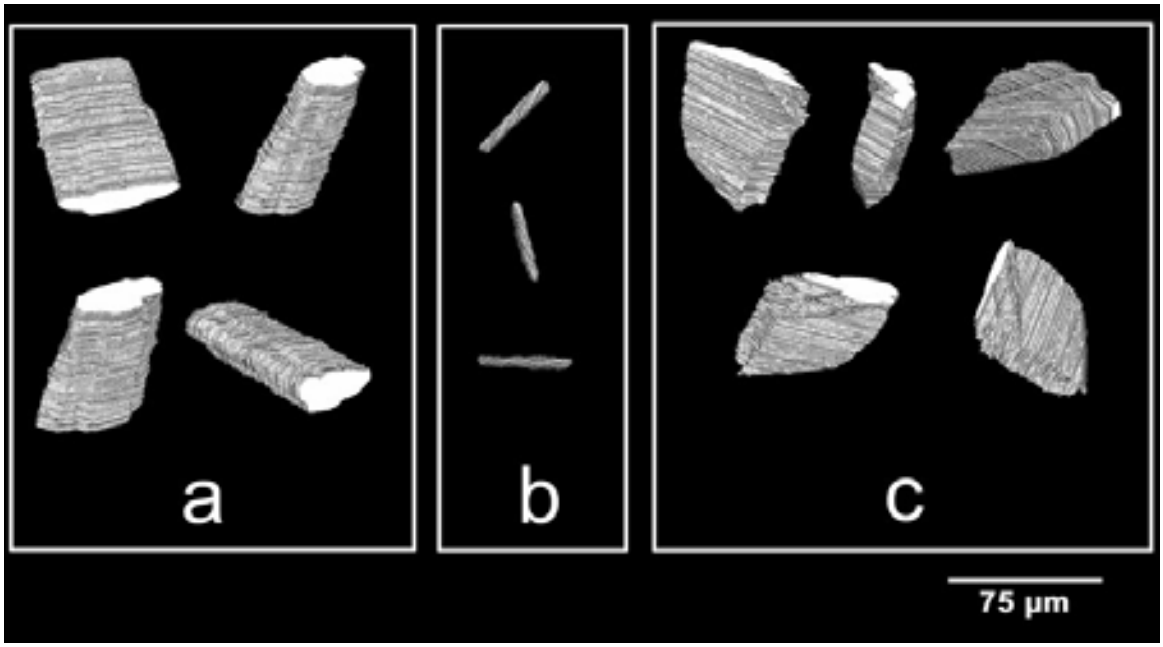

Figure 3.20 (a) Three-dimensional views of the primary TiB particle extracted from the surface rendered three-dimensional microstructure of the extruded Ti-6Al-4V-1.6B alloy sample shown in Figure 3.19. (b) Three-dimensional views of a eutectic TiB whisker extracted from the surface rendered three-dimensional microstructure of the compacted Ti-6Al-4V-1.6B alloy sample shown in Figure 3.16. (c) Three-dimensional views of the primary TiB particle extracted from the surface rendered three-dimensional microstructure of the compacted Ti-6Al-4V-1.6B alloy shown in Figure 3.17.

3.3 Hypoeutectic Pre-Alloyed Boron-Modified Ti-6Al-4V Alloy

Samples of pre-alloyed Ti-6Al-4V-1B alloys were examined, both in the as-compacted condition and following extrusion. This composition is in the hypoeutectic regime of the quaternary system of titanium, alloying elements aluminum and vanadium, and boron. It was expected that only the eutectic TiB whiskers, and no particles of the primary TiB phase, were to be found in these alloys. The absence of the larger primary TiB particles was hoped to improve the fracture properties of these alloys while still providing an increase in strength as compared to unreinforced Ti-6Al-4V.

3.3.1 Materials and Processing Details

Similarly to the hypereutectic alloy samples, pre-alloyed powder of boron-modified Ti-6Al-4V was produced at Crucible Research Corporation, Pittsburgh, Pennsylvania. In this process, the melting procedure involved induction skull (made of titanium) melting of appropriate amounts of the raw materials (titanium, Al-V master alloy, and TiB_2), in a water-cooled copper crucible. Boron additions to the melt were contributed in the form of TiB_2, which dissolves in the liquid melt and forms TiB during solidification by the in situ eutectic phase transformation reaction $Ti + TiB_2 \rightarrow 2TiB$. The liquid melt was then rapidly solidified using inert gas atomization to produce Ti-6Al-4V-1B powder. The atomized powder was then sieved to obtain -100 mesh size (average particle size of 150 μm).

Colleagues at the Air Force Research Laboratory, Wright-Patterson Air Force Base, Ohio, then received the pre-alloyed powder for further P/M processing. The Ti-6Al-4V-1B powder was packed inside a thick-walled can of Ti-6Al-4V, vacuum outgassed at 300°C for 24 hours, and sealed. The can was coated with glass for

lubrication and environmental protection, heated to 1200°C, soaked for 1 hour, and then blind-die compacted in an extrusion chamber heated to 260°C. The billet height was reduced by about 30% at a ram speed of 6.35 mm/s. The compact was then held at a pressure of 1400 MPa for 180 seconds and subsequently air-cooled to room temperature. A second billet blind die compacted by the same method was subsequently hot extruded, heated to 1100°C and soaked for 1 hour prior to extrusion through a circular die with an extrusion reduction ratio of 16.5:1, at a ram speed of 6.35 mm/s, and air-cooled to room temperature. Specimens were then sectioned from the compacted billet and extruded rod.

3.3.2 Optical Microscopy and Quantitative Characterization

Specimens of the compacted billet and extruded rod were mounted in thermoplastic using standard techniques for metallography. Suitable grinding and polishing schemes developed for Ti-B modified alloys and composites were utilized, taking into account the hardness differences between the relatively soft Ti-6Al-4V alloy matrix and the relatively hard TiB whisker reinforcement. Using these metallographic techniques, a final surface finish of 0.05 μm was obtained.

Samples of both compacted and extruded Ti-6Al-4V-1B modified alloy were examined using a Carl Zeiss, Inc. Axiovert 200 MAT optical microscopy system with AxioVision image analysis software. For each sample, montages were created using the automated AxioVision digital image analysis system that utilizes the image cross correlation function-based technique for matching the borders between contiguous microstructural fields. For these samples, each montage is a microstructural image of a large area (~1.75 mm^2), having a high resolution (~0.5 μm).

Figure 3.21 shows one such montage of 195 fields of view of compacted Ti-6Al-4V-1B alloy. Figure 3.22 shows a higher magnification image of the compacted alloy specimen. The images have been compressed for display. These micrographs show eutectic TiB whiskers randomly dispersed and oriented in a Ti-6Al-4V matrix. In these figures, the TiB whiskers are a darker gray than the gray titanium matrix. No coarse primary TiB particles were observed. Montages were taken from different regions and different samples of each alloy specimen to ensure that observations were performed on representative examples of the microstructures.

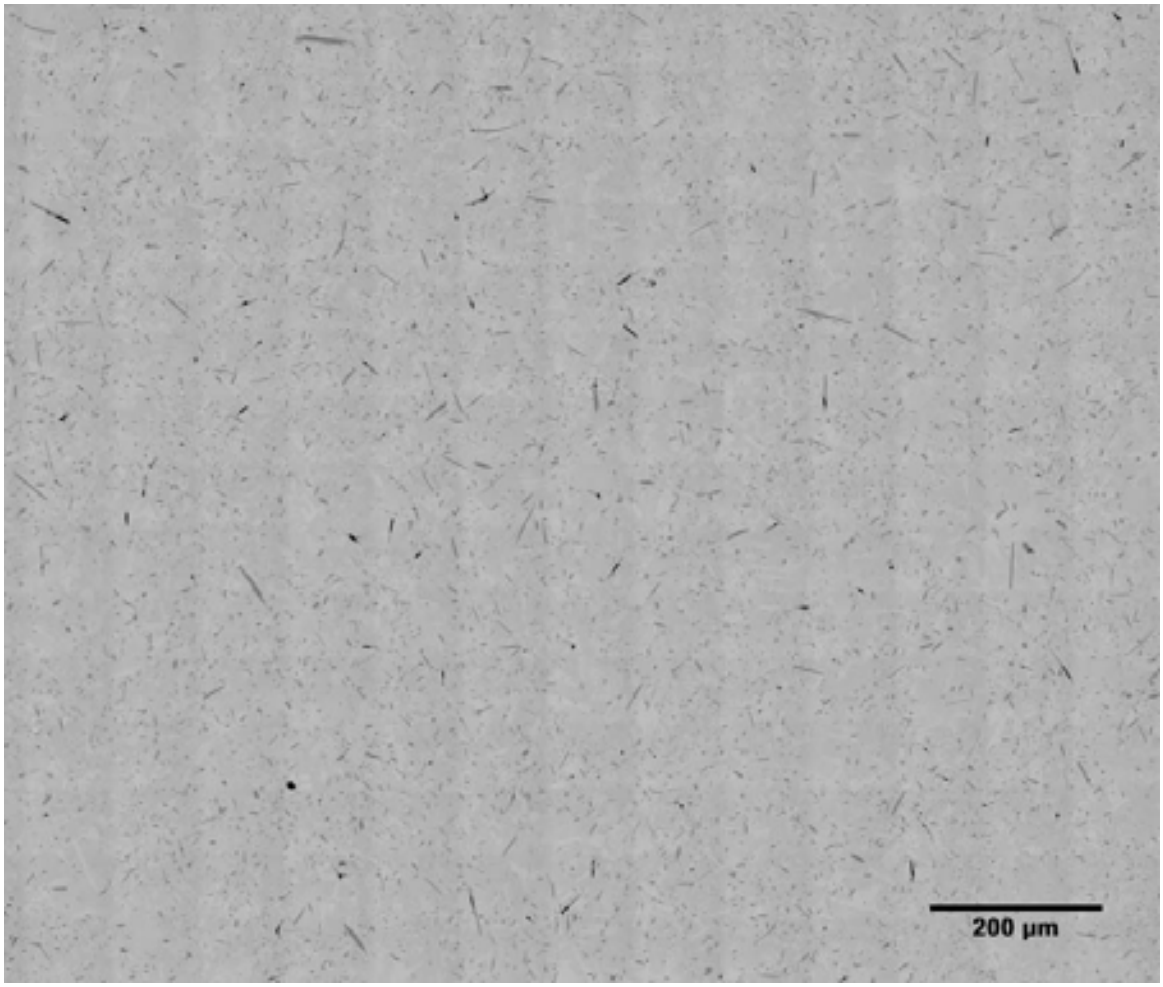

Figure 3.21 Montage of the microstructure of compacted Ti-6Al-1B alloy showing randomly oriented eutectic TiB whiskers. This micrograph is a montage of 195 fields of view covering an area of approximately 1.75 mm^2, and has been digitally compressed for presentation.

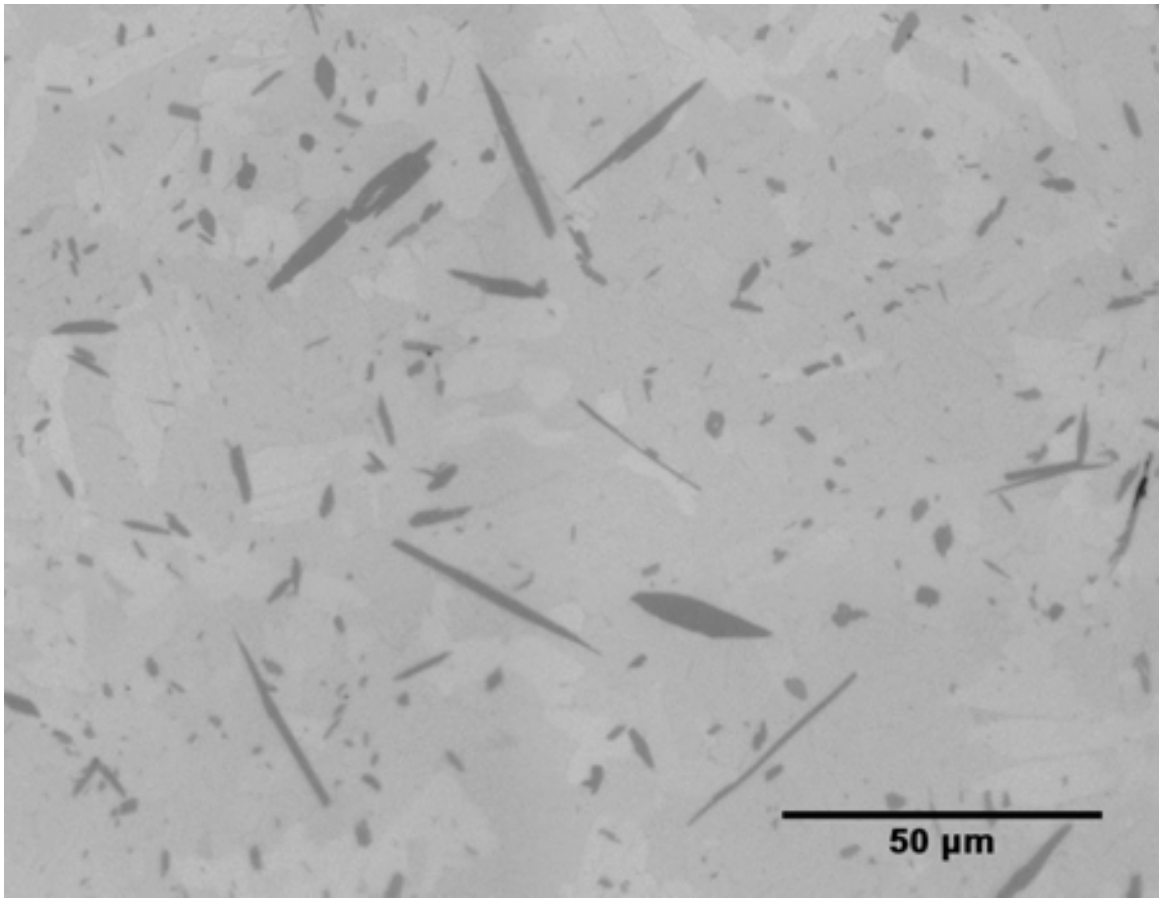

Figure 3.22 Microstructure of compacted Ti-6Al-4V-1B alloy showing randomly oriented eutectic TiB whiskers.

A montage from the extruded sample of Ti-6Al-4V-1B alloy is shown in Figure 3.23. The extrusion direction is normal to the plane of the micrograph. As in the micrographs of the compacted boron-modified alloy, the eutectic TiB whiskers are seen as dark gray in a gray matrix of Ti-6Al-4V alloy. Coarse primary TiB particles are again not observed in the material, as its composition lies in the hypoeutectic regime of the alloy system.

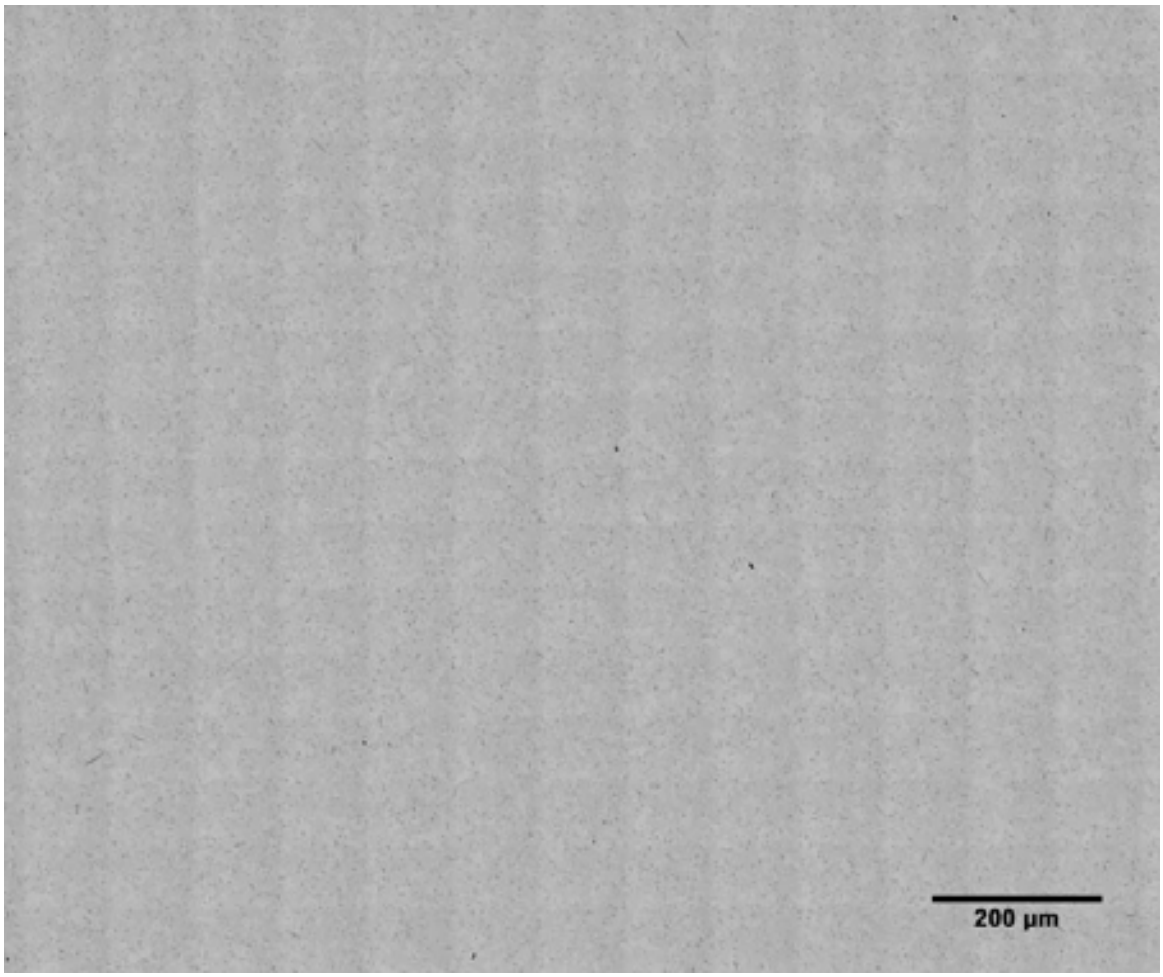

Figure 3.23 Montage of the microstructure of extruded Ti-6Al-4V-1B alloy. The extrusion direction is normal to the micrograph.

The microstructure of the extruded Ti-6Al-4V-1B alloy at higher magnification is shown in Figure 3.24. Only the eutectic TiB phase is seen, and confirms alignment of TiB whiskers following extrusion that was previously observed, although some of the TiB whiskers are not completely aligned in the extrusion direction [23]. The roughly hexagonal cross-section of the eutectic TiB whiskers is also seen [87].

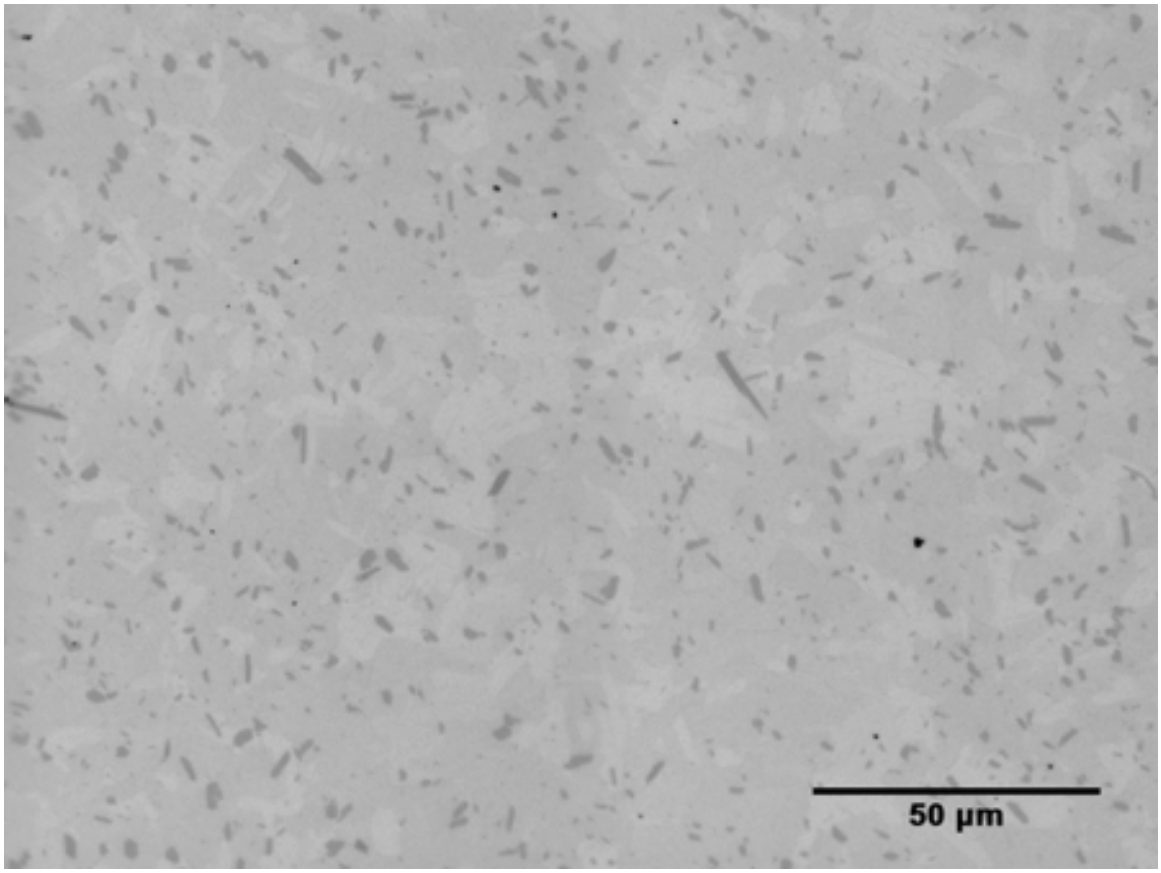

Figure 3.24 Microstructure of extruded Ti-6Al-4V-1B alloy showing eutectic TiB whiskers mostly aligned with the extrusion direction normal to the micrograph.

Microstructural data for these compacted and extruded Ti-6Al-4V-1B alloy samples were calculated using conventional two-dimensional stereology techniques. For the extruded alloy, measurements were made on montages in the plane parallel as well as on montages in the plane normal to the extrusion direction. Average values are shown in Table 3.3, but these results do not take into account the stochastic nature of microstructures. Overall, it was found that the eutectic TiB whiskers typically had a length of approximately 20-30 μm and a width of approximately 2.5-6 μm, for an aspect ratio range of between 3.3 and 12. The overall volume fraction of TiB whiskers in these samples is approximately 4%. In addition, although the angular orientation of the TiB

whiskers was affected by extrusion, the morphology of the TiB phases was not observed to have been affected by extrusion.

Table 3.3 Microstructural data of Ti-6Al-4V-1B modified alloy samples calculated using standard two-dimensional stereology techniques.

sample	avg length (μm)	avg width (μm)	aspect ratio	volume fraction
compacted	21.13	3.20	6.60	4.35
extruded	23.41	3.37	6.95	3.98

3.3.3 SEM Fractography

To investigate fracture behavior, samples of Ti-6Al-4V-1B alloy were sectioned from both the compacted billet and from the extruded rod, and machined into ¼”-20 round tensile specimens by colleagues at the Air Force Research Laboratory. These specimens then underwent room temperature tensile tests according to ASTM standard E8-04 [88]. Tensile test results are shown in Table 3.4. Note the improvement in tensile elongation to failure compared to the hypereutectic alloy specimens (Table 3.2), with the extruded sample having an elongation to failure well above the aerospace structural design limit of approximately 7% [6]. In addition, these samples also show an improvement over the elastic modulus of unreinforced Ti-6Al-4V alloy of approximately 110 GPa. Prior to examination of the tensile fracture surfaces using scanning electron microscopy (SEM), the specimens underwent ultrasonic cleaning in ethanol for 5 minutes.

Table 3.4 Tensile test results of Ti-6Al-4V-1B alloy, using ASTM E8-04.

sample	E (GPa)	σ_y (MPa)	σ_{uts} (MPa)	e (%)
compacted	127	927	1038	6.2
extruded	143	1078	1214	13.3

The fracture surfaces of the tensile test specimens were examined with a Sirion FEI scanning electron microscope, using secondary electron emission. The fracture surface of the compacted Ti-6Al-4V-1B alloy specimen is shown in Figures 3.25-3.28. In Figure 3.25, at a magnification of 120X, a somewhat jagged and ductile fracture surface is observed, that appears similar to the fracture surface of the compacted hypereutectic specimen shown in Figure 3.5. At a higher magnification of 250X in Figure 3.26, it can clearly be seen that fracture has occurred down the length of the eutectic TiB whiskers. Further evidence of the brittle fracture of eutectic TiB whiskers is shown in Figures 3.27 and 3.28. Very little, if any, whisker pullout was observed. No primary TiB phase was seen in this specimen. In addition, the fracture surface has a higher TiB content than the bulk material, as was similarly observed in the hypereutectic specimens. The Ti-6Al-4V matrix shows ductile failure.

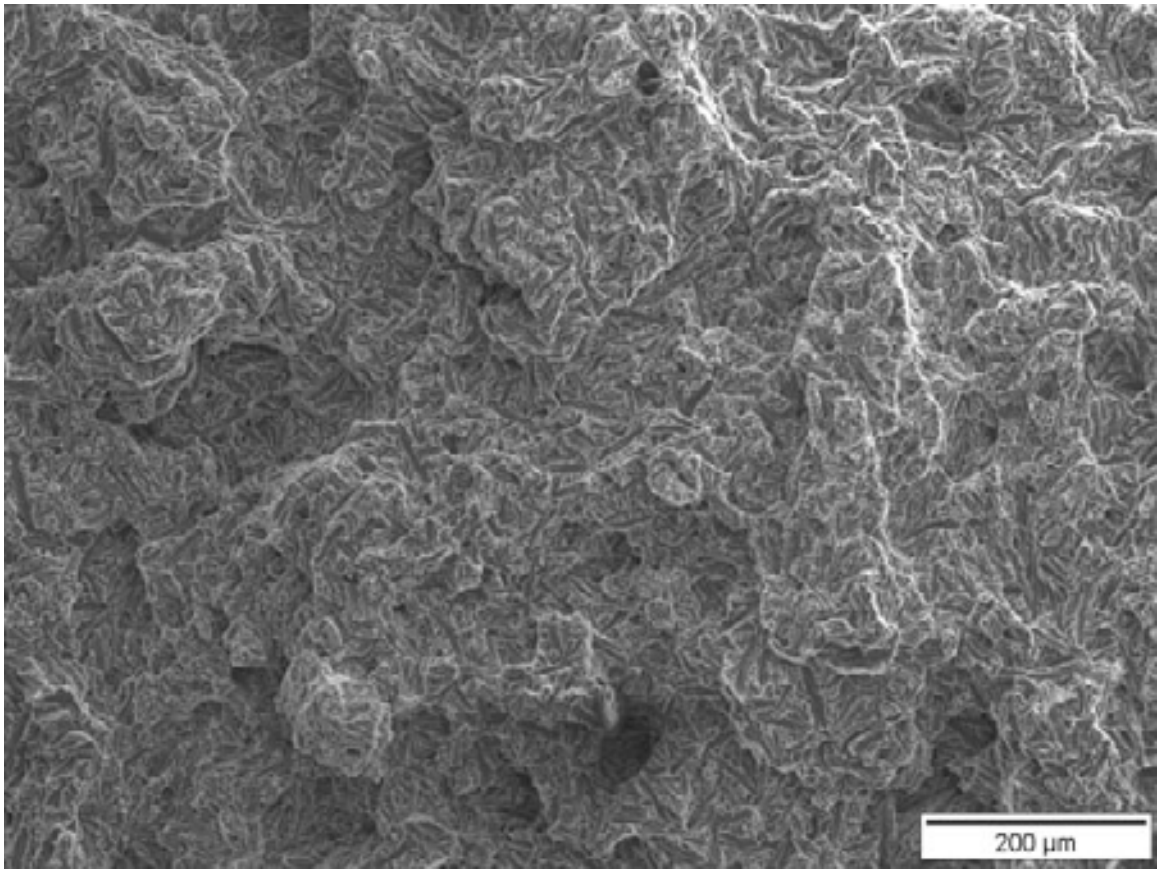

Figure 3.25 Fracture surface of compacted Ti-6Al-4V-1B modified alloy showing a jagged fracture surface, suggesting brittle fracture.

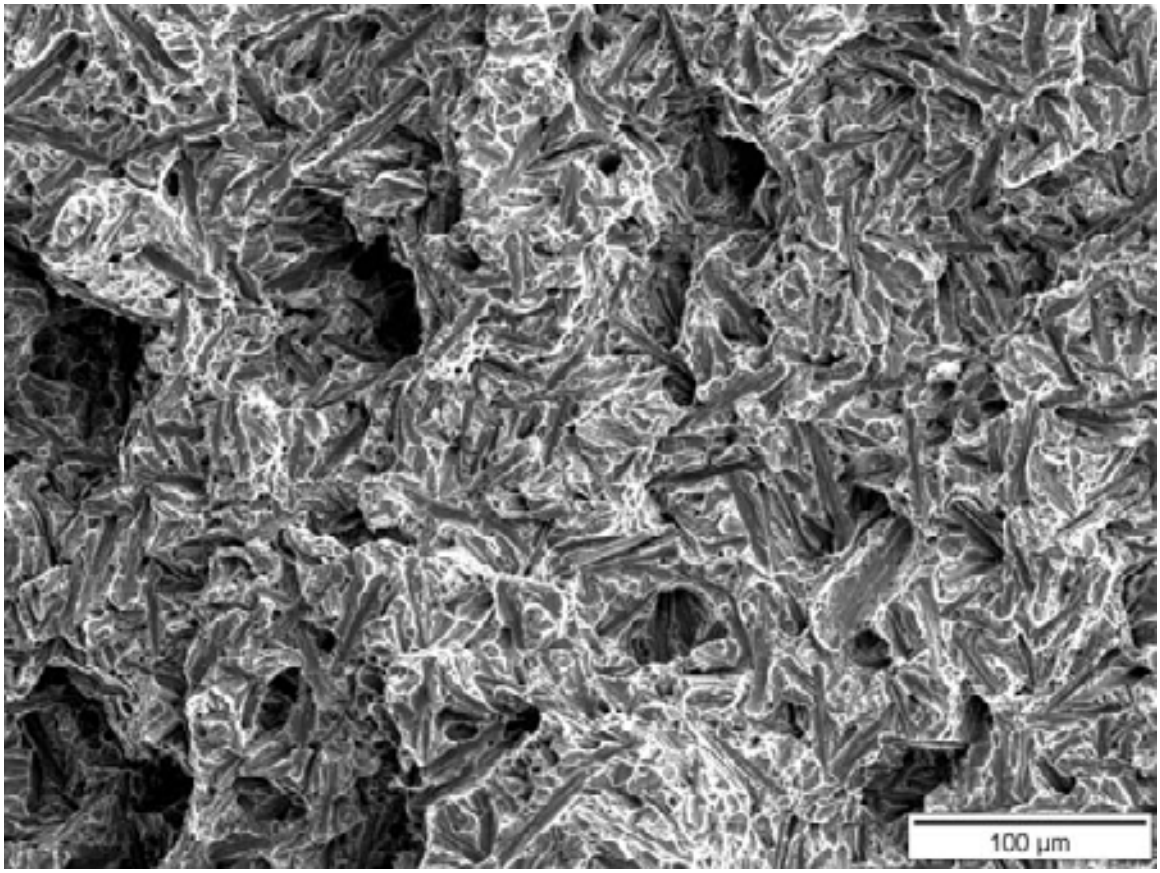

Figure 3.26 Fracture surface of compacted Ti-6Al-4V-1B modified alloy, showing brittle fracture down the length of the eutectic TiB whiskers and ductile fracture of the Ti-6Al-4V matrix.

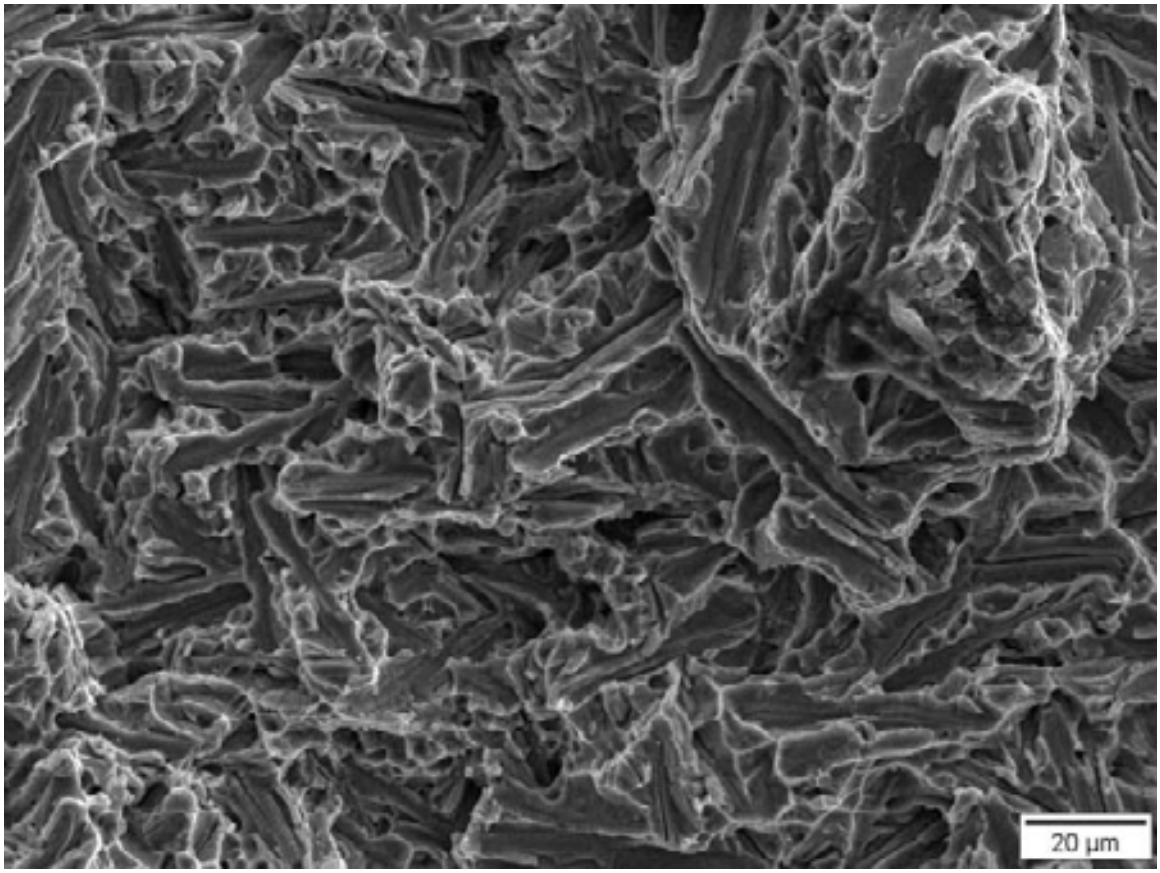

Figure 3.27 Fracture surface of compacted Ti-6Al-4V-1B modified alloy, showing brittle fracture down the length of the eutectic TiB whiskers and ductile fracture of the Ti-6Al-4V matrix.

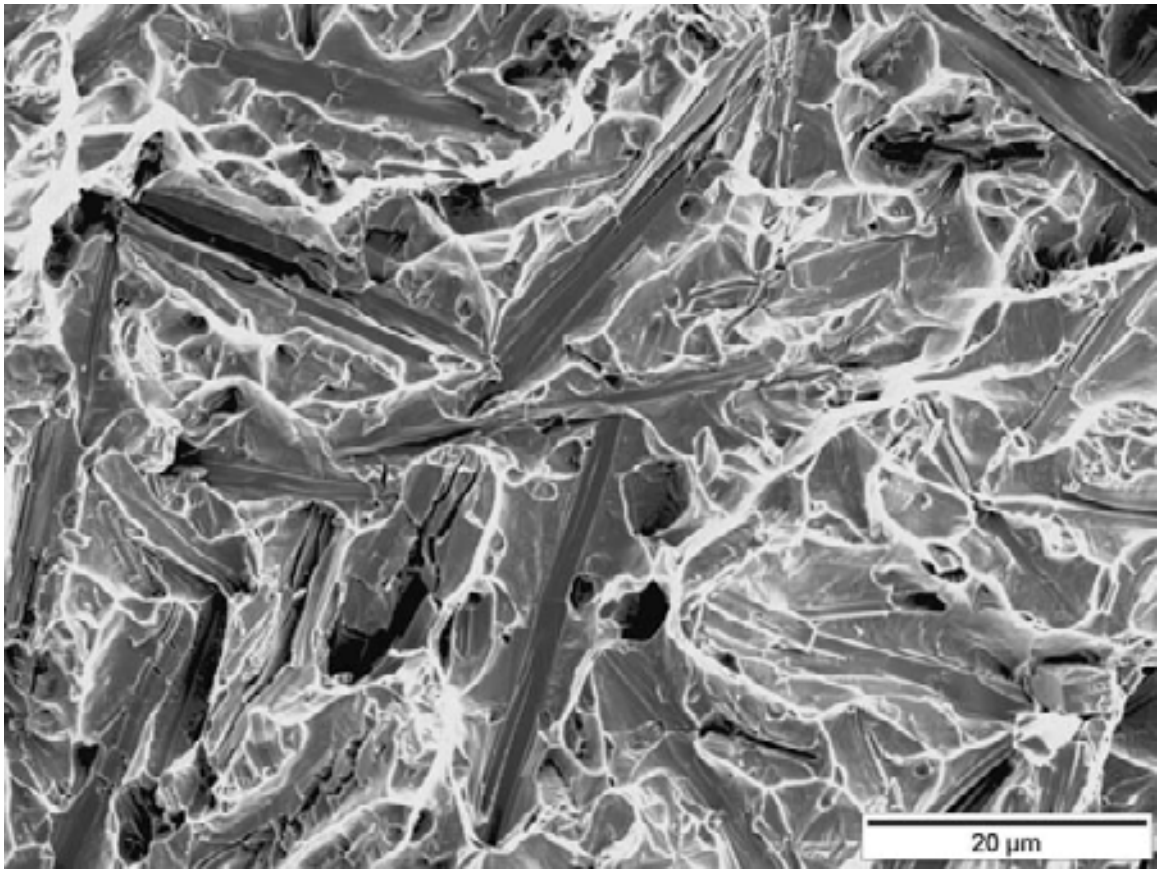

Figure 3.28 Fracture surface of compacted Ti-6Al-4V-1B modified alloy, showing brittle fracture down the length of the eutectic TiB whiskers and ductile fracture of the Ti-6Al-4V matrix.

For the extruded Ti-6Al-4V-1B alloy specimen, the extrusion direction is parallel to the tensile test direction. Fracture behavior of this specimen during tensile testing suggested a more ductile fracture compared with the hypereutectic specimens and with the compacted Ti-6Al-4V-1B alloy. The fracture surface of this extruded specimen is shown in Figures 3.29-3.34. In Figure 3.29, the fracture surface is seen at a magnification of 250X, showing a relatively ductile fracture surface. In Figures 3.30 and 3.31, the fracture surface is shown at higher magnifications, and predominantly ductile fracture of the Ti-6Al-4V matrix can be clearly seen. Unlike the compacted alloy

specimen, fracture of the TiB whiskers is predominantly across the width of the whiskers, not down the length of the whiskers, as shown in Figures 3.32 and 3.33. These figures also clearly demonstrate the roughly hexagonal cross-section of the eutectic TiB whiskers. Although the majority of TiB whiskers were aligned with the extrusion direction and failed across their widths, some misaligned TiB whiskers were observed on the fracture surface, and showed brittle fracture down their lengths, as in Figure 3.34.

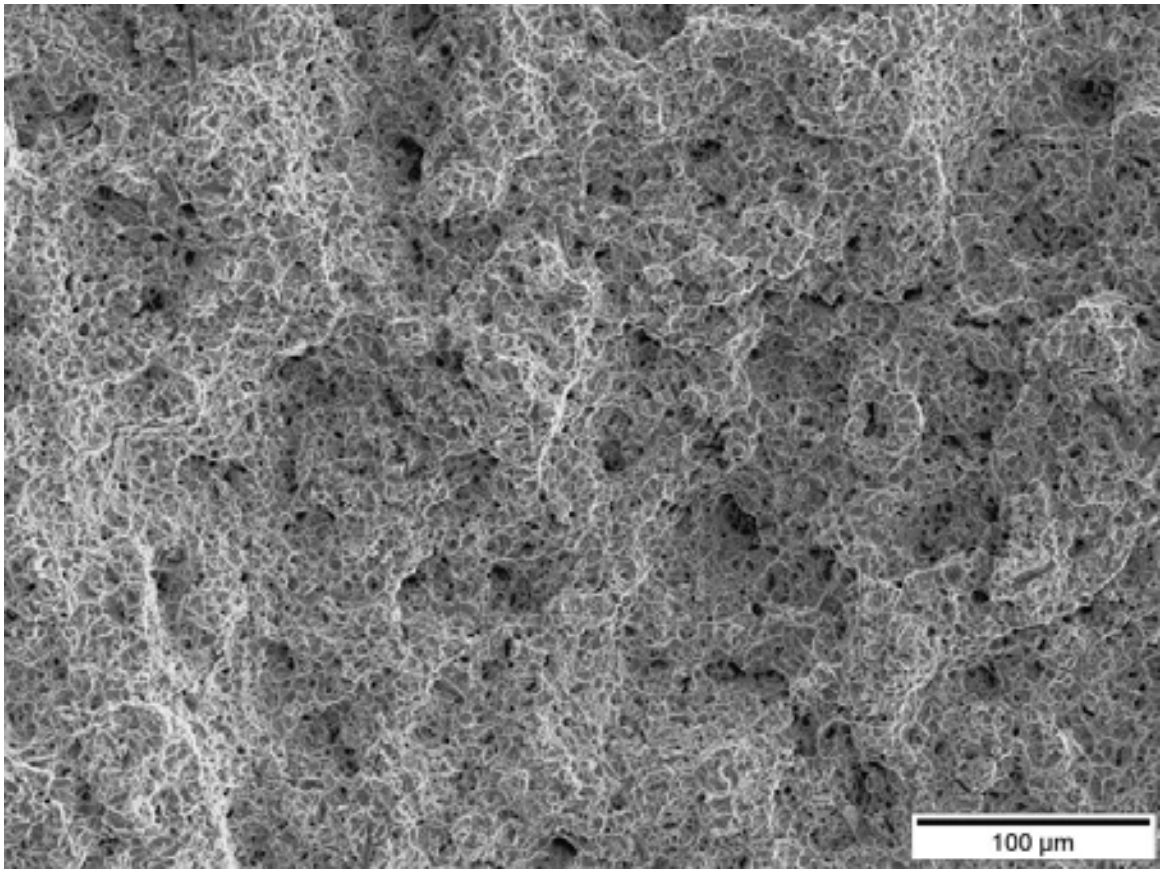

Figure 3.29 Fracture surface of extruded Ti-6Al-4V-1B modified alloy showing a relatively ductile fracture behavior.

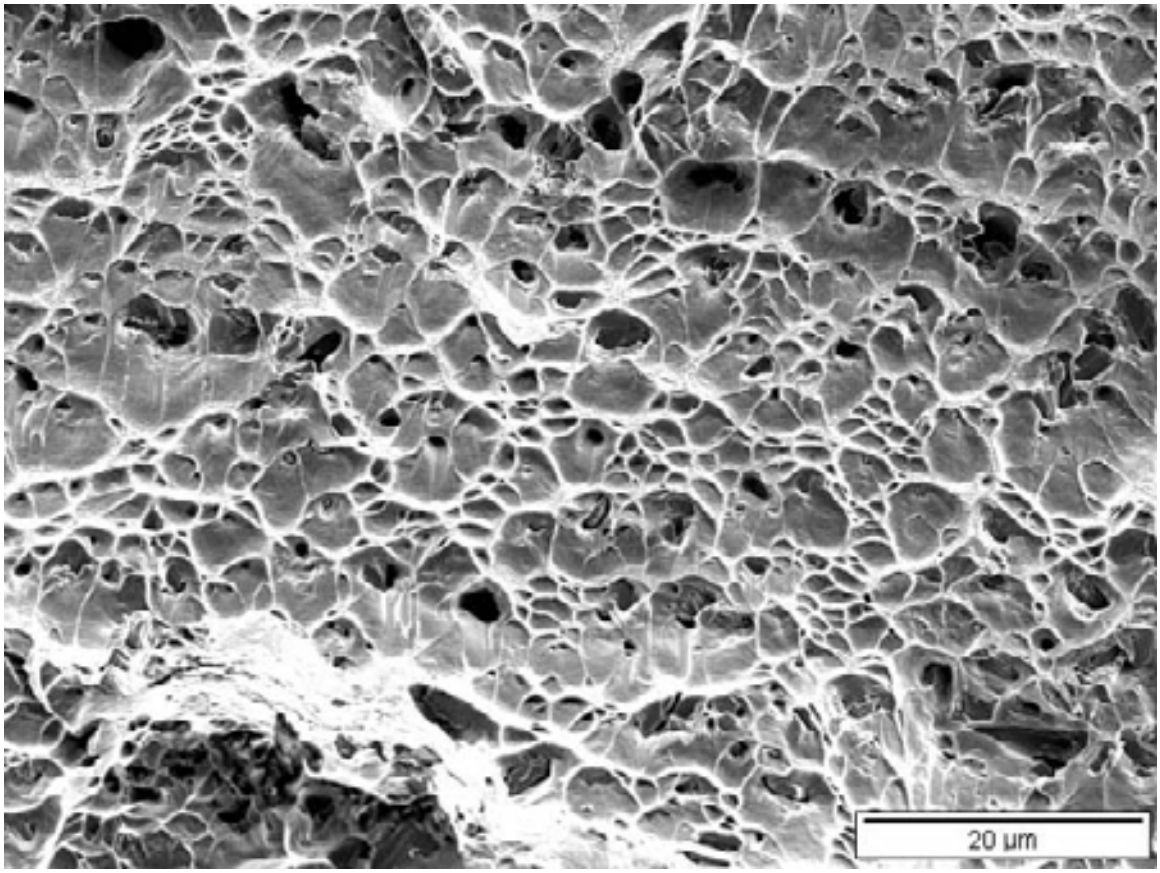

Figure 3.30 Fracture surface of extruded Ti-6Al-4V-1B modified alloy showing predominantly ductile fracture behavior of the Ti-6Al-4V matrix.

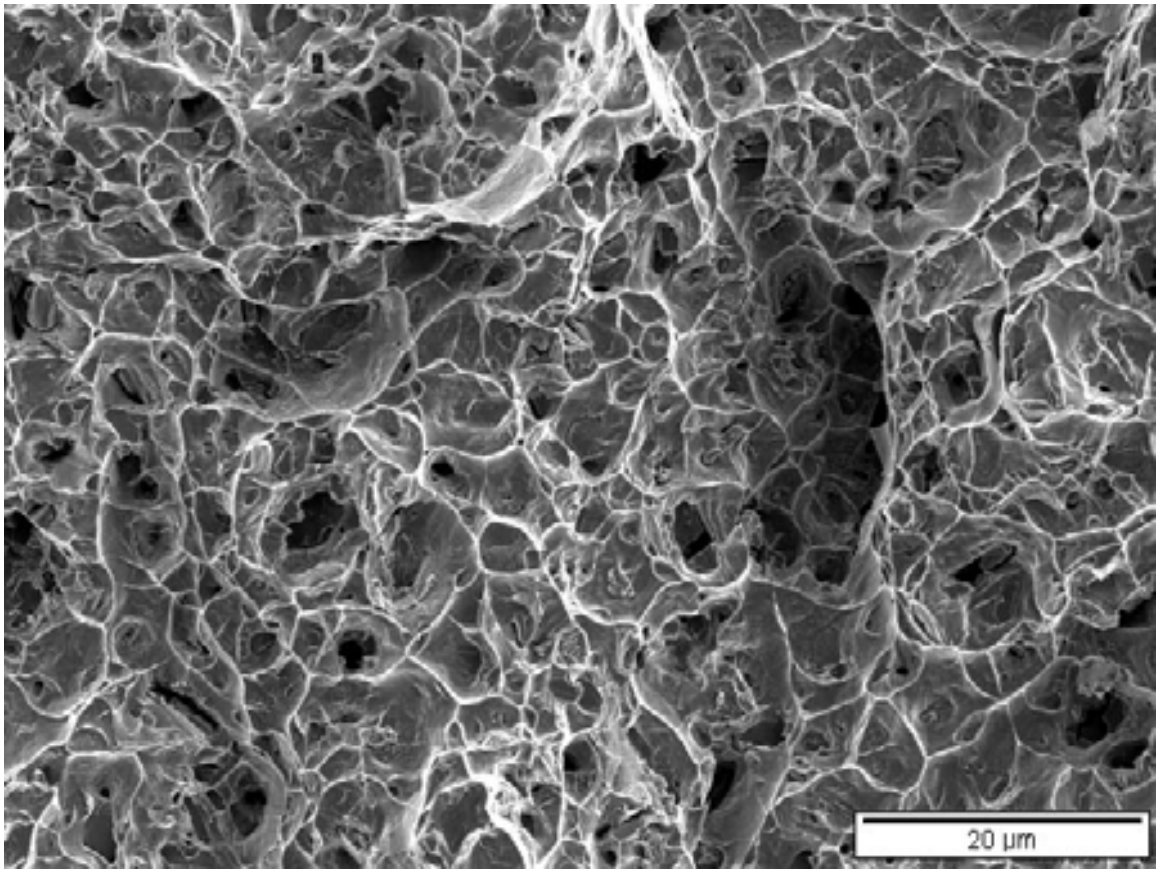

Figure 3.31 Fracture surface of extruded Ti-6Al-4V-1B modified alloy showing predominantly ductile fracture behavior of the Ti-6Al-4V matrix.

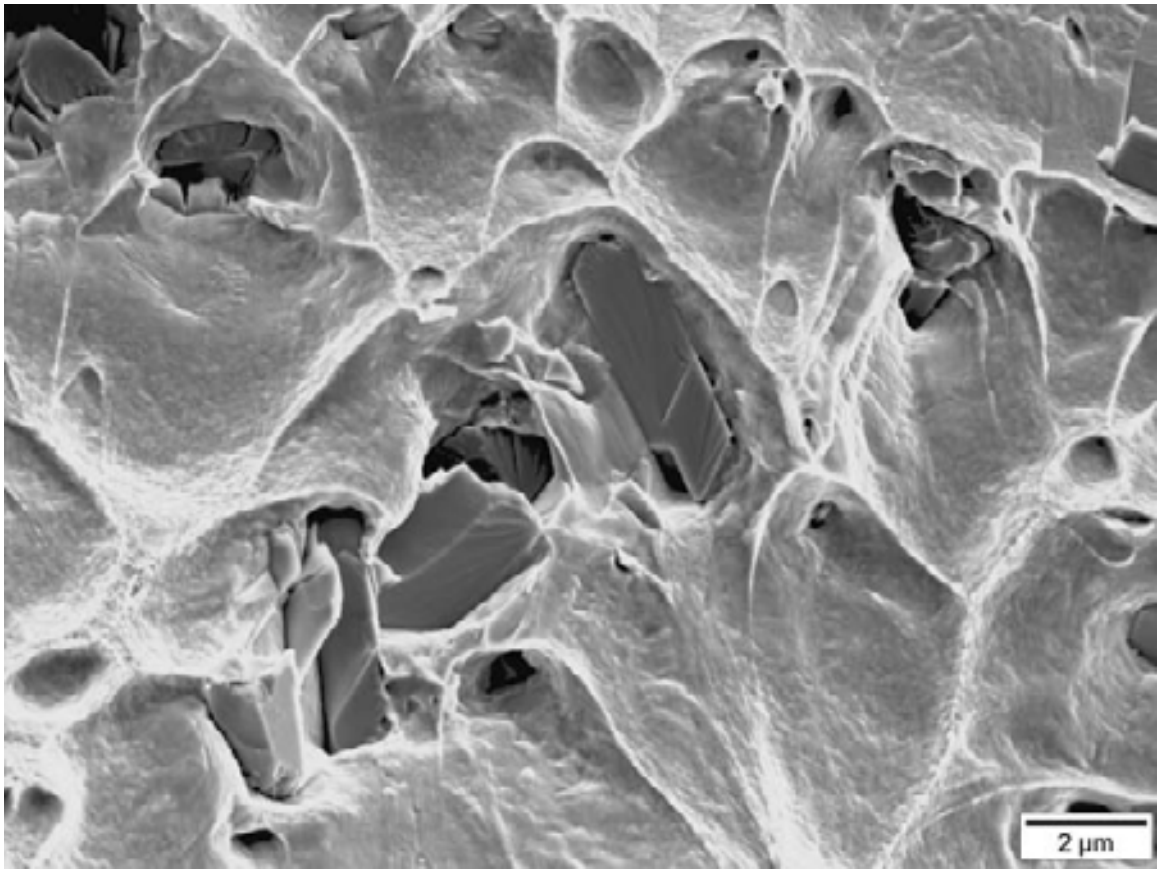

Figure 3.32 Fracture surface of extruded Ti-6Al-4V-1B modified alloy, showing brittle fracture across the width of the eutectic TiB whiskers and ductile fracture of the Ti-6Al-4V matrix.

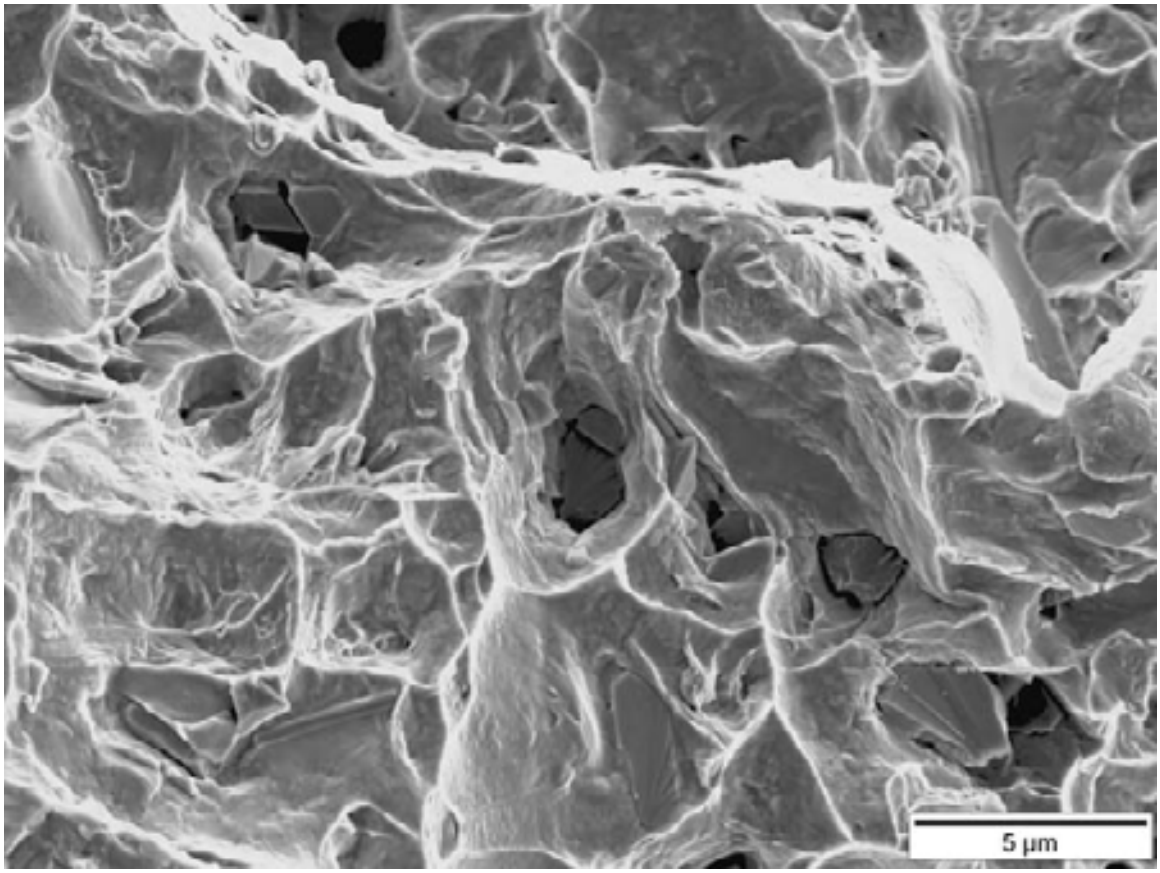

Figure 3.33 Fracture surface of extruded Ti-6Al-4V-1B modified alloy, showing brittle fracture across the width of the eutectic TiB whiskers and ductile fracture of the Ti-6Al-4V matrix.

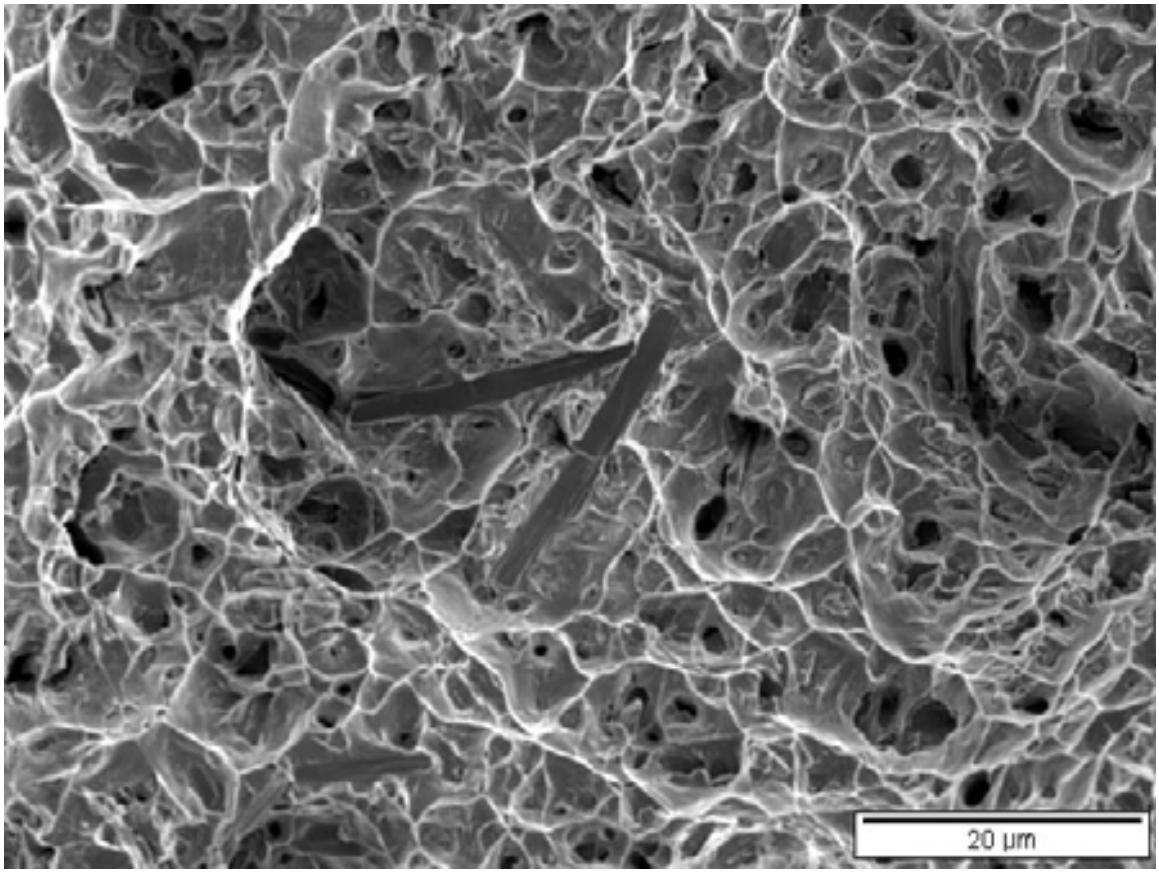

Figure 3.34 Fracture surface of extruded Ti-6Al-4V-1B modified alloy, showing brittle fracture down the length of eutectic TiB whiskers misaligned from the extrusion direction.

As with the compacted Ti-6Al-4V-1B alloy specimen, very little whisker pullout was observed. Unlike the more brittle hypereutectic and compacted hypoeutectic specimens, however, the fracture surface does not seem to have a significantly higher TiB content than the bulk material. It is notable that the strength of the extruded specimen is increased compared to the compacted alloy, and the elongation to failure is nearly doubled compared to the compacted alloy to a level acceptable for fracture-critical aerospace structural applications.

3.3.4 3D Microstructural Visualization

A montage serial sectioning technique was applied for the reconstruction and visualization of TiB particles in both compacted and extruded boron-modified Ti-6Al-4V-1B alloy samples. Visualization of the three-dimensional microstructures was used to observe the effects of the processing parameters on the morphology, anisotropy, and spatial distribution of the TiB particles.

In the present work, the montages were created using the automated AxioVision digital image analysis system from Carl Zeiss, Inc., that utilizes the image cross correlation function-based technique for matching the borders between contiguous microstructural fields. In this study, each montage is a microstructural image of an area of approximately 1.75 mm^2, having a high resolution of approximately 0.5 μm. Once the montage of the first serial section was created and stored in the computer memory, a small thickness of the specimen (approximately 1 μm) was removed by polishing, and then a second montage was created at the region exactly below that in the first metallographic plane. This polish-montage-polish procedure was repeated to obtain a stack of 75 montage serial sections.

Microhardness indents were used to locate the exact region of interest in successive serial sections and also to precisely measure the distance between consecutive serial sections. In the present work, alignment was accomplished using the image analysis software KS400 from Carl Zeiss, Inc., in which the images of the montage were digitally translated and rotated until they were aligned within ±1 pixel to the respective previous sections.

The stack of aligned serial sections constituted a volume image data set for three-dimensional microstructure visualization. The marching cube algorithm was employed for surface rendering of the three-dimensional microstructures, using the image analysis software VayTek VoxBlast 3.10 [82]. The effective resolution of the three-dimensional microstructures is approximately 1 μm, which is the depth of material removed between serial sections.

The three-dimensional microstructure visualizations were completed using 75 montage serial sections, with each montage serial section containing 225 contiguous microstructural fields imaged at a magnification of 800X. Therefore, the resulting three-dimensional data sets are useful for the characterization and visualization of the microstructure at fine as well as at coarse length scales.

Figure 3.35a shows a stack of 20 aligned montage serial sections of the microstructure of compacted Ti-6Al-4V-1B having isotropic, uniform random eutectic TiB whiskers of unimodal length scale. This figure shows 16 contiguous fields of view cropped from serial sections of 225 contiguous microstructural fields (this figure has been digitally compressed for presentation). Figure 3.35b shows the magnified view of the outlined region in Figure 3.35a, where each section is exactly the stack of serial sections generated by the single field of view-type classical serial sectioning technique [90-95]. This is the magnification at which all microstructural fields of the montages have been imaged. In Figure 3.35b, changes in the sizes of the whiskers at the edges of these serial sections, as well as the appearance and disappearance of features in successive serial sections, can be observed.

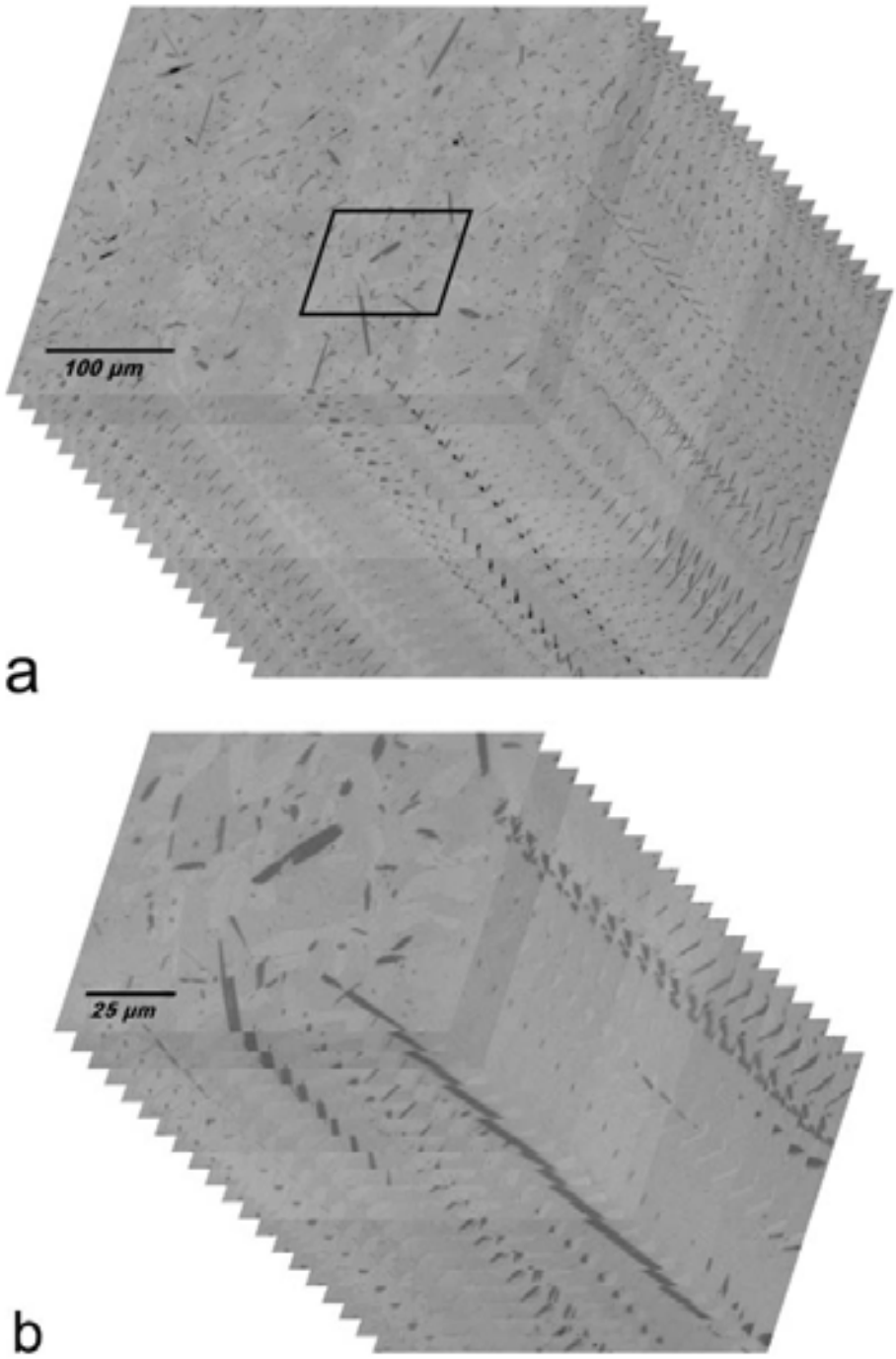

Figure 3.35 (a) Stack of 20 montage serial sections of the compacted Ti-6Al-4V-1B microstructure. Each serial section in this figure contains 16 contiguous microstructural fields. (b) The magnified view of the outlined region of the stack of 20 montage serial sections in (a). This is the resolution of the individual microstructural fields.

Figure 3.36a shows a stack of 20 aligned montage serial sections of the microstructure of the extruded Ti-6Al-4V-1B alloy with aligned TiB whiskers. The extrusion direction is perpendicular to the plane of the serial sections in this micrograph. This figure shows 16 contiguous fields of view cropped from serial sections of 225 contiguous microstructural fields (this figure has been digitally compressed for presentation). Figure 3.36b shows the magnified view of the outlined region in Figure 3.36a. In Figure 3.36b, as with the compacted alloy, changes in the sizes of the whiskers at the edges of these serial sections, as well as the appearance and disappearance of features in successive serial sections, can be observed.

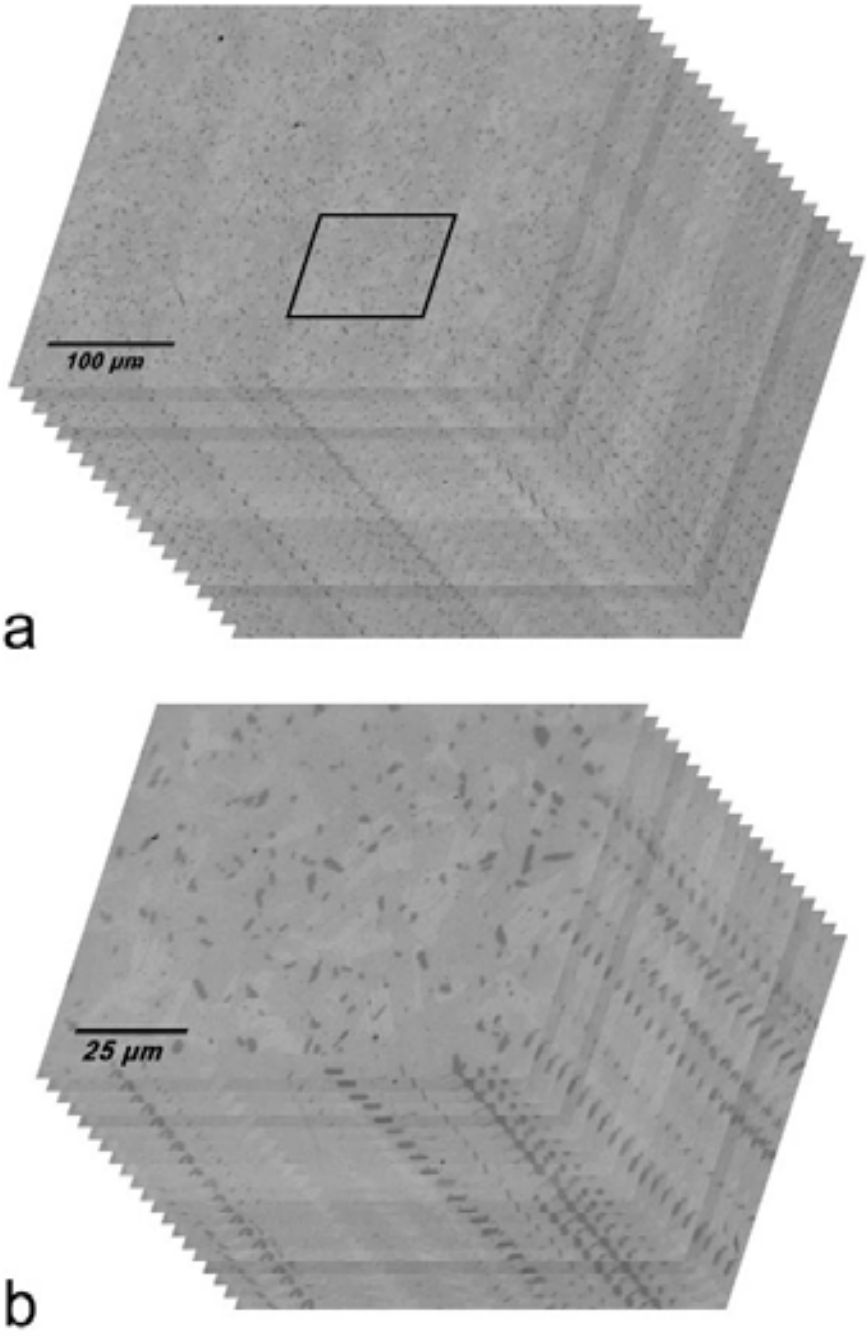

Figure 3.36 (a) Stack of 20 montage serial sections of the extruded Ti-6Al-4V-1B microstructure. The extrusion axis is perpendicular to the serial sections. Each serial section in this figure contains 16 contiguous microstructural fields. (b) The magnified view of the outlined region of the stack of 20 montage serial sections in (a). This is the resolution of the individual microstructural fields.

Figure 3.37 shows a volume segment of the surface rendered three-dimensional microstructure of the compacted Ti-6Al-4V-1B alloy. In this rendering, images were digitally segmented to completely remove the Ti-6Al-4V matrix and reveal only the TiB whiskers. Note that this volume segment is only approximately 0.5% of the total microstructure volume collected from the stack of 75 montage serial sections (to produce the three-dimensional rendering at the resolution of the TiB whiskers). No primary TiB particles were observed in this hypoeutectic alloy, as expected. The eutectic TiB whiskers in this microstructure are observed to have uniform random morphological orientations of a single length scale.

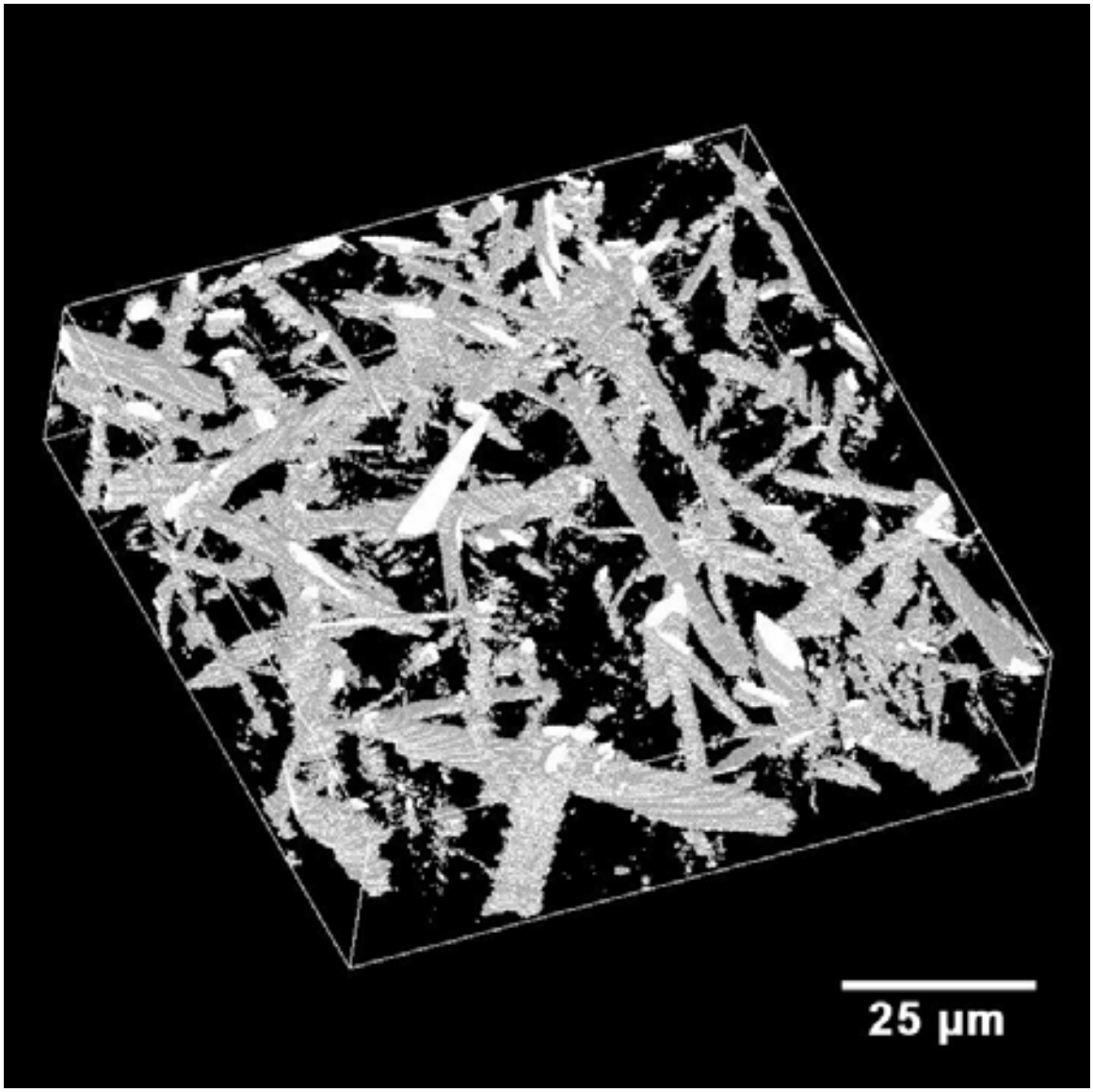

Figure 3.37 Small segment of surface rendered three-dimensional microstructure of compacted Ti-6Al-4V-1B. The TiB whiskers have isotropic uniform random orientations in this microstructure. The whisker size distribution is unimodal without any coarse primary TiB particles.

Figure 3.38 shows a volume segment of the surface rendered three-dimensional microstructure of the extruded Ti-6Al-4V-1B alloy specimen depicting the spatial distribution of the anisotropic eutectic TiB whiskers. In this reconstructed three-dimensional microstructure segment, the majority of the eutectic TiB whiskers are

aligned along the extrusion direction (which is normal to the top and bottom faces of the volume segment), although in the individual two-dimensional sections perpendicular to the extrusion direction (Figure 3.36), they appear to have random orientations due to their non-circular cross-sections. Further, this three-dimensional microstructure also reveals unimodal size distribution of the eutectic TiB whiskers, and no coarse primary TiB particles were observed in this hypoeutectic specimen.

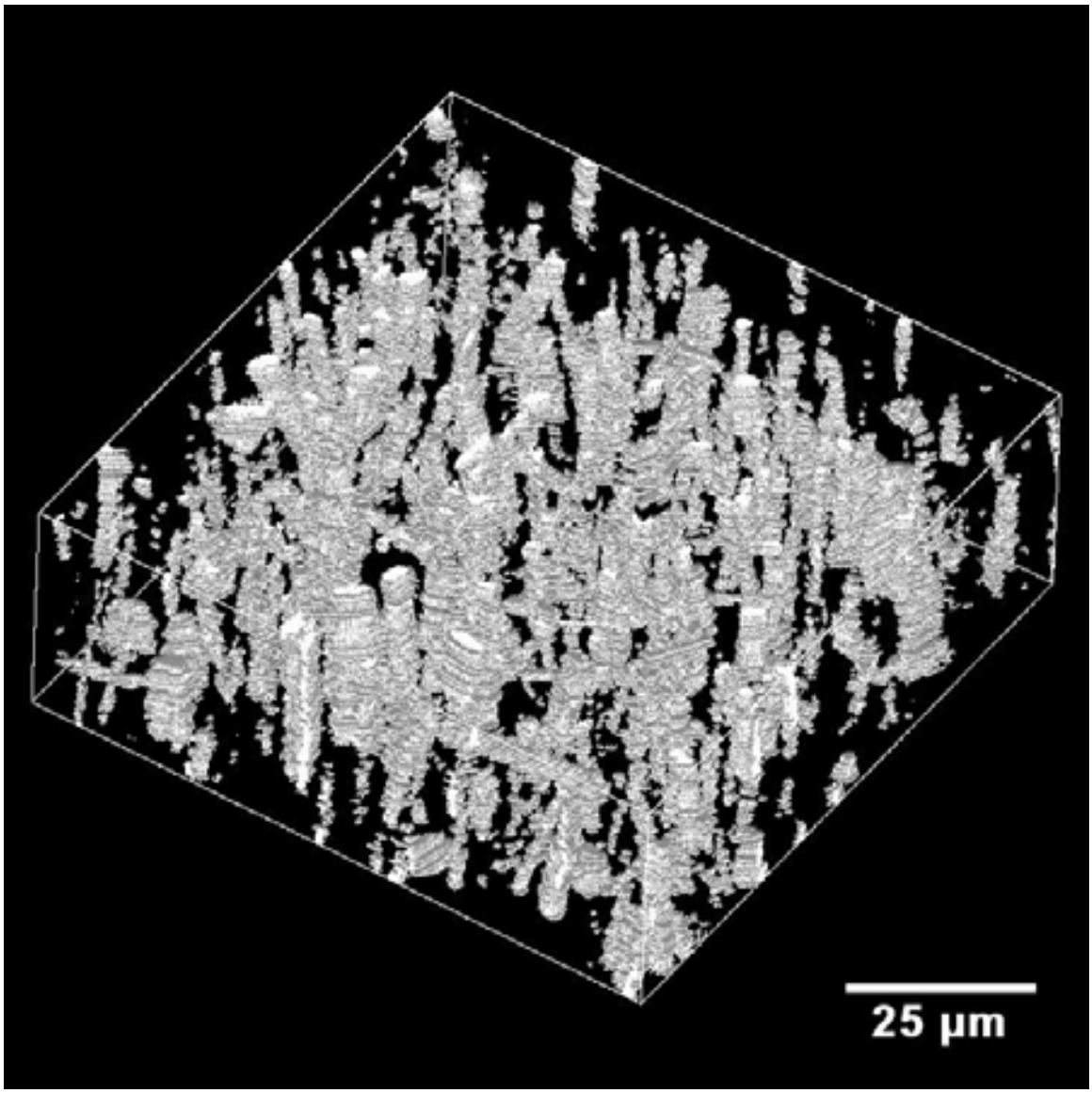

Figure 3.38 Small segment of surface rendered three-dimensional microstructure of extruded Ti-6Al-4V-1B. The eutectic TiB whiskers of unimodal distribution have anisotropic orientations with the majority of the whiskers aligned parallel to the extrusion direction, which is the z-axis of the volume segment.

Figure 3.38 clearly shows that the eutectic TiB whiskers have anisotropic orientations after extrusion and that the majority of these whiskers are aligned along the extrusion direction, which is the z-axis of the volume segment. Therefore, it can be concluded that plastic deformation during the extrusion process gives rise to rigid body

rotations of the eutectic TiB whiskers, which confirms the conclusion reached by Schuh and Dunand on the basis of two-dimensional microstructural observations [23]. Although the morphological orientation distribution of the eutectic TiB whiskers is different in the compacted microstructure as compared to the extruded microstructure, the spatial arrangement of the eutectic TiB whiskers appears to be uniformly random in both of the three-dimensional microstructures. Consequently, although the extrusion process leads to TiB whisker rotations, as in the hypereutectic specimen it does not give rise to spatial clustering of the TiB whiskers.

Figure 3.39 shows multiple views of a single eutectic TiB whisker extracted from the volume segment of the surface rendered three-dimensional microstructure of the compacted Ti-6Al-4V-1B microstructure shown in Figure 3.37. Note that the surface "roughness" of the whisker is an artifact of the rendering software; from observations of the two-dimensional serial sections, the TiB whisker surfaces are smooth. The three-dimensional morphology of the TiB whisker is clearly revealed in this reconstruction and is consistent among eutectic TiB whiskers in the microstructures of both the compacted and extruded specimens.

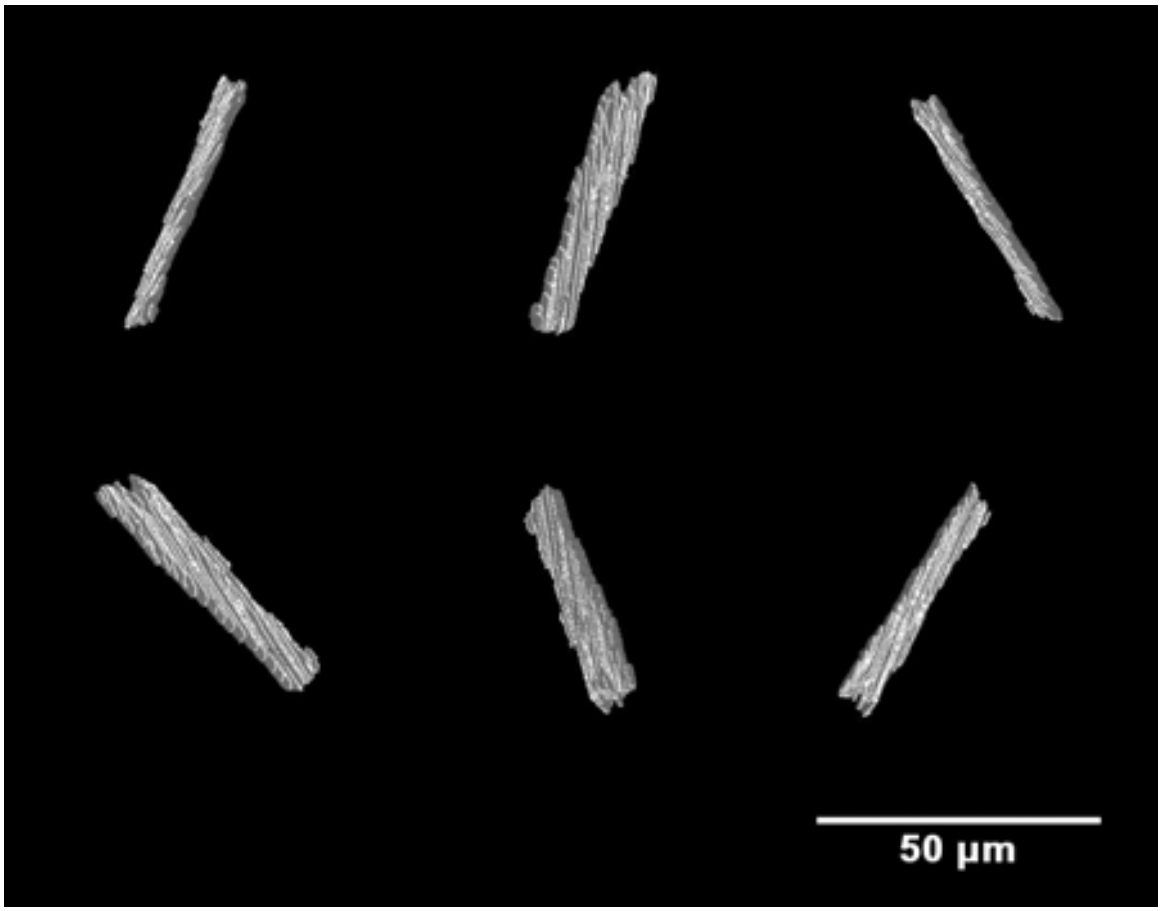

Figure 3.39 Multiple views of a eutectic TiB whisker extracted from the three-dimensional microstructure of compacted Ti-6Al-4V-1B alloy.

3.4 Conclusions

Samples of boron-modified Ti-6Al-4V alloys were produced using pre-alloyed (PA) powder metallurgy processes. Two compositions were chosen, hypereutectic Ti-6Al-4V-1.6B and hypoeutectic Ti-6Al-4V-1B, to examine the microstructures in different regimes of the quaternary system of titanium, alloying elements aluminum and vanadium, and boron. Samples of each blind die compacted alloy also underwent hot extrusion to examine the effect of this type of thermomechanical processing on the microstructures and resultant material properties.

The hypereutectic alloy, Ti-6Al-4V-1.6B, showed the presence of two different TiB phases, a fine eutectic TiB phase and a coarser primary TiB phase. From observations via optical microscopy and three-dimensional visualization using montage-based serial sectioning, both phases showed an anisotropic whisker morphology with roughly hexagonal cross-sections. For the primary TiB phase, this conclusion differed from previous assumptions about the morphology of this phase, where an equiaxed cluster morphology had been suggested.

Extrusion of this alloy showed TiB whisker alignment with the extrusion direction, with no damage to the TiB phases or change in morphology observed. Examination of the tensile fracture surfaces of both compacted and extruded samples revealed brittle fracture down the length of TiB whiskers in the compacted sample, and across the width of aligned TiB whiskers in the extruded sample (with the TiB whiskers aligned by extrusion in the tensile direction). The Ti-6Al-4V matrix showed relatively ductile fracture. Extrusion improved the yield strength and ultimate tensile strength while effectively doubling the tensile elongation to failure. These samples, however, did not meet the fracture-critical properties required for aerospace structural applications.

The hypoeutectic alloy, Ti-6Al-4V-1B, showed only the presence of the eutectic TiB phase. No primary TiB was observed, as expected. The eutectic TiB whiskers in this alloy had a similar morphology to those in the hypereutectic alloy, although they were present in smaller amounts due to the decreased amount of boron in the composition of this alloy.

Extrusion of this alloy also showed TiB whisker alignment with the extrusion direction, with no damage to the TiB whiskers or change in morphology observed.

Examination of the tensile fracture surfaces of both compacted and extruded samples again revealed brittle fracture down the length of TiB whiskers in the compacted sample, and across the width of aligned TiB whiskers in the extruded sample (with the TiB whiskers aligned by extrusion in the tensile direction). The Ti-6Al-4V matrix showed relatively ductile fracture. Similarly to the hypereutectic alloy, extrusion improved the yield strength and ultimate tensile strength while effectively doubling the tensile elongation to failure. The extruded sample of this alloy did meet the fracture-critical properties required for aerospace structural applications and significantly improved the mechanical properties compared to unreinforced Ti-6Al-4V.

CHAPTER 4

BLENDED ELEMENTAL Ti-B COMPOSITES

4.1 Introduction

The earliest Ti-B materials produced for potential commercial applications were discontinuously reinforced titanium matrix composites (DRTi) utilizing blended elemental (BE) powder metallurgy processing. Research included development of Ti-B composite parts for automotive applications by the Toyota Central Research & Development Laboratories, as well as development of a cold and hot isostatic pressing (CHIP) process by Dynamet Technology, Inc. to produce parts for a variety of industrial and commercial applications such as housings and ice hockey skate blades [55, 96-98]. Very little of the early work, however, focused on fracture-critical applications such as aerospace structural components.

The BE powder metallurgy process is conducted completely in the solid state [6]. When this process is used to produce Ti-B composites, powders of the appropriate titanium alloy and a boron source are intermixed in either a wet or dry blending process. The powder blend is then outgassed and consolidated to prepare a green compact. This compact is then subjected to a reaction heat treatment to convert the boron source (often TiB_2 or elemental boron) into TiB.

The BE process can produce either near-net shapes via compaction, or net shapes via compaction and subsequent thermomechanical processing. The BE approach provides the ability to introduce higher amounts of TiB without the formation of coarse primary TiB particles than the pre-alloying (PA) process, because the processing is

conducted completely in the solid state. The BE process, however, results in a microstructure with coarser features than pre-alloying and other approaches due to long times at high temperatures required for TiB conversion. In addition, there are limited options for controlling the conversion reactions.

Samples of Ti-B composites produced by the BE process were examined to investigate the effect of composition and processing parameters on the microstructure and resultant mechanical properties. There was a focus on studying and characterizing the difference between the microstructures of these BE Ti-B composites and the PA boron-modified titanium alloys. Also of particular interest was determining suitability for fracture-critical aerospace structural applications.

4.2 Materials and Processing Details

Ti-B composites produced by the BE process were made by research colleagues at at the Air Force Research Laboratory, Wright-Patterson Air Force Base, Ohio. Powders of Ti-6Al-4V and commercially pure titanium (CP-Ti) were first produced using inert gas atomization by Crucible Research Corporation, Pittsburgh, Pennsylvania. The boron source for these composites, TiB_2 powder, was produced using a continuous chemical process by Advanced Ceramics Corporation, Cleveland, Ohio. The metallic Ti-6Al-4V and CP-Ti powders exhibited smooth spherical shapes, while the TiB_2 powder was in the form of platelets with irregular hexagonal cross-sections [99].

Two composites, Ti-6Al-4V-1.7B and Ti-6Al-4V-2.9B, were prepared by colleagues at AFRL by blending appropriate amounts of Ti-6Al-4V, CP-Ti, and TiB_2 powders in *n*-butanol using a Turbula mixer for 24 hours. The mixture was then dried and dry blended for an additional 30 minutes to eliminate any agglomerates.

Approximately 1 kg of the blended powder mixture was then packed inside a thick-walled (6.35 mm) can of Ti-6Al-4V (70 mm in diameter and 130 mm in height), vacuum outgassed at 300°C for 24 hours, and sealed. The can was subsequently heated to 1200°C, soaked for 1 hour, and then blind-die compacted in an extrusion chamber heated to 260°C. The compact was held at a pressure of 1400 MPa for 180 seconds and subsequently air-cooled to room temperature. A height reduction of 30% occurred during compaction. The compacted billet was then subjected to an annealing heat treatment in vacuum at 1300°C for 6 hours to ensure that the solid-state in situ reaction $Ti + TiB_2 \rightarrow 2TiB$ was complete. The additional CP-Ti blended with the powder mixture ensured that the TiB conversion reaction did not result in the depletion of titanium and consequent enrichment of aluminum and vanadium in the matrix.

A second billet of the Ti-6Al-4V-2.9B composite blind die compacted by the same method was subsequently hot extruded. This billet was first heated to 1300°C and soaked for 1 hour prior to extrusion through a circular die with an extrusion reduction ratio of 10:1, at a ram speed of 4.23 mm/s, and then air-cooled to room temperature. The higher soaking temperature, lower extrusion ratio, and lower ram speed compared to the extrusions of the PA boron-modified alloys were chosen to keep the extrusion loads within the extrusion press load limits. Specimens were then sectioned from the compacted billets and extruded rod.

4.3 Optical Microscopy and Quantitative Characterization

Specimens from the compacted billets and extruded rod were mounted in thermoplastic using standard techniques for metallography. Suitable grinding and polishing schemes developed for Ti-B alloys and composites were utilized, taking into

account the hardness differences between the relatively soft Ti-6Al-4V alloy matrix and the relatively hard TiB whisker reinforcement. Using these metallographic techniques, a final surface finish of 0.05 μm was obtained.

Samples of compacted Ti-6Al-4V-1.7B composite, and both compacted and extruded Ti-6Al-4V-2.9B composite, were examined using a Carl Zeiss, Inc. Axiovert 200 MAT optical microscopy system with AxioVision image analysis software. For each sample, montages were created using the automated AxioVision digital image analysis system that utilizes the image cross correlation function-based technique for matching the borders between contiguous microstructural fields. For these samples, each montage is a microstructural image of a large area (~4.75 mm^2), having a high resolution (~1 μm).

Figure 4.1 shows one such montage of 35 fields of view of compacted Ti-6Al-4V-1.7B composite. Figure 4.2 shows a higher magnification image of the compacted composite specimen. The images have been compressed for display. These micrographs show TiB whiskers randomly dispersed and oriented in a Ti-6Al-4V matrix. In these figures, the TiB whiskers are a darker gray than the gray titanium matrix, and in Figure 4.2 the $\alpha + \beta$ grain structure of the Ti-6Al-4V matrix can be seen. Montages were taken from different regions and different samples of each alloy specimen to ensure that observations were performed on representative examples of the microstructures.

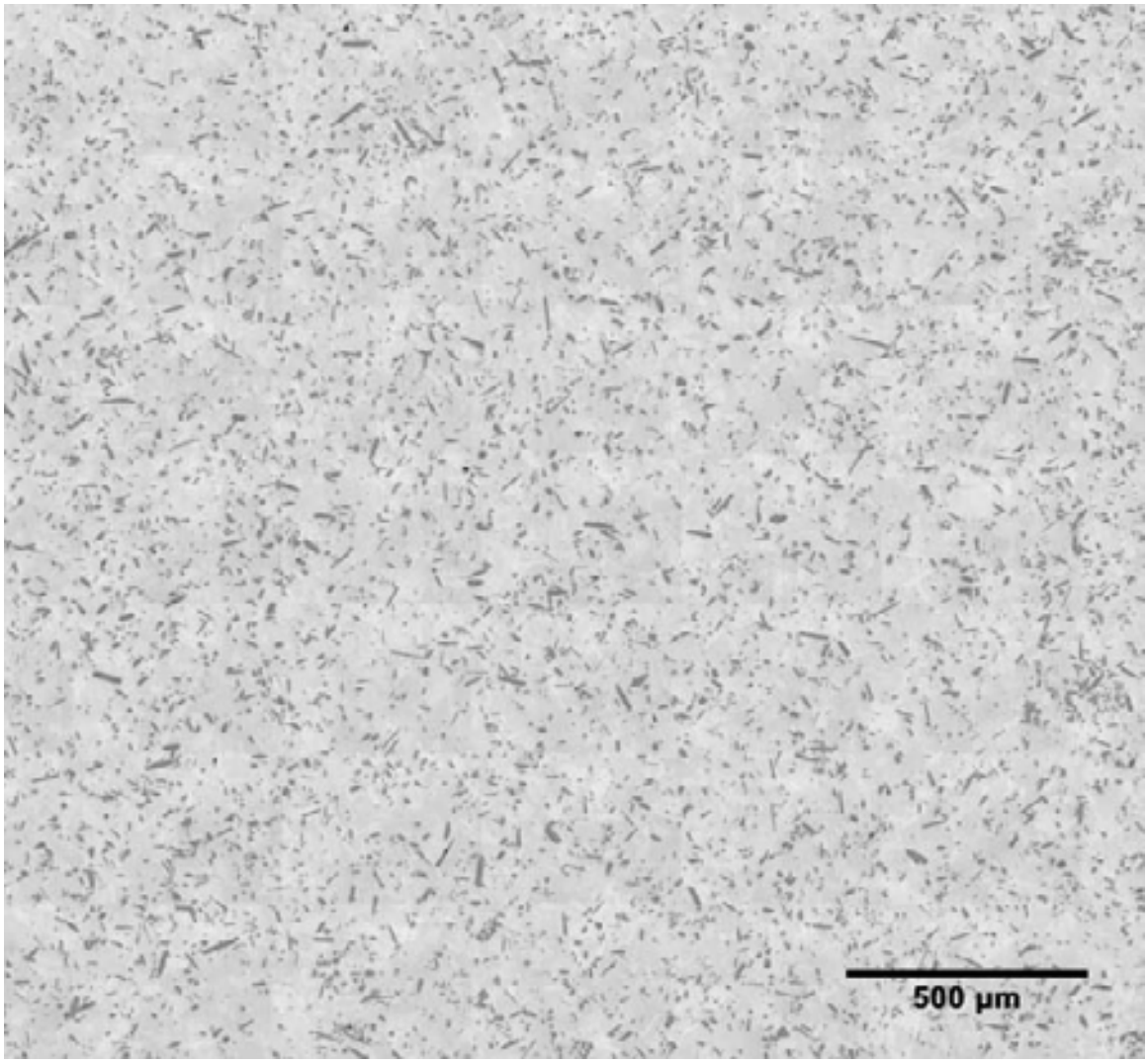

Figure 4.1 Montage of the microstructure of compacted Ti-6Al-4V-1.7B composite showing randomly oriented TiB whiskers. This micrograph is a montage of 35 fields of view covering an area of approximately 4.75 mm^2, and has been digitally compressed for presentation.

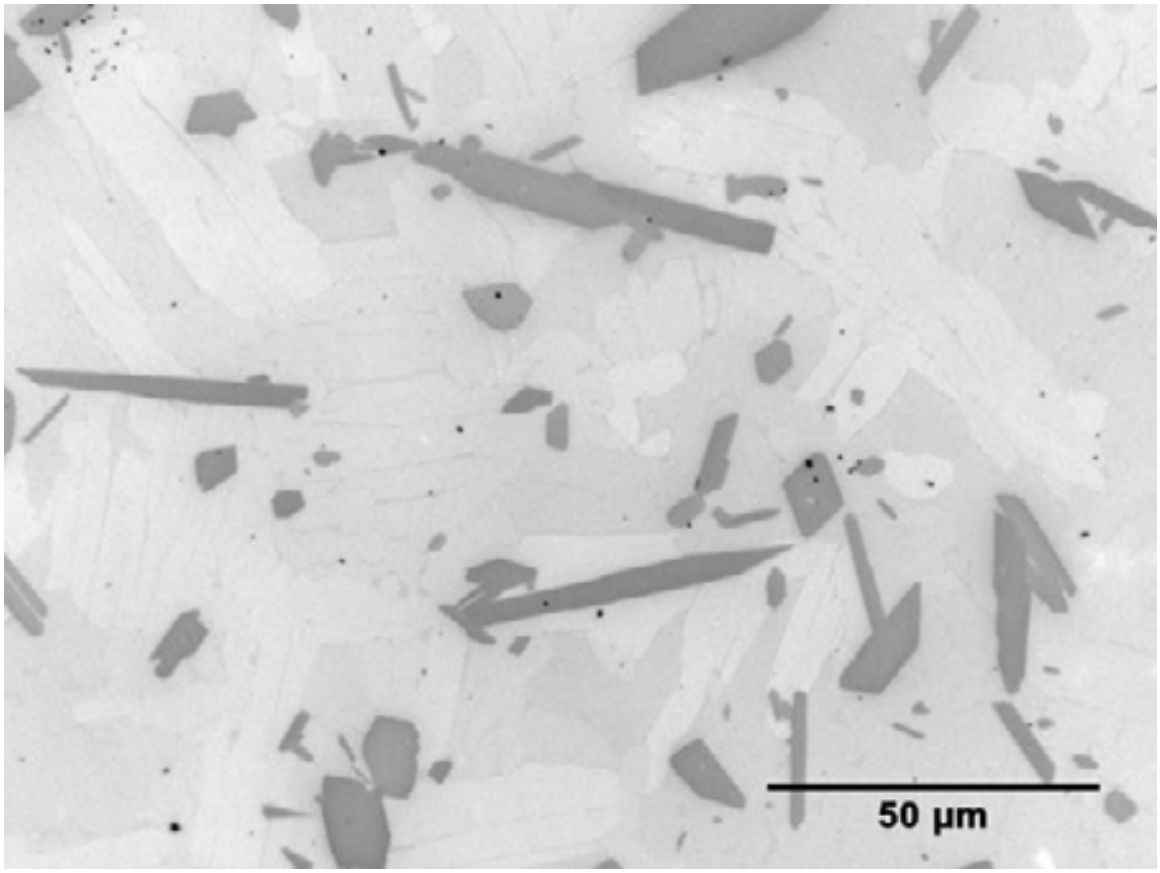

Figure 4.2 Microstructure of compacted Ti-6Al-4V-1.7B composite showing randomly oriented TiB whiskers.

A montage of 35 fields of view of the microstructure of the compacted Ti-6Al-4V-2.9B composite is shown in Figure 4.3. Figure 4.4 shows a higher magnification image of this specimen. The images have been compressed for display. Similarly to the Ti-6Al-4V-1.7B composite but with a higher volume fraction of TiB reinforcement, these micrographs show TiB whiskers randomly dispersed and oriented in a Ti-6Al-4V matrix. In these figures, the TiB whiskers are a darker gray than the gray titanium matrix. In Figure 4.4, some damage to the TiB whiskers caused by polishing can be seen as black regions on the whiskers.

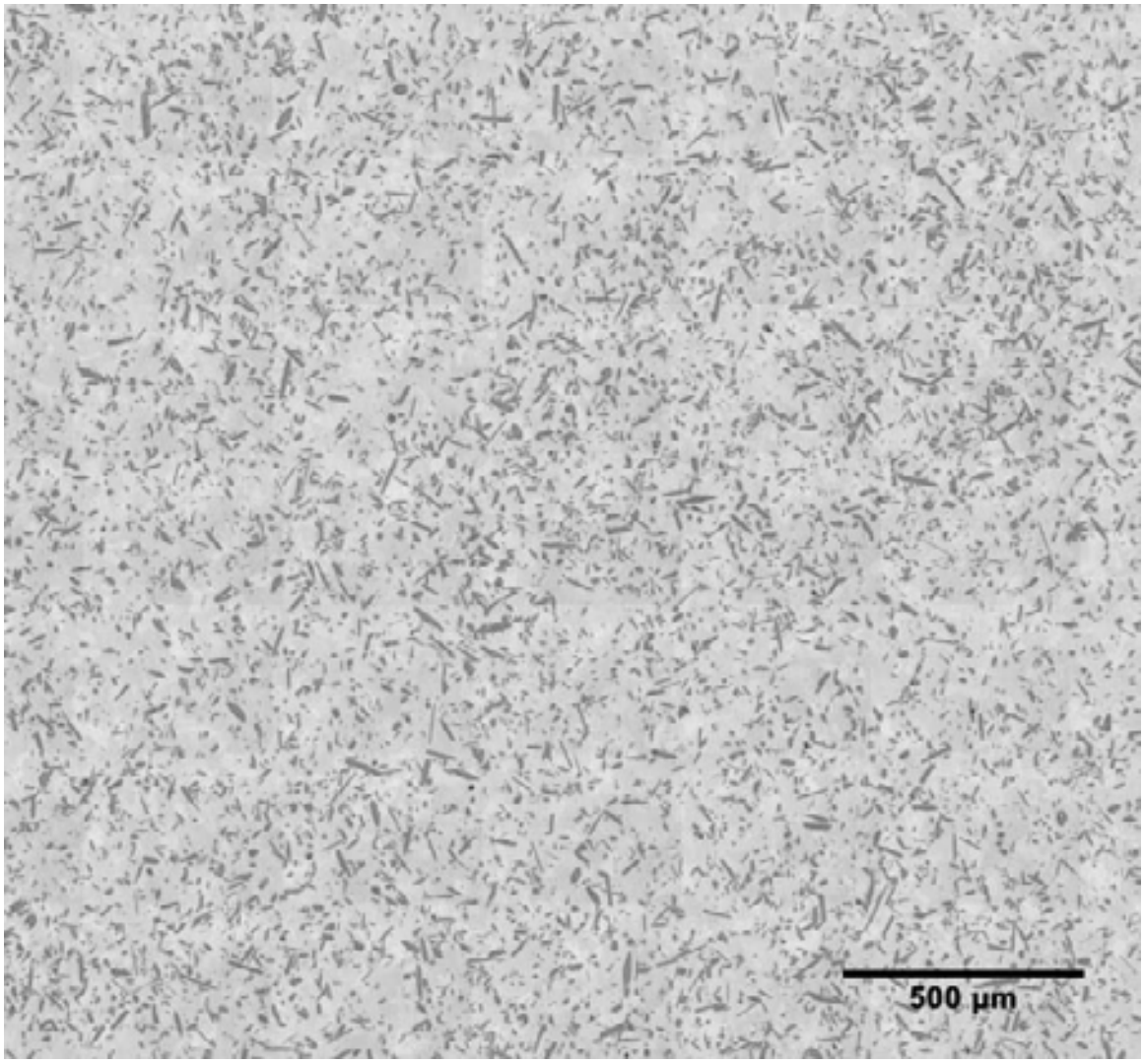

Figure 4.3 Montage of the microstructure of compacted Ti-6Al-4V-2.9B composite showing randomly oriented TiB whiskers. This micrograph is a montage of 35 fields of view covering an area of approximately 4.75 mm^2, and has been digitally compressed for presentation.

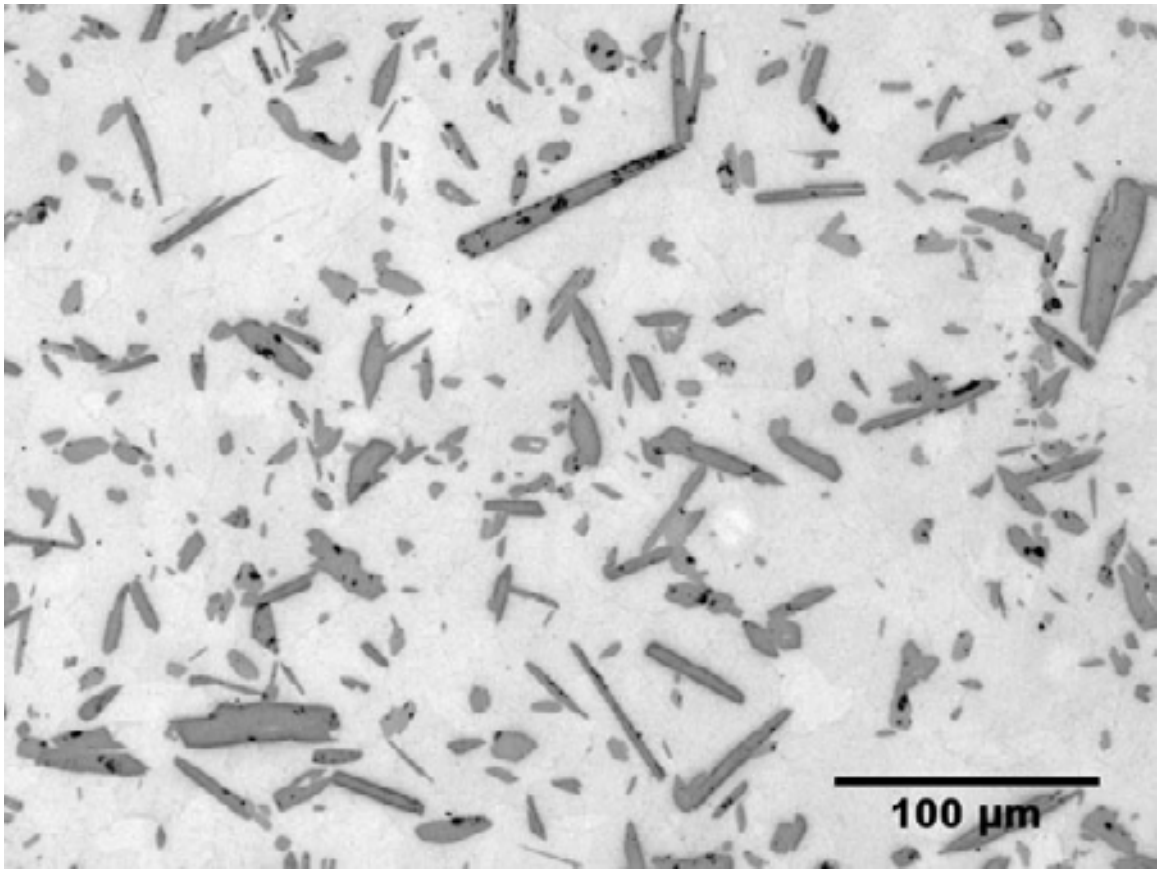

Figure 4.4 Microstructure of compacted Ti-6Al-4V-2.9B composite showing randomly oriented TiB whiskers.

Figure 4.5 shows a montage of 16 fields of view of the extruded Ti-6Al-4V-2.9B composite specimen. The extrusion direction is perpendicular to the metallographic plane, with most TiB whiskers aligned in the extrusion direction. As in the micrographs of the compacted Ti-B composites, the eutectic TiB whiskers are seen as dark gray in a gray matrix of Ti-6Al-4V alloy.

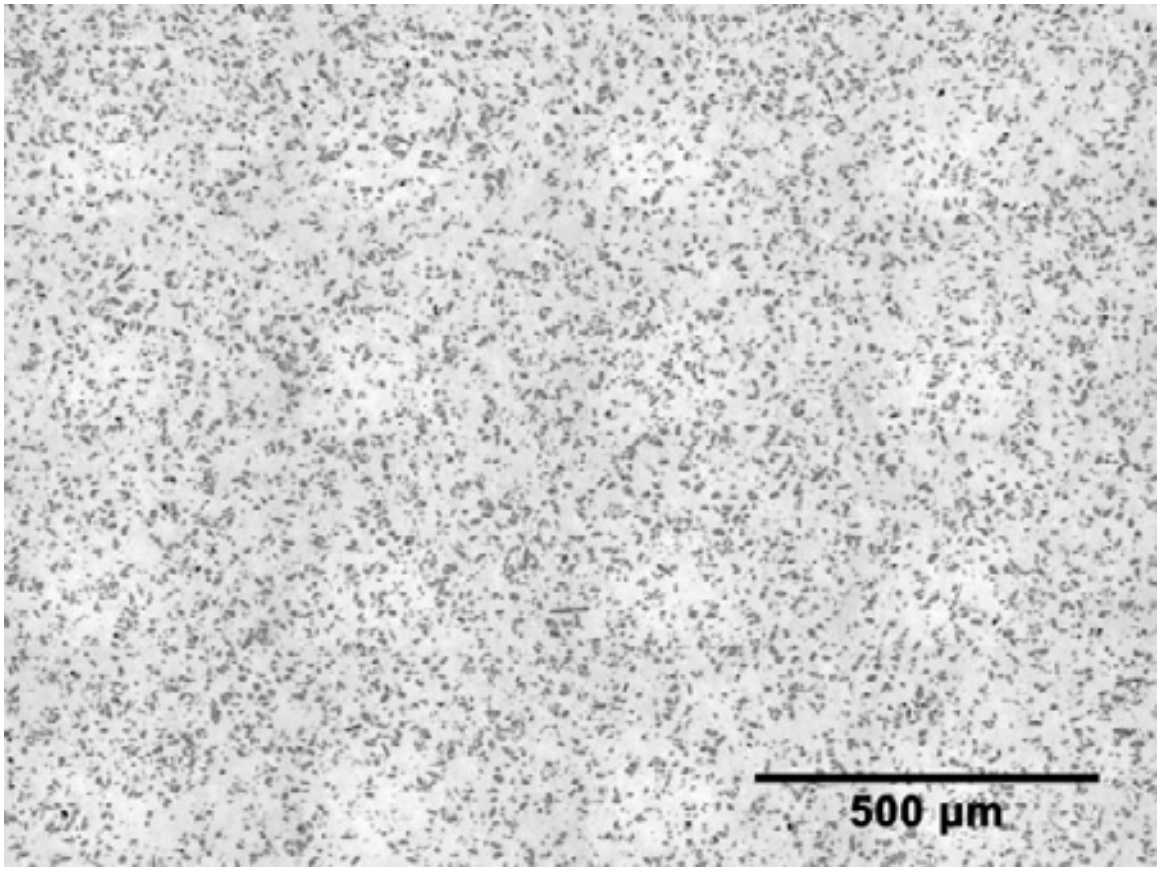

Figure 4.5 Montage of the microstructure of extruded Ti-6Al-4V-2.9B composite. The extrusion direction is normal to the micrograph.

The microstructure of the extruded Ti-6Al-4V-2.9B composite at higher magnification is shown in Figure 4.6. The extrusion direction is also normal to the metallographic plane. Alignment of most of the TiB whiskers in the extrusion direction is seen, confirming previous observations [23]. The roughly hexagonal cross-section of the TiB whiskers is also seen [87]. Some damage to the TiB whiskers caused by metallographic polishing is seen as black regions on the dark gray TiB particles.

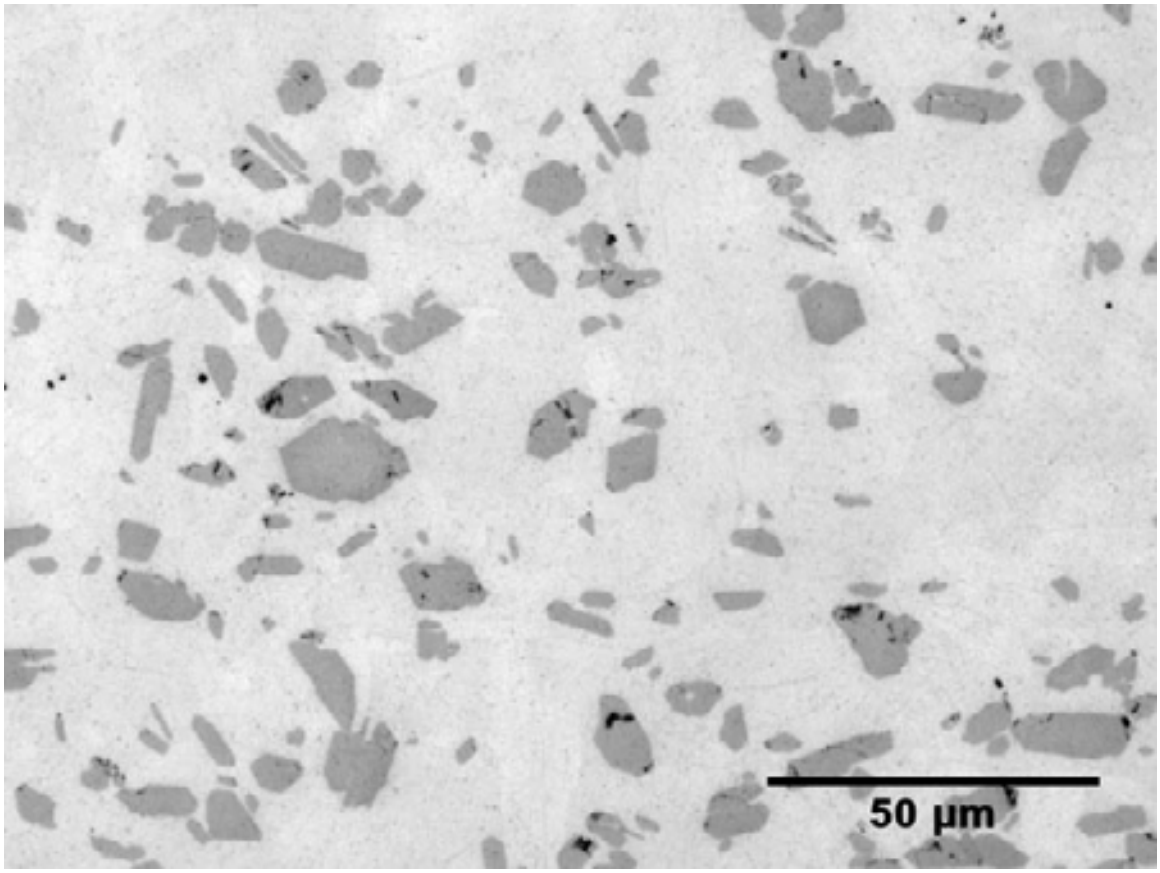

Figure 4.6 Microstructure of extruded Ti-6Al-4V-2.9B composite. The extrusion direction is normal to the micrograph.

Figure 4.7 shows the microstructure of the extruded Ti-6Al-4V-2.9B composite in the metallographic plane parallel to the extrusion direction. This view further confirms that the TiB whiskers are mostly aligned in the extrusion direction. Some damage to the TiB whiskers due to metallographic polishing is seen in this micrograph.

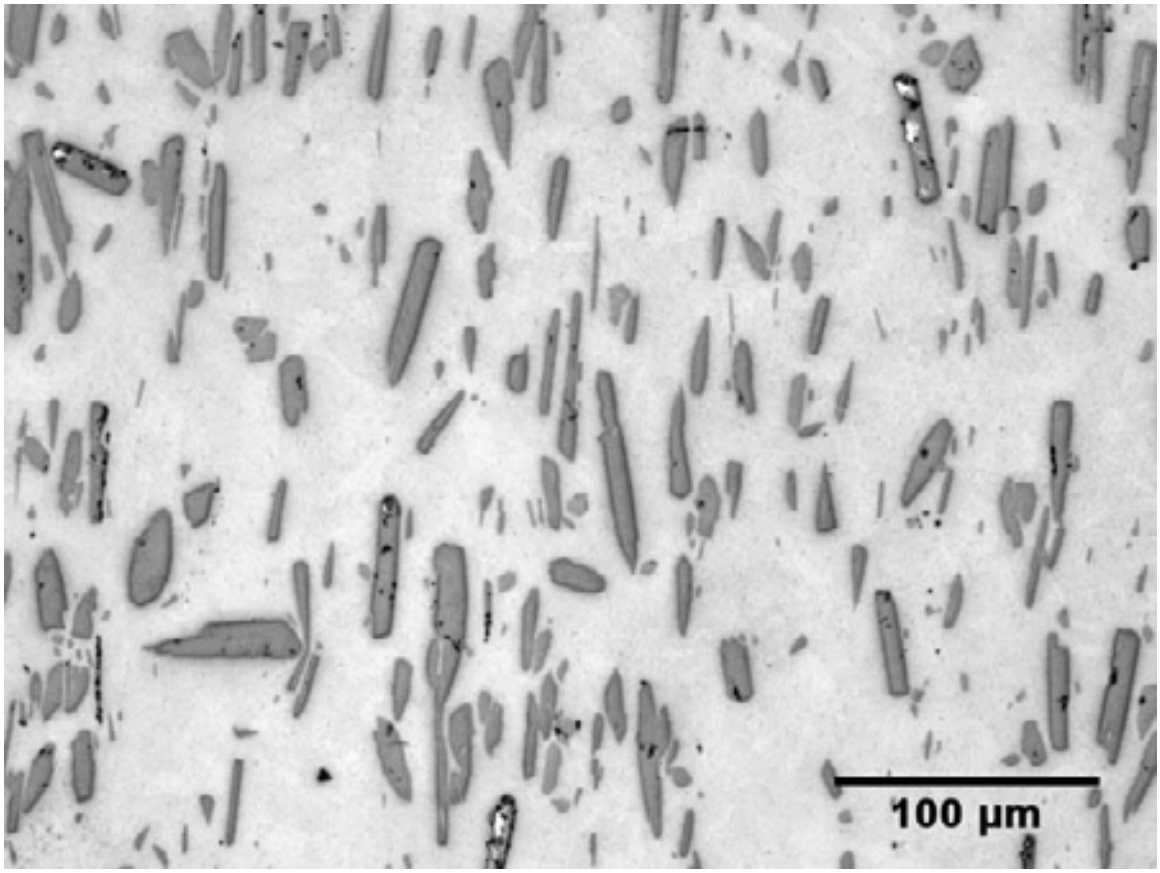

Figure 4.7 Microstructure of extruded Ti-6Al-4V-2.9B composite. The extrusion direction is parallel to the micrograph.

Microstructural data for these compacted and extruded Ti-6Al-4V-1.7B and 2.9B composite samples were calculated using conventional two-dimensional stereology techniques. For the extruded composite, measurements were made on montages in the plane parallel as well as on montages in the plane normal to the extrusion direction. Average values are shown in Table 4.1, but these results do not take into account the stochastic nature of microstructures. In the Ti-6Al-4V-1.7B composite, it was found that the TiB whiskers typically had a length of approximately 25-50 µm and a width of approximately 3-8 µm, for an aspect ratio range of between 3.2 and 16.7. The overall volume fraction of TiB whiskers in this composite is approximately 9%. In the Ti-6Al-

4V-2.9B composite, it was found that the TiB whiskers typically had a length of approximately 35-60 μm and a width of approximately 4-10 μm, for an aspect ratio range of between 3.5 and 15. The overall volume fraction of TiB whiskers in these samples is approximately 17%.

Table 4.1 Microstructural data of Ti-6Al-4V-1.7B and 2.9B composite samples calculated using standard two-dimensional stereology techniques.

sample	avg length (μm)	avg width (μm)	aspect ratio	volume fraction
compacted 1.7B	34.11	5.22	6.53	9.30
compacted 2.9B	39.12	5.37	7.28	17.86
extruded 2.9B	48.27	6.12	7.89	16.87

Although the angular orientation of the TiB whiskers was affected by extrusion, the morphology of the TiB phases was not observed to have been affected by extrusion. In addition, research colleagues have suggested the presence in these blended elemental composites of a second TiB phase with a platelike morphology. This second phase was not observed. Overall, the TiB whiskers in the BE composites showed a single whisker morphology (with roughly hexagonal cross-sections) and a unimodal size distribution.

4.4 SEM Fractography

Established applications of blended elemental Ti-B composite materials include use in the automotive and sporting goods industries, where wear resistance and corrosion resistance are the important material properties. For aerospace structural applications, however, fracture behavior is a critical material property, and the industry has set a structural design limit of tensile elongation to failure of approximately 7% [6]. In this

research, the fracture behavior of BE Ti-B composites were investigated to determine their suitability for aerospace applications.

Samples of Ti-6Al-4V-2.9B composite were sectioned from both the compacted billet and from the extruded rod, and machined into ¼"-20 round tensile specimens by colleagues at the Air Force Research Laboratory. These specimens then underwent room temperature tensile tests according to ASTM standard E8-04 [88]. Tensile test results are shown in Table 4.2. Note the substantial improvement in the elastic modulus over the elastic modulus of unreinforced Ti-6Al-4V alloy of approximately 110 GPa. The extruded specimen shows an elastic modulus in the range of steel alloys. It is also notable that, as with the previous boron-modified alloy tensile samples, the strength of the extruded specimen is increased compared to the compacted composite, and the elongation to failure is nearly doubled compared to the compacted composite. Prior to examination of the tensile fracture surfaces using scanning electron microscopy (SEM), the specimens underwent ultrasonic cleaning in ethanol for 5 minutes.

Table 4.2 Tensile test results of Ti-6Al-4V-2.9B composite, using ASTM E8-04.

sample	E (GPa)	σ_y (MPa)	σ_{uts} (MPa)	e (%)
compacted	160	1107	1119	1.5
extruded	200	1189	1331	3.0

The fracture surfaces of the tensile test specimens were examined with a Sirion FEI scanning electron microscope, using secondary electron emission. The fracture surface of the compacted Ti-6Al-4V-2.9B composite specimen is shown in Figures 4.8-4.10. In Figure 4.8, at a magnification of 250X, a jagged fracture surface can be seen, suggesting brittle fracture behavior of the composite. Very little, if any, whisker pullout

was observed, and fracture has taken place predominantly along the length of each whisker. At higher magnifications (Figures 4.9 and 4.10), however, significant damage to the TiB whiskers is clearly visible, which differs from the mostly smooth fracture of TiB whiskers observed in the compacted boron-modified alloy specimens. Overall, the fracture surface has a higher TiB content than the bulk material, and the Ti-6Al-4V matrix shows ductile failure.

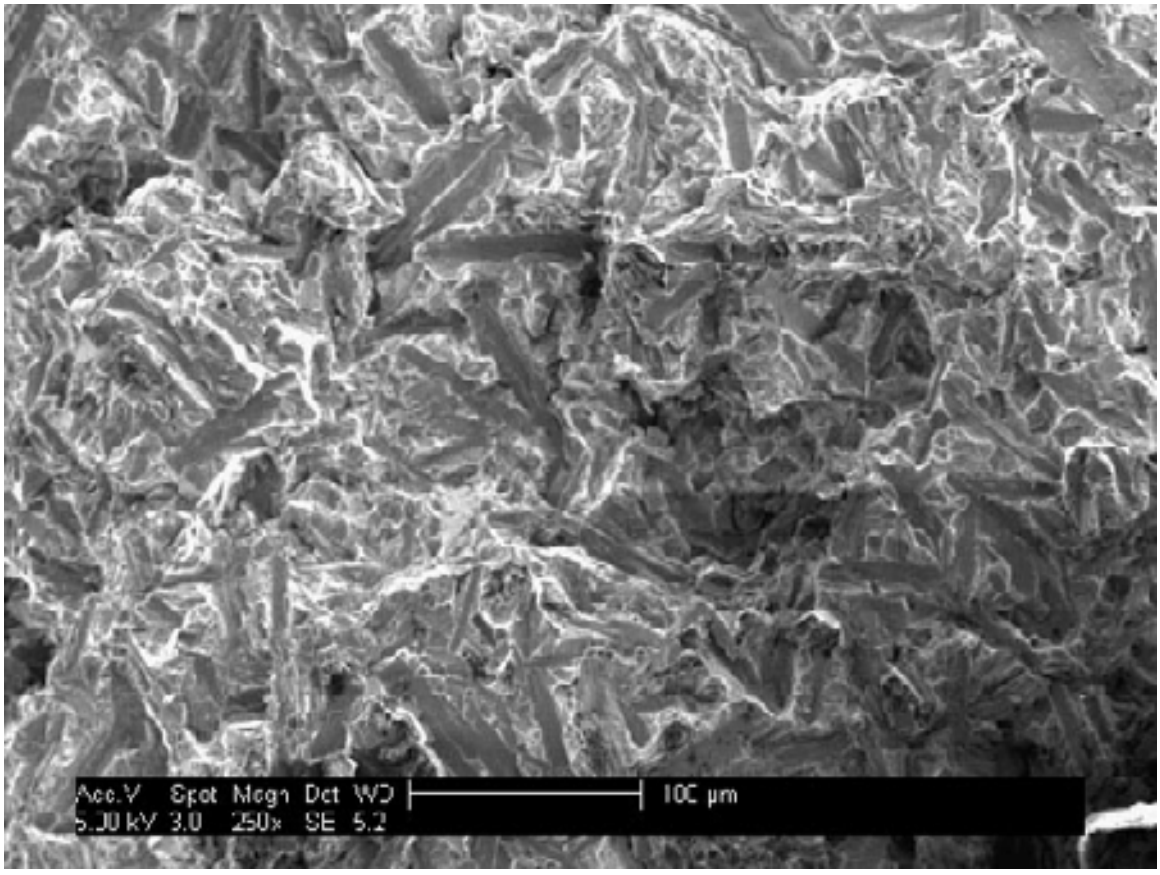

Figure 4.8 Fracture surface of compacted Ti-6Al-4V-2.9B composite showing a jagged fracture surface, with brittle fracture down the length of the TiB whiskers and ductile fracture of the Ti-6Al-4V matrix.

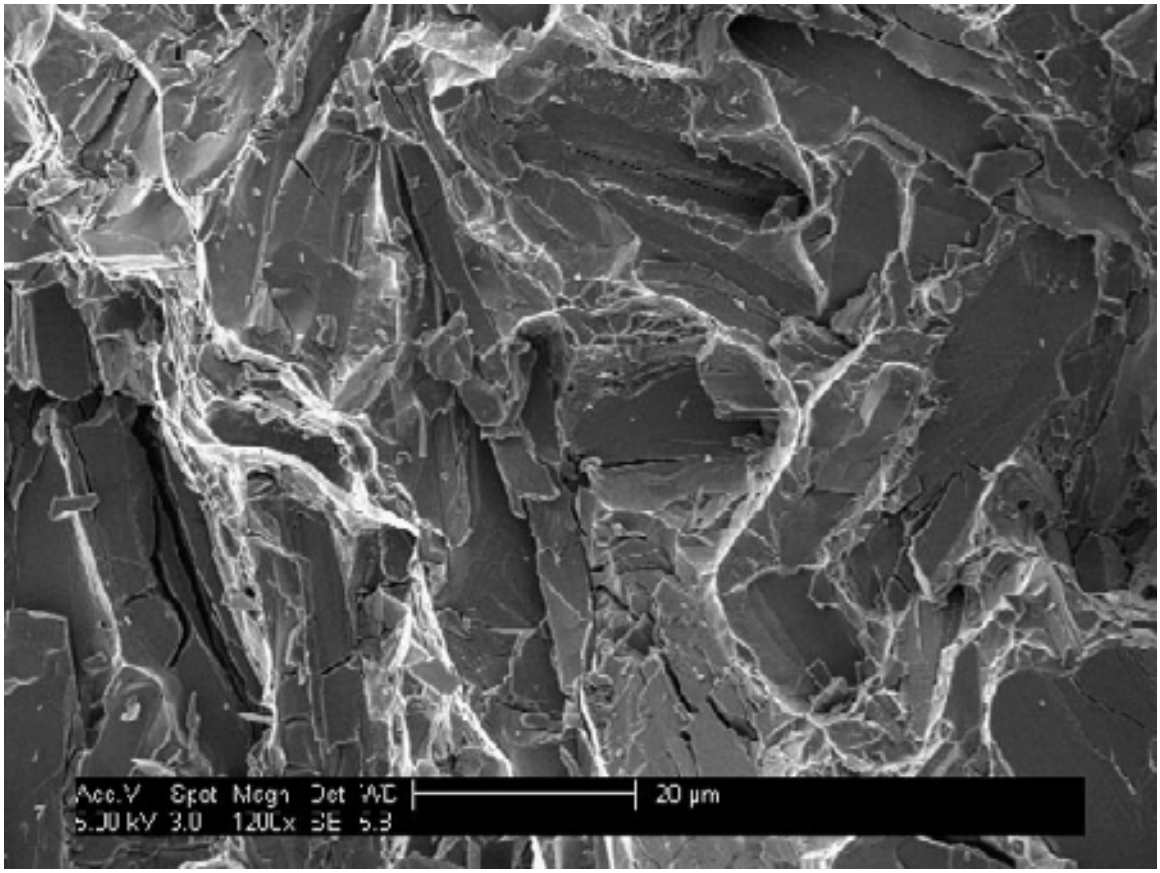

Figure 4.9 Fracture surface of compacted Ti-6Al-4V-2.9B composite, showing significant damage to the TiB whiskers.

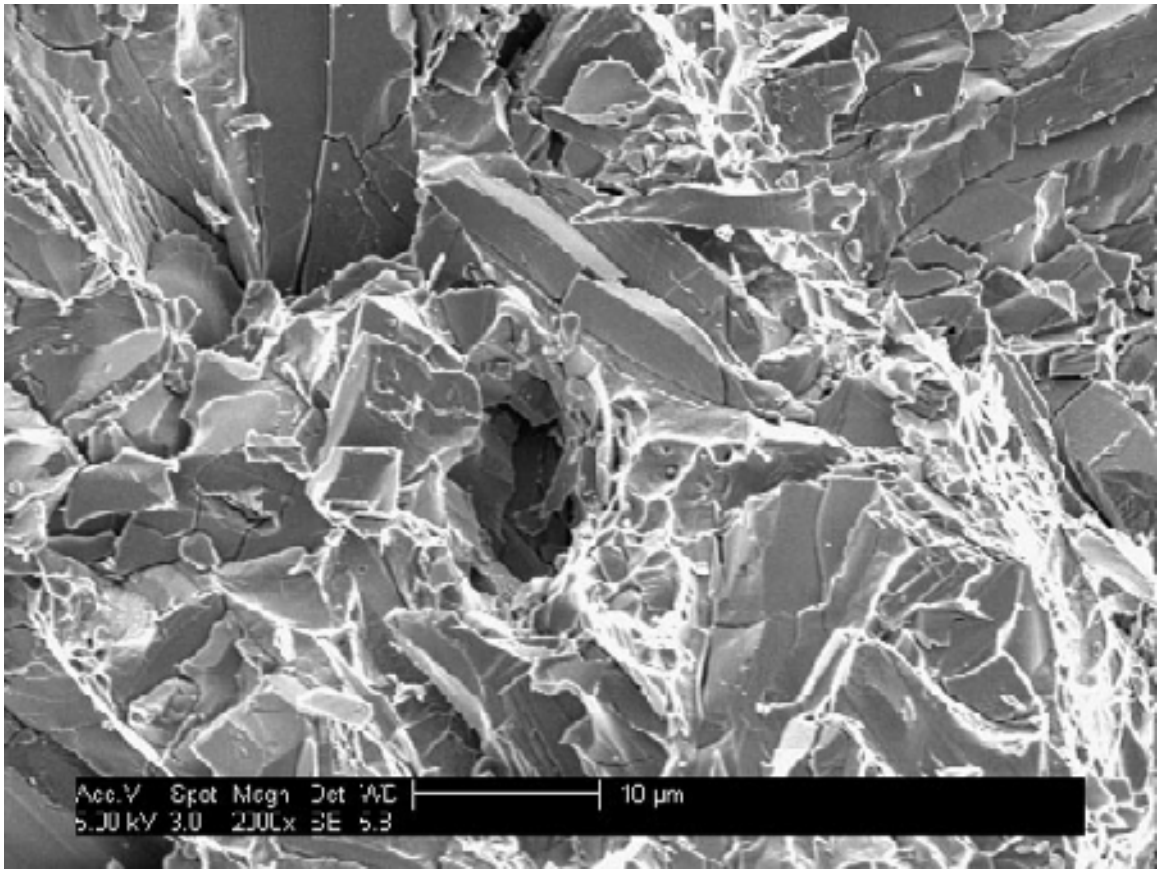

Figure 4.10 Fracture surface of compacted Ti-6Al-4V-2.9B composite, showing significant damage to the TiB whiskers.

For the extruded Ti-6Al-4V-2.9B composite specimen, the extrusion direction is parallel to the tensile test direction. The fracture surface of this specimen is shown in Figures 4.11-4.14. In Figure 4.11, the specimen is seen at a magnification of 800X, showing a predominantly brittle fracture surface. Unlike the compacted composite specimen, fracture of the TiB whiskers is predominantly across the width of the whiskers, not down the length of the whiskers, although in Figure 4.12 fracture is observed down the length of a TiB whisker misaligned from the extrusion direction. In Figures 4.13 and 4.14, the fracture surface is shown at higher magnifications, and the fracture surfaces of the TiB whiskers can be clearly seen. The roughly hexagonal cross-section of TiB

whiskers is observed in Figure 4.13, and TiB whisker damage is shown in Figure 4.14. Very little whisker pullout is observed, and the Ti-6Al-4V matrix shows ductile fracture behavior. As with the compacted specimen, the fracture surface has a higher TiB content than the bulk material.

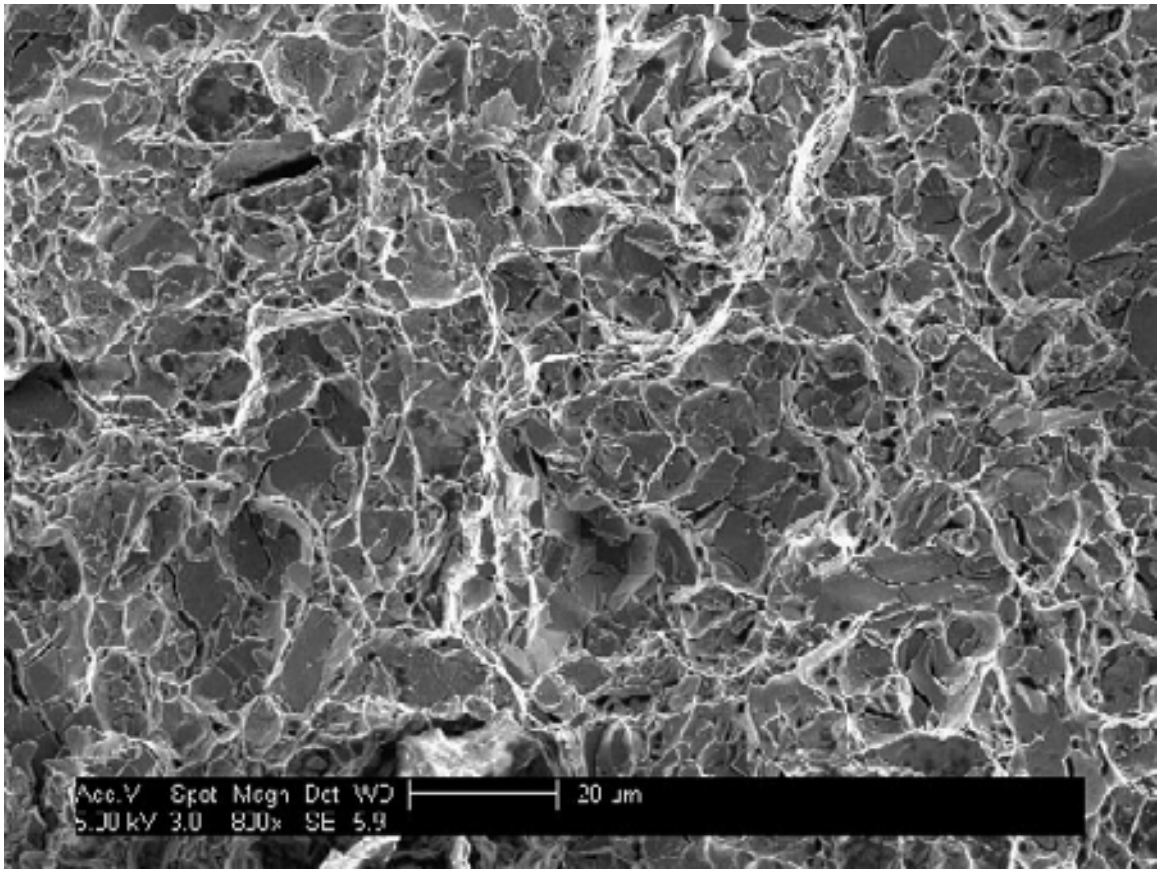

Figure 4.11 Fracture surface of extruded Ti-6Al-4V-2.9B composite showing brittle fracture across the width of TiB whiskers aligned in the extrusion direction and ductile fracture of the Ti-6Al-4V matrix.

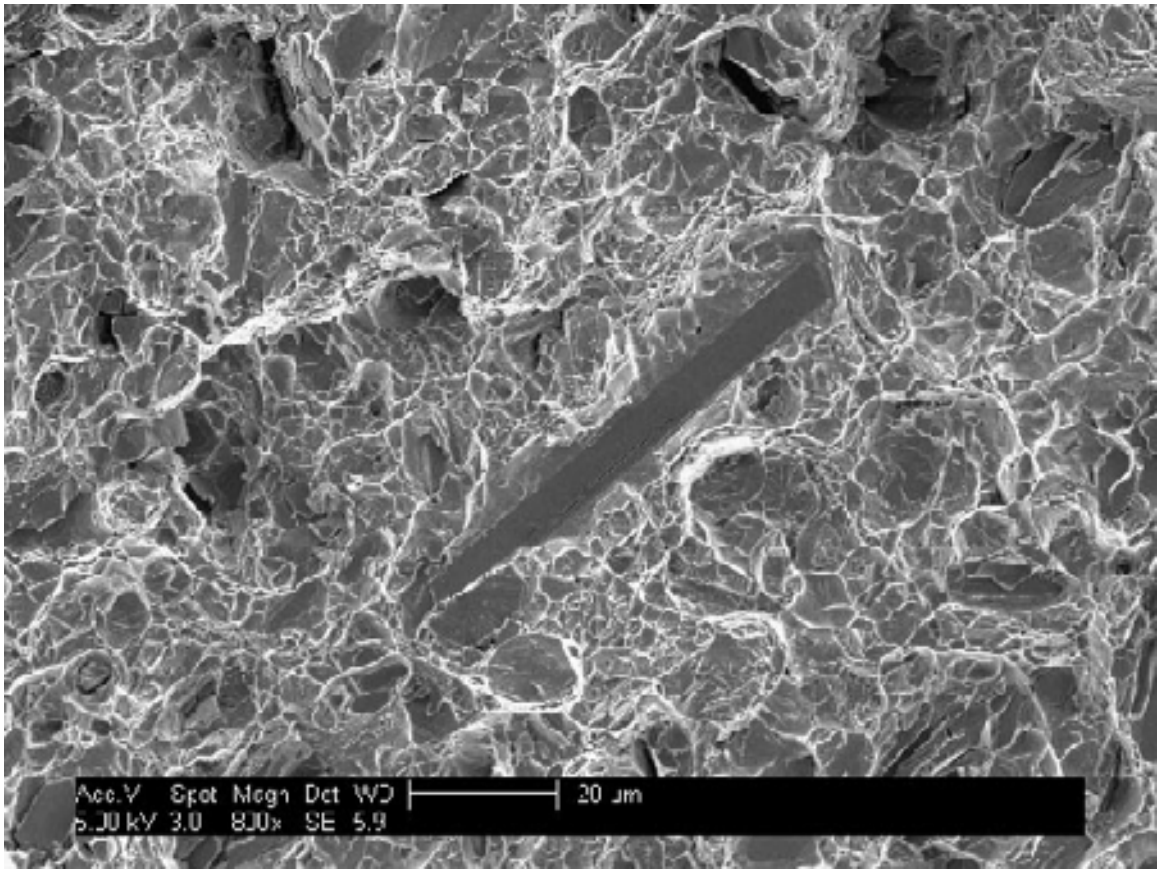

Figure 4.12 Fracture surface of extruded Ti-6Al-4V-2.9B composite showing brittle fracture down the length of a TiB whisker misaligned from the extrusion direction.

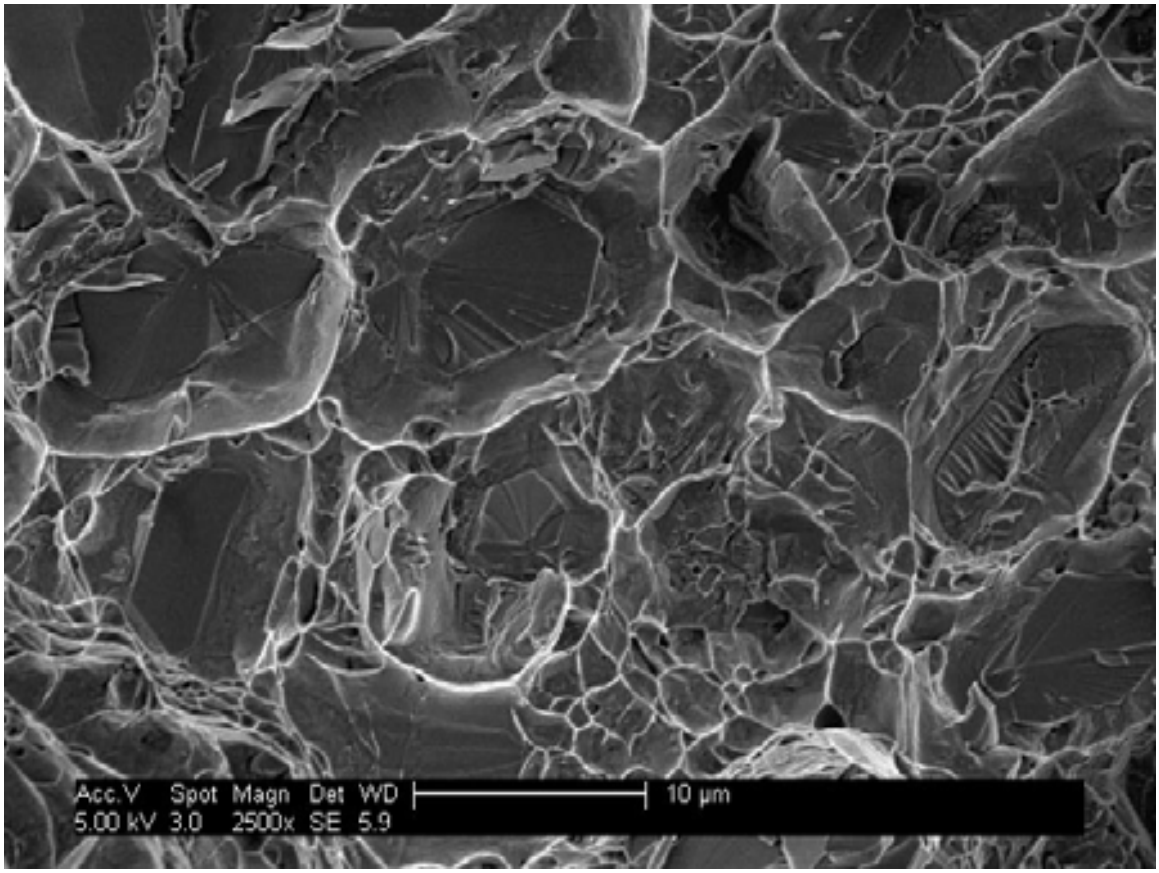

Figure 4.13 Fracture surface of extruded Ti-6Al-4V-2.9B composite showing brittle fracture across the width of TiB whiskers with roughly hexagonal cross-sections aligned with the extrusion direction.

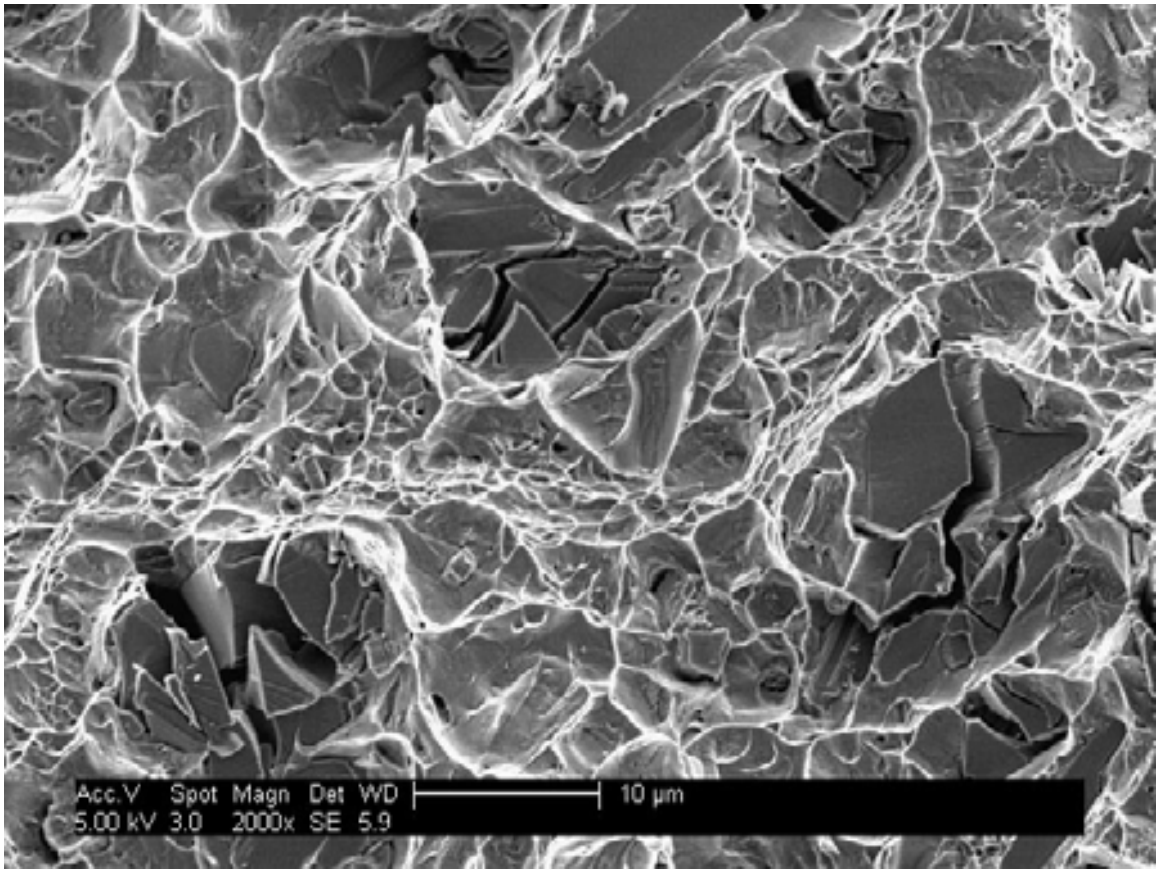

Figure 4.14 Fracture surface of extruded Ti-6Al-4V-2.9B composite showing significant damage to TiB whiskers aligned with the extrusion direction.

4.5 3D Microstructural Visualization

A montage serial sectioning technique was applied for the reconstruction and visualization of TiB particles in compacted Ti-6Al-4V-1.7B and 2.9B composite samples. Visualization of the three-dimensional microstructures was used to observe the effects of the processing parameters on the morphology, anisotropy, and spatial distribution of the TiB particles. In addition, three-dimensional visualization would confirm the absence of a second TiB morphology as observed with two-dimensional optical microscopy.

In the present work, the montages were created using the automated AxioVision digital image analysis system from Carl Zeiss, Inc., that utilizes the image cross

correlation function-based technique for matching the borders between contiguous microstructural fields. In this study, each montage is a microstructural image of an area of approximately 6.25 mm^2, having a high resolution of approximately 0.5 μm. Once the montage of the first serial section was created and stored in the computer memory, a small thickness of the specimen (approximately 1.2 μm) was removed by polishing, and then a second montage was created at the region exactly below that in the first metallographic plane. This polish-montage-polish procedure was repeated to obtain a stack of 75 montage serial sections.

Microhardness indents were used to locate the exact region of interest in successive serial sections and also to precisely measure the distance between consecutive serial sections. In the present work, alignment was accomplished using the image analysis software KS400 from Carl Zeiss, Inc., in which the images of the montage were digitally translated and rotated until they were aligned within ±1 pixel to the respective previous sections.

The stack of aligned serial sections constituted a volume image data set for three-dimensional microstructure visualization. The marching cube algorithm was employed for surface rendering of the three-dimensional microstructures, using the image analysis software VayTek VoxBlast 3.10 [82]. The effective resolution of the three-dimensional microstructures is approximately 1.2 μm, which is the depth of material removed between serial sections.

The three-dimensional microstructure visualizations were completed using 75 montage serial sections, with each montage serial section containing 49 contiguous microstructural fields imaged at a magnification of 200X. Therefore, the resulting three-

dimensional data sets are useful for the characterization and visualization of the microstructure at fine as well as at coarse length scales.

Figure 4.15 shows a volume segment of the surface rendered three-dimensional microstructure of the compacted Ti-6Al-4V-1.7B composite. A volume segment of the microstructure of the compacted Ti-6Al-4V-2.9B composite is shown in Figure 4.16. In these renderings, images were digitally segmented to completely remove the Ti-6Al-4V matrix and reveal only the TiB whiskers. Note that for each sample, these volume segments are only approximately 1.5% of the total microstructure volume collected from the stack of 75 montage serial sections (to produce the three-dimensional rendering at the resolution of the TiB whiskers). The TiB whiskers in both of these microstructures are observed to have similarly uniform random morphological orientations of a single length scale. A second platelike morphology was not observed in either composite specimen.

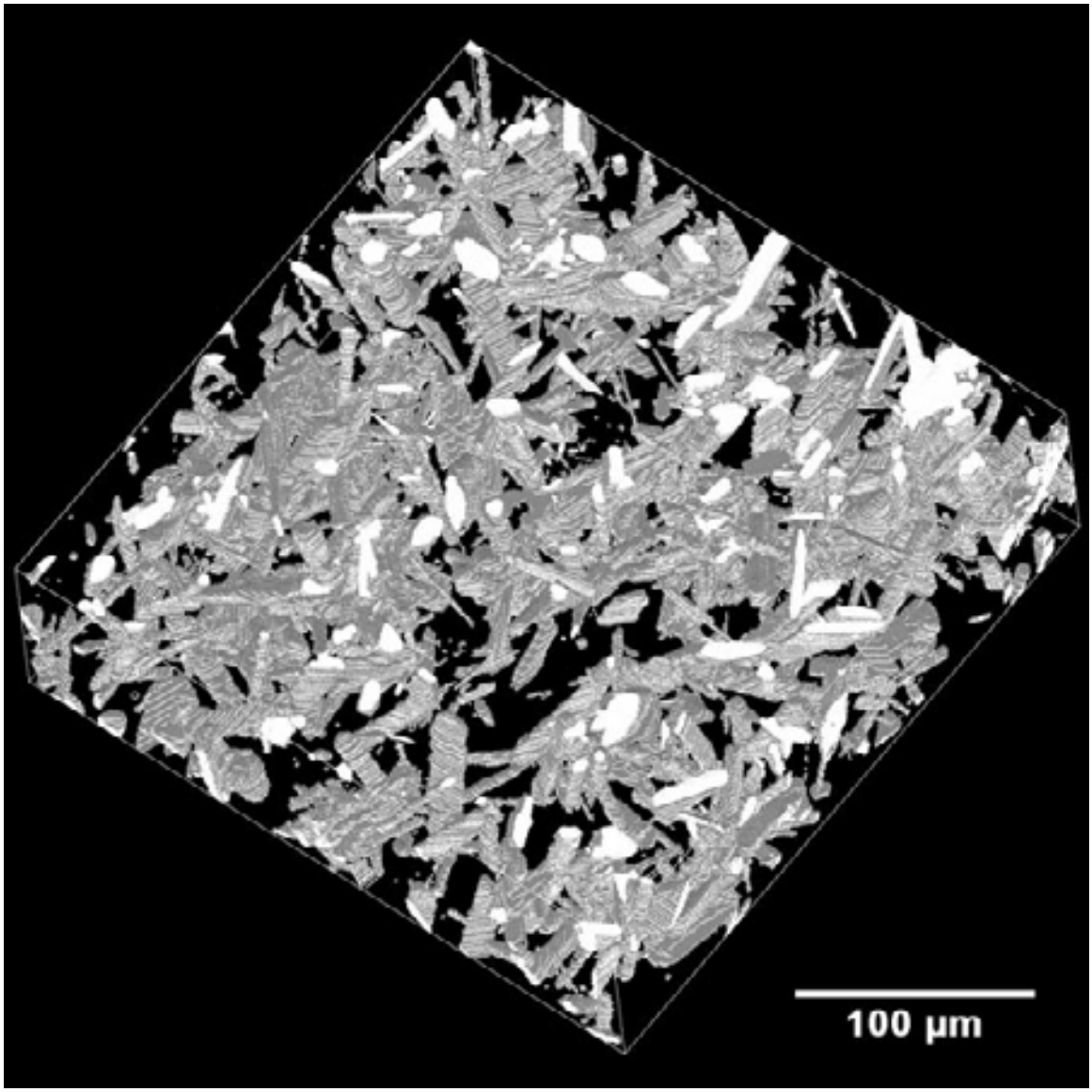

Figure 4.15 Small segment of surface rendered three-dimensional microstructure of compacted Ti-6Al-4V-1.7B composite revealing uniform random angular orientation of the TiB whiskers.

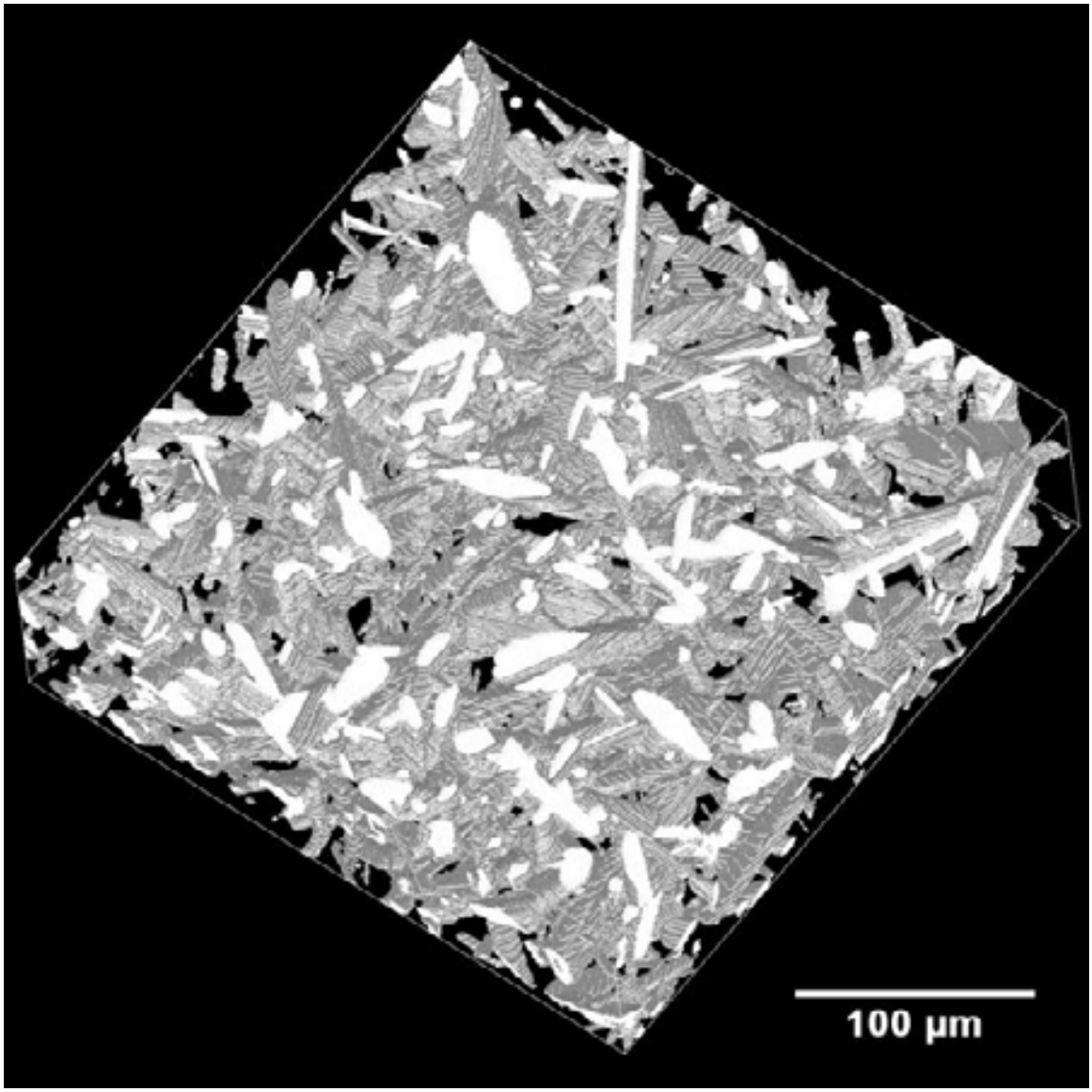

Figure 4.16 Small segment of surface rendered three-dimensional microstructure of compacted Ti-6Al-4V-2.9B composite revealing uniform random angular orientation of the TiB whiskers.

4.6 Conclusions

Samples of Ti-B composites were produced utilizing blended elemental (BE) powder metallurgy processes. Unlike pre-alloying, BE processes are conducted entirely in the solid state. Two different compositions were chosen, Ti-6Al-4V-1.7B and Ti-6Al-

4V-2.9B, and the composites were produced by blind-die compaction. A sample of the Ti-6Al-4V-2.9B composite was also hot extruded.

From observations via optical microscopy and three-dimensional visualization using montage-based serial sectioning, both Ti-B composites showed microstructures containing a unimodal size and morphology distribution of TiB whiskers. These TiB whiskers were somewhat larger on average than the eutectic TiB whiskers seen in the PA boron-modified alloys, but smaller than the primary TiB particles in those alloys. The anisotropic whisker morphology with roughly hexagonal cross-sections was similar to the eutectic and primary TiB morphologies in the PA boron-modified alloys. Observation of the extruded Ti-6Al-4V-2.9B composite using optical microscopy showed alignment of the TiB whiskers with the extrusion direction.

Examination of the tensile fracture surfaces of both compacted and extruded samples of the Ti-6Al-4V-2.9B composite revealed brittle fracture down the length of TiB whiskers in the compacted sample, and across the width of aligned TiB whiskers in the extruded sample (with the TiB whiskers aligned by extrusion in the tensile direction). The Ti-6Al-4V matrix showed relatively ductile fracture. Extrusion improved the yield strength and ultimate tensile strength while effectively doubling the tensile elongation to failure. These samples, however, did not meet the fracture-critical properties required for aerospace structural applications, although the extruded Ti-6Al-4V-2.9B composite sample demonstrated an elastic modulus in the range of steel alloys.

CHAPTER 5

EXTRUDED PRE-ALLOYED Ti-6Al-4V-1B MODIFIED ALLOYS

5.1 Introduction

The performance in tensile and fatigue tests of extruded Ti-6Al-4V-1B modified alloy produced using pre-alloyed (PA) powder metallurgy techniques showed promise that this particular alloy may be suitable for fracture-critical aerospace structural applications. As shown in Table 3.4, tensile test specimens exceeded the 7% elongation to failure requirement for aerospace structural design. Further study of this boron-modified alloy, however, is necessary to optimize the processing parameters for commercial production of aerospace components.

From previous research, it was expected that these Ti-6Al-4V-1B alloy samples processed at temperatures below the β transus of the Ti-6Al-4V matrix would contain eutectic TiB whiskers as well as the sub-micron precipitated TiB phase in the Ti-6Al-4V matrix. The PA approach can produce supersaturated boron due to non-equilibrium cooling conditions, and this supersaturated boron can then be forced out of the titanium alloy matrix through subsequent thermal exposure to form the sub-micron precipitated TiB phase via a solid state process. In this research, the effect of the heat treatments on the presence of the sub-micron TiB phase, and the extent of alignment of both eutectic and sub-micron TiB phases with different extrusion parameters would be investigated.

A variety of extruded specimens of Ti-6Al-4V-1B alloy were produced, with the same initial composition and pre-alloyed powder metallurgy processing, but with the differing extrusion parameters of extrusion temperature and extrusion ratio. Detailed

investigation and characterization of the microstructures of these specimens would determine the effects of these processing parameters on the resultant microstructures and material properties. In addition, understanding these effects would hasten the development of materials design methodologies for Ti-B modified alloys and composites.

5.2 Materials and Processing Details

Pre-alloyed powder of Ti-6Al-4V-1B modified alloy was produced at Crucible Research Corporation, Pittsburgh, Pennsylvania. In this process, the melting procedure involved induction skull (made of titanium) melting of appropriate amounts of the raw materials (titanium, Al-V master alloy, and TiB_2), in a water-cooled copper crucible. Boron additions to the melt were contributed in the form of TiB_2, which dissolves in the liquid melt and forms TiB during solidification by the in situ eutectic phase transformation reaction $Ti + TiB_2 \rightarrow 2TiB$. The liquid melt was then rapidly solidified using inert gas atomization to produce Ti-6Al-4V-1B powder. The atomized powder was then sieved to obtain -100 mesh size (average particle size of 150 μm).

Colleagues at the Air Force Research Laboratory, Wright-Patterson Air Force Base, Ohio, then received the pre-alloyed powder for further P/M processing. The Ti-6Al-4V-1B powder was packed inside thick-walled cans of Ti-6Al-4V, vacuum outgassed at 300°C for 24 hours, and sealed. Each can was coated with glass for lubrication and environmental protection, and then compacted by hot isostatic pressing (HIP) at a temperature of 900°C and a pressure of 100 MPa for 3 hours.

Nine compacts of Ti-6Al-4V-1B alloy were produced for extrusion. Each compact was soaked at its selected extrusion temperature for 1 hour prior to extrusion. Following the extrusions, specimens were then sectioned from the extruded rods and

machined into ½" diameter round tensile test specimens. Room temperature tensile tests were conducted according to ASTM standard E8-04 [88]. Extrusion parameters and tensile test results are shown in Table 5.1.

Table 5.1 Extrusion parameters and tensile test results for extruded Ti-6Al-4V-1B modified alloy samples, using ASTM E8-04.

Sample ID	Extrusion Temperature (^{o}C)	Extrusion Ratio	RT Tensile Properties			
			E (GPa)	YS (MPa)	UTS (MPa)	*e* (%)
A	1010	8:1	139	1185	1270	4
B	1010	12:1	142.5	1189	1278	4
C	1010	16:1	140.5	1182	1273	4.7
D	1057	8:1	142	1161	1245	3.6
E	1057	12:1	144.5	1204	1294	4
F	1057	16:1	145	1206	1297	4
G	1104	8:1	140.5	1127	1210	6.1
H	1104	12:1	140.5	1097	1189	5.9
I	1104	16:1	141	1096	1187	6.8

5.3 Optical Microscopy and Quantitative Characterization

Samples from the grip sections of the ½" tensile test specimens of the extruded Ti-6Al-4V-1B modified alloy were mounted in thermoplastic using standard techniques for metallography. These samples were labeled A-I in accordance with the AFRL tensile test procedures. Suitable grinding and polishing schemes developed for Ti-B alloys and composites were utilized, taking into account the hardness differences between the relatively soft Ti-6Al-4V alloy matrix and the relatively hard TiB whisker reinforcement. Using these metallographic techniques, a final surface finish of 0.05 μm was obtained.

The extruded samples of Ti-6Al-4V-1B modified alloy were examined using a Carl Zeiss, Inc. Axiovert 200 MAT optical microscopy system with AxioVision image analysis software. For each sample, montages were created using the automated AxioVision digital image analysis system that utilizes the image cross correlation function-based technique for matching the borders between contiguous microstructural fields. For these samples, each montage is a microstructural image of a large area (~2.05 mm^2), having a high resolution (~0.5 μm).

Figure 5.1 shows one such montage of 100 fields of view of sample C, and Figure 5.2 shows a montage of 100 fields of view of sample I. The images have been compressed for display. These micrographs show eutectic TiB whiskers predominantly aligned with the extrusion direction (parallel to the horizontal axis across the metallographic planes) in a Ti-6Al-4V matrix. Observations on all 9 samples showed similar microstructures. In these figures, the TiB whiskers are a darker gray than the gray titanium matrix. No coarse primary TiB particles were observed, as expected. Montages were taken from different regions and different samples of each specimen to ensure that observations were performed on representative examples of the microstructures.

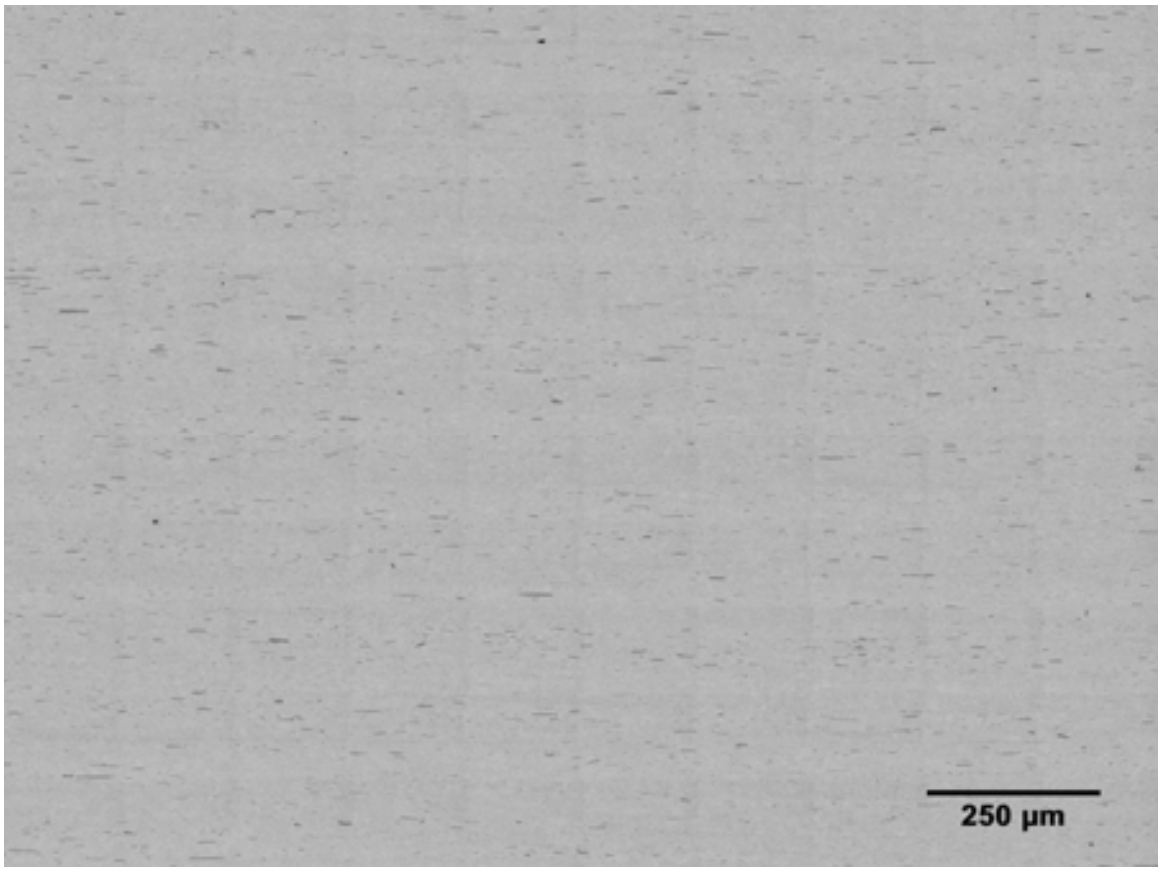

Figure 5.1 Montage of the microstructure of sample C, an extruded Ti-6Al-4V-1B modified alloy. The extrusion direction is parallel to the horizontal axis of the metallographic plane.

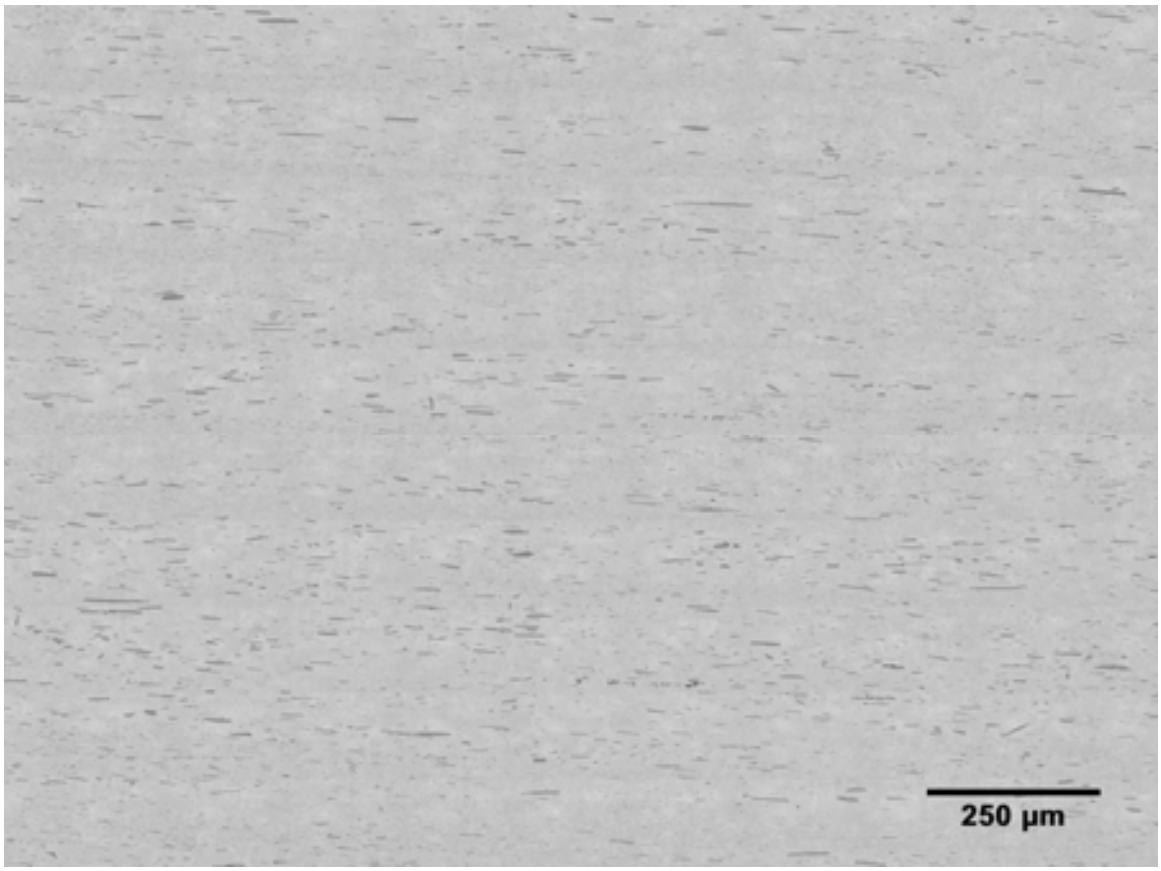

Figure 5.2 Montage of the microstructure of sample I, an extruded Ti-6Al-4V-1B modified alloy. The extrusion direction is parallel to the horizontal axis of the metallographic plane.

Examination of these microstructures at higher magnifications, however, revealed the presence of significant amounts of the sub-micron precipitated TiB phase that were not present in the previously studied blind-die compacted Ti-6Al-4V-1B alloy processed at temperatures above the β transus of the alloy. Figure 5.3 shows the microstructure of sample C, and Figure 5.4 shows the microstructure of sample I (the other samples showed similar microstructures). The larger gray TiB whiskers are the eutectic phase, and the smaller gray TiB particles are the sub-micron phase, named as such because the width of these particles are less than 1 μm. The size of the sub-micron TiB phase is near the limits

of the resolution of optical microscopy, and may look slightly out of focus as a result. Black particles seen in these micrographs are artifacts from metallographic polishing.

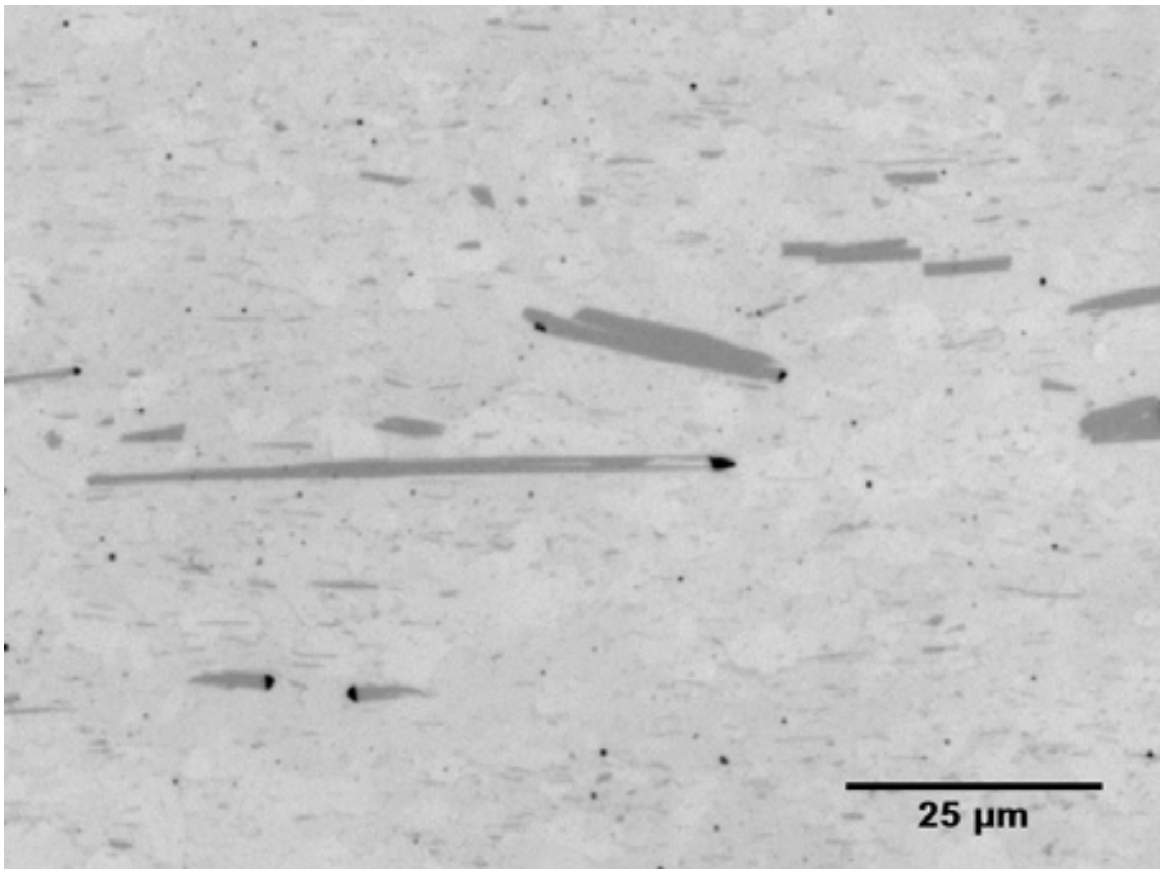

Figure 5.3 Microstructure of extruded Ti-6Al-4V-1B sample C, showing eutectic TiB whiskers as well as sub-micron precipitated TiB particles. The extrusion direction is parallel to the horizontal axis of the metallographic plane.

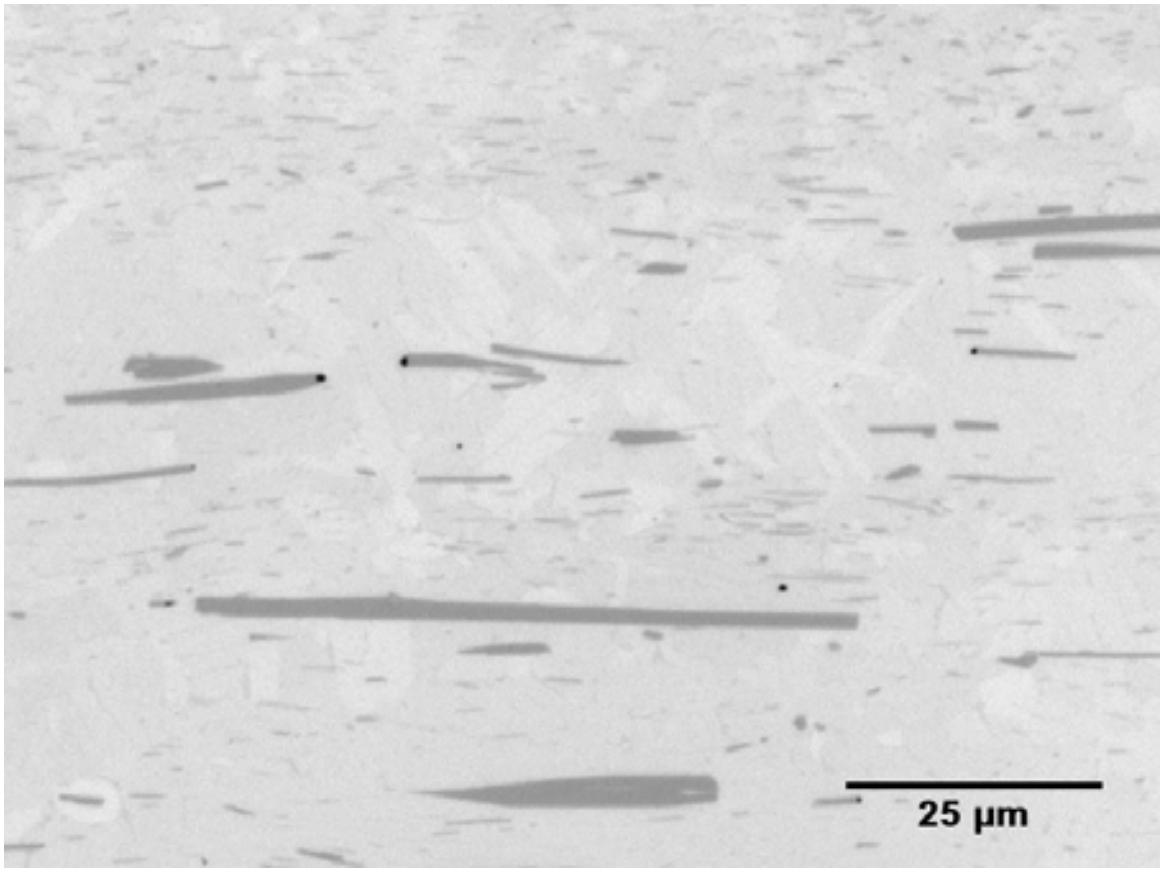

Figure 5.4 Microstructure of extruded Ti-6Al-4V-1B sample I, showing eutectic TiB whiskers as well as sub-micron precipitated TiB particles. The extrusion direction is parallel to the horizontal axis of the metallographic plane.

Examination of the microstructures with the metallographic plane perpendicular to the extrusion direction showed similar alignment with extrusion as was seen in previously extruded Ti-B alloys and composites. High-magnification micrographs of sample C and sample I are shown in Figure 5.5 and Figure 5.6, respectively. The roughly hexagonal cross-sections of the eutectic TiB whiskers can be observed, as well as the presence of the sub-micron TiB precipitated phase.

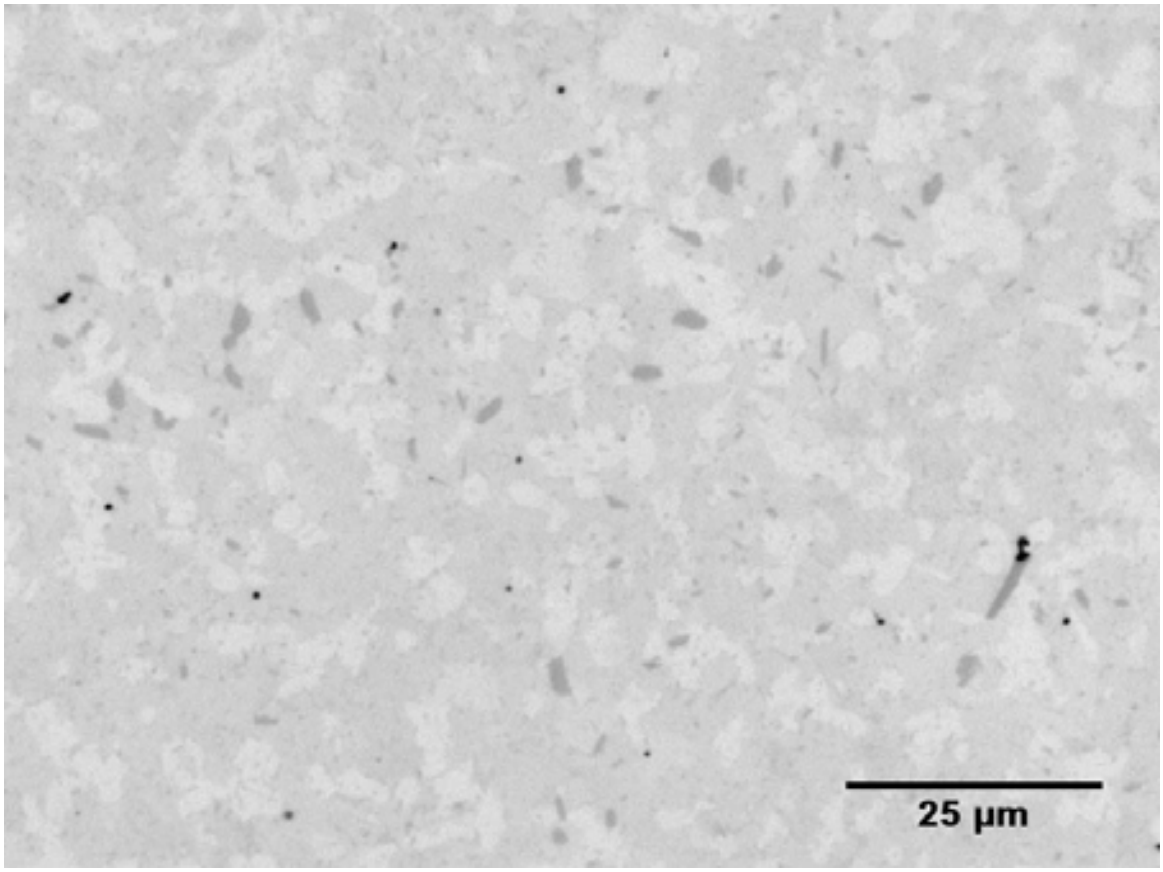

Figure 5.5 Microstructure of extruded Ti-6Al-4V-1B sample C, showing eutectic TiB whiskers as well as sub-micron precipitated TiB particles. The extrusion direction is perpendicular to the metallographic plane.

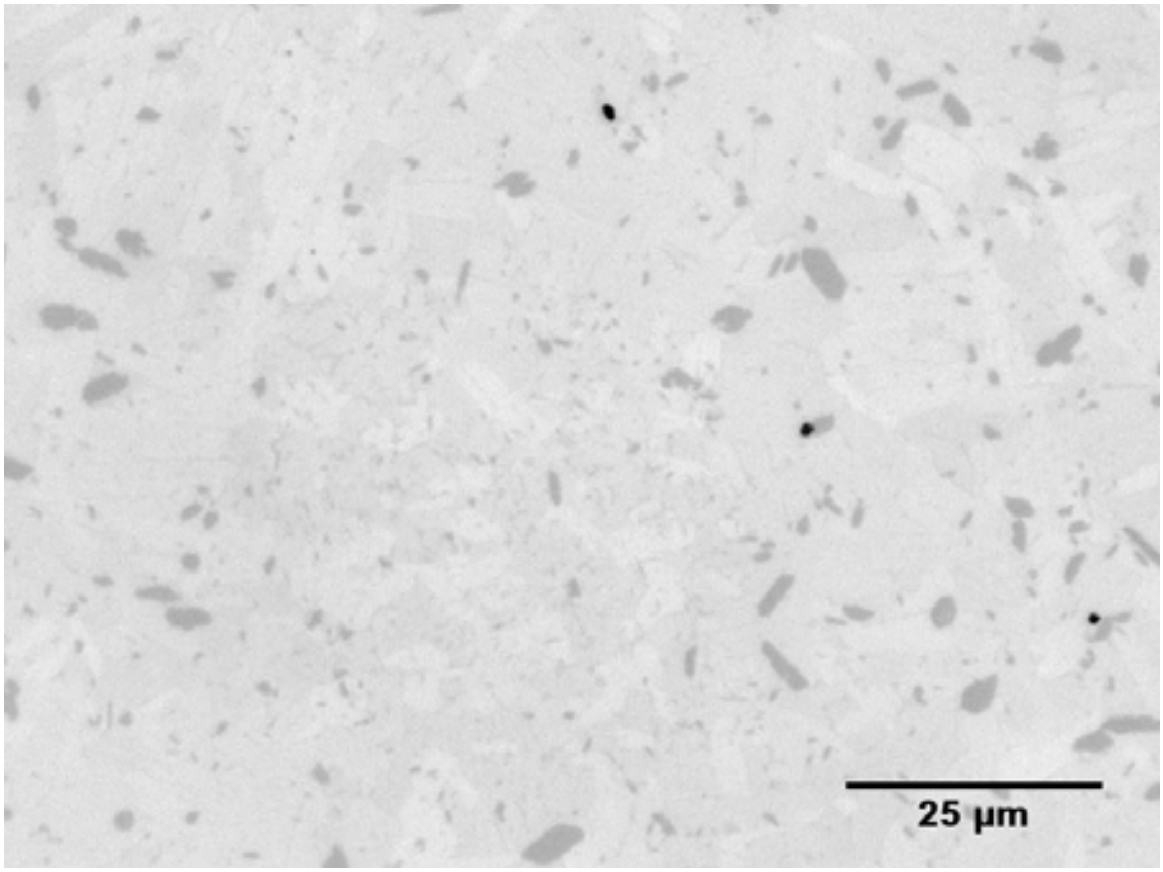

Figure 5.6 Microstructure of extruded Ti-6Al-4V-1B sample I, showing eutectic TiB whiskers as well as sub-micron precipitated TiB particles. The extrusion direction is perpendicular to the metallographic plane.

Unlike the previous Ti-B modified alloys and composites processed using blind die compaction, these extruded Ti-6Al-4V-1B alloy samples processed by hot isostatic pressing (HIP) showed a small amount of porosity. No porosity had been seen in earlier studies of the blind die compacted materials. An example of the porosity in these HIP and extruded samples is shown in Figure 5.7, showing a pore in the microstructure of sample G. Porosity was observed in all 9 samples.

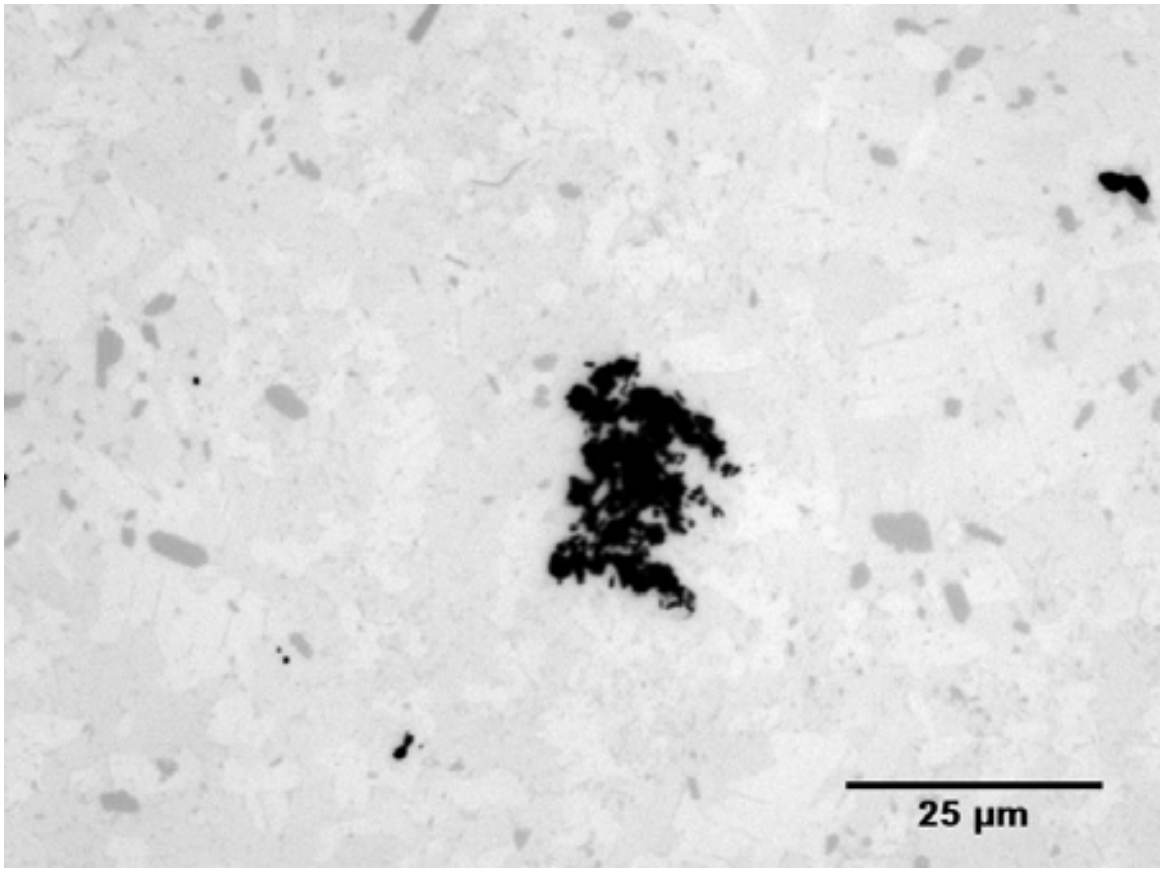

Figure 5.7 Porosity observed in the microstructure of extruded Ti-6Al-4V-1B sample G. The extrusion direction is perpendicular to the metallographic plane.

Discussions with research colleagues at AFRL prior to this study had suggested that depending on the cooling rate, up to approximately 2 volume percent of sub-micron TiB could precipitate in Ti-6Al-4V-1B modified alloys. It was believed that sub-micron TiB can give rise to Orowan strengthening, but may be detrimental to ductility and fatigue in the alloy. This seems to be confirmed in the tensile behavior of the HIP and extruded samples (Table 5.1) when compared with the earlier blind die compacted and extruded Ti-6Al-4V-1B specimen (Table 3.4). The elastic modulus is effectively the same, but the presence of sub-micron TiB in the HIP samples increases the yield strength

and ultimate tensile strength while significantly decreasing the tensile elongation to failure.

In addition, research colleagues had suggested that the sub-micron precipitated TiB phase did not align with extrusion. They had believed that the particles were too small to see the flow of the Ti-6Al-4V matrix during extrusion (or other thermomechanical processing). The morphology of the sub-micron TiB particles had also yet to be definitively determined. Examination of these samples with optical microscopy, however, suggested that the sub-micron TiB particles were predominantly aligned with extrusion, and that they had a whisker-like morphology similar to the larger particles of other TiB phases. The limited resolution at the size range of the sub-micron TiB particles required investigation using methods to examine the microstructures at higher magnifications, such as scanning electron microscopy (SEM).

Microstructural data for these extruded Ti-6Al-4V-1B alloy samples were calculated using conventional two-dimensional stereology techniques. Measurements were made on montages in the plane parallel as well as on montages in the plane normal to the extrusion direction. Average values for the eutectic TiB whiskers are shown in Table 5.2, but these results do not take into account the stochastic nature of microstructures. Overall, it was found that the eutectic TiB whiskers typically had a length of approximately 15-30 μm and a width of approximately 2.5-5 μm, for an aspect ratio range of between 3 and 12. The overall volume fraction of eutectic TiB whiskers in these samples is between approximately 2 and 4%, with the difference in volume fraction likely due to a larger amount of sub-micron precipitated TiB phase in samples with a lower measured volume fraction. In addition, although the angular orientation of the TiB

whiskers was affected by extrusion, the morphology of the TiB phases was not observed to have been affected by extrusion.

Table 5.2 Microstructural data of extruded Ti-6Al-4V-1B modified alloy samples calculated using standard two-dimensional stereology techniques.

sample	avg length (μm)	avg width (μm)	aspect ratio	volume fraction
A	19.38	2.90	6.68	2.53
B	18.97	2.94	6.45	2.00
C	20.73	2.81	7.38	1.83
D	19.88	2.99	6.65	2.35
E	19.79	2.87	6.90	2.26
F	18.95	2.95	6.42	2.45
G	21.42	3.42	6.26	3.74
H	24.01	3.16	7.60	4.03
I	26.11	3.43	7.61	4.24

The sub-micron precipitated TiB particles could not be accurately measured using standard two-dimensional stereology techniques because their size was near the limit of the resolution of optical microscopy. From basic observations, sub-micron TiB particles seemed to be 5 μm or less in length, and less than 1 μm in width.

The angular orientation of the eutectic TiB whiskers was also calculated using conventional two-dimensional stereology techniques. Measurements were made on montages in the plane parallel to the extrusion direction. Results are shown as the percentage of TiB whiskers at orientations relative to the extrusion direction. The angular orientation of TiB whiskers in the low temperature (1010°C) extrusion samples A-C are shown in Figure 5.8; the medium temperature (1057°C) extrusion samples D-F are shown in Figure 5.9; and the high temperature (1104°C) samples G-I are shown in Figure 5.10. At the low and medium extrusion temperatures, there is a sharper peak

around the extrusion axis for the highest extrusion ratio of 16:1. At the high extrusion temperature, there is an overall sharper peak around the extrusion axis for all three extrusion ratios. In general, for the angular orientation of eutectic TiB whiskers, microstructures produced at higher extrusion ratios and higher extrusion temperatures have a sharper range around the extrusion axis.

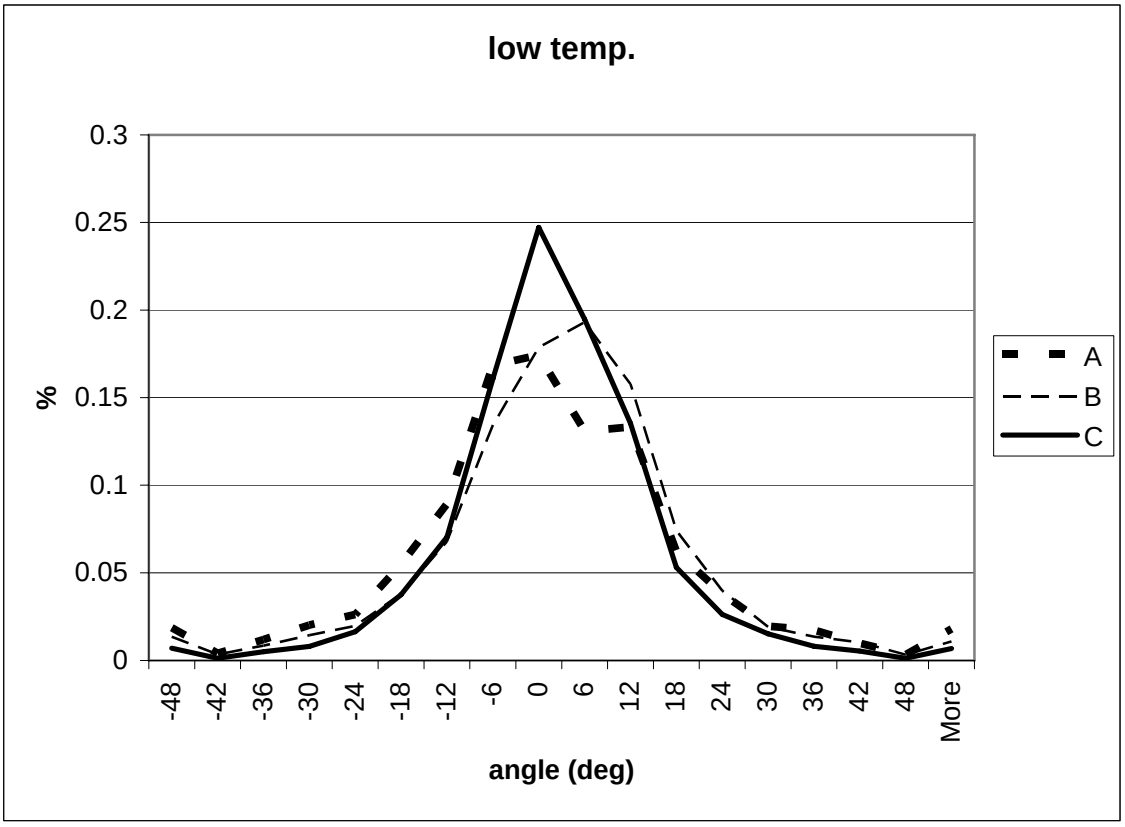

Figure 5.8 Angular orientation of eutectic TiB whiskers in Ti-6Al-4V-1B alloy samples extruded at 1010°C.

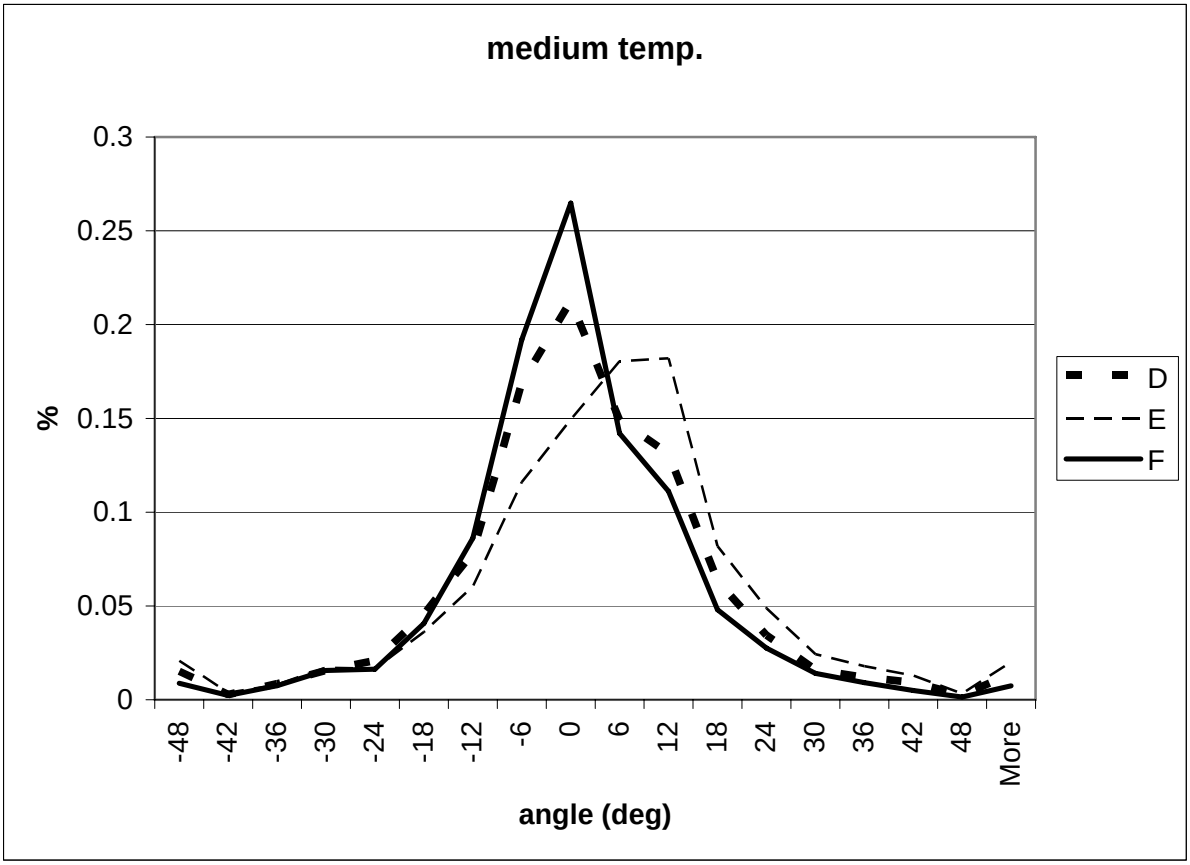

Figure 5.9 Angular orientation of eutectic TiB whiskers in Ti-6Al-4V-1B alloy samples extruded at 1057°C.

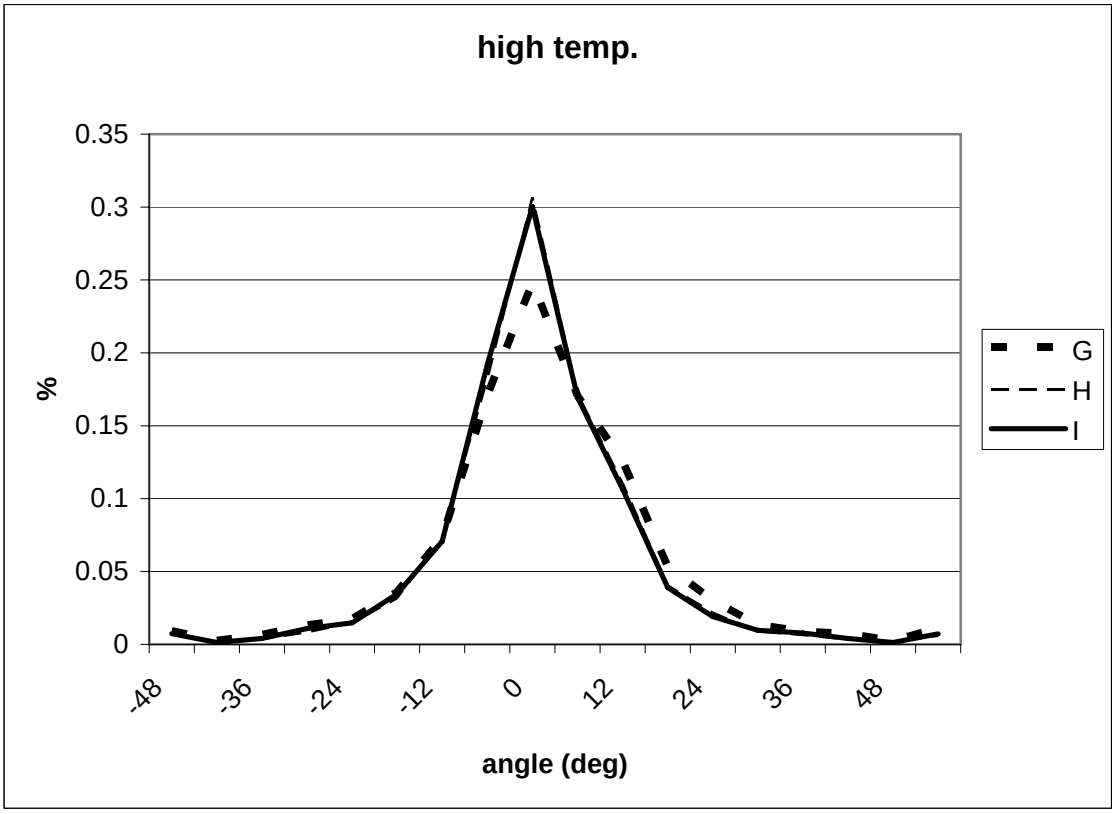

Figure 5.10 Angular orientation of eutectic TiB whiskers in Ti-6Al-4V-1B alloy samples extruded at 1104°C.

5.4 SEM Characterization

In order to observe the microstructures of extruded Ti-6Al-4V-1B modified alloys at a higher resolution than is possible with optical microscopy, samples were examined using scanning electron microscopy (SEM). Polished samples underwent SEM characterization utilizing a LEO 1550 scanning electron microscope, using secondary electron emission. The focus of this study was the morphology, size, and possible extrusion alignment of sub-micron precipitated TiB particles.

Figure 5.11 shows the microstructure of sample C, at a magnification of 4000X. Figure 5.12 shows the microstructure of sample G, also at a magnification of 4000X. In

both micrographs, the $\alpha + \beta$ grain structure of the Ti-6Al-4V matrix can be seen, along with the larger eutectic TiB whiskers and the sub-micron precipitated TiB phase. The sub-micron TiB particles are thin, but it can be clearly observed that their morphologies are similar to the larger eutectic TiB whiskers, and that the sub-micron TiB whiskers are predominantly aligned with the extrusion direction, which is parallel to the horizontal axis of the micrographs. The earlier suggestion that the sub-micron TiB phase did not see the flow of the Ti-6Al-4V matrix during thermomechanical processing is incorrect. This finding is important for further developing Ti-B modified alloys, where the sub-micron TiB whiskers can be useful or detrimental depending on the application, and can potentially be tailored to needed amounts depending on the processing methods used.

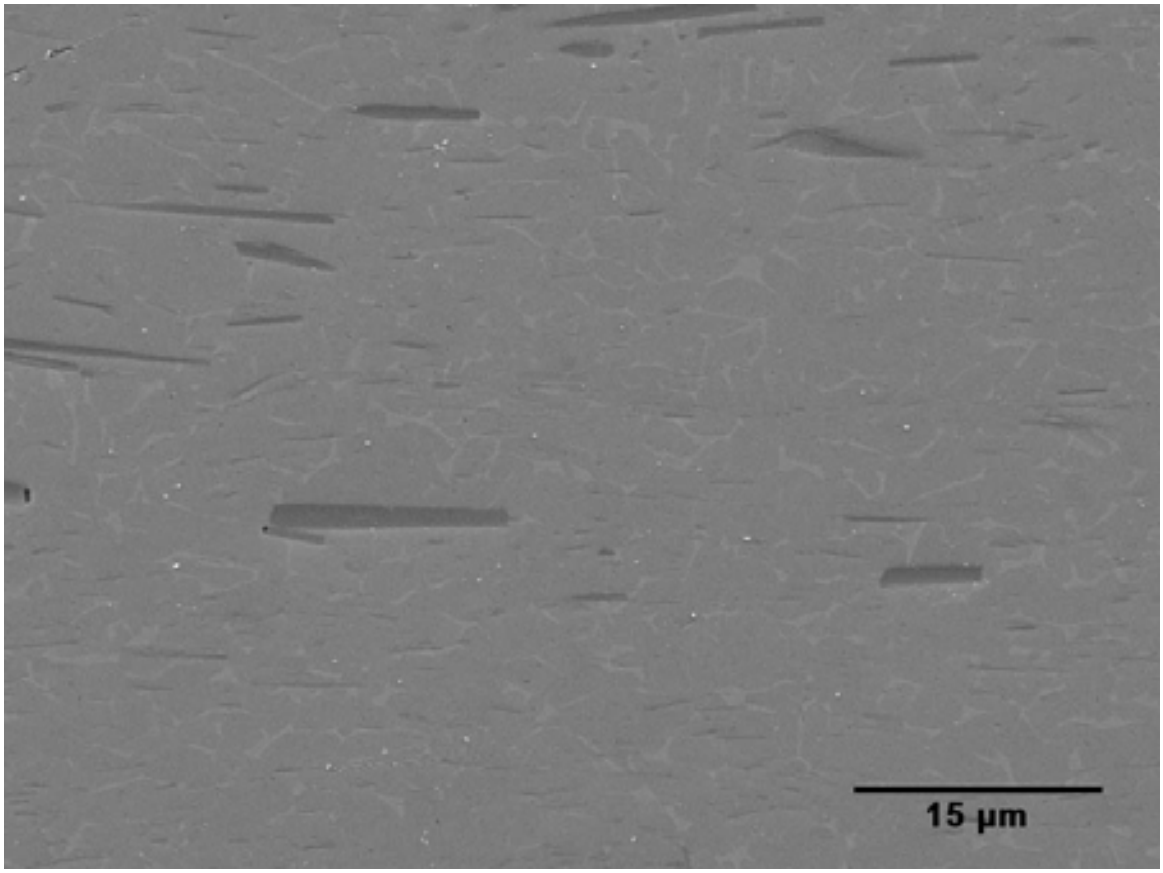

Figure 5.11 Scanning electron micrograph of extruded Ti-6Al-4V-1B sample C, showing the whisker morphology and extrusion alignment of sub-micron precipitated TiB whiskers.

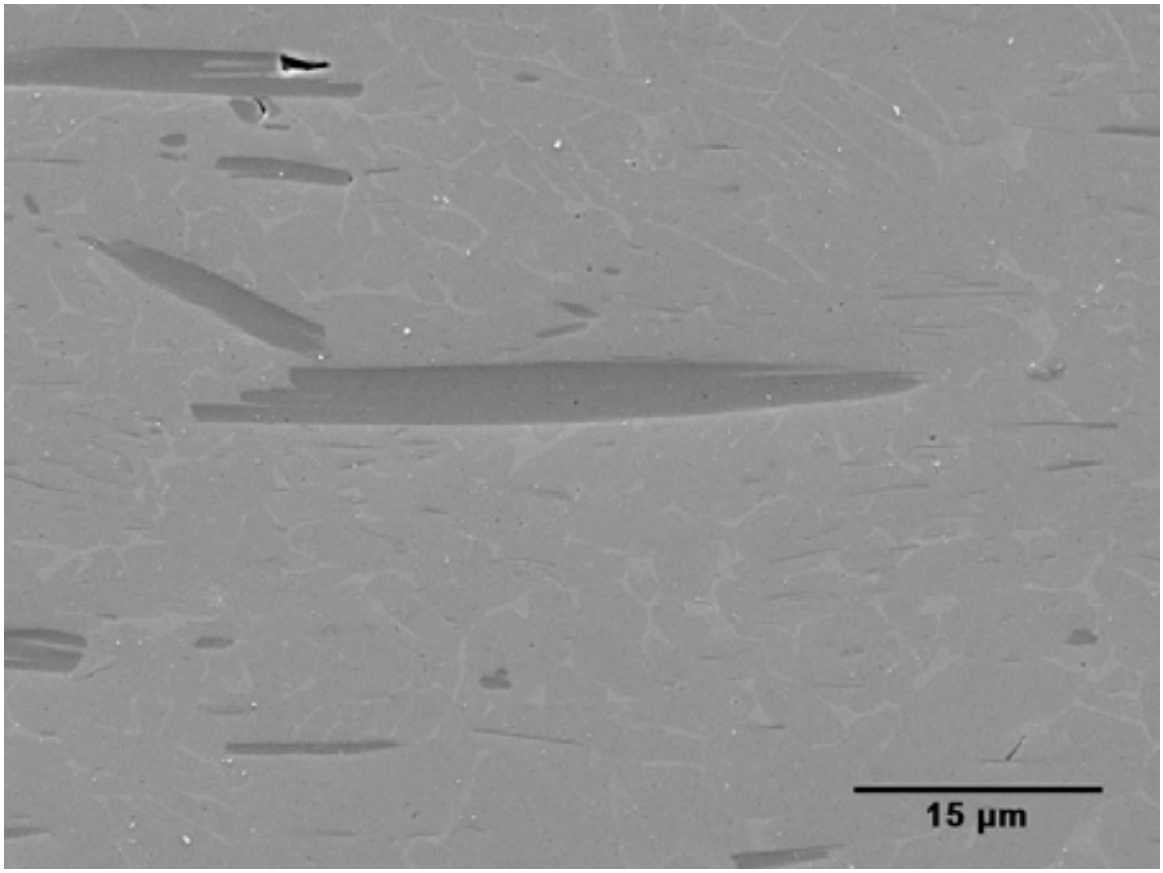

Figure 5.12 Scanning electron micrograph of extruded Ti-6Al-4V-1B sample G, showing the whisker morphology and extrusion alignment of sub-micron precipitated TiB whiskers.

5.5 3D Microstructural Visualization

A montage serial sectioning technique was applied for the reconstruction and visualization of TiB particles in extruded Ti-6Al-4V-1B modified alloy samples. Visualization of the three-dimensional microstructures was used to observe the effects of the processing parameters on the morphology, anisotropy, and spatial distribution of the TiB particles. A particular focus was on the varying amounts of eutectic TiB whiskers depending on the processing conditions.

In the present work, the montages were created using the automated AxioVision digital image analysis system from Carl Zeiss, Inc., that utilizes the image cross correlation function-based technique for matching the borders between contiguous microstructural fields. In this study, each montage is a microstructural image of an area of approximately 2.05 mm^2, having a high resolution of approximately 0.5 μm. Once the montage of the first serial section was created and stored in the computer memory, a small thickness of the specimen (approximately 1 μm) was removed by polishing, and then a second montage was created at the region exactly below that in the first metallographic plane. This polish-montage-polish procedure was repeated to obtain a stack of 110 montage serial sections.

Microhardness indents were used to locate the exact region of interest in successive serial sections and also to precisely measure the distance between consecutive serial sections. In the present work, alignment was accomplished using the image analysis software KS400 from Carl Zeiss, Inc., in which the images of the montage were digitally translated and rotated until they were aligned within ±1 pixel to the respective previous sections.

The stack of aligned serial sections constituted a volume image data set for three-dimensional microstructure visualization. The marching cube algorithm was employed for surface rendering of the three-dimensional microstructures, using the image analysis software VayTek VoxBlast 3.10 [82]. The effective resolution of the three-dimensional microstructures is approximately 1 μm, which is the depth of material removed between serial sections.

The three-dimensional microstructure visualizations were completed using 110 montage serial sections, with each montage serial section containing 100 contiguous microstructural fields imaged at a magnification of 500X. Therefore, the resulting three-dimensional data sets are useful for the characterization and visualization of the microstructure at fine as well as at coarse length scales.

Figure 5.13 shows a volume segment of the surface rendered three-dimensional microstructure of the extruded Ti-6Al-4V-1B alloy sample C. A volume segment of the microstructure of sample F is shown in Figure 5.14, and a volume segment of the microstructure of sample I is shown in Figure 5.15. In these renderings, images were digitally segmented to completely remove the Ti-6Al-4V matrix and reveal only the TiB whiskers. Note that for each sample, these volume segments are only approximately 0.5% of the total microstructure volume collected from the stack of 110 montage serial sections (to produce the three-dimensional rendering at the resolution of the TiB whiskers), and are representative of the overall volume of each sample. All three of these samples were extruded with an extrusion ratio of 16:1, at the extrusion temperatures of 1010°C, 1057°C, and 1104°C, respectively. The eutectic TiB whiskers show alignment with the extrusion direction, which is normal to the top and bottom faces of these volume segments. The small particles in Figures 5.13 and 5.14 seen amongst the larger eutectic TiB whiskers are likely some of the sub-micron precipitated TiB phase that are near the resolution limit of the optical microscopy used to create the montages rendered in the three-dimensional visualization. For the most part, the sub-micron TiB whiskers are too small to be accurately visualized using the montage-based serial sectioning techniques. The microstructure of sample I in Figure 5.15 clearly shows a greater amount of eutectic

TiB whiskers than the samples extruded at lower temperatures, as suggested from two-dimensional optical microscopy observations. All of the samples have identical compositions, so this result suggests a coarsening of the eutectic TiB phase from the sub-micron precipitated TiB phase at temperatures approaching 1100°C. Samples G and H, also extruded like sample I at 1104°C, showed a similar coarsening effect. These high-temperature samples, processed above the β transus of the alloy, show microstructures very similar to the pre-alloyed Ti-6Al-4V-1B modified alloy previously studied that was blind die compacted at 1200°C and then extruded at 1100°C.

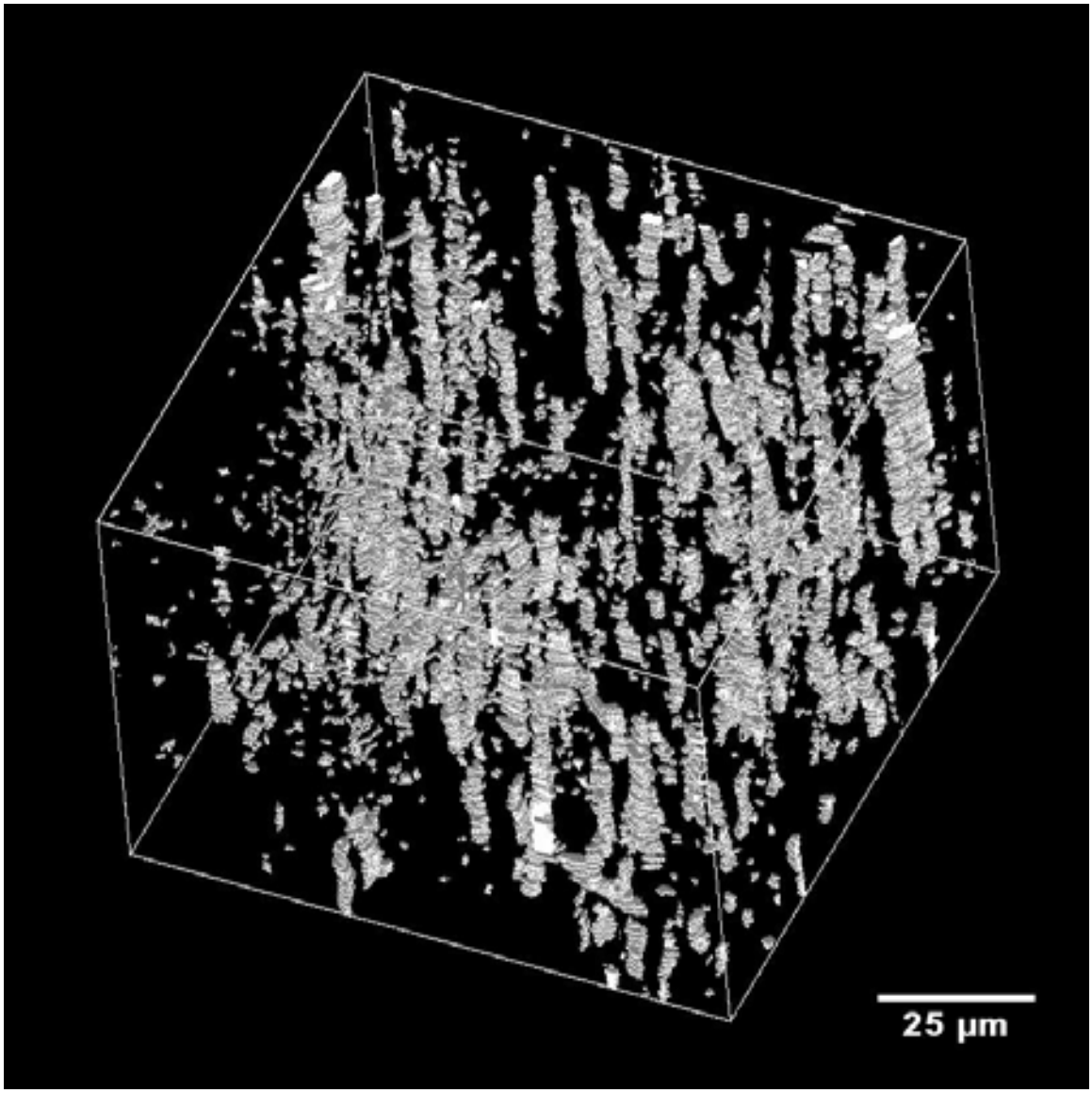

Figure 5.13 Small segment of surface rendered three-dimensional microstructure of extruded Ti-6Al-4V-1B alloy sample C. The extrusion direction is parallel to the depth of the volume segment.

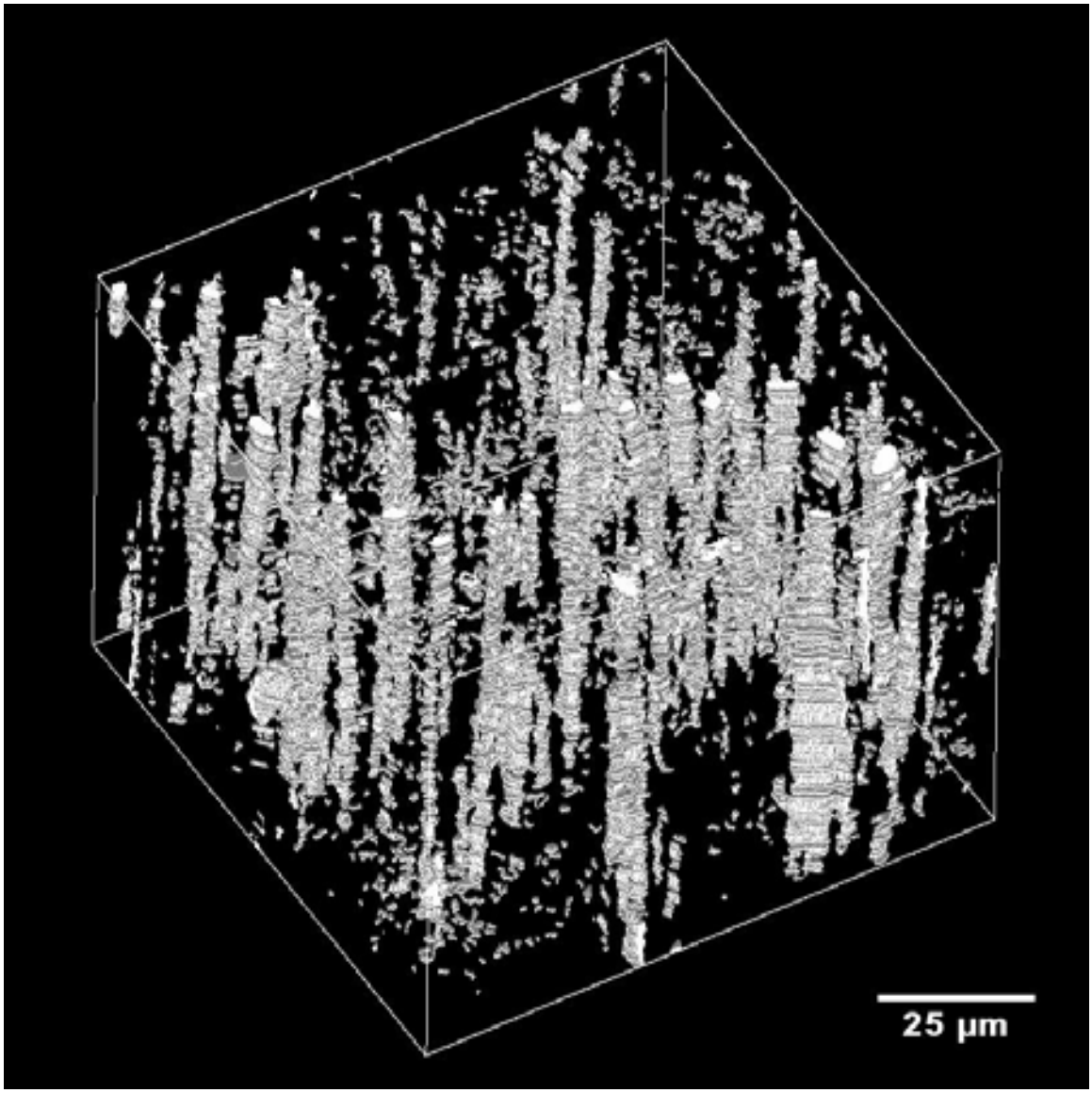

Figure 5.14 Small segment of surface rendered three-dimensional microstructure of extruded Ti-6Al-4V-1B alloy sample F. The extrusion direction is parallel to the depth of the volume segment.

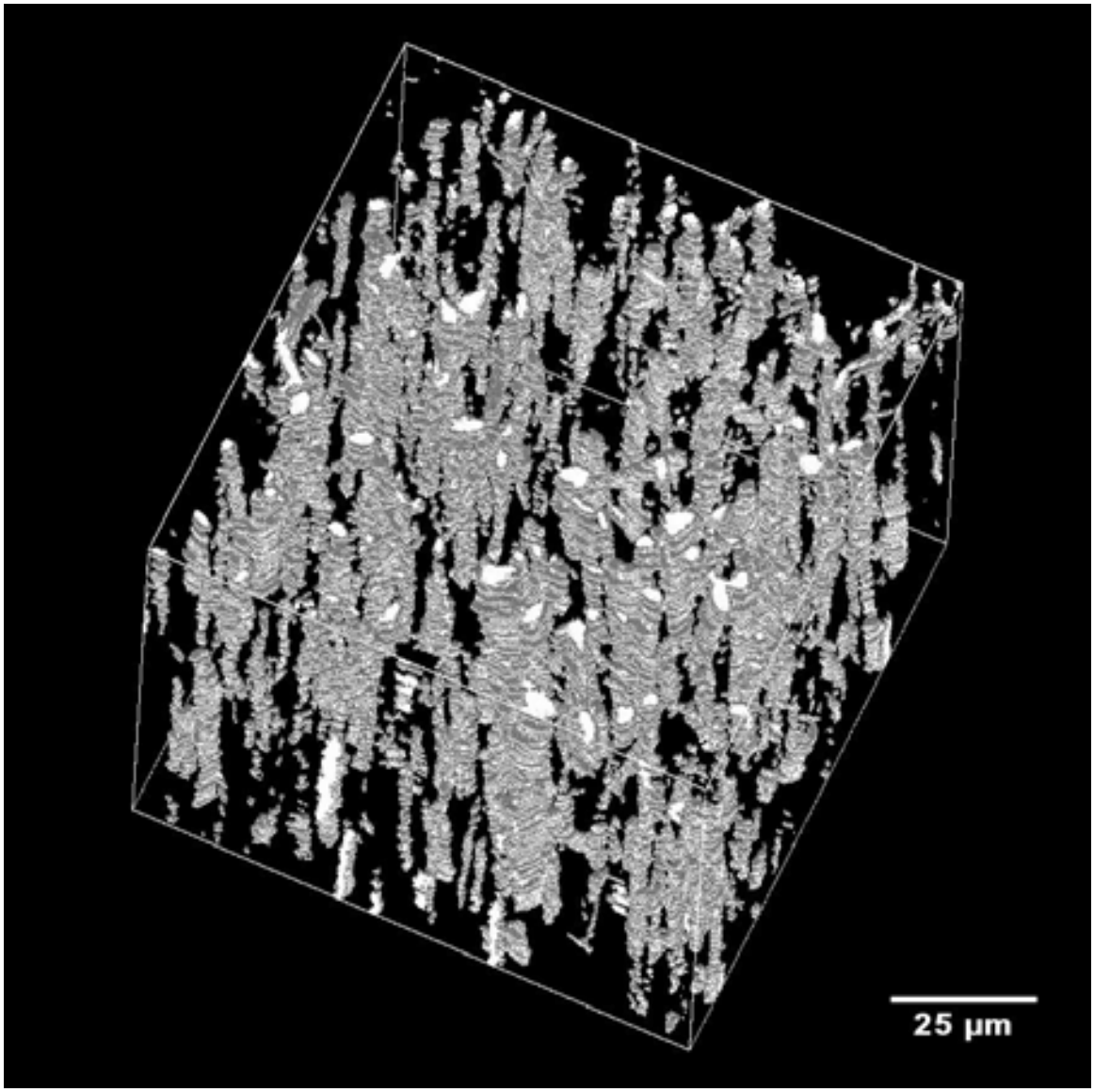

Figure 5.15 Small segment of surface rendered three-dimensional microstructure of extruded Ti-6Al-4V-1B alloy sample I. The extrusion direction is parallel to the depth of the volume segment.

5.6 Conclusions

Samples of extruded Ti-6Al-4V-1B modified alloy were produced using three different extrusion ratios and at three different extrusion temperatures (following compaction by hot isostatic pressing (HIP) of pre-alloyed powders), to investigate the

effect of these processing parameters on the resultant microstructures and material properties. Optical microscopy and characterization using conventional stereology techniques suggested the presence of a sub-micron precipitated TiB phase in addition to the eutectic TiB whiskers. A small amount of porosity was also observed in all of the extruded samples. Measurement of the angular orientation of the eutectic TiB whiskers demonstrated a sharper range around the extrusion axis with higher extrusion ratios and at higher extrusion temperatures.

Scanning electron microscopy confirmed the presence of the sub-micron TiB precipitated phase, as well as showed a whisker-like morphology and alignment with extrusion similar to the larger eutectic TiB whiskers. These observations are crucial to develop accurate materials design methodologies for similar boron-modified titanium alloys.

Montage-based serial sectioning and three-dimensional visualization confirmed alignment with extrusion of the eutectic TiB whiskers, as well as significant TiB coarsening at extrusion temperatures near 1100°C. Although the sub-micron TiB whiskers are present in all of the extruded Ti-6Al-4V-1B samples, they are present in smaller volume fractions in the samples extruded at the highest temperature. The sub-micron TiB whiskers improved the yield strength and ultimate tensile strength of these alloy samples compared to the previously studied Ti-6Al-4V-1B blind die compacted and extruded alloy, but significantly decreased the tensile elongation to failure, a critical material property for aerospace structural applications.

CHAPTER 6

DEVELOPMENT OF MATERIALS DESIGN METHODOLOGIES

6.1 Introduction

With successful research involving Ti-B materials, commercial industry is beginning to scale up to production of Ti-B applications. To enhance this development, prediction and modeling of the properties and microstructures of these alloys and composites has become increasingly important. If the relationships between the processing, microstructures, and resultant properties can be more thoroughly understood, implementation of Ti-B products will more likely be accepted in the aerospace, automotive, and biomedical industries.

As part of a collaborative effort, research colleagues are developing materials design methodologies combining traditional materials characterization and stereology techniques with computer simulations and finite element-based analyses. In this process, the microstructure of an existing material will be quantified in terms of a few mathematical parameters, both in two and three dimensions. Then, computer simulated virtual microstructures will be created that are statistically similar to the real microstructures. These simulations will be verified using finite element micromechanical analyses to determine the global and local constitutive behavior of these microstructures, and to ensure they agree with the experimental mechanical behavior of the real material. Then, an “atlas” of computer simulated realistic microstructures can be created by varying the mathematical parameters that correspond to changes in the processing such as composition or spatial orientation. In this way, a range of potential alloys or composites

can be investigated and tested using computer simulations without having to produce a large number of different material samples. This will make the materials development process more efficient and less expensive for a range of metals and composites.

Characterization and visualization research of Ti-B modified alloys and composites is being used to help establish the foundation for these materials design techniques. A particular focus involves aspects of the microstructures such as whisker morphology and spatial distribution. This work, combined with colleagues' investigations of cast magnesium alloys and aluminum matrix composites, will demonstrate the robustness of the new methodologies.

6.2 Simulations of Realistic Microstructures

The complexity of the microstructures of Ti-B modified alloys and composites is an obstacle towards accurate materials simulation. Current computer models are utilizing oversimplifications of TiB morphologies, assuming the whiskers are round cylinders uniformly distributed and oriented in the Ti-6Al-4V matrix [100]. Applying this type of incorrect microstructural simulation to finite element analyses will not provide accurate predictions of material behavior.

In this work, the newly developed techniques for simulations of realistic Ti-B microstructures avoid those assumptions by using morphologies from the features of interest in the microstructures of real materials. To create a simulation of a realistic microstructure, a large number (~1000) of TiB particle images are digitally removed from the original microstructural montages and stored such that the data set is representative of the size, shape, and morphology distributions of the TiB particle population in the microstructure of the real material. Next, a simulation of TiB particle

centroids (with a specified spatial arrangement and number density), is generated in a digitized simulation space where the pixel size is the same as that in the original microstructural images from which the TiB particles were removed. Finally, one TiB particle image is selected at random from the set, and placed at one simulated centroid point. The process is repeated until there is a TiB particle image centered on each simulated centroid point.

The result is a simulated microstructure containing the same TiB whisker morphologies as those in a real microstructural image, but (depending on the simulation parameters and algorithm), with a different spatial arrangement of the whiskers, different TiB volume fraction, average size, number density, anisotropy, etc. Further details of the methodology are given elsewhere [101-103]. The two-point correlation function of the TiB whiskers in the simulated microstructure is then computed and compared with the experimentally measured two-point correlation function of the TiB whiskers in the real microstructure. Simulation parameters are varied until a satisfactory match between the two-point correlation functions of the real and simulated microstructures is achieved.

A simulated microstructure with the metallographic plane parallel to the extrusion axis corresponding to blind die compacted and extruded pre-alloyed Ti-6Al-4V-1B modified alloy is shown in Figure 6.1 [104]. Results shown in Figure 6.2 demonstrate that there is a good agreement between the experimental data of the two-point correlation function parallel to the extrusion direction for the real microstructure with the corresponding two-point correlation function of the simulated microstructure.

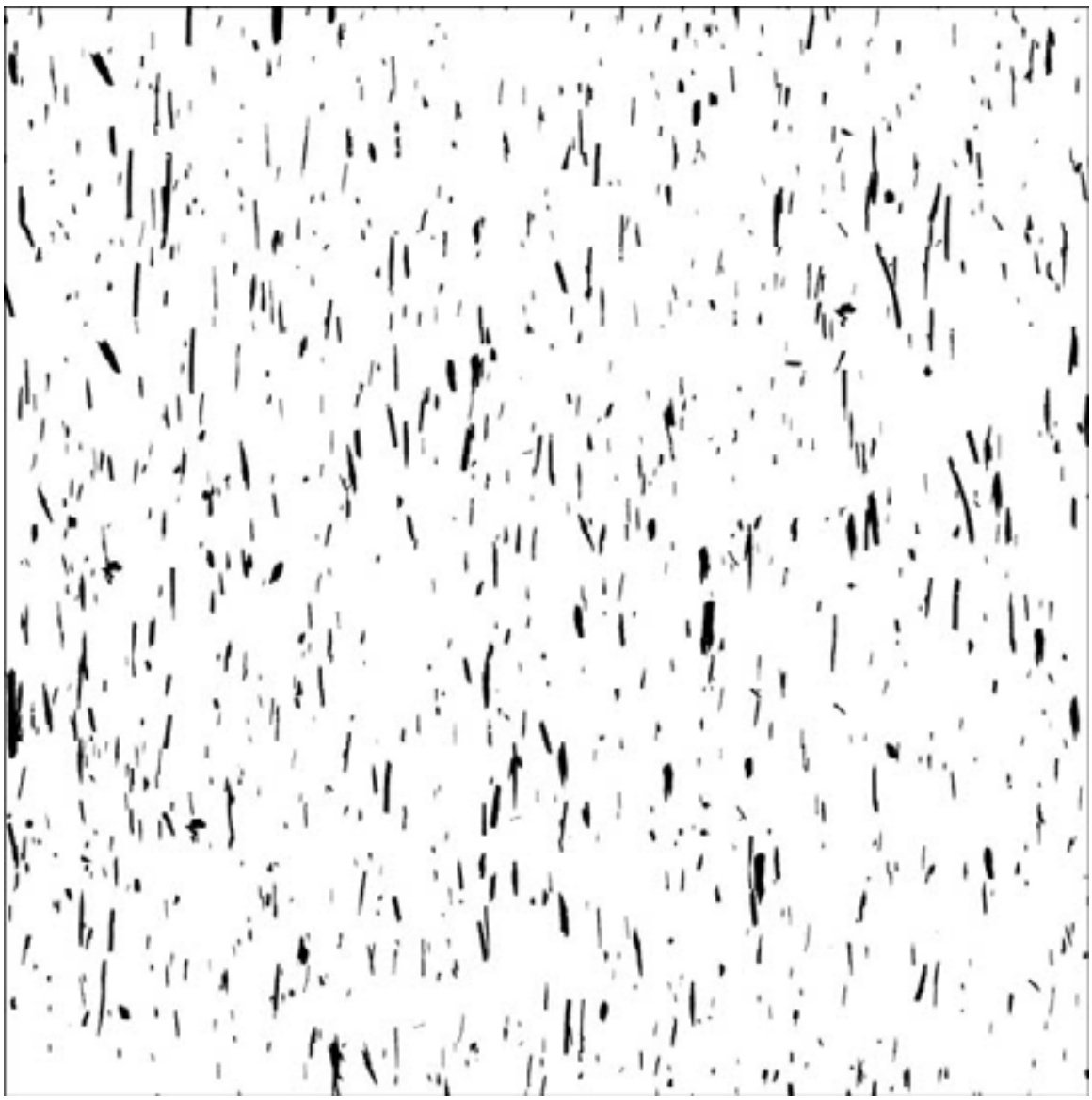

Figure 6.1 A portion of a simulated microstructure corresponding to the real microstructure of extruded pre-alloyed Ti-6Al-4V-1B modified alloy [104].

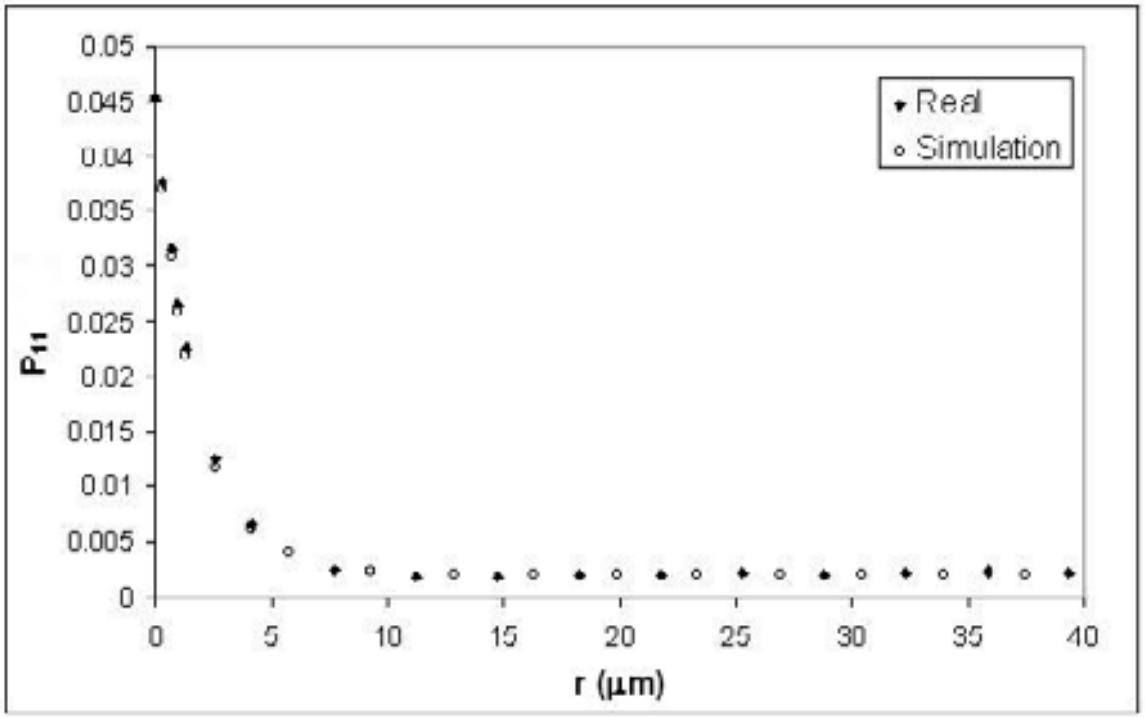

Figure 6.2 Two-point correlation data parallel to the extrusion direction for both the real and simulated microstructures of extruded pre-alloyed Ti-6Al-4V-1B modified alloy [104].

Figure 6.3 depicts a simulated microstructure corresponding to blind die compacted Ti-6Al-4V-1B alloy. Once the simulation model is validated, it is possible to generate virtual microstructures of alloys that have been processed differently than those from which the original data sets were obtained. For example, Figure 6.4 is the simulation of one such partially anisotropic virtual microstructure that may represent the Ti-6Al-4V-1B alloy extruded at a lower extrusion temperature and/or a lower extrusion ratio.

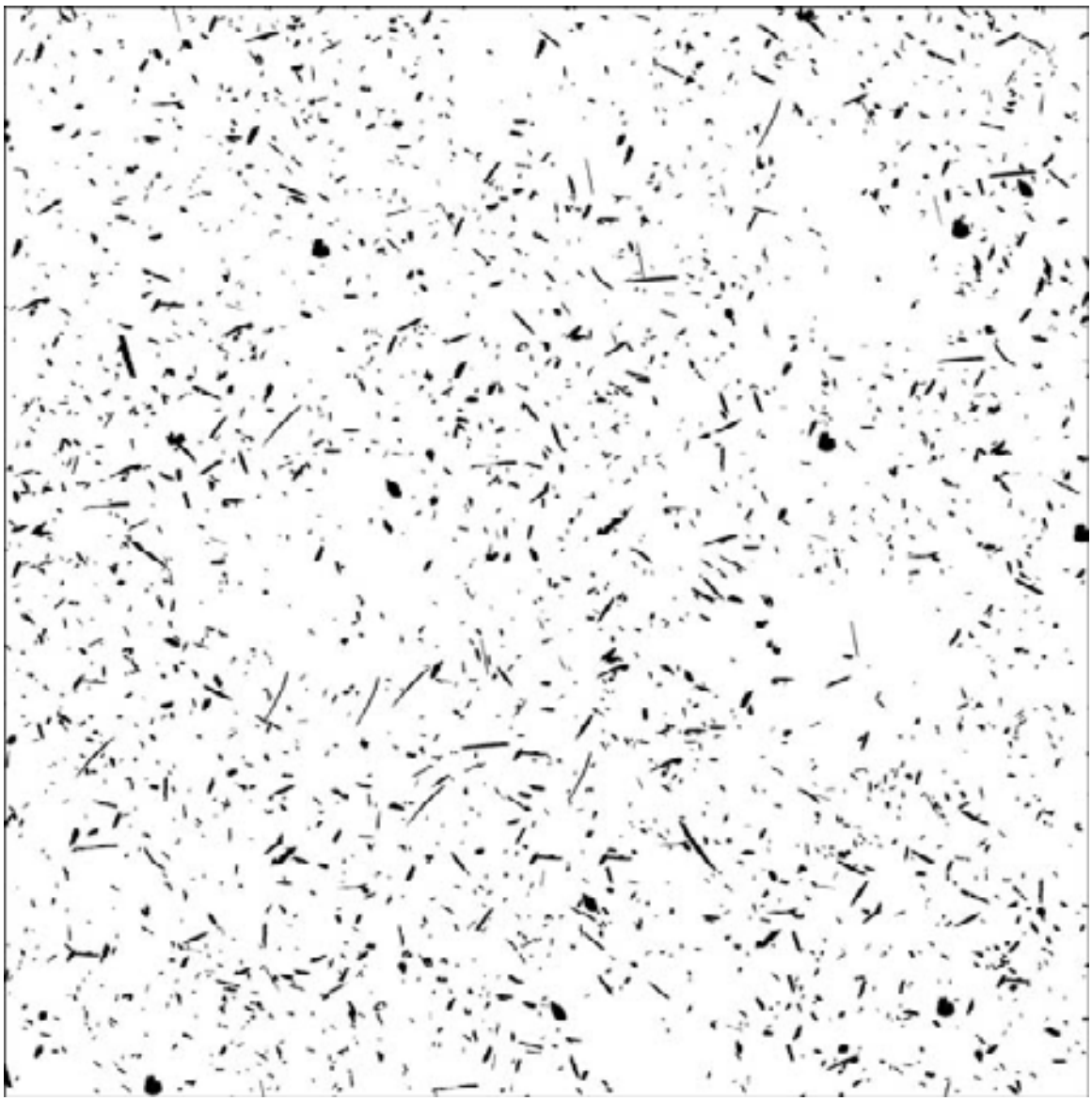

Figure 6.3 A portion of a simulated microstructure corresponding to the real microstructure of compacted pre-alloyed Ti-6Al-4V-1B modified alloy [104].

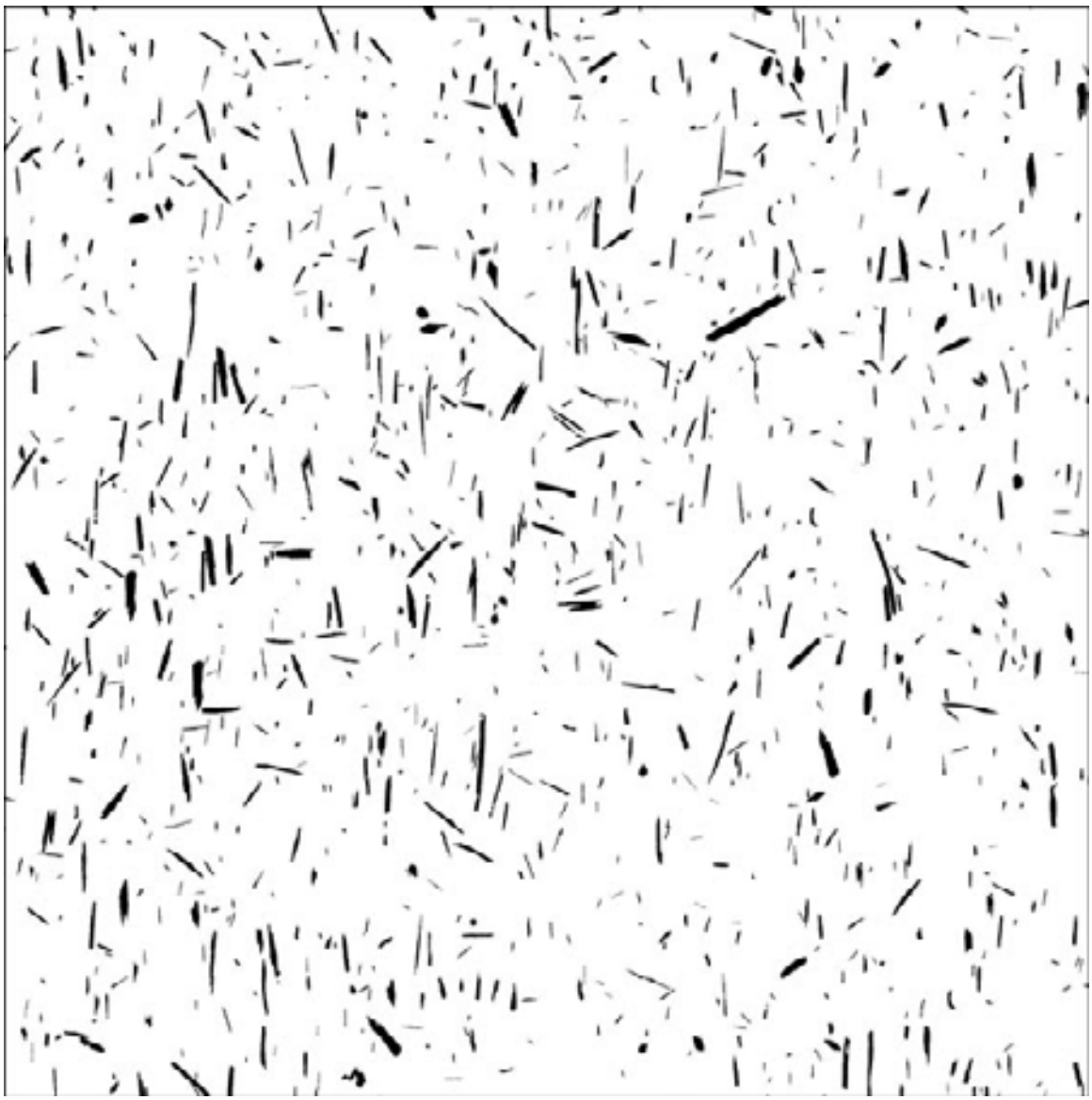

Figure 6.4 A portion of a simulated, partially anisotropic virtual microstructure that may represent a Ti-6Al-4V-1B alloy extruded at lower extrusion temperature and/or a lower extrusion ratio than the microstructure depicted in Figure 6.1 [104].

The simulated images of the real and virtual microstructures can then be implemented in finite element computations to simulate the mechanical response of the corresponding real and virtual materials. Figure 6.5 shows the complementary cumulative distributions of local maximum principal stress in the TiB whiskers under

tensile loading for the three simulated microstructures shown in Figures 6.1 (extruded), 6.3 (compacted), and 6.4 (virtual) [105, 106]. In the microstructures of Figures 6.1 and 6.4, tensile loading is along the extrusion direction. Such simulations can provide useful input for optimization of the processing routes as well as for materials design.

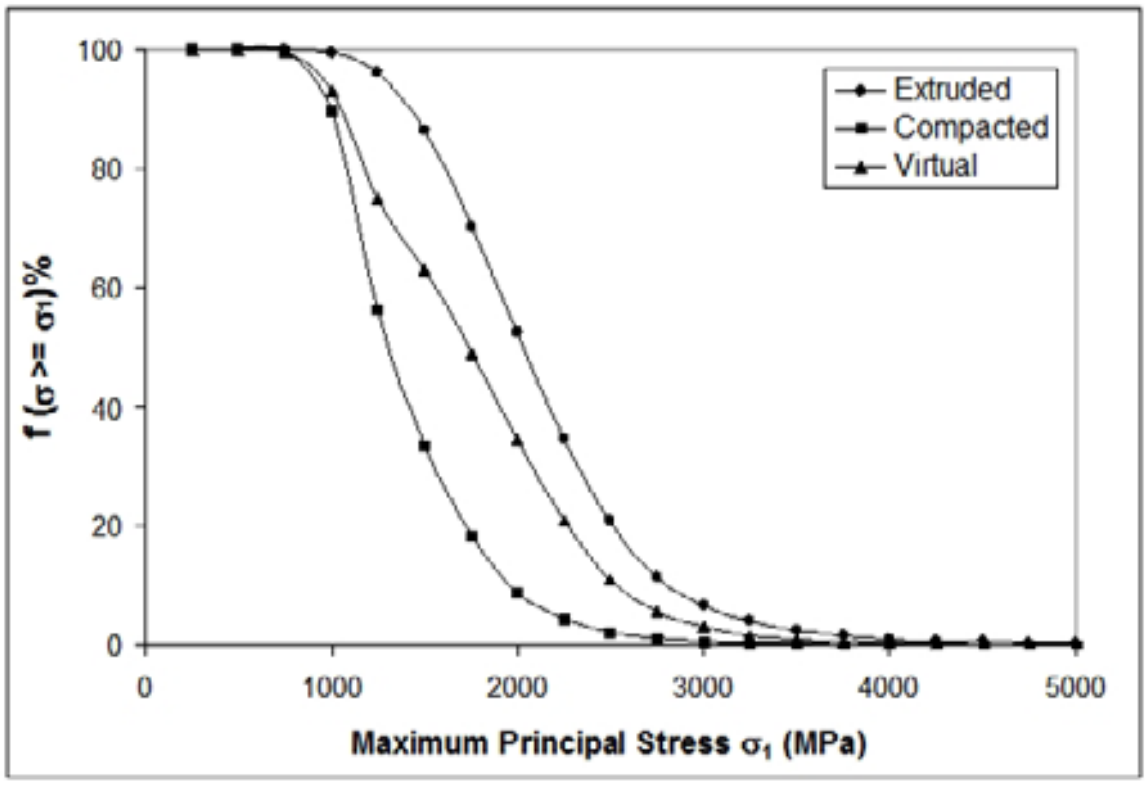

Figure 6.5 The complementary cumulative distributions of local maximum principal stress in the TiB whiskers under tensile loading for the three simulated microstructures shown in Figures 6.1 (extruded), 6.3 (compacted), and 6.4 (virtual). In the microstructures of Figures 6.1 and 6.4, tensile loading is along the extrusion direction [105, 106].

6.3 Determination of TiB Constitutive Properties

Because TiB is stable only within a titanium matrix and forms in situ during high-temperature processing, accurate determination of the mechanical properties is a focus of

current research. Several studies have attempted to determine the properties of both the TiB phase alone and the overall Ti-B modified alloys and composites. Consensus in the field of the properties of TiB remains a goal of these investigations.

This situation is a particular problem for finite element micromechanical analyses of Ti-B materials. Accurate input of material constitutive properties is crucial for finite element-based micromechanical simulations. Because the TiB phases are formed in situ, macroscopic stress-strain data, such as tensile test results, are not suitable (or often available) for micromechanical studies of Ti-B modified alloys and composites. As a result, microindentation coupled with finite element analyses were used to compute the elastic modulus of TiB.

Microindentation provides a continuous record of the variation of indentation load as a function of the depth of penetration into the specimen. From this load-depth curve, properties such as the elastic modulus of a material can be calculated. Microindentation was performed on primary TiB particles in extruded pre-alloyed Ti-6Al-4V-1.6B modified alloy [106]. An indent is shown in Figure 6.6. On the same specimen, 15 indentations (each of 1 μm depth), were placed on different primary TiB whiskers. The resultant load-depth curves are given in Figure 6.7, and show a wide variation in the mechanical response, which is problematic for determining the overall constitutive properties.

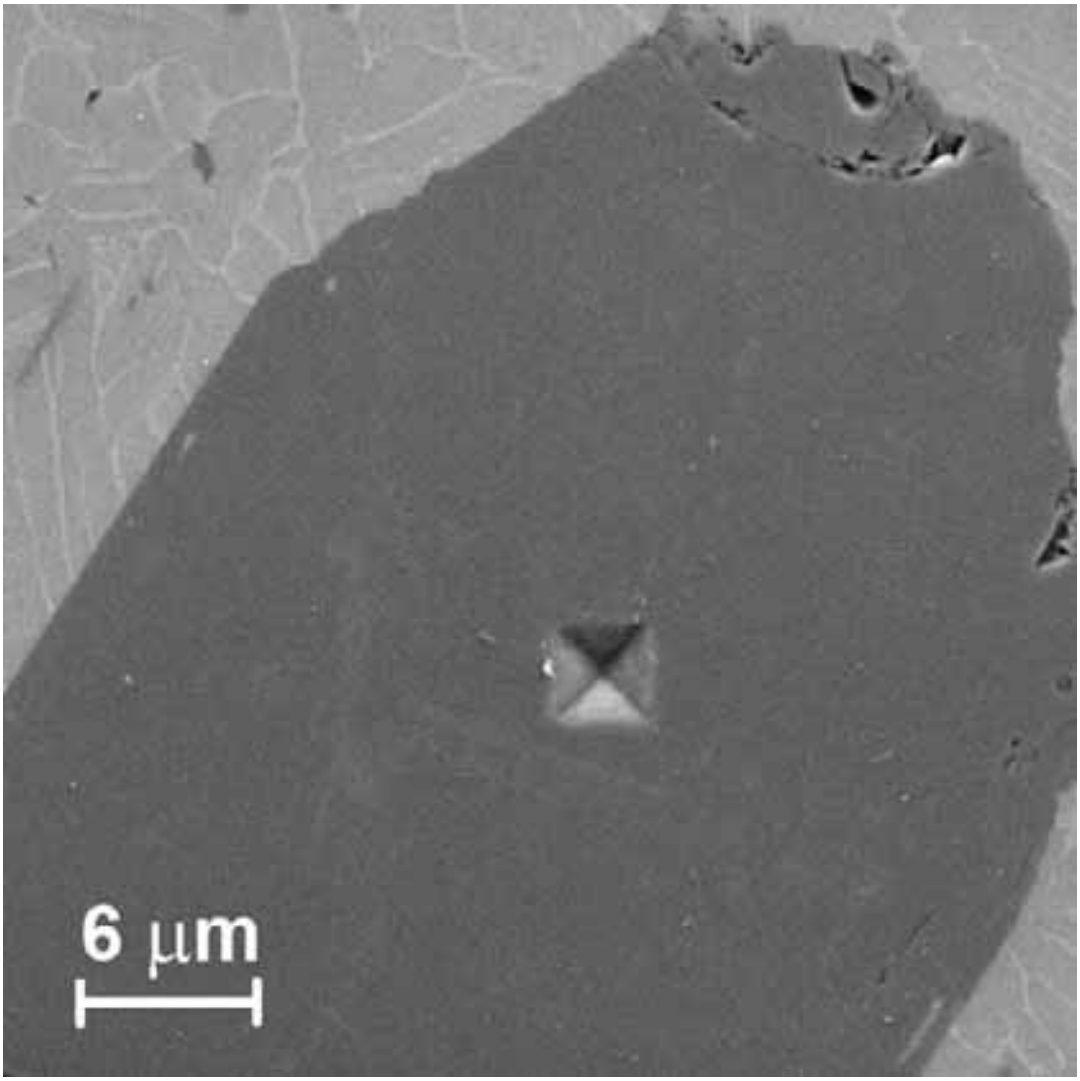

Figure 6.6 Microindent of 1 μm depth on a primary TiB whisker in extruded Ti-6Al-4V-1.6B modified alloy [106].

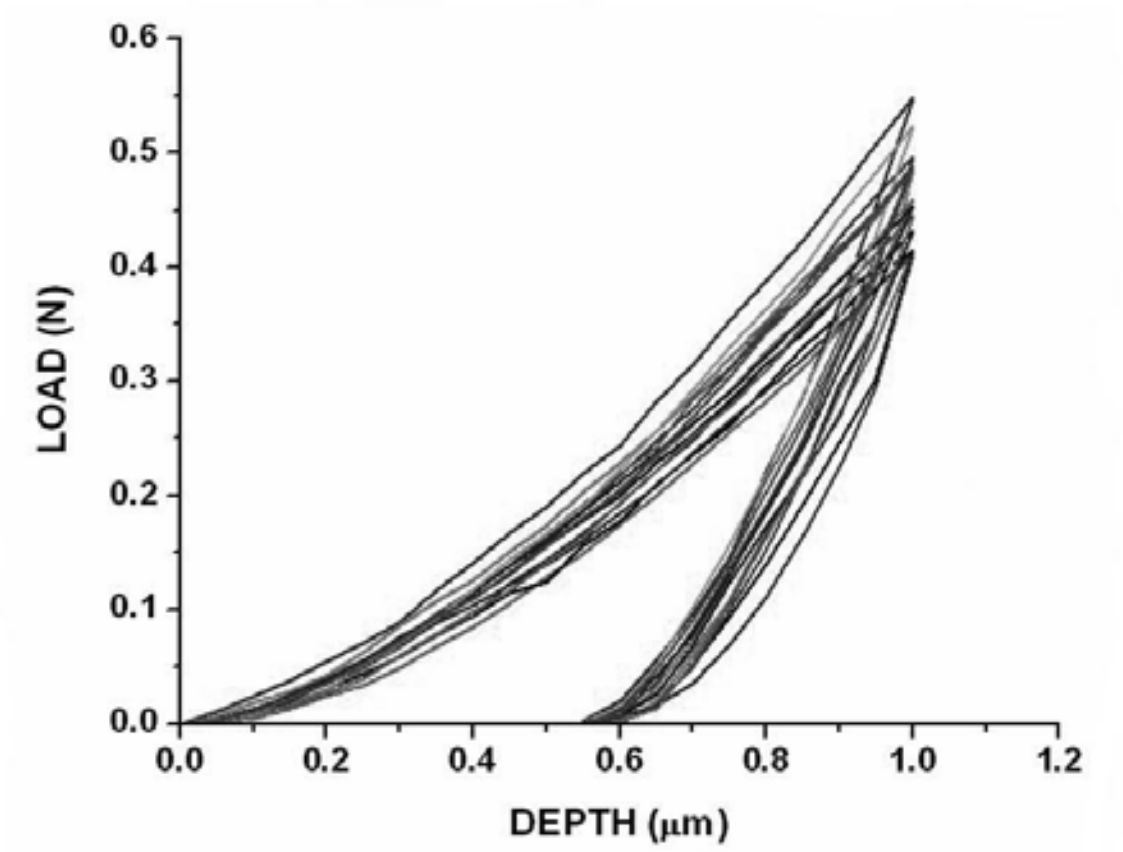

Figure 6.7 Load-depth curves for 15 microindentations of 1 μm depth on primary TiB whiskers in extruded Ti-6Al-4V-1.6B alloy, showing a wide variation in the mechanical response [106].

In order to determine whether the variation was caused by the microindentation apparatus or from the TiB whiskers, multiple indents were placed on the same primary TiB whisker, as shown in Figure 6.8. The three indents showed consistent load-depth curves, as shown in Figure 6.9. This suggests that the variation is not due to the apparatus, but is inherent in the different TiB whiskers in the Ti-6Al-4V-1.6B alloy specimen.

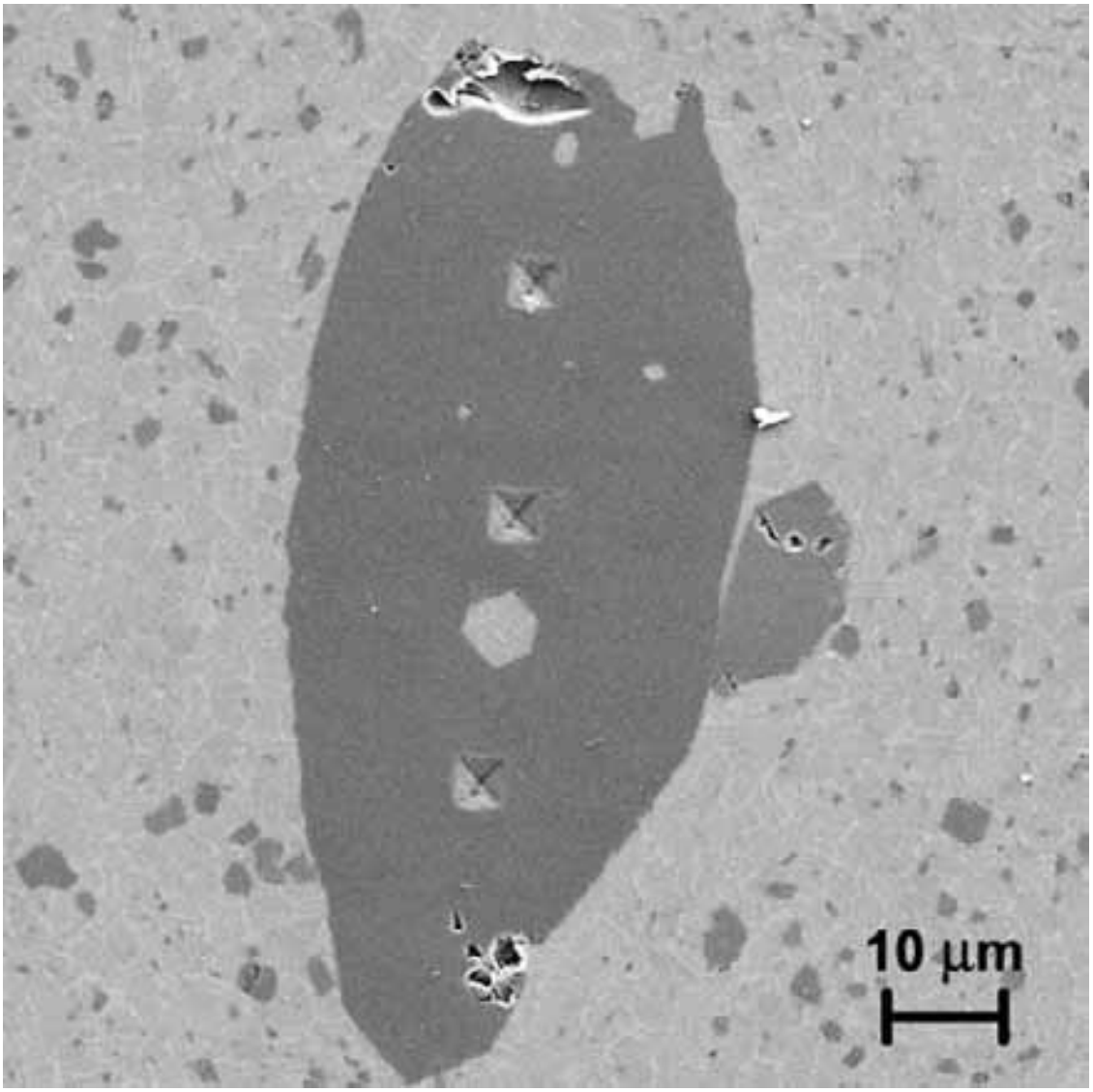

Figure 6.8 Three microindents of 1 μm depth on a primary TiB whisker in extruded Ti-6Al-4V-1.6B modified alloy [106].

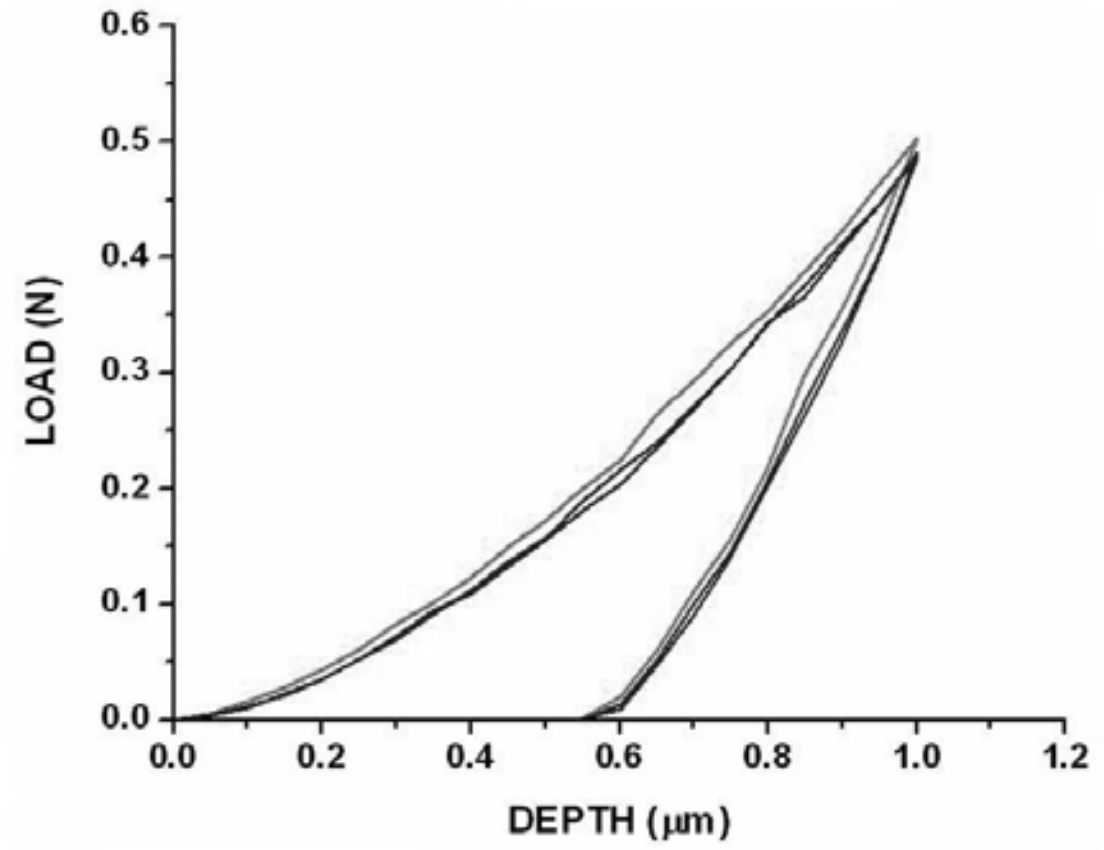

Figure 6.9 Load-depth curves for 3 microindentations of 1 μm depth on the same primary TiB whisker in extruded Ti-6Al-4V-1.6B alloy, showing a consistent mechanical response [106].

It was concluded that the variation in the mechanical response may be attributed to the anisotropy of the primary TiB single crystal whiskers. If indents are placed on TiB whiskers at slightly different alignments with respect to the anisotropic crystallographic orientation of TiB, there will be different micromechanical responses. For simplicity of the simulations, an averaged isotropic behavior is more practical for micromechanical modeling. The averaged load-depth curve for TiB is shown in Figure 6.10.

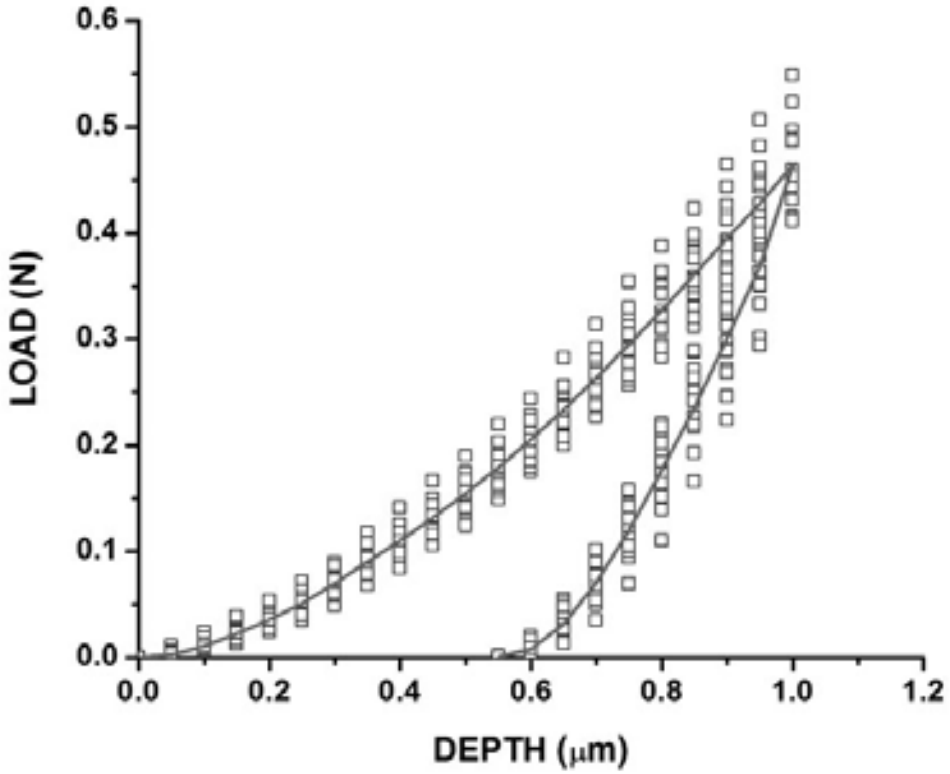

Figure 6.10 Averaged load-depth curve for microindentations of 1 μm depth on primary TiB whiskers in extruded Ti-6Al-4V-1.6B alloy. This averaged isotropic behavior is more practical for micromechanical modeling [106].

Following this conclusion, research colleagues developed a finite element microindentation model to verify the experimental results. The TiB whiskers were assumed to have averaged elastic properties with a kinematic hardening plastic behavior, and the diamond tip indenter was modeled as perfectly elastic. A comparison of the experimental and finite element simulated load-depth curves are shown in Figure 6.11, and show good agreement, confirming the elastic modulus of TiB as approximately 410 GPa.

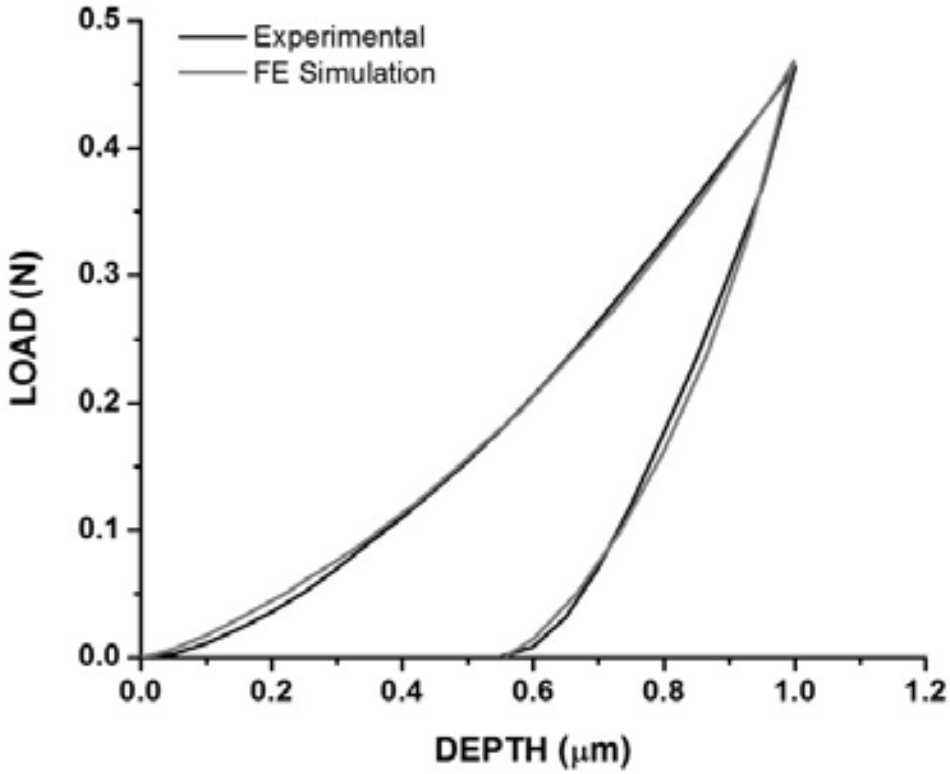

Figure 6.11 Comparison of experimental and simulated load-depth curves for microindentations of 1 μm depth on primary TiB whiskers in extruded Ti-6Al-4V-1.6B alloy [106].

6.4 Conclusions

Conventional characterization procedures, combined with montage serial sectioning and microstructural simulation techniques, are being used to develop new methodologies for materials design. Previous computer prediction models for Ti-B materials have been limited by using simplified, unrealistic morphologies and poorly assumed constitutive values. New methodologies, such as computer simulations using the morphologies from real microstructures, and microindentation to determine the

constitutive properties of TiB phases, are allowing for more accurate predictions of material properties. Overall, Ti-B materials have shown promise for these state of the art materials design methodologies.

CHAPTER 7

RECOMMENDATIONS FOR FUTURE RESEARCH

Research and development of Ti-B materials over the last decade has shown the potential of boron-modified titanium alloys and Ti-B composites in a variety of applications for multiple industries. Significant improvements in critical material properties can be made, with a range of available compositions and processing methods. Further research is necessary, however, before Ti-B materials can achieve full acceptance by commercial industry.

This work has investigated the two leading powder metallurgy techniques for producing Ti-B materials, pre-alloyed and blended elemental, and examined several boron compositions with the Ti-6Al-4V matrix alloy. A composition just below the eutectic point should be studied, to determine the limit of TiB reinforcement that meets the fracture-critical standards for aerospace structural applications in extruded boron-modified Ti-6Al-4V alloys. Lower boron compositions should also be studied for Ti-B materials produced using blended elemental powder metallurgy techniques.

In addition to powder metallurgy, Ti-B materials can be produced by ingot metallurgy techniques such as casting. Boron-modified alloys and Ti-B composites formed using these methods should be investigated, as these are methods often used by industry for large-scale production of titanium alloys. The effect of a mostly liquid processing technique on the alignment of TiB whiskers will need to be more fully understood.

The thermomechanical processing (TMP) technique of extrusion was extensively studied in this work, showing alignment of TiB whiskers. Other important TMP techniques, such as forging and rolling, should also be studied to determine their effects on TiB alignment. Near-net shape processing methods are important for commercial production, and industry acceptance of Ti-B materials is more likely if it can be demonstrated that these methods are capable of forming improved titanium alloys and composites with TiB reinforcement.

Examination of the boron-modified Ti-6Al-4V alloys produced by hot isostatic pressing (HIP) in this work showed the presence of a small amount of porosity. This porosity would be detrimental to the material properties of Ti-B materials. Further studies are needed to determine if the TiB reinforcement has an effect on the formation of porosity in these alloys, and whether porosity can be eliminated in boron-modified Ti-6Al-4V alloys produced by HIP.

This work focused exclusively on TiB reinforcement in the Ti-6Al-4V alloy matrix, the most widely used titanium alloy. Ti-B materials using other common titanium alloys also warrant further investigations. Particularly for biomedical applications, Ti-6Al-4V alloys cannot be used because vanadium is toxic in vivo. Studies are needed to determine if the effects and behavior of TiB reinforcement phases are consistent between different titanium alloys.

This research, and other work in the field, has shown that heating and cooling rates during processing have significant effects on the spatial length scale of the TiB reinforcement phases. This study has shown similar anisotropic whisker morphologies amongst all TiB phases, suggesting that greater understanding of the heating and cooling

rates in the processing of Ti-B materials will result in improved accuracy in predicting the microstructures and resultant mechanical properties. Optimization of the processing techniques for particular applications could be achieved with this insight.

While conducting this research, input was provided to colleagues at the Air Force Research Laboratory (AFRL) in their development of an automated serial sectioning system, *Robo-Met.3D* [107]. Successful efforts have been made in using this system to examine unreinforced metal alloys and other materials that are uniform and relatively soft, but boron-modified titanium alloys and Ti-B composites are more complicated due to the significant differences in hardness between the titanium alloy matrix and the TiB intermetallic reinforcement phases. Further work on the *Robo-Met.3D* system, likely in conjunction with the metallography industry, is needed before Ti-B materials can be successfully serial sectioned with this apparatus. Automated serial sectioning of Ti-B materials, however, would make the study of the microstructures of these modified alloys and composites significantly more efficient.

CHAPTER 8

SUMMARY AND CONCLUSIONS

Specimens of boron-modified Ti-6Al-4V alloys and Ti-B composites were studied using conventional characterization techniques, optical microscopy, scanning electron microscopy, and newly developed techniques such as montage serial sectioning for three-dimensional microstructural visualization. All samples were produced by powder metallurgy processing methods in use for titanium alloys. Insight was gained into how the TiB reinforcement phases are affected by the processing parameters and how these phases affect the microstructure and resultant mechanical properties of the overall Ti-B material.

Samples of boron-modified Ti-6Al-4V alloys were produced using pre-alloyed (PA) powder metallurgy processes. Two compositions were chosen, hypereutectic Ti-6Al-4V-1.6B and hypoeutectic Ti-6Al-4V-1B, to examine the microstructures in different regimes of the quaternary system of titanium, alloying elements aluminum and vanadium, and boron. Samples of each blind die compacted alloy also underwent hot extrusion to examine the effect of this type of thermomechanical processing on the microstructures and resultant material properties.

The hypereutectic alloy, Ti-6Al-4V-1.6B, showed the presence of two different TiB phases, a fine eutectic TiB phase and a coarser primary TiB phase. From observations via optical microscopy and three-dimensional visualization using montage-based serial sectioning, both phases showed an anisotropic whisker morphology with

roughly hexagonal cross-sections. For the primary TiB phase, this conclusion differed from previous assumptions about the morphology of this phase, where an equiaxed cluster morphology had been suggested.

Extrusion of this alloy showed TiB whisker alignment with the extrusion direction, with no damage to the TiB phases or change in morphology observed. Examination of the tensile fracture surfaces of both compacted and extruded samples revealed brittle fracture down the length of TiB whiskers in the compacted sample, and across the width of aligned TiB whiskers in the extruded sample (with the TiB whiskers aligned by extrusion in the tensile direction). The Ti-6Al-4V matrix showed relatively ductile fracture. Extrusion improved the yield strength and ultimate tensile strength while effectively doubling the tensile elongation to failure. These samples, however, did not meet the fracture-critical properties required for aerospace structural applications.

The hypoeutectic alloy, Ti-6Al-4V-1B, showed only the presence of the eutectic TiB phase. No primary TiB was observed, as expected. The eutectic TiB whiskers in this alloy had a similar morphology to those in the hypereutectic alloy, although they were present in smaller amounts due to the decreased amount of boron in the composition of this alloy.

Extrusion of this alloy also showed TiB whisker alignment with the extrusion direction, with no damage to the TiB whiskers or change in morphology observed. Examination of the tensile fracture surfaces of both compacted and extruded samples again revealed brittle fracture down the length of TiB whiskers in the compacted sample, and across the width of aligned TiB whiskers in the extruded sample (with the TiB whiskers aligned by extrusion in the tensile direction). The Ti-6Al-4V matrix showed

relatively ductile fracture. Similarly to the hypereutectic alloy, extrusion improved the yield strength and ultimate tensile strength while effectively doubling the tensile elongation to failure. The extruded sample of this alloy exceeded the fracture-critical properties required for aerospace structural applications while also significantly improving the mechanical properties compared to unreinforced Ti-6Al-4V.

Samples of Ti-B composites were produced utilizing blended elemental (BE) powder metallurgy processes. Unlike pre-alloying, BE processes are conducted entirely in the solid state. Two different compositions were chosen, Ti-6Al-4V-1.7B and Ti-6Al-4V-2.9B, and the composites were produced by blind-die compaction. A sample of the Ti-6Al-4V-2.9B composite was also hot extruded.

From observations via optical microscopy and three-dimensional visualization using montage-based serial sectioning, both Ti-B composites showed microstructures containing a unimodal size and morphology distribution of TiB whiskers. These TiB whiskers were somewhat larger on average than the eutectic TiB whiskers seen in the PA boron-modified alloys, but smaller than the primary TiB particles in those alloys. The anisotropic whisker morphology with roughly hexagonal cross-sections was similar to the eutectic and primary TiB morphologies in the PA boron-modified alloys. Observation of the extruded Ti-6Al-4V-2.9B composite using optical microscopy showed alignment of the TiB whiskers with the extrusion direction.

Examination of the tensile fracture surfaces of both compacted and extruded samples of the Ti-6Al-4V-2.9B composite revealed brittle fracture down the length of TiB whiskers in the compacted sample, and across the width of aligned TiB whiskers in

the extruded sample (with the TiB whiskers aligned by extrusion in the tensile direction). The Ti-6Al-4V matrix showed relatively ductile fracture. Extrusion improved the yield strength and ultimate tensile strength while effectively doubling the tensile elongation to failure. These samples, however, did not meet the fracture-critical properties required for aerospace structural applications, although the extruded Ti-6Al-4V-2.9B composite sample demonstrated an elastic modulus in the range of steel alloys.

Samples of extruded Ti-6Al-4V-1B modified alloy were produced using three different extrusion ratios and at three different extrusion temperatures (following compaction by hot isostatic pressing (HIP) of pre-alloyed powders), to investigate the effect of these processing parameters on the resultant microstructures and material properties. Optical microscopy and characterization using conventional stereology techniques suggested the presence of a sub-micron precipitated TiB phase in addition to the eutectic TiB whiskers. A small amount of porosity was also observed in all of the extruded samples. Measurement of the angular orientation of the eutectic TiB whiskers demonstrated a sharper range around the extrusion axis with higher extrusion ratios and at higher extrusion temperatures.

Scanning electron microscopy confirmed the presence of the sub-micron TiB precipitated phase, as well as showed a whisker-like morphology and alignment with extrusion similar to the larger eutectic TiB whiskers. These observations are crucial to develop accurate materials design methodologies for similar boron-modified titanium alloys.

Montage-based serial sectioning and three-dimensional visualization confirmed alignment with extrusion of the eutectic TiB whiskers, as well as significant TiB coarsening at extrusion temperatures near 1100°C. Although the sub-micron TiB whiskers are present in all of the extruded Ti-6Al-4V-1B samples, they are present in smaller volume fractions in the samples extruded at the highest temperature, which is above the β transus of the alloy. The sub-micron TiB whiskers improved the yield strength and ultimate tensile strength of these alloy samples compared to the previously studied Ti-6Al-4V-1B blind die compacted and extruded alloy, but significantly reduced the tensile elongation to failure, a critical material property for aerospace structural applications.

Conventional characterization procedures, combined with montage serial sectioning and microstructural simulation techniques, are being used to develop new methodologies for materials design. Previous computer prediction models for Ti-B materials have been limited by using simplified, unrealistic morphologies and assumed constitutive values. New methodologies, such as computer simulations using the morphologies from real microstructures, and microindentation to determine the constitutive properties of TiB phases, are allowing for more accurate predictions of material properties. Overall, Ti-B materials have shown promise for these state of the art materials design methodologies.

REFERENCES

1. S. Tamirisakandala, B.V. Vedam, and R.B. Bhat, "Recent Advances in the Deformation Processing of Titanium Alloys," *Journal of Materials Engineering and Performance*, Vol. 12 (6), 2003, 661-673.

2. E.H. Froes, "How to Market Titanium: Lower the Cost," *JOM*, Vol. 56 (2), 2004, 39.

3. M.J. Donachie, *Titanium: A Technical Guide*. 2nd edition, Materials Park, OH: ASM International, 2004.

4. K.S. Ravi Chandran and D.B. Miracle, "Titanium-Boron Alloys and Composites: Processing, Properties, and Applications," *JOM*, Vol. 56 (5), 2004, 32, 41.

5. D.B. Miracle, "Metal matrix composites - From science to technological significance," *Composites Science and Technology*, Vol. 65 (15-16), 2005, 2526-2540.

6. S. Tamirisakandala, D.B. Miracle, R. Srinivasan, and J.S. Gunasekera, "Titanium Alloyed with Boron," *Advanced Materials & Processes*, Vol. 162 (12), 2006, 41-43.

7. M.J.R. Barboza, E.A.C. Perez, M.M. Medeiros, D.A.P. Reis, M.C.A. Nono, F.P. Neto, and C.R.M. Silva, "Creep behavior of Ti-6Al-4V and a comparison with titanium matrix composites," *Materials Science and Engineering A*, Vol. 428 (1-2), 2006, 319-326.

8. E.W. Collings, *The Physical Metallurgy of Titanium Alloys*. ASM Series in Metal Processing, ed. F. Harold L. Gegel, Metals Park, OH: American Society for Metals, 1984.

9. S. Tamirisakandala, R.B. Bhat, D.B. Miracle, S. Boddapati, R. Bordia, R. Vanover, and V.K. Vasudevan, "Effect of boron on the beta transus of Ti-6Al-4V alloy," *Scripta Materialia*, Vol. 53 (2), 2005, 217-222.

10. J. Tiley, T. Searles, E. Lee, S. Kar, R. Banerjee, J.C. Russ, and H.L. Fraser, "Quantification of microstructural features in α/β titanium alloys," *Materials Science and Engineering A*, Vol. 372 (1-2), 2004, 191-198.

11. D.E. Alman and J.A. Hawk, "The abrasive wear of sintered titanium matrix-ceramic particle reinforced composites," *Wear*, Vol. 225-229 (Part 1), 1999, 629-639.

12. T.B. Massalski, J.L. Murray, L.H. Bennett, and H. Baker, eds. *Binary Alloy Phase Diagrams*. Metals Park, OH: American Society for Metals, 1986.

13. X. Ma, C. Li, Z. Du, and W. Zhang, "Thermodynamic assessment of the Ti-B system," *Journal of Alloys and Compounds*, Vol. 370 (1-2), 2004, 149-158.

14. Z. Xinghong, X. Qiang, H. Jiecai, and V.L. Kvanin, "Self-propagating high temperature combustion synthesis of TiB/Ti composites," *Materials Science and Engineering A*, Vol. 348 (1-2), 2003, 41-46.

15. Z. Peng, S.B. Bhaduri, and G.L. Watt, "Synthesis of TiB-TiB_2 Reinforced Titanium Matrix Composites by Combustion Synthesis," *Advanced Synthesis and Processing of Composites and Advanced Ceramics II*, edited by K.V. Logan, Z.A. Munir, and R.M. Spriggs, 1996, 11-18.

16. R. Banerjee, A. Genç, P.C. Collins, and H.L. Fraser, "Comparison of Microstructural Evolution in Laser-Deposited and Arc-Melted *In-Situ* Ti-TiB Composites," *Metallurgical and Materials Transactions A: Physical Metallurgy and Materials Science*, Vol. 35 A (7), 2004, 2143-2152.

17. K.B. Panda and K.S. Ravi Chandran, "First principles determination of elastic constants and chemical bonding of titanium boride (TiB) on the basis of density functional theory," *Acta Materialia*, Vol. 54 (6), 2006, 1641-1657.

18. W.Y. Yang, H.C. Yi, and A. Petric, "Microstructure of the Ti_3Al(Nb)/TiB Composite Produced by Combustion Synthesis," *Metallurgical and Materials Transactions A*, Vol. 26 (11), 1995, 3037-3043.

19. B.F. Decker and J.S. Kasper, "The crystal structure of TiB," *Acta Crystallographica*, Vol. 7, 1953, 77-80.

20. M.E. Hyman, C. McCullough, C.G. Levi, and R. Mehrabian, "Evolution of Boride Morphologies in TiAl-B Alloys," *Metallurgical Transactions A*, Vol. 22, 1991, 1647-1662.

21. B.J. Kooi, Y.T. Pei, and J.T.M. De Hosson, "The evolution of microstructure in a laser clad TiB-Ti composite coating," *Acta Materialia*, Vol. 51 (3), 2003, 831-845.

22. H. Feng, Y. Zhou, D. Jia, and Q. Meng, "Stacking faults formation mechanism of in situ synthesized TiB whiskers," *Scripta Materialia*, Vol. 55 (8), 2006, 667-670.

23. C. Schuh and D.C. Dunand, "Whisker alignment of Ti-6Al-4V/TiB composites during deformation by transformation superplasticity," *International Journal of Plasticity*, Vol. 17 (3), 2001, 317-340.

24. D.X. Li, D.H. Ping, Y.X. Lu, and H.Q. Ye, "Characterization of the microstructure in TiB-whisker reinforced Ti alloy matrix composite," *Materials Letters*, Vol. 16 (6), 1993, 322-326.

25. S. Gorsse, J.P. Chaminade, and Y. Le Petitcorps, "In situ preparation of titanium base composites reinforced by TiB single crystals using a powder metallurgy technique," *Composites Part A: Applied Science and Manufacturing*, Vol. 29 (9-10), 1998, 1229-1234.

26. K. Geng, W. Lu, Y. Qin, and D. Zhang, "In situ preparation of titanium matrix composites reinforced with TiB whiskers and Y_2O_3 particles," *Materials Research Bulletin*, Vol. 39 (6), 2004, 873-879.

27. A. Genç, R. Banerjee, D. Hill, and H.L. Fraser, "Structure of TiB precipitates in laser deposited in situ, Ti-6Al-4V-TiB composites," *Materials Letters*, Vol. 60 (7), 2006, 859-863.

28. S. Tamirisakandala, R.B. Bhat, V.A. Ravi, and D.B. Miracle, "Powder Metallurgy Ti-6Al-4V-xB Alloys: Processing, Microstructure, and Properties," *JOM*, Vol. 56 (5), 2004, 60-63.

29. S. Tamirisakandala, R.B. Bhat, J.S. Tiley, and D.B. Miracle, "Grain refinement of cast titanium alloys via trace boron addition," *Scripta Materialia*, Vol. 53 (12), 2005, 1421-1426.

30. S. Gorsse and D.B. Miracle, "Mechanical properties of Ti-6Al-4V/TiB composites with randomly oriented and aligned TiB reinforcements," *Acta Materialia*, Vol. 51 (9), 2003, 2427-2442.

31. S. Gorsse, Y.L. Petitcorps, S. Matar, and F. Rebillat, "Investigation of the Young's modulus of TiB needles in situ produced in titanium matrix composite," *Materials Science and Engineering A*, Vol. 340 (1-2), 2003, 80-87.

32. R.R. Atri, K.S. Ravichandran, and S.K. Jha, "Elastic properties of in-situ processed Ti-TiB composites measured by impulse excitation of vibration," *Materials Science and Engineering A*, Vol. 271 (1-2), 1999, 150-159.

33. G. Constantinides, K.S. Ravi Chandran, F.-J. Ulm, and K.J. Van Vliet, "Grid indentation analysis of composite microstructure and mechanics: Principles and validation," *Materials Science and Engineering: A*, Vol. 430 (1-2), 2006, 189-202.

34. W.O. Soboyejo, W. Shen, and T.S. Srivatsan, "An investigation of fatigue crack nucleation and growth in a Ti-6Al-4V/TiB in situ composite," *Mechanics of Materials*, Vol. 36 (1-2), 2004, 141-159.

35. T.M.T. Godfrey, A. Wisbey, P.S. Goodwin, K. Bagnall, and C.M. Ward-Close, "Microstructure and tensile properties of mechanically alloyed Ti-6A1-4V with boron additions," *Materials Science and Engineering A*, Vol. 282 (1-2), 2000, 240-250.

36. C.J. Boehlert, C.J. Cowen, S. Tamirisakandala, D.J. McEldowney, and D.B. Miracle, "In situ scanning electron microscopy observations of tensile deformation in a boron-modified Ti-6Al-4V alloy," *Scripta Materialia*, Vol. 55 (5), 2006, 465-468.

37. S. Kumari, N.E. Prasad, K.S.R. Chandran, and G. Malakondaiah, "High-Temperature Deformation Behavior of Ti-TiB_w In-Situ Metal-Matrix Composites," *JOM*, Vol. 56 (5), 2004, 51-55.

38. K. Kawabata, E. Sato, and K. Kuribayashi, "Composite weakening and strengthening of Ti/TiB(w) composites during steady-state creep at high temperature in the [beta]-matrix region," *Scripta Materialia*, Vol. 50 (4), 2004, 523-527.

39. S.I. Rhee, S.W. Nam, and M. Hagiwara, "Effect of TiB_p particle reinforcement on the creep resistance of near [alpha] titanium alloy made by blended elemental powder metallurgy," *Journal of Alloys and Compounds*, Vol. 359 (1-2), 2003, 186-192.

40. C.F. Yolton, "The Pre-Alloyed Powder Metallurgy of Titanium with Boron and Carbon Additions," *JOM*, Vol. 56 (5), 2004, 56-59.

41. T. Saito, H. Takamiya, and T. Furuta, "Thermomechanical properties of P/M [beta] titanium metal matrix composite," *Materials Science and Engineering A*, Vol. 243 (1-2), 1998, 273-278.

42. M. Bram, F. Aubertin, A. Venskutonis, and J. Breme, "Kinetics of the phase transformation and wear resistance of in-situ processed titanium matrix composites based on Ti-Fe-B," *Materials Science and Engineering A*, Vol. 264 (1-2), 1999, 74-80.

43. Z.Y. Ma, S.C. Tjong, and L. Gen, "In-situ Ti-TiB metal-matrix composite prepared by a reactive pressing process," *Scripta Materialia*, Vol. 42 (4), 2000, 367-373.

44. R.B. Bhat, J. Subramanyam, and V.V. Bhanu Prasad, "Preparation of Ti-TiB-TiC & Ti-TiB composites by in-situ reaction hot pressing," *Materials Science and Engineering A*, Vol. 325 (1-2), 2002, 126-130.

45. K.B. Panda and K.S. Ravi Chandran, "Titanium-Titanium Boride (Ti-TiB) Functionally Graded Materials through Reaction Sintering: Synthesis, Microstructure, and Properties," *Metallurgical and Materials Transactions A*, Vol. 34A (9), 2003, 1993-2003.

46. J. Ma, G.E.B. Tan, and Z. He, "Fabrication and Characterization of Ti-TiB_2 Functionally Graded Material System," *Metallurgical and Materials Transactions A*, Vol. 33A (3), 2002, 681-685.

47. M. Kobayashi, K. Funami, S. Suzuki, and C. Ouchi, "Manufacturing process and mechanical properties of fine TiB dispersed Ti-6Al-4V alloy composites obtained by reaction sintering," *Materials Science and Engineering A*, Vol. 243, 1998, 279-284.

48. K. Funami, M. Kobayashi, S. Suzuki, and C. Ouchi, "Superplasticity of fine TiB dispersed Ti-6Al-4V Alloy Composites obtained by Reaction Sintering," *Materials Science Forum*, Vol. 243-245, 1997, 515-520.

49. T. Yamamoto, A. Otsuki, K. Ishihara, and P.H. Shingu, "Synthesis of near net shape high density TiB/Ti composite," *Materials Science and Engineering A*, Vol. 239-240, 1997, 647-651.

50. K. Geng, W. Lu, Z. Yang, and D. Zhang, "In situ preparation of titanium matrix composites reinforced by TiB and Nd_2O_3," *Materials Letters*, Vol. 57 (24-25), 2003, 4054-4057.

51. K. Geng, W. Lu, D. Zhang, T. Sakata, and H. Mori, "Tensile properties of in situ synthesized titanium matrix composites reinforced by TiB and Nd_2O_3 at elevated temperature," *Materials & Design*, Vol. 24 (6), 2003, 409-414.

52. R. Banerjee, A. Genç, D. Hill, P.C. Collins, and H.L. Fraser, "Nanoscale TiB precipitates in laser deposited Ti-matrix composites," *Scripta Materialia*, Vol. 53 (12), 2005, 1433-1437.

53. E.H. Froes, H. Friedrich, J. Kiese, and D. Bergoint, "Titanium in the Family Automobile: The Cost Challenge," *JOM*, Vol. 56 (2), 2004, 40-44.

54. T. Saito, "The Automotive Application of Discontinuously Reinforced TiB-Ti Composites," *JOM*, Vol. 56 (5), 2004, 33-36.

55. T. Saito, "A Cost-Effective P/M Titanium Matrix Composite for Automobile Use," *Advanced Performance Materials*, Vol. 2 (2), 1995, 121-144.

56. T. Saito, H. Takamiya, and T. Furuta, "Hot Workability and Mechanical Properties of a TiB Particle Reinforced PM Beta-Titanium Matrix Composite," *Titanium '95: Science and Technology: proceedings of the Eighth World Conference on Titanium held at the International Convention Centre, Birmingham, UK, 22-26 October 1995*, edited by P.A. Blenkinsop, W.J. Evans, and H.M. Flower, 1995, 2859-2866.

57. T. Saito, T. Furuta, and H. Takamiya, "Sintering Behavior and Thermal Stability of a TiB Particle Reinforced PM Beta-Titanium Matrix Composite," *Titanium '95: Science and Technology: proceedings of the Eighth World Conference on Titanium held at the International Convention Centre, Birmingham, UK, 22-26 October 1995*, edited by P.A. Blenkinsop, W.J. Evans, and H.M. Flower, 1995, 2763-2770.

58. T. Saito, T. Furuta, and H. Takamiya, "Sintered titanium alloy material and process for producing the same," United States Patent No. 6,117,204, September 2000.

59. W. Hanusiak, C.F. Yolton, J. Fields, V. Hammond, and R. Grabow, "The Prospects for Hybrid Fiber-Reinforced Ti-TiB-Matrix Composites," *JOM*, Vol. 56 (5), 2004, 49-50.

60. S. Abkowitz, S.M. Abkowitz, H. Fisher, and P.J. Schwartz, "CermeTi Discontinuously Reinforced Ti-Matrix Composites: Manufacturing, Properties, and Applications," *JOM*, Vol. 56 (5), 2004, 37-41.

61. S. Abkowitz, S.M. Abkowitz, H.L. Heussi, and P.F. Weihrauch, "Titanium composite skate blades," United States Patent No. 6,620,523, September 2003.

62. S. Abkowitz, S.M. Abkowitz, H.L. Heussi, and P.F. Weihrauch, "Titanium composite skate blades," United States Patent No. 6,318,738, November 2001.

63. J. Zhu, A. Kamiya, T. Yamada, W. Shi, and K. Naganuma, "Influence of boron addition on microstructure and mechanical properties of dental cast titanium alloys," *Materials Science and Engineering A*, Vol. 339 (1-2), 2003, 53-62.

64. E.E. Underwood, *Quantitative Stereology*, Reading, MA: Addison Wesley, 1970.

65. R.T. DeHoff and F.N. Rhines, *Quantitative Microscopy*, New York: McGraw-Hill Publishing Co., 1968.

66. S.A. Saltykov, *Stereometric Metallography*. Second edition, Moscow: Metallurgizdat, 1958.

67. A. Tewari, A.M. Gokhale, J.E. Spowart, and D.B. Miracle, "Quantitative Characterization of Spatial Clustering in Three-Dimensional Microstructures Using Two-Point Correlation Functions," *Acta Materialia*, Vol. 52 (1), 2004, 307-319.

68. P.B. Corson, "Correlation functions for predicting properties of heterogeneous materials - I. Correlation functions in multiphase solids," *Journal of Applied Physics*, Vol. 45, 1974, 3159-3164.

69. P.B. Corson, "Correlation functions for predicting properties of heterogeneous materials - III. Effective elastic moduli of two-phase materials," *Journal of Applied Physics*, Vol. 45, 1974, 3171-3179.

70. S. Lin, H. Garmestani, and B. Adams, "The evolution of probability functions in an inelasticly deforming two-phase medium," *International Journal of Solids and Structures*, Vol. 37 (3), 2000, 423-434.

71. H. Garmestani, S. Lin, B.L. Adams, and S. Ahzi, "Statistical continuum theory for large plastic deformation of polycrystalline materials," *Journal of the Mechanics and Physics of Solids*, Vol. 49 (3), 2001, 589-607.

72. P. Louis and A.M. Gokhale, "Computer simulation of spatial arrangement and connectivity of particles in three-dimensional microstructure: Application to model electrical conductivity of polymer matrix composite," *Acta Materialia*, Vol. 44 (4), 1996, 1519-1528.

73. S. Yang, A. Tewari, and A.M. Gokhale, "Modeling of non-uniform spatial arrangement of fibers in a ceramic matrix composite," *Acta Materialia*, Vol. 45 (7), 1997, 3059-3069.

74. S. Yang, A.M. Gokhale, and Z. Shan, "Utility of microstructure modeling for simulation of micro-mechanical response of composites containing non-uniformly distributed fibers," *Acta Materialia*, Vol. 48 (9), 2000, 2307-2322.

75. Z. Shan and A.M. Gokhale, "Representative volume element for non-uniform micro-structure," *Computational Materials Science*, Vol. 24 (3), 2002, 361-379.

76. H. Singh and A.M. Gokhale, "Visualization of three-dimensional microstructures," *Materials Characterization*, Vol. 54 (1), 2005, 21-29.

77. A. Tewari and A.M. Gokhale, "Estimation of three-dimensional grain size distribution from microstructural serial sections," *Materials Characterization*, Vol. 46 (4), 2001, 329-335.

78. M.D. Dighe, A. Tewari, G.R. Patel, T. Mirabelli, and A.M. Gokhale, "Application of digital image processing to reconstruct three-dimensional micro-porosity in a cast A356.0 alloy," *Transactions of the American Foundry Society*, Vol. 99, 2000, 353-356.

79. A. Tewari, Ph.D. Dissertation, Georgia Institute of Technology, 1999.

80. P. Sabella, "Rendering algorithm for visualizing 3D scalar fields," *Computer Graphics (ACM)*, Vol. 22 (4), 1988, 51-58.

81. E. Keppel, "Approximating Complex Surfaces by Triangulation of Contour Lines," *IBM Journal of Research and Development*, Vol. 19 (1), 1975, 2-11.

82. W.E. Lorensen and H.E. Cline, "Marching Cubes: A High Resolution 3D Surface Construction Algorithm," *Computer Graphics (ACM)*, Vol. 21 (4), 1987, 163-169.

83. J.E. Spowart, H.M. Mullens, and B.T. Puchala, "Collecting and Analyzing Microstructures in Three Dimensions: A Fully Automated Approach," *JOM*, Vol. 55 (10), 2003, 35-37.

84. O.M. Ivasishin, Institute for Metal Physics, Ukraine, private communication, 2005.

85. A. Tewari and A.M. Gokhale, "Efficient estimation of number density in opaque material microstructures: the large-area disector," *Journal of Microscopy*, Vol. 200 (3), 2000, 277-283.

86. P. Louis and A.M. Gokhale, "Application of image analysis for characterization of spatial arrangements of features in microstructure," *Metallurgical and Materials Transactions A: Physical Metallurgy and Materials Science*, Vol. 26A (6), 1995, 1449-1456.

87. H. Feng, Y. Zhou, D. Jia, and Q. Meng, "Microstructure and mechanical properties of in situ TiB reinforced titanium matrix composites based on Ti-FeMo-B prepared by spark plasma sintering," *Composites Science and Technology*, Vol. 64 (16), 2004, 2495-2500.

88. ASTM E8-04, "Standard Test Methods for Tension Testing of Metallic Materials," ASTM International.

89. A. Tewari, A.M. Gokhale, and R.M. German, "Effect of gravity on three-dimensional coordination number distribution in liquid phase sintered microstructures," *Acta Materialia*, Vol. 47 (13), 1999, 3721-3734.

90. F.N. Rhines, K.R. Craig, and D.A. Rousse, "Measurement of average grain volume and certain topological parameters by serial section analysis," *Metallurgical Transactions A (Physical Metallurgy and Materials Science)*, Vol. 7A (11), 1976, 1729-1734.

91. R.S. Sidhu and N. Chawla, "Three-dimensional microstructure characterization of Ag_3Sn intermetallics in Sn-rich solder by serial sectioning," *Materials Characterization*, Vol. 52 (3), 2004, 225-230.

92. M. Li, S. Ghosh, O. Richmond, H. Weiland, and T.N. Rouns, "Three dimensional characterization and modeling of particle reinforced metal matrix composites: Pt. I. Quantitative description of microstructural morphology," *Materials Science & Engineering A (Structural Materials: Properties, Microstructure and Processing)*, Vol. A265 (1-2), 1999, 153-173.

93. K.M. Wu and M. Enomoto, "Three-dimensional morphology of degenerate ferrite in an Fe-C-Mo alloy," *Scripta Materialia*, Vol. 46 (8), 2002, 569-574.

94. M.V. Kral, M.A. Mangan, G. Spanos, and R.O. Rosenberg, "Three-dimensional analysis of microstructures," *Materials Characterization*, Vol. 45 (1), 2000, 17-23.

95. T. Yokomizo, M. Enomoto, O. Umezawa, G. Spanos, and R.O. Rosenberg, "Three-dimensional distribution, morphology, and nucleation site of intragranular ferrite formed in association with inclusions," *Materials Science and Engineering A*, Vol. 344 (1-2), 2003, 261-267.

96. S. Abkowitz and P. Weihrauch, "Trimming the Cost of MMCs," *Advanced Materials & Processes*, Vol. 1989, 31-34.

97. S. Abkowitz, H.L. Heussi, H.P. Ludwig, D.M. Rowell, and S.A. Kraus, "Titanium diboride/titanium alloy metal matrix microcomposite material and process for powder metal cladding," United States Patent No. 4,968,348, November 1990.

98. S. Abkowitz, P.F. Weihrauch, S.M. Abkowitz, and H.L. Heussi, "The Commercial Application of Low-Cost Titanium Composites," *JOM*, Vol. 47 (8), 1995, 40-41.

99. R.B. Bhat, S. Tamirisakandala, D.B. Miracle, and V.A. Ravi, "Thermomechanical Response of a Powder Metallurgy Ti-6Al-4V Alloy Modified with 2.9 Pct Boron," *Metallurgical and Materials Transactions A*, Vol. 36A (March 2005), 2005, 845-857.

100. G.I. Giannopoulos, D. Karagiannis, and N.K. Anifantis, "Micromechanical modeling of mechanical behavior of Ti-6Al-4V/TiB composites using FEM analysis," *Computational Materials Science*, In Press, Corrected Proof, 2006.

101. H. Singh, Y. Mao, A. Sreeranganathan, and A.M. Gokhale, "Application of digital image processing for implementation of complex realistic particle shapes/morphologies in computer simulated heterogeneous microstructures," *Modelling and Simulation in Materials Science and Engineering*, Vol. 14 (3), 2006, 351-363.

102. H. Singh, A.M. Gokhale, Y. Mao, and J.E. Spowart, "Computer simulations of realistic microstructures of discontinuously reinforced aluminum alloy (DRA) composites," *Acta Materialia*, Vol. 54 (8), 2006, 2131-2143.

103. Y. Mao, A.M. Gokhale, and J. Harris, "Computer simulations of realistic microstructures of coarse constituent particles in a hot-rolled aluminum alloy," *Computational Materials Science*, Vol. 37 (4), 2006, 543-556.

104. H. Singh and A.M. Gokhale, Private Research, Georgia Institute of Technology, 2006.

105. S.I. Lieberman, H. Singh, Y. Mao, A. Sreeranganathan, A.M. Gokhale, S. Tamirisakandala, and D.B. Miracle, "The Microstructural Characterization and Simulation of Titanium Alloys Modified with Boron," *JOM*, Vol. 59 (1), 2007, 59-63.

106. A. Sreeranganathan and A.M. Gokhale, Private Research, Georgia Institute of Technology, 2006.

107. J.E. Spowart, "Automated serial sectioning for 3-D analysis of microstructures," *Scripta Materialia*, Vol. 55 (1), 2006, 5-10.